The Tropopause Region Thermal Structure and Tropical Cyclones

by

Daniel Michael Gilford

B.S., The Florida State University (2012)

Submitted to the Department of Earth, Atmospheric, and Planetary Sciences
in partial fulfillment of the requirements for the degree of

Doctor of Philosophy in Atmospheric Science

at the

MASSACHUSETTS INSTITUTE OF TECHNOLOGY

February 2018

Author .....
Department of Earth, Atmospheric, and Planetary Sciences
January 12, 2018

Certified by .....
Susan Solomon
Lee and Geraldine Martin Professor of Environmental Studies
Thesis Supervisor

Accepted by .....
Robert D. van der Hilst
Schlumberger Professor of Earth and Planetary Sciences
Head of Department of Earth, Atmospheric, and Planetary Sciences

The Tropopause Region Thermal Structure and Tropical Cyclones

by

Daniel Michael Gilford

Submitted to the Department of Earth, Atmospheric, and Planetary Sciences
on January 12, 2018, in partial fulfillment of the
requirements for the degree of
Doctor of Philosophy in Atmospheric Science

Abstract

This thesis is an exploration of two seemingly unrelated questions: First, how do water vapor and ozone variations radiatively influence the thermal structure of the tropopause region? Second, what sets the thermodynamic limits of tropical cyclone intensity across the seasonal cycle? The link between these subjects is tropical cyclone outflow, which often reaches into the tropopause region, allowing the thermal structure there to impact tropical cyclone potential intensity.

A radiative transfer model is employed to calculate the radiative effects of the 2000 and 2011 tropopause region abrupt drops—events in which temperatures, water vapor, and ozone plunge suddenly to anomalously low levels. Results show that radiative effects partially offset in the region above the tropopause, but nonlocally combine to cool the layers below the tropopause. Persistently low water vapor concentrations associated with the abrupt drops spread to extratropical latitudes, and produce a total negative radiative forcing that offsets ∼12% of the carbon dioxide forcing over 1990-2013.

Next, the importance of local and nonlocal radiative heating/cooling for tropopause region temperature seasonal cycles is examined. The radiative effects of water vapor seasonality are weak and local to the tropopause, whereas ozone radiatively amplifies temperature seasonality in the tropopause region by 30%, in part because stratospheric ozone seasonality nonlocally affects the tropopause region thermal structure.

To determine how the tropopause region thermal structure affects thermodynamic limits on tropical cyclone intensity, this study presents the first comprehensive seasonal cycle climatology of potential intensity. Perennially warm sea surface temperatures in the Western Pacific result in outflow altitudes that are near the tropical tropopause region throughout the seasonal cycle, whereas the seasonalities of other ocean basins are less influenced by the tropopause region. Probing the potential intensity environmental drivers reveals that the seasonality of near-tropopause temperatures in the Western Pacific damps potential intensity seasonal variability by ∼30%. Incorporating a best track tropical cyclone archive shows that this result

is relevant for real-world tropical cyclones: the tropopause region thermal structure permits intense Western Pacific tropical cyclones in every month of the year, which may have critical consequences for coastal societies.

Thesis Supervisor: Susan Solomon
Title: Lee and Geraldine Martin Professor of Environmental Studies

Acknowledgments

I cannot look back at my MIT experience without significant gratitude.

I am deeply grateful to Professor Susan Solomon for her support as my advisor at MIT. Her insights greatly improved the style and science of each of these chapters, and her unceasing optimism has re-routed many of my natural pessimistic instincts. I appreciate her including me in the sea-level rise research, which was a wonderful opportunity to explore a new arena in climate science. Thank you, Susan, for your patience and expertise while molding me into a scientist. Without your financial, academic, and personal support, this thesis couldn't have happened. If I become even a fraction of the scientist you are, I will count my career a great success.

Thank you to my committee members, who have each played a vital role in this process. I want to thank Kerry Emanuel for helpful advice and teaching me so much about tropical cyclones. Thanks to Paul O'Gorman, who advised me for my second generals project and continued to support me in my thesis work. Thanks Qiang Fu for being willing to wake up early for meetings and for being continually enthusiastic about our research.

I would like to thank Melissa Griffin who first taught me how to program (and probably encouraged my addiction to morning coffee!). Thanks to Anthony Arguez for his encouragement in programming, statistics, and professional development. I wouldn't have considered applying to MIT without Professor Zhaohua Wu's gentle push, I am grateful for his confidence in my passion for science.

Much of this thesis has been published in volumes of the *Journal of Climate* by the American Meteorological Society (AMS). I appreciate the time and constructive comments of each AMS editor and reviewer. The cluster where the vast majority of my model runs and data analyses were conducted is managed by Greg Shomo and Jeff Scott. They promptly answered my frantic emails mid-morning when the server went down, helped me get CESM running again and again when it kept crashing, etc. Thanks Jeff and Greg.

Basic scientific research isn't possible without funding. My first year was partially

supported by the AMS Graduate Fellowship. My third through fifth years were partially supported by the NASA Earth Science and Space Science Fellowship Program (Grant NNX14AK83H). Finally, much of this work was supported by NSF Grant AGS-1461517. I also want to thank the PAOC Houghton Fund and its committee for often providing travel assistance these past five years, which enabled me to share my work from Phoenix, AZ to Edinburgh, Scotland. Thanks also to Roberta Allard and Margaret Lankow, who both helped immensely with all things travel, journal submissions, staplers, etc.

I've enjoyed so many transformative moments with amazing colleagues at MIT. In no particular order, these are Jareth, Andy, Andy, Vince, Aditi, Tom, Charles, Marianna, Brian, Colin, Maria, Alli, Diamy, Paul, Catherine, Erik, Megan, Alec, Mike, Michael, Rohini, and so many more. Thanks to everyone who accommodated my love for games by participating in Gilford Game Nights. I must especially thank Justin for his daily friendship and putting up with me as an officemate for over five years. I am grateful to Sarvesh, a great friend and communicator who consistently challenges me to think about the world differently. And finally, although there were (are?) so many Daniels in the department, it was Daniel Rothenberg that became such a wonderful friend and reliable colleague; thanks Daniel.

I'm deeply indebted to my family: Mom, Dad, Luke, and Tom and Karon, for steady love and support. These hundreds of miles make sharing life difficult, but I hope in the end it is worth it. Finally, I want thank my beautiful wife, Kaley. Your love, kindness, sacrifice, and encouragement in this process was the glue that held me together. You are the living embodiment of God's grace in my life.

Who causes the vapors to ascend from the ends of the earth,
Who makes lightnings for the rain,
Who brings forth the wind out of his treasuries?
(Psalm 135, ACV)

Contents

List of Figures

List of Tables

Chapter 1

Overview

The famous "Blue Marble" image is at once stunning in its colorful contrast with the dark depths of space, and evocative of our home planet's vulnerability and isolation. The striking hues of blue and white that cover Earth reveal the presence of the molecule that sets our home planet apart from most others in the known universe: water (Fig. 1-1a). Water is not only critical for life, but is also an essential piece of the climate system in each of its three phases. The earth's oceans regulate and store heat. Clouds, ice, and snow strongly impact the Earth's solar reflectivity. Tropical cyclones and midlatitude storms redistribute atmospheric heat horizontally and vertically. Water vapor is an extremely active radiative species and warms the surface as a powerful greenhouse gas. (And this list is by no means comprehensive.)

Though it may be the least obvious in the Blue Marble depiction, this latter property of water vapor—its radiative effect—is perhaps most compelling. Water vapor molecules are strong absorbers and emitters of longwave terrestrial radiation (and to a much lesser extent, absorbers of solar radiation). Water vapor warms the surface by emitting longwave radiation downward (its greenhouse effect) and simultaneously net cools the middle troposphere by emitting radiation from relatively warm atmosphere layers back out to space. This cooling effect persists with height, though its magnitude falls off as temperatures cool and water vapor concentrations are reduced. Temperature and water vapor are strongly linked through the Clausius-Clapeyron relationship; vapor pressures that exceed the saturation vapor pressure (a

function of temperature alone) will condense or deposit out, so as the temperature falls off with the tropospheric lapse rate, water vapor concentrations do as well.

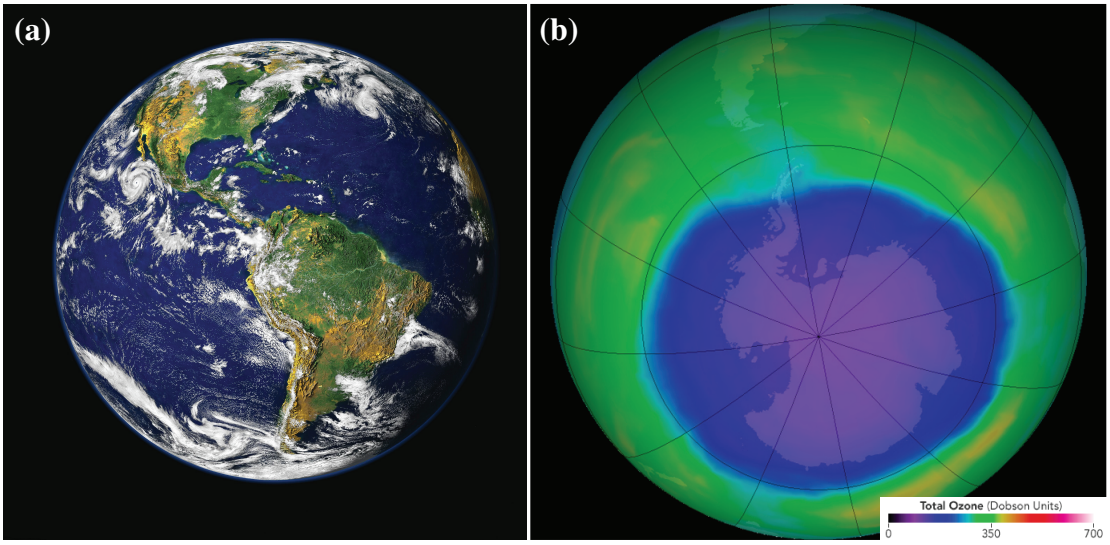

Figure 1-1: (a) The "Blue Marble", a satellite composite true-color image of Earth. Created by Stöckli, Nelson, and Hasler (2000, Laboratory for Atmospheres, Goddard Space Flight Center, NASA). (b) A satellite composite of the 2015 "ozone hole" on October 2nd. Created by the NASA Ozone Hole Watch (Goddard Space Flight Center, NASA).

Rather than continue to fall off with height, higher in the atmosphere the temperature profile warms considerably, in the region known as the stratosphere. Ozone molecules, which are produced and reside in the stratosphere, dominate its thermal profile through absorption of high energy solar radiation. This absorption is critical for life on earth, as harmful ultraviolet rays are largely unable to penetrate the ozone layer and reach the planet's surface. Ozone also absorbs and emits longwave radiation, a property which enables satellite observations to provide a global perspective on ozone. Although satellites were not the first instruments to detect the "ozone hole," in the late 1980s they produced a second famous image in earth science (e.g. Fig. 1-1b) which confirmed the extent of polar ozone depletion and helped galvanize public opinion against ozone-destroying chlorofluorocarbons (Morrisette, 2009). The ozone hole presents a clear narrative: ozone's dominant radiative absorption and emission diminishes with reduced concentrations, presenting public health risks and altering the stratospheric radiative budget. At low latitudes, lower stratospheric

ozone depletion is lessened, and ozone's radiative warming persists even though mean concentrations are much smaller and local ultraviolet radiation is weaker (having been largely absorbed above).

These distant layers, the troposphere radiatively cooled by water vapor and the stratosphere radiatively warmed by ozone, collide at an interface known as the "tropopause region." This transition region is caught between the distinct properties and circulations of troposphere and stratosphere, and displays elements of both (e.g. Fueglistaler et al., 2009a). It is the barrier that must be traversed by any air parcels (and the chemicals they contain) propagating into the stratosphere. The stratosphere is incredibly dry, with a mean water vapor concentration of only about 5 parts per million by volume. The extremely dry air and the spatial structure of the ozone layer both proved to be historically important. Brewer (1949) and Dobson (1956) used these respective stratospheric observations to infer a global stratospheric circulation that bears their names, with rising motion in the tropics (through the tropopause region) and sinking motions at the poles.

The Brewer-Dobson circulation implies that there must be net radiative heating in the tropical tropopause region to balance its dynamical cooling (e.g. Brewer, 1949; Holton et al., 1995). The radiative sensitivities of water vapor and ozone, sharp opacity changes, and temperature contrasts between the tropopause and the surrounding atmospheric layers mean that both species are critical to the region's radiative balance (Gettelman et al., 2004). Variations in either will transiently change the region's thermal structure and could simultaneously affect the local circulation. Tropical near-tropopause water vapor and ozone concentrations are also strongly tied to the circulation: positive anomalies in upwelling adiabatically cool temperatures, reduce water vapor (via flash-freezing across the very cold tropopause), and advect lower ozone concentrations up through the tropopause region—and vice versa for negative anomalies in upwelling.

Variability in tropical tropopause region upwelling is not infrequent, and it has both stratospheric ("top-down") and tropospheric ("bottom-up") origins (see section 6.2.1). These variations manifest in observations as dramatic temperature and chem-

ical constituent changes. But when water vapor and ozone concentrations change in the radiatively sensitive tropopause region, their radiative impacts do as well. While many studies have explored the individual radiative effects of water vapor and ozone anomalies (e.g. Forster and Shine, 1997, 1999; Randel et al., 2006; Grise et al., 2009; Solomon et al., 2010), their *combined* radiative impacts (in space and time) are not well understood. To what extent do the colliding deviations in the molecules coloring the Blue Marble and the molecules highlighting the ozone hole radiatively influence their interface's thermal structure? Establishing these radiative contributions, and linked nonlocal impacts on the troposphere below, is important for a more complete understanding of climate.

A specific feature on the Blue Marble that often draws the eye (and may be found in Fig. 1-1a) is a violent vortex known as a tropical cyclone; surprisingly, these storms are linked in part to the tropopause region thermal structure. It is difficult to overstate the importance of understanding tropical cyclones. These storms, especially very intense tropical cyclones, cause billions of dollars in damage annually and can exact a heavy human toll on vulnerable populations (Mendelsohn et al., 2012; Rappaport, 2014). But although skill in predicting tropical cyclone tracks has increased over the last three decades, much less progress has been made on predicting tropical cyclone intensities (e.g. Landsea and Franklin, 2013). Gaining a better understanding of the factors important for tropical cyclone intensity is an endeavor with not only scientific but societal benefits.

The tropopause region and tropical cyclone intensities are connected through the tropical cyclone outflow, which often resides in the tropopause region. Fully developed tropical cyclones may be idealized as Carnot heat engines which are supplied energy by enthalpy transfer from the sea surface (e.g. Emanuel, 2003). The efficiency of the heat engine is proportional to the temperature differential between the surface and the tropical cyclone outflow. The associated power output of the idealized heat engine is a limit on the wind speeds of the tropical cyclone, known as potential intensity. Processes which cool or warm tropical cyclone outflow temperatures—such as the radiative effects of tropopause region water vapor and ozone anomalies—will affect

the efficiency and hence the maximum intensity at which a tropical cyclone may spin. The maximum lifetime intensity of an observed tropical cyclone is correlated with, and often limited by, potential intensity (e.g. Emanuel, 2000; Wing et al., 2007).

I seek to answer two questions in this thesis. First, how do the important radiative effects of water vapor and ozone combine in the tropical tropopause region to alter its thermal structure? Then, how do tropopause region temperatures affect tropical cyclone intensities?

In the first half of the thesis (chapters 2 and 3) I begin with an exploration of tropopause region radiative processes. In chapter 2 I employ and test a radiative transfer model to investigate how large interannual anomalies (known as "abrupt drops", e.g. Randel et al. (2006)) in water vapor and ozone can radiatively drive changes in the temperatures of the tropopause region. Although there are local radiative effects related to water vapor and ozone changes in the region just above the tropopause, I also find nonlocal radiative impacts on the thermal structure of the layers just below the tropopause. Unlike the heterogeneous distribution of visible clouds on the Blue Marble, the tropical abrupt drop leads to large patches of low water vapor invisible to the naked eye, which propagate poleward and cover the subtropical lower stratospheric regions. This horizontal redistribution of anomalously low water vapor concentrations contributes about half of its overall radiative effect. Following the 2000 and 2011 abrupt drops, the climate system as a whole was nonlocally affected by large persistent reductions in lower stratospheric water vapor through negative radiative forcing; I find that persistently low abundances of tropopause region water vapor offset about 12% of anthropogenic carbon dioxide forcing over 1990-2013.

The vertically distributed radiative impacts in chapter 2 hint that any consistent vertical structures in water vapor and ozone could have important radiative implications. The most iconic of these is the tropical "tape recorder" signal first fully described by Mote et al. (1996). Following temperature variability through the flash-freezing process in tropopause region, water vapor has a consistent annual cycle of slowly ascending anomalies, with anomalously dry air appearing at the tropopause in the boreal winter, and anomalously moist air appearing in the summer (Fig. 1-2).

The seasonal cycles of tropopause region temperatures in both hemispheres predominantly follow the seasonal cycle of stratospheric wave-driving (Yulaeva et al., 1994), with a minimum in the boreal winter, a maximum in the boreal summer, and an amplitude of nearly 8 K. Accompanying these is a seasonal cycle in ozone that also has a distinct vertical structure: a miniature ozone tape recorder in the lowermost stratosphere. I explore tropopause region water vapor and ozone seasonality in chapter 3, using the radiative transfer methods introduced in the previous chapter to evaluate their "radiative seasonal cycles". I show that water vapor seasonal cycles have a highly localized effect on the lower stratospheric seasonal cycles, damping temperature seasonality there by ∼10%. In contrast, ozone reasserts its role as the dominant stratospheric gas through the lower stratospheric thermal seasonal cycle, amplifying temperature seasonality there by ∼30%. Furthermore, the horizontal structures of ozone seasonality suggests that this amplifying effect is stronger in the northern hemisphere than the southern hemisphere, and vertical structures indicate that about a third of ozone's effect is related to nonlocal longwave radiation from ozone in the stratospheric layers about the tropopause region.

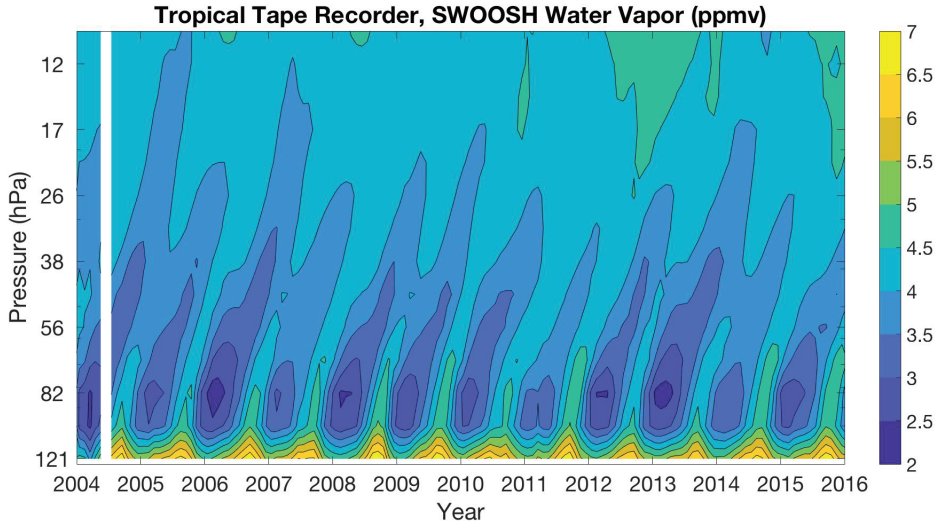

Figure 1-2: The "tropical tape recorder" (e.g. Mote et al., 1996) of stratospheric water vapor averaged between 20°S-20°N from the combined SWOOSH data product (Davis and Rosenlof, 2013). Contours are every 0.5 ppmv and saturate at the colorbar's extent.

The second half of this thesis explores how the seasonal cycles of the tropopause

region thermal structure affect tropical cyclone intensity (chapters 4 and 5). I begin by computing and presenting the first complete climatological analysis of tropical cyclone potential intensity seasonal cycles in chapter 4. This seasonal cycle climatology is particularly relevant in the Western Pacific ocean basin, where tropical cyclones have been historically observed in all months of the year. Western Pacific sea surface temperatures are always warm, allowing tropical cyclone outflow to reach up into the tropopause region year-round. The very cold tropopause temperatures in the boreal winter and warmer tropopause temperatures in the boreal summer combine with a limited sea surface temperature seasonality to flatten the seasonal cycles of Western Pacific tropical cyclone potential intensity, thermodynamically permitting powerful (Saffir-Simpson Category 5) tropical cyclones in every month of the year. North Atlantic (and other ocean basin) potential intensities do not likewise "feel" the tropopause region thermal structure throughout the year, because their sea surface temperatures are more variable. Instead, potential intensities in these regions vary with large seasonal amplitudes, driven almost completely by sea surface temperature seasonal cycles. Lastly, I briefly consider how seasonal potential intensities would change in the absence of ozone layer variations, quantifying ozone's importance for storms with outflow reaching the tropical lower stratosphere.

One may wonder how relevant these tropical cyclone potential intensity seasonal cycles are for the intensities of storms actually observed on the Blue Marble; this is the subject of chapter 5. I combine best track archives of tropical cyclones over the satellite-era with climatological potential intensities to develop a dataset of tropical cyclone maximum intensities along the tracks of each observed historical storm over 1980-2015. The methodology allows me to determine how seasonal differences in real-world tropical cyclone tracks and monthly frequencies affect the interpretation of tropical cyclone potential intensity in the seasonal cycle context. In every month with at least 25 storms, regional along-track seasonal cycles of potential intensity compare favorably with the lifetime maximum intensities of observed tropical cyclones. While most ocean basins have limited storm frequencies outside a traditional hurricane season, observed Western Pacific storms occur year-round, and have maximum intensities

that maintain a relatively flat seasonality. There is a Western Pacific storm intensity depression that is found to be related to warm tropopause region temperatures in the boreal summer, and an accompanying intensity amplification in the colder tropopause months of November and December. This result is a strong indication that the tropopause region thermal structure influences the real-world intensities of tropical cyclones, particularly in the seasonal cycle context.

A summary of the key results from this thesis is presented chapter 6. I connect the broad strokes of my research and consider some open questions that arise at the interface of the Blue Marble and the ozone layer. First, what are the origins of the large persistent water vapor anomalies (i.e. abrupt drops) in the tropopause region, and are they contextually important for lower stratospheric temperatures? Second, what are the respective contributions of radiation and dynamics in the thermal budget of the tropopause region? Third, when tropical cyclone intensities are normalized by their potential intensity are these distributions truly uniform? And what are the implications for tropical cyclone maximum intensities subject to changes caused by, for instance, anthropogenic climate change? Finally, how do tropical cyclone outflow temperatures respond to climate change, and what are the implications for potential intensity? I conclude with a reflection on how our study at the interface speaks to a simple but meaningful question inextricably linking humans and the climate system.

A brief note: Outside the scope of this thesis, but still within the scope of my professional development at MIT, I participated in two major ventures that warrant mention:

First, I co-authored a study (Zickfeld et al., 2017) where we investigated the irreversibility of sea-level rise when the climate system is subjected to the emissions of short-lived climate pollutants (e.g. methane). The primary conclusion of this work was that even if such emissions are ceased altogether, sea level will continue to rise for centuries because of the ocean's thermal inertia. My specific contribution to Zickfeld et al. (2017) was the development/testing of a simple 0-D model to describe

the relationship between radiative forcing, temperature anomalies, and sea-level rise, and the inspiration that climate sensitivity was a key parameter in the simple model.

Second, I served as a teaching assistant (TA) for the course "Global Warming Science" (MIT 12.340x, co-taught by Profs. Kerry Emanuel, Dan Cziczo, and David McGee). Unlike traditional courses at MIT, it was a Massive Open Online Course (MOOC), with over seven thousand students across the globe initially enrolled and hundreds of students actively engaged during the term. As a TA I learned how to manage the logistics of a large/broad course, to moderate climate discussions among students and keep them civil yet engaging, and to rigorously yet clearly teach the science of global warming in an on-call forum.

These opportunities enriched my learning, improved my communication and teaching abilities, and broadened my perspectives on climate science.

Chapter 2

Radiative Impacts of the 2011 Abrupt Drops in Water Vapor and Ozone in the Tropical Tropopause Layer

Abstract

An abrupt drop in tropical tropopause layer (TTL) water vapor, similar to that observed in 2000, recently occurred in 2011, and was concurrent with reductions in TTL temperature and ozone. Previous studies have indicated that such large water vapor variability can have significant radiative impacts. This study uses *Aura* Microwave Limb Sounder observations, the Stratospheric Water Vapor and Ozone Satellite Homogenized dataset, and two radiative transfer models to examine the radiative effects of the observed changes in TTL water vapor and ozone on TTL temperatures and global radiative forcing (RF). The analyses herein suggest that quasi-isentropic poleward propagation of TTL water vapor reductions results in a zonal-mean structure with "wings" of extratropical water vapor reductions, which account for about half of the 2011 abrupt drop global radiative impact. RF values associated with the mean water vapor concentrations differences between 2012/13 and 2010/11 are between -0.01 and -0.09 Wm^{-2}, depending upon the altitude above

This chapter was published in the *Journal of Climate* (Gilford et al., 2015) and is reproduced with permission. The publication is available at `https://doi.org/10.1175/JCLI-D-15-0167.1`.

which perturbations are considered. TTL water vapor and ozone variability during this period jointly lead to a transient radiative cooling of ∼0.25-0.5K in layers below the tropopause. The 2011 abrupt drop also prolonged the reduction in stratospheric water vapor that followed the 2000 abrupt drop, providing a longer-term radiative forcing of climate. Water vapor concentrations from 2005 to 2013 are lower than those from 1990 to 1999, resulting in a RF between these periods of about -0.045 Wm^{-2}, approximately 12% as large as, but of opposite sign to, the concurrent estimated CO2 forcing.

2.1 Introduction

Transport of air from the troposphere to the stratosphere largely occurs across the tropical tropopause layer (TTL), typically located between 20°S to 20°N latitude and from 150 to 70 hPa (Fueglistaler et al., 2009a). Water vapor and ozone concentrations vary in the TTL as air parcels cross the cold point tropopause (CPT, ∼ 90hPa) into the stratosphere, and have been shown to have substantial radiative impacts within the lower stratosphere and on the troposphere below (e.g. Forster and Shine, 1999; Gettelman et al., 2004; Randel et al., 2006; Solomon et al., 2010; Maycock et al., 2014). In this chapter, we examine the local and nonlocal radiative effects associated with a recently observed 2011 sudden drop in TTL water vapor (Dessler et al., 2013; Urban et al., 2014; Dessler et al., 2014) that was accompanied by reductions in temperature and ozone. We also examine the radiative effects of longer-term changes in water vapor from 1990 through 2013.

A sudden reduction in TTL water vapor was observed in 2000, and was described by Randel et al. (2006) as an "abrupt drop". They showed that the water vapor reductions were also associated with reductions in ozone, reductions in temperature, and increases in TTL upwelling circulation. Their model results showed that idealized ozone reductions in a single lower stratospheric layer played a radiative role in the local 2000 temperature reductions, but nonlocal radiative impacts on layers below the reductions were not fully assessed. Solomon et al. (2010) explored the radiative

effects of water vapor reductions during the 2000 abrupt drop, and found decreases in net downwelling LW radiation at the tropopause (a negative climate radiative forcing of -0.098 Wm^{-2}), suggesting a contribution to the "slow down" of global warming during 2000-2009. Other studies (e.g. Forster and Shine, 1999; Shindell, 2001; Forster and Shine, 2002; Joshi and Jones, 2009; Wenshou, 2009; Joshi et al., 2010; Maycock et al., 2011; Dessler et al., 2013; Maycock et al., 2014) have similarly shown that lower stratospheric water vapor is radiatively important for surface as well as stratospheric climate.

In addition to the notable 2000 reductions, another such "abrupt drop" in water vapor occurred in 2011-2012 (Dessler et al., 2013; Urban et al., 2014; Dessler et al., 2014), again accompanied by reductions in TTL temperatures and ozone concentrations. Following the 2000 abrupt drop, water vapor concentrations remained relatively low compared with 1990-1999 concentrations (see section 2.3.4), but increased to a peak in September 2011 before suddenly dropping to a local minimum anomaly in May 2013 (Figure 2-1); herein for convenience we refer to this ∼21 month variability event (maximum to minimum) as the "2011 abrupt drop". The 2011 abrupt drop provides a unique opportunity to explore the structure of such changes and to assess its radiative impacts on climate and tropospheric temperatures, due to improved data coverage compared to the earlier event in 2000. The advent of the *Aura* Microwave Limb Sounder (MLS, Livesey et al. (2014)) offers a robust dataset with which to characterize this recent 2011 abrupt drop event. *Aura* MLS measurements are an improvement on the earlier Halogen Occultation Experiment (HALOE) record because they have increased horizontal resolution and accurate observations of ozone and water vapor in the TTL (Livesey et al., 2014; Hegglin et al., 2013; Tegtmeier et al., 2013).

The TTL radiative timescale ranges from 15-100 days (e.g. Fueglistaler et al., 2009a), a timescale shorter than the ∼21 month period of the 2011 abrupt drop. This suggests that short-term radiative adjustments associated with the 2011 abrupt drop would have impacted atmospheric temperatures. Furthermore, the long-term radiative impacts on the climate system could be important if relatively low concentrations

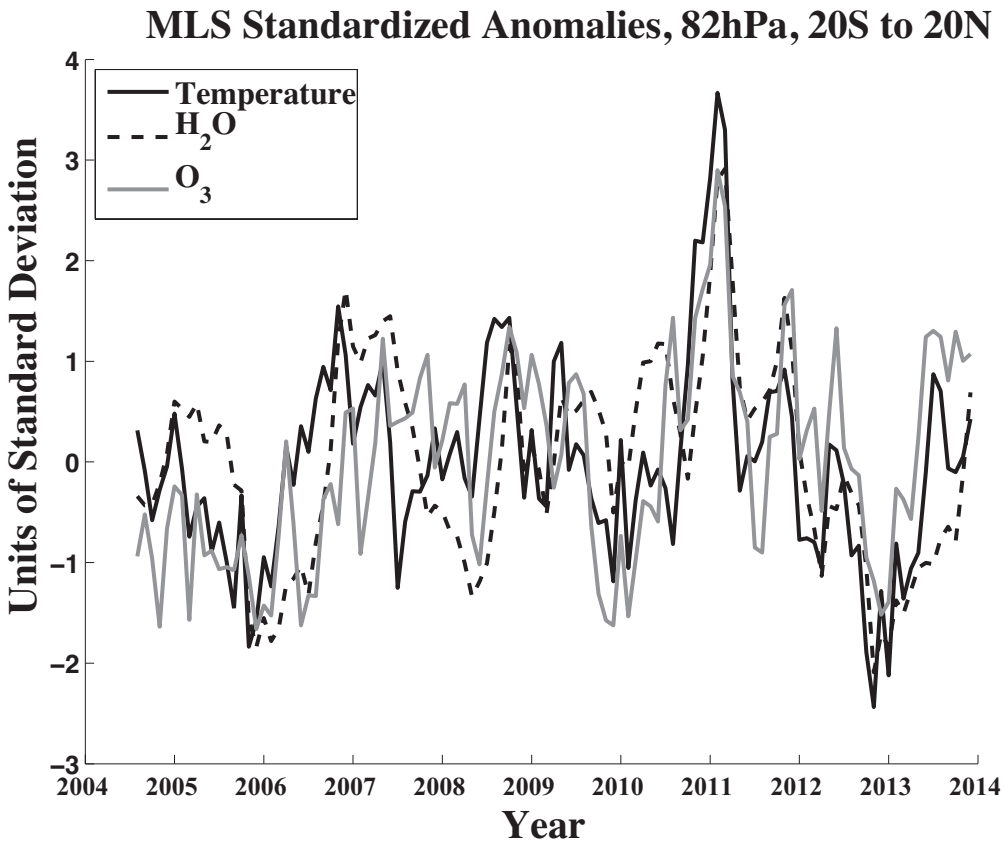

Figure 2-1: Standardized monthly time series of temperature (solid black curve), water vapor (dashed black curve), and ozone (gray curve) deseasonalized anomalies from 2005-2013 Aura MLS observations averaged over 20°S-20°N at 82 hPa.

persist. Here we show that water vapor concentrations in the period of MLS observations from 2005-2013 have remained low relative to the 1990-1999 period (see Figure 2-9), leading to a long-term negative radiative forcing on the troposphere that is in part related to the 2011 abrupt drop. The structure of the 2011 abrupt drop is characterized in this chapter, and the radiative effects of TTL concentration changes (both short-term and long-term) are investigated using raw *Aura* MLS observations and the combined Stratospheric Water Vapor and OzOne Satellite Homogenized (SWOOSH) data set (Davis and Rosenlof, 2013), along with two radiative transfer models.

The largest perturbations in water vapor and ozone during the 2011 abrupt drop are found at or just below the CPT altitude. The "substratosphere" (Folkins et al., 1999, 2000; Thuburn and Craig, 2002)—a region of the TTL defined as above the main convective outflow level (typically ∼150hPa) and below the CPT (∼90hPa)—is

a region where temperature variability is radiatively rather than dynamically dominated, and generally small in magnitude compared with the variability at and above the CPT (Randel and Wu, 2014). Thus, short-term radiative adjustments related to TTL chemical constituent perturbations could be an important contribution to temperature variability in the substratosphere. A goal of this study is to ascertain the magnitude of substratospheric radiative temperature adjustments associated with the 2011 abrupt drops in water vapor and ozone.

This chapter is organized as follows. Section 2.2 describes the data used in this study, defines the 2011 abrupt drop, and analyzes the abrupt drop structure. The three-dimensional structure of the abrupt drop is used to perturb TTL ozone and water vapor concentrations in two offline radiative transfer models. In section 2.3, we describe the radiative transfer models and study methods, and present the radiative forcing and resulting temperature adjustments associated with the abrupt drop perturbations. Furthermore, the role of the 2011 abrupt drop is examined in the context of the long-term changes in water vapor and the associated radiative forcing over about the past two decades. A summary of study results follows in section 2.4.

2.2 Abrupt Drop Analysis

2.2.1 Satellite Observations and TTL Relationships

This study uses measurements of water vapor, ozone, and temperature from the *Aura* Microwave Limb Sounder (MLS) Level-2 version 3.3 dataset (Livesey et al., 2014) from 2005-2013. Satellite swaths are quality controlled according to NASA's quality field recommendations and are regridded onto a 5° x 5° horizontal grid. For water vapor there are 31 recommended useful vertical levels from 316-1 hPa, whereas for ozone and temperature there are 29 recommended useful vertical levels from 216-1 hPa. *Aura* MLS measurements of TTL water vapor and ozone generally compare well with multi-instrument means in comprehensive SPARC instrument studies (Hegglin et al., 2013; Tegtmeier et al., 2013).

For analyses of satellite data earlier than the *Aura* MLS period (prior to 2005) and for analyses on isentropic surfaces, we use observations from the Stratospheric Water Vapor and OzOne Satellite Homogenized (SWOOSH) dataset (Davis and Rosenlof, 2013). SWOOSH is a monthly and zonal-mean data product available on isentropic and pressure surfaces (identical to those of *Aura* MLS Level-2 data), and separated by every 2.5° latitude. The "combined" SWOOSH dataset homogenizes measurements from the HALOE, UARS MLS, SAGE-II, SAGE-III, and *Aura* MLS instruments to form a coherent observational dataset of stratospheric water vapor concentrations. To retain coherence between coincident space and time instrument measurements during the overlap time period (2004-2005), the SWOOSH methodology adds corrective offsets to the HALOE, SAGE, and UARS MLS data to force agreement with *Aura* MLS (as in Solomon et al., 2010; Maycock et al., 2014). These offsets vary in latitude and height, but are constant in time. Following the discontinuation of HALOE and SAGE contributions in mid-2005, the SWOOSH combined dataset and *Aura* MLS measurements are identical.

The gridded *Aura* MLS data are used to examine the linkages between ozone, water vapor, and temperature in the TTL. At each grid point, monthly averages of temperature, water vapor, and ozone are deseasonalized to determine monthly anomalies. Time series of water vapor, ozone, and temperature anomalies at 82 hPa averaged zonally and meridionally over 20°S-20°N show significant correlations with one another in Figure 2-1 (time series are standardized for illustration). Pearson correlation coefficients (R) between these time series are determined by first detrending the data. A null-hypothesis that each correlation is significantly different from zero is tested with a two-sided student t-test using an effective number of degrees of freedom accounting for the lag-1 autocorrelations of each individual time series (e.g. Bretherton et al., 1999; Santer et al., 2000; Bandoro et al., 2014). Correlation coefficients corresponding to these tropical time series (20°S-20°N, 2005-2013) at each vertical level are shown in Figure 2-2.

Ozone and temperatures in the TTL are linked both dynamically and radiatively. Anomalous increases in upwelling are associated with adiabatic decreases in tem-

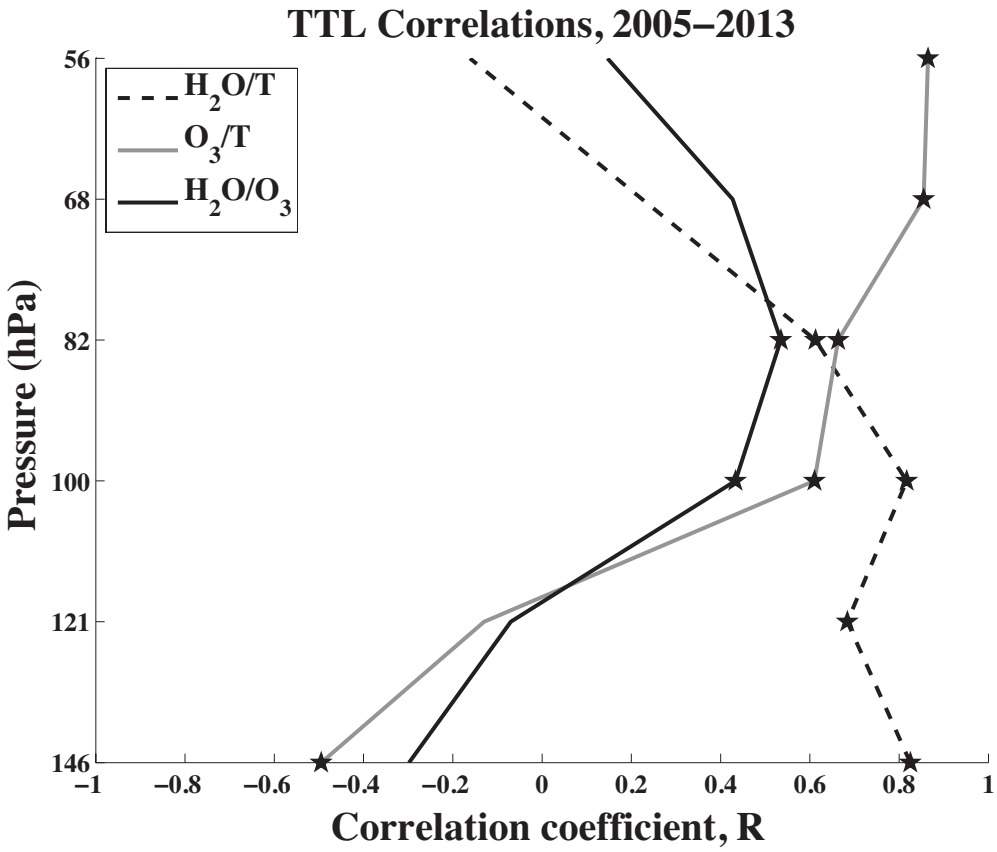

Figure 2-2: TTL vertical profiles of correlation coefficients (R) between water vapor/temperature (dashed black curve), ozone/temperature (gray curve), and water vapor/ozone (solid black curve), calculated from detrended MLS observed monthly deseasonalized anomaly time series from 2005-2013 averaged over 20°S-20°N. Stars indicate correlations that are significant at 95% confidence, determined with a two-sided student t-test and with the effective degrees of freedom adjusted to account for autocorrelation (see text).

perature, and act on the positive vertical gradient of ozone in the TTL, advecting ozone-poor air up from below and decreasing ozone mixing ratios (e.g. Randel et al., 2006; Schoeberl et al., 2008; Lamarque and Solomon, 2010). Conversely, anomalous decreases in upwelling are associated with increases in temperature and increased ozone mixing ratios. The ozone perturbations have a positive radiative feedback, with negative ozone anomalies locally cooling the TTL and positive ozone anomalies locally warming the TTL. This radiative feedback enhances the seasonal cycle of temperatures in the TTL, for instance, and long-term changes in TTL ozone can be associated with local long-term temperature trends (e.g. Folkins et al., 2006; Chae

and Sherwood, 2007; Fueglistaler et al., 2011; Polvani and Solomon, 2012). Thus a notable portion of TTL temperature variability is due to ozone radiative effects, as a response to an initial change in TTL circulation. In accordance with these processes, Figure 2-2 shows that ozone and temperature are significantly and positively correlated at levels near and above the CPT (100 hPa, 82 hPa and 68 hPa). This relationship increases with height in the TTL, both because of the increasing ozone gradient with height and the increasing radiative influence of ozone on temperature at these altitudes. Relationships between dynamic influences and ozone concentrations during the 2011 abrupt drop are discussed further in section 2.2.2.

Water vapor and temperature are significantly and positively correlated locally at and below the CPT (121 hPa, 100 hPa, and 82 hPa). Anomalously cold temperatures (related to adiabatic cooling through anomalous increased upwelling) reduce the water vapor content of parcels traveling up through the TTL and into the lower stratosphere (e.g. Dhomse et al., 2008); conversely, anomalous warm temperatures related to adiabatic warming through reduced upwelling lead to positive water vapor anomalies in the upward propagating parcels. Stratospheric water vapor can also vary in response to the ozone radiative feedback on temperatures discussed above, an additional mechanism of water vapor variability that has been shown to be radiatively important for tropospheric forcing (Stuber et al., 2001). Above 82 hPa in the tropics, the CPT has been traversed by upward propagating parcels and water vapor concentrations are near constant (with slight increases due to methane oxidation and mixing in of older stratospheric air, e.g. (Fueglistaler et al., 2009a)). These parcels propagate further into the stratosphere in accordance with the concept of a tropical "tape recorder" Mote et al. (1996), and poleward along quasi-isentropic surfaces (Holton et al., 1995, section 2.2.2 and Figure 2-4).

The correlations between water vapor and ozone deseasonalized anomalies at TTL heights show which regions of the TTL display linked changes in water vapor and ozone. We find that ozone and water vapor are significantly positively correlated over 100-82 hPa over the full period of record. If only 2011-2012 are considered, the vertical range of significant positive correlations increases to 121-68 hPa, suggesting

a common origin in anomalous TTL upwelling during the 2011 abrupt drop.

2.2.2 2011 Abrupt Drop Temporal and Spatial Structure

Following Rosenlof and Reid (2008) and Solomon et al. (2010) we define the 2011 abrupt drop in water vapor and ozone as the mean difference between the annual average mixing ratios from 2012-2013 and the annual average mixing ratios from 2010-2011. This definition is chosen so that the maximum/minimum in TTL concentrations reside in the earlier/later periods, respectively (see Figure 2-1). Abrupt drop mean differences are calculated at every three-dimensional location within the useful ranges of *Aura* MLS. Because of the sensitivity of radiative forcing calculations to the tropopause (Forster et al., 1997), we define a "cutoff altitude" at and above which we consider changes during the abrupt drop, and changes below the cutoff altitude are set to zero. The cutoff altitude is the three-dimensionally varying, monthly-averaged, cold-point tropopause (CPT). As sensitivity tests, we also vary the cutoff altitude by selecting it to be one or multiple levels above or below the CPT (MLS vertical levels are separated by $\sim$1.3 log-pressure km). Varying the cutoff altitude demonstrates the sensitivity of changes relative to the tropopause level, which is particularly relevant because large perturbations associated with the 2011 abrupt drop are observed below the CPT but within the substratosphere.

The 2011 abrupt drop zonal-mean structures of percentage changes in water vapor and ozone are shown in Figure 2-3. These results are shown on the PORT radiative transfer model's grid (described in Appendix B, section 2.6) for direct comparison with model output results described in section 2.3.2. For reference, the model's zonal- and annual mean climatological tropopause is plotted (black dashed curve) along with the zonal-mean 380K isentropic surface (white dashed curve) calculated with MLS temperature data.

The largest percentage water vapor reductions during the 2011 abrupt drop (Figure 2-3a) are observed in the TTL region, maximizing at the level nearest the CPT (82hPa). Much of the recent emphasis on connections between changes in stratospheric water vapor and their links to climate has focused on these tropical regions

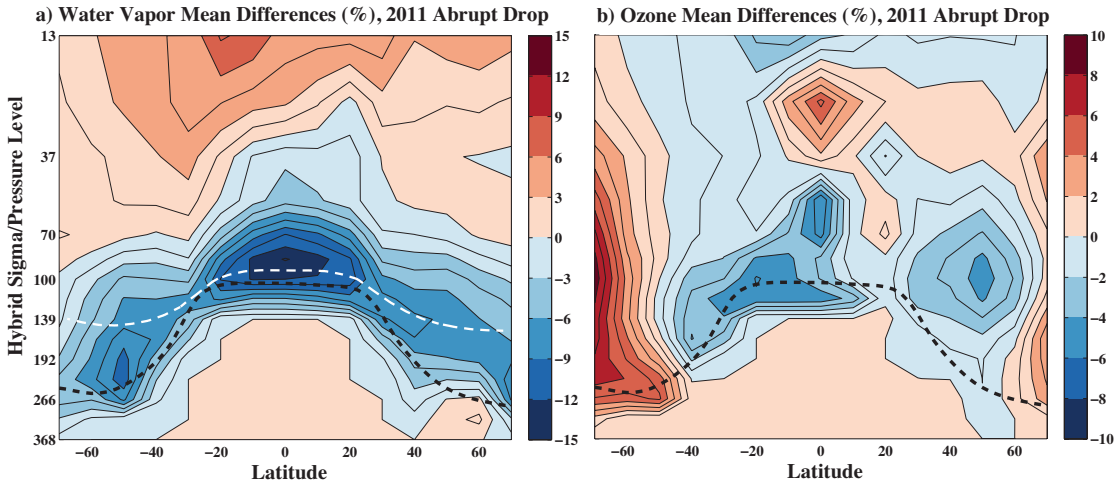

Figure 2-3: Zonal-mean distribution of Aura MLS observed percent mean differences in (a) water vapor and (b) ozone during the 2011 abrupt drop (between 2012-2013 and 2010-2011 concentrations). These changes are used to perturb the radiative transfer model (PORT), and thus are shown on the PORT grid for comparison with radiation results, and down to one level below the tropopause for illustration. The dashed black curve is the zonal- and annual mean tropopause. The dashed white curve is the 380K zonal-mean isentropic surface averaged from 2010-2013. Contour intervals are 1.5% (a, water vapor) and 1% (b, ozone) respectively.

(e.g. Randel et al., 2006; Rosenlof and Reid, 2008; Solomon et al., 2010). A key result of this chapter, however, is the substantial role of extratropical changes in water vapor that are associated with the tropical anomalies. Figure 2-3a shows that there is a "wing" behavior in the reductions of water vapor, with considerable reductions at higher latitudes in both hemispheres. These extratropical reductions, maximizing at 50°S and 40°N respectively, have important radiative influences (see sections 2.3.2 and 2.3.3). These reductions appear to be associated with poleward quasi-isentropic transport away from anomalous upwelling in the tropics (Holton et al., 1995; Rosenlof et al., 1997; Randel and Jensen, 2013). The 380 K isentropic surface (dashed white curve in Figure 2-3a) is indicative of this, with water vapor reductions approximately following the adiabat and then sinking below it as the pole is approached in both hemispheres.

Water vapor anomalies on a time/latitude section of the 380 K surface (similar to Randel and Jensen (2013)) are plotted in Figure 2-4a using SWOOSH data. Zonal-mean water vapor anomalies of up to ±15% originate at tropical latitudes during

both the early and the late periods of the 2011 abrupt drop (2010-2011 and 2012-2013, respectively) and propagate poleward in time along the surface to the extratropics, see Figure 2-3a. To analyze this propagation in greater detail, we compute the lead/lag cross-correlations between the zonal- and monthly mean time series of deseasonalized water vapor anomalies on the 380 K isentropic surface averaged over 20°S-20°N, and the corresponding time series at each latitude bin (separated by every 2.5°) from 90°S-90°N. The lead/lag correlation coefficients between these time series are shown in Figure 2-4b. The significance of these correlations is computed using the two-sided student t-test described in section 2.2.1. Figure 2-4b shows that tropical anomalies are significantly correlated with anomalies propagating out of the tropics and poleward in both hemispheres, typically reaching 60° latitude in 3-4 months. This is consistent with the timescale of poleward isentropic propagation in this region estimated by Rosenlof et al. (1997). Results are qualitatively similar if we consider anomalies only during the 2011 abrupt drop period (2010-2013), with extratropical anomalies lagging tropical anomalies by 1-4 months with significant correlations. In addition to this quasi-isentropic transport, horizontal mixing between the midlatitudes and tropics in the lower stratosphere may have also impacted the water vapor changes associated with the 2011 abrupt drop (e.g. Mote et al., 1998; Ploeger et al., 2011).

The ozone reductions during the 2011 abrupt drop (Figure 2-3b) appear prominently in a shallow region of the TTL, and maximize from 30°S to the equator at 100 hPa. North of the equator there are slight increases in lower stratospheric ozone, showing that ozone changes are much less spatially extensive than the water vapor changes during the 2011 abrupt drop. This suggests that processes besides vertical advection, such as horizontal mixing and photochemistry, are likely impacting ozone's spatial distribution (Konopka et al., 2009; Ploeger et al., 2011). In contrast to the tropical reductions, ozone increases during the 2011 abrupt drop over the pole in northern hemisphere (NH), and also increases in the "collar" region of the jet stream (e.g. Randel et al., 2002b) and poleward in the southern hemisphere (SH). This result appears to be consistent with an increased stratospheric circulation averaged over the abrupt drop period.

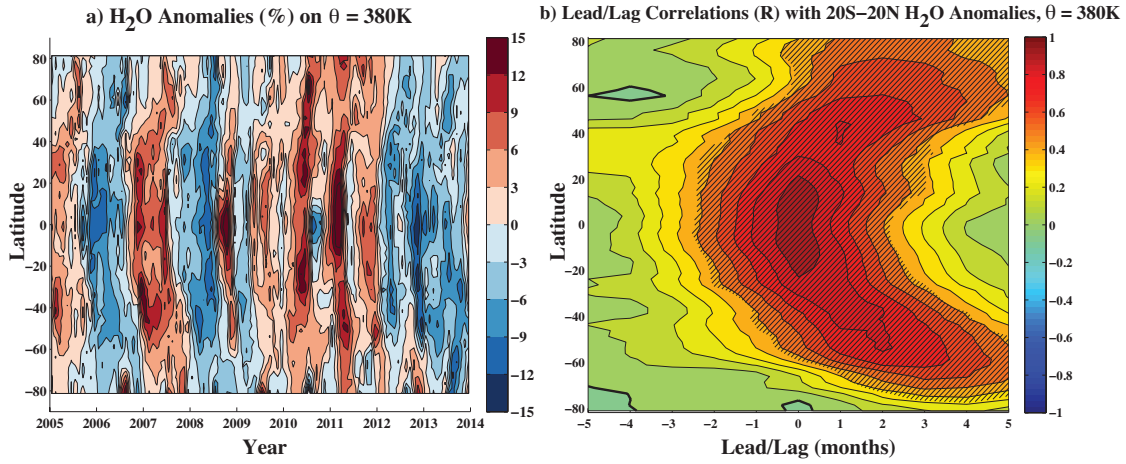

Figure 2-4: (a) Zonal- and monthly mean time/latitude cross-section of deseasonalized water vapor anomalies (%) on the 380 K isentropic surface (denoted by dashed white line in Figure 2-3). Contour intervals are 3%. (b) The monthly lead/lag correlation coefficients, on the 380 K isentropic surface, between the deseasonalized zonal- and monthly mean time series of water vapor anomalies averaged over 20°S-20°N, and the zonal- and monthly mean time series at each latitude. Contour intervals are every 0.1. The thick black contour denotes where R=0.0. Hatching indicates significant correlations at 95% confidence, determined with a two-sided student t-test and with the effective degrees of freedom adjusted to account for autocorrelation (see text). Data for (a) and (b) are drawn from the combined SWOOSH dataset from 2005-2013.

To investigate this further, we determine the linear congruence of the anomaly time series of temperature and ozone concentrations, averaged zonally and over 68-100hPa, as in Thompson and Solomon (2009). Details of this analysis are found in Appendix A (section 2.5). The analysis is intended to isolate the correlated nature of the ozone and temperature relationship in these atmospheric layers across latitude bands, with positive temperature anomalies relating to positive ozone anomalies both dynamically and radiatively as discussed in section 2.2.1 (the analysis cannot distinguish between these physical processes). Results are shown in Figure 2-5. The temperature anomalies congruent with ozone display a consistent pattern, with opposite signed anomalies between the equator and the poles, especially during periods of large temperature variability in the tropics (e.g. 2006, 2011, 2013). These results support the hypothesis that increased stratospheric circulation played a role in tropical ozone reductions and polar ozone increases (Figure 2-3b) during the 2011 abrupt drop

period. This offsetting ozone variability between low and high latitudes has radiative consequences in the troposphere, which we discuss in sections 2.3.2 and 2.3.3.

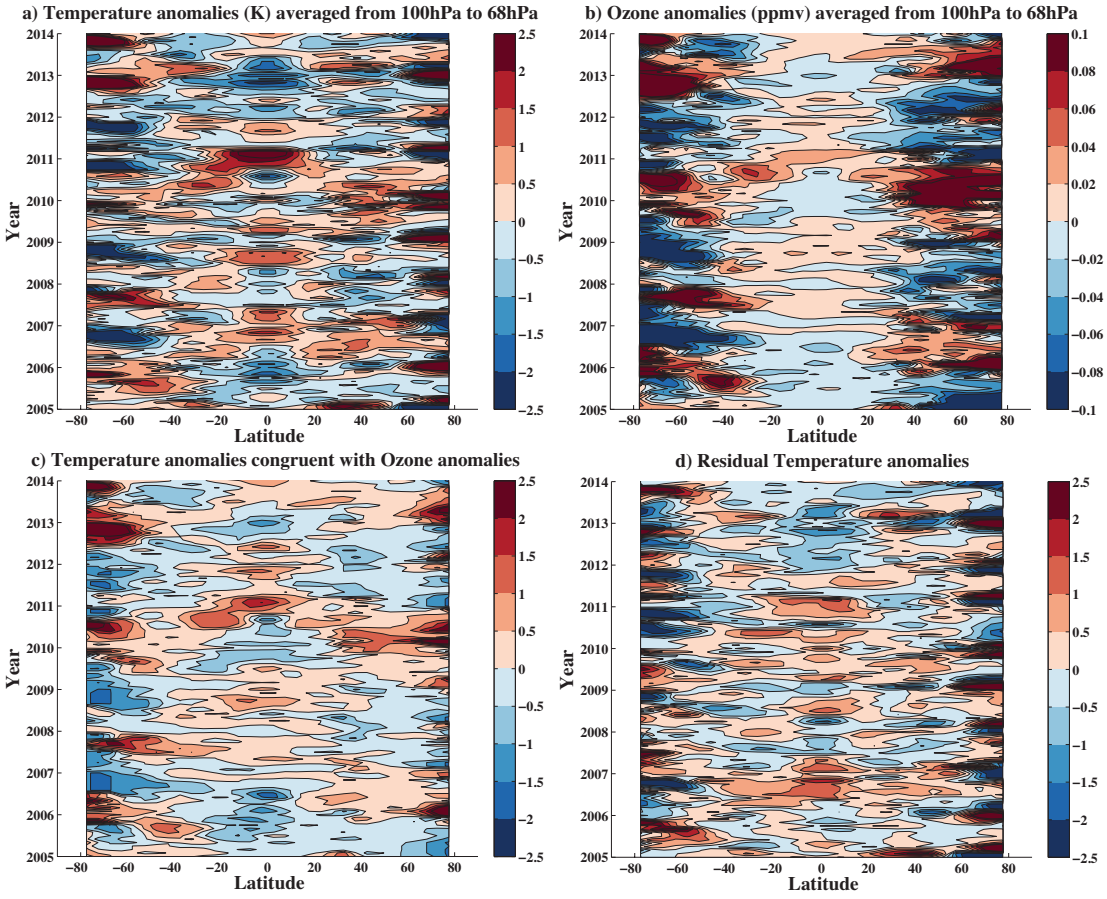

Figure 2-5: Zonal- and monthly mean time/latitude cross-sections of (a) temperature anomalies (K) and (b) absolute ozone anomalies (ppmv), (c) temperature anomalies congruent with ozone anomalies (K) [as computed from Equation 2.1] and (d) the residual temperature anomalies (K) [i.e. the difference between (a) and (c)]. All quantities are averaged over 100-68 hPa from *Aura* MLS. Contour intervals are 0.5 K and 0.02 ppmv, Color bars saturate above ± 2.5 K and ± 0.1 ppmv for temperature and ozone, respectively.

We note that the processes controlling water vapor and ozone variability are distinct, as discussed in section 2.2.1. Water vapor anomalies originating in the TTL are largely set by the temperatures near the CPT and stratospheric water vapor is long-lived, such that its abundance is conserved as parcels travel into the stratosphere away from locations of anomalous vertical motion (e.g. the tropical tape recorder signal). In contrast, the chemical lifetime for ozone decreases rapidly as air rises in the

tropical lower stratosphere (Brasseur and Solomon, 1986), such that ozone concentrations are not conserved as parcels travel away from the regions of upwelling or downwelling (e.g. Schoeberl et al., 2008). Observations from both species are consistent with an overall increase in stratospheric circulation between the two periods of the 2011 abrupt drop (2012-2013 and 2010-2011).

2.3 Radiation

2.3.1 Methods

The primary tool used herein to investigate the radiative influences of the 2011 abrupt drop in water vapor and ozone is the Parallel Offline Radiative Transfer model (PORT, Conley et al. (2013)), a configuration of the Community Atmosphere Model (CAM4) in the Community Earth System Model (CESM1) which runs the radiative transfer code offline. The model uses seasonally evolving fixed-dynamical heating (FDH, (Fels et al., 1980; Forster et al., 1997)) to determine temperature adjustments (T_{adj}) and adjusted radiative forcing (RF) at the tropopause (IPCC, 2013) associated with perturbations in chemical constituents (a description of the model and implementation details are found in Appendix B, section 2.6). Use of PORT facilitates comparison to a wide range of studies using the CESM framework.

PORT results are compared to the line-by-line (LBL) model used in Solomon et al. (2010) in Appendix C (section 2.7). Therein we also present an evaluation of PORT following the approach of Maycock and Shine (2012). Overall, there is good agreement between PORT and the LBL code, and PORT performs within the level of uncertainty found for other broadband models compared to the line-by-line model in Maycock and Shine (2012).

We perturb PORT using the definition of the 2011 abrupt drop described and analyzed in section 2.2.2, imposing the three-dimensional absolute mixing ratio changes in water vapor and ozone above various cutoff altitudes. Our methodology is formulated to consistently apply observed constituent changes vertically in the model

and account for the extreme radiative sensitivity to the tropopause altitude. Specifically, water vapor and ozone MLS gridded abrupt drop perturbations lie on a log pressure vertical grid relative to the log pressure height of the CPT, and are linearly interpolated to PORT's log pressure vertical grid relative to the log pressure height of PORT's tropopause. This method preserves the vertical distribution of changes in water vapor and ozone relative to the tropopause and thus the radiative effects of that distribution.

Water vapor and ozone perturbations are applied in separate runs to isolate their individual effects. We then linearly add water vapor and ozone outputs to obtain the total effect of their perturbations (there is a less than 1% quantitative difference between nonlinearly imposed and linearly added results). To determine both RF and radiative temperature changes associated with the 2011 abrupt drop in water vapor and ozone, PORT is run in two distinct modes:

1) RF is computed at the climatological tropopause assuming FDH in the stratosphere (all atmospheric layers above the CPT). In this mode the cutoff altitude is varied to determine the sensitivity of perturbations relative to the tropopause level. RF results are shown in Figures 2-7 and 2-8 and are discussed in sections 2.3.3 and 2.3.4.

2) In addition to the FDH stratospheric temperature adjustments in mode (1), temperatures below the CPT (within 400 hPa of the tropopause) are also allowed to adjust radiatively to the imposed composition perturbations, assuming FDH. In this mode water vapor and ozone perturbations are only imposed at and above the tropopause (the cutoff altitude is not varied). Radiative adjustments can be expected in the substratosphere just below the tropopause. While dynamical temperature adjustments would also be expected at altitudes below the tropopause in the real world, runs in this mode estimate the impact of radiation on temperatures alone. Radiative temperature adjustment (hereafter simply "temperature adjustment") results are shown in Figure 2-6 and are discussed in section 2.3.2.

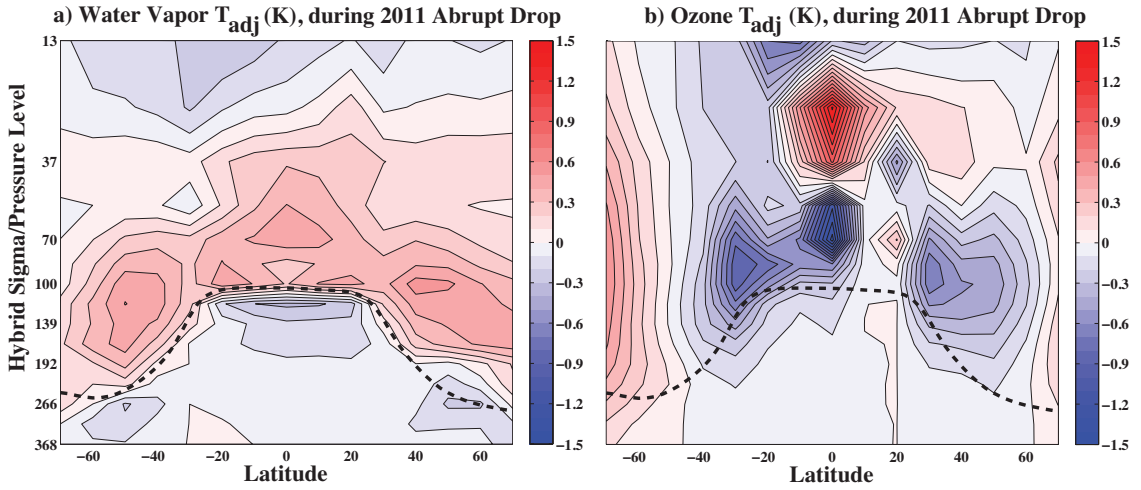

Figure 2-6: Temperature adjustments (K) from radiative calculations using PORT and assuming fixed-dynamical heating. Results are associated with applications of three-dimensional perturbations (mean absolute differences between 2012-2013 and 2010-2011 concentrations) above the climatological tropopause to (a) water vapor and (b) ozone fields, respectively. The dashed black curve is the zonal- and annual mean tropopause. Contour intervals are 0.1 K.

2.3.2 Radiative Temperature Adjustments

Zonal-mean temperature adjustments associated with the 2011 abrupt drop perturbations in water vapor and ozone are shown in Figure 2-6. The total zonal-mean temperature adjustment associated with the perturbations in both constituents is the sum of Figure 2-6a and 2-6b (as noted in section 2.3.1). As in Figure 2-3, PORT's zonal- and annual mean climatological tropopause is plotted for reference (black dashed curve).

Water vapor-related temperature adjustments (Figure 2-6a) display a distinct pattern of radiative warming above the tropopause and radiative cooling below the tropopause. Because water vapor locally cools the TTL (Gettelman et al., 2004), reductions during the 2011 abrupt drop locally warm the layers above the tropopause. This local warming increases the layer emission temperatures and therefore implies a nonlocal warming response in the surrounding layers. However, in the case of water vapor the net nonlocal response below the tropopause (i.e. below levels where the perturbations are applied), is a cooling rather than a warming. This result suggests another radiative effect, in particular a reduced exchange term in the layers below the tropopause due to the reductions in water vapor above the tropopause, is larger and more

important than the aforementioned changes in the emission temperatures.

The largest local warming above the climatological tropical tropopause, about 0.4-0.5 K, is found at 70 hPa over the equator and near 100 hPa at 20°S and 20°N. A minimum in warming is found in the equatorial 100hPa layer that arises from portions of the tropopause (here, the fixed cutoff altitude) lying above these levels over the Pacific Warm Pool region. Cooling occurs across the substratospheric levels just below the tropopause, with adjustments ranging from about -0.2 K to -0.3 K from 20°S-20°N at 118 hPa. Below this level, the cooling remains broad across tropical latitudes and is between -0.02 K and -0.17 K over 192-139 hPa.

Temperature adjustments in the extratropical wings show a similar behavior to those in the tropics, but with larger swaths of warming above the tropopause in agreement with large absolute reductions in water vapor. There is deep warming above the tropopause in the extratropics, with adjustments between +0.3 K and +0.55 K in the NH wing and between +0.35 K and +0.5 K in the SH wing. While substantially contrasting with the warming above, cooling below the extratropical tropopause (adjustments between about -0.1 K to -0.2 K) is weaker than that found in the tropical substratosphere. Here we note that although the extratropical percentage water vapor changes are smaller than those in the TTL, their radiative effect is similar in magnitude. This is because a) at higher pressures the absolute concentration change in water vapor is large, b) spectral absorption line widths are larger at higher pressures, and c) the temperatures adjust through a larger depth above the tropopause in the extratropics than the tropics (as in Maycock et al., 2011). Thus extratropical water vapor reductions, which are linked in part to the quasi-isentropic poleward propagation of tropical anomalies, are important for the overall radiative signal associated with the 2011 abrupt drop.

Ozone-related temperature adjustments (Figure 2-6b) show strong local radiative effects. Ozone reductions locally cool the atmosphere whereas ozone increases locally warm the atmosphere. Large cooling adjustments above the tropopause of between -0.3 K and -1.45 K are found the deep tropics, over 40°S-20°S, and over 30°N-50°N. These local radiative signals are largely dominated by shortwave absorption, with

longwave emission changes playing a smaller role. Ozone reductions and the resulting local cooling reduces these layers' blackbody emission temperatures. This in turn reduces the longwave emission down into the troposphere, and results in cooling below the layers of ozone reductions (e.g. Grise et al., 2009). The majority of this nonlocal longwave exchange term cooling associated with the 2011 abrupt drop in ozone is found at the levels just below the tropical tropopause (Figure 2-6b), leading to adjustment of about -0.2 K between the equator and 20°S at 118 hPa. Adjustments range from 0.0 K to -0.2 K in other parts of the tropical substratosphere.

The lack of spatial coherence in the ozone signal (discussed in section 2.2.2) impacts these nonlocal radiative effects, with warming adjustments over 10°N-20°N, and cooling adjustments over 40°S-30°S and 30°N-50°N. Large high latitude ozone increases—likely a consequence of increased stratospheric circulation during the 2011 abrupt drop (see Figure 2-5 and discussion in section 2.2.2)—are associated with local warming anomalies above the polar tropopause (NH$\sim$ +0.2 K, SH$\sim$ +0.5 K) that similarly reach into the layers below the tropopause.

The temperature adjustments associated with the 2011 abrupt drops in water vapor and ozone are of the same sign in the tropical substratosphere. The consequence of this is net radiative cooling just below the tropical tropopause varying from about -0.25 K to -0.5 K. The mean total cooling associated with water vapor and ozone reductions at 118 hPa and averaged over 20°S-20°N is about 0.4 K. Lowering the cutoff level in these experiments produces a qualitatively similar result (not shown), with an increased magnitude of net radiative cooling adjustments that are located just below the tropical layers where the 2011 abrupt drop perturbations are applied.

2.3.3 Radiative Forcing Associated with the 2011 Abrupt Drop

Figure 2-7 shows the latitudinal structure of the calculated RFs associated with the 2011 abrupt drops in water vapor and ozone. The globally averaged RF from each run is reported in the legend. The global RF associated with the water vapor reductions with the tropopause as the cutoff altitude is -0.057 Wm^{-2}, $\sim$42% less than the forcing associated with the 2000 abrupt drop as reported in Solomon et al. (2010). The forcing

difference is largely due to smaller water vapor changes in 2011 because of the shorter timescale of the 2011 abrupt drop compared with the 2000 abrupt drop (two-year as opposed to four-year windows used to define the periods for mean differencing, section 2.2.2); water vapor reductions have not yet fully propagated into the mid-upper stratosphere (Figure 2-3a) compared with the 2000 abrupt drop, leading to a shallower signal and smaller magnitude 2011 abrupt drop water vapor forcing. In the latter months in the 2011 abrupt drop period, water vapor concentrations began to climb, in contrast with the temporal structure of the 2000 abrupt drop. We consider the long-term changes in stratospheric water vapor (along with the role of the 2011 abrupt drop) and the associated radiative forcing in section 2.3.4.

Negative RF is pronounced in the extratropical wing regions (Figure 2-7); RF poleward of 35° accounts for ∼57% of the cosine-weighted global radiative impact. Thus a large part of the radiative water vapor forcing associated with the 2011 abrupt drop is attributable to anomalies in the extra-tropics. Although not shown explicitly herein, examination of the latitudinal variation of the RF associated with 2000 abrupt drop (using the definition of Solomon et al. (2010)) reveals that extratropical water vapor reductions were similarly important for the 2000 abrupt drop global radiative forcing, with changes over 65°S-35°S and 35°N-65°N accounting for ∼42% of the cosine-weighted global radiative impact.

Figure 2-7 and Table 2.1 show the results from varying the cutoff altitude. By lowering the cutoff level and allowing deeper reductions in water vapor to perturb the climate system and affect radiative calculations, the global RF increases compared with calculations using the tropopause as the cutoff altitude (Table 2.1). The largest differences appear in the extratropical wings, where there are considerable observed reductions below the climatological tropopause. The tropical RF increases only slightly when deeper reductions are passed to the model, suggesting reduced tropopause sensitivity at lower latitudes, and emphasizing the importance of the depth that reductions reach at higher latitudes (e.g. Maycock et al., 2011). When raising the cutoff altitude, the RF signal is reduced across the globe (Table 2.1). With the exception of the contrasting small increases in water vapor just below the tropopause

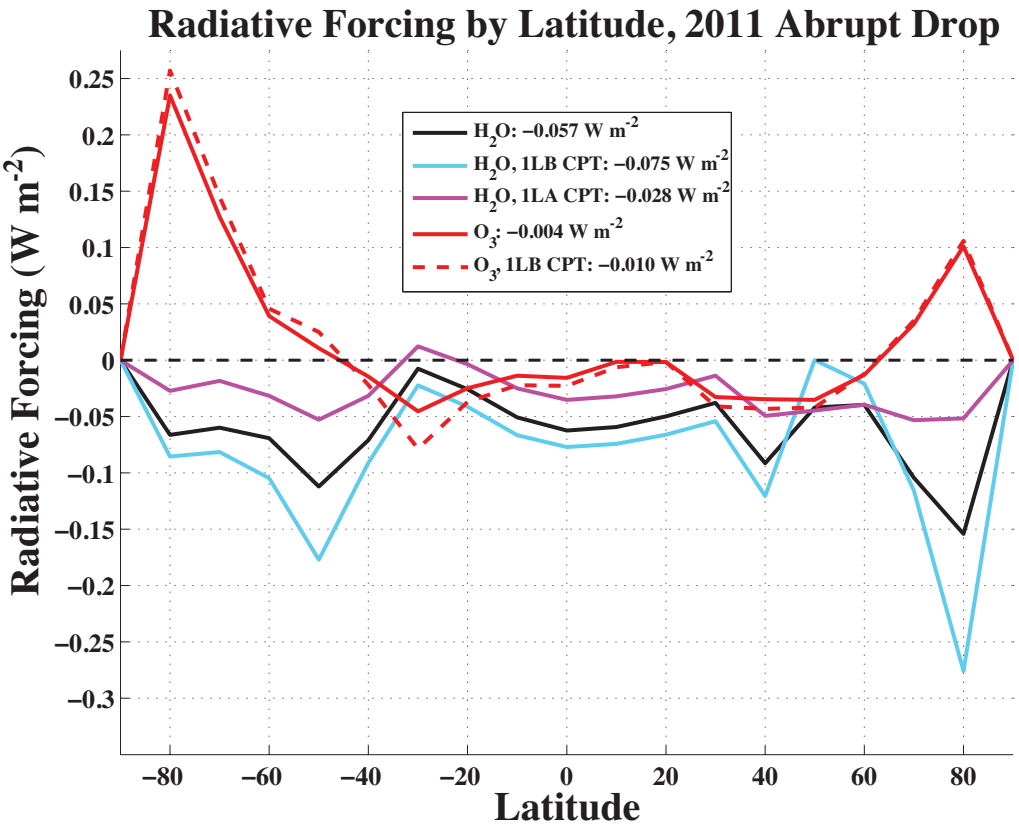

Figure 2-7: Radiative forcing (Wm^{-2}) by latitude from radiative calculations using PORT and assuming fixed-dynamical heating. Results are associated with applications of three-dimensional perturbations (mean absolute differences between 2012-2013 and 2010-2011 concentrations) to water vapor (black, blue, and magenta curves) and ozone (red curves) fields, respectively. Several lines are associated with perturbations applied 1 level above (1LA) or 1 level below (1LB) the model tropopause (CPT), to illustrate the radiative sensitivity to tropopause height (see text). The global average radiative forcing from each run is shown in the legend.

at 50°N, a notable portion of the observed water vapor reduction signal is found below the climatological tropopause in our abrupt drop definition (Figure 2-3a), but is still in the substratospheric portion of the TTL. Because these substratospheric changes are likely to be radiatively important, applying constituent changes only above the tropopause (i.e. using the tropopause as the cutoff altitude, yielding RF = -0.057 Wm^{-2}) is conservative.

Ozone reductions in the TTL have two main radiative effects (Ramanathan and Dickinson, 1979): 1) they locally reduce temperatures through the FDH temperature

Table 2.1: Global radiative forcing (Wm^{-2}) associated with water vapor or ozone mean differences between specific periods (each row, described in text), determined with radiative calculations using PORT assuming fixed-dynamical heating. The cut-off altitude at and above which perturbations are applied is denoted by column, where "LA" is levels above the tropopause and "LB" is levels below the tropopause (described in text), illustrating the radiative sensitivity of changes relative to the tropopause height. The mean differences for the 2011 Abrupt Drop period are calculated as 2012-2013 minus 2010-2011; the mean differences for the 2000 Abrupt Drop period are calculated as Aug. 2004-Dec. 2013 minus 1990-1999, excluding Pinatubo.

Drop Period & Constituent	2 LB	1 LB	Tropopause	2 LA	1 LA
H_2O (2011)	-0.094	-0.075	-0.057	-0.028	-0.010
O_3 (2011)	-0.014	-0.010	-0.004	-0.001	-0.001
H_2O (2000)	—	-0.050	-0.045	-0.036	-0.029

adjustment (Forster et al., 1997), limiting LW fluxes downward through the tropopause and 2) they nonlocally increase the SW fluxes penetrating into the troposphere. The LW flux reductions are the larger of these two competing effects associated with the 2011 abrupt drop perturbations, and the result is a net cooling of the tropical troposphere as shown in Figure 2-7. The global RF associated with the 2011 abrupt drop in ozone is -0.005 Wm^{-2}, but a new finding in this study is that this near-zero result arises from offsetting negative RF at low latitudes and positive RF at high latitudes. Whereas the near-exact offset of ozone radiative forcing is not necessarily constrained to be so, the nature of stratospheric circulation with anomalous advective upwelling in the tropics correlated with anomalous advective downwelling at higher latitudes (e.g. Randel et al., 2002b, Figure 2-5) suggests that ozone radiative effects during abrupt dynamically-driven variability events should offset to some extent when averaging globally.

2.3.4 Long-term Changes in Water Vapor and 2011 Abrupt Drop Implications

In the preceding sections we have discussed the short-term radiative impacts of the large variability in water vapor during the 2011 abrupt drop. The extent to which RF associated with abrupt drops in water vapor cool surface climate and offset greenhouse

gas warming is dependent not only on the spatial extent but also on the temporal extent of the reductions, compared to a reference value of water vapor. Short-term variability, such as the four-year period considered in this study's definition of the 2011 abrupt drop, will transiently force the climate system, whereas low water vapor concentrations in the longer-term would result in prolonged forcing of the climate system (e.g. over time scales of a decade or more).

To examine the long-term changes in water vapor and their radiative effects in greater detail, we use observations from the SWOOSH dataset. Following Randel et al. (2009), the two-year period following the Pinatubo eruption (June 1991-May 1993) is excluded from each of the following analyses. We compute the mean differences between water vapor concentrations in the *Aura* MLS period (August 2004-December 2013) and in the decade prior to the 2000 abrupt drop (1990-1999). Results are very similar if 1996-1999 (the period employed in Solomon et al. (2010)) is instead used as the period prior to the 2000 abrupt drop, or if 2000-2013 is used instead of the *Aura* MLS period alone following the 2000 abrupt drop. We consider only mean differences observed at 100hPa or above because HALOE observations (on which a portion of the pre-2005 SWOOSH water vapor data are based) below 100hPa are of limited quality (Harries et al., 1996).

The absolute observed mean differences are used to perturb PORT following the methodology described in section 2.3.1. The zonal-mean structure of these mean differences is shown in Figure 2-8 on the PORT radiative transfer model's grid. Mean differences falling below 100 hPa in Figure 2-8 indicate that at some longitude in that latitudinal band the PORT mean tropopause has a lower altitude than the *Aura* MLS mean tropopause. The adjusted RFs from the associated radiative calculations with PORT (assuming FDH in the stratosphere, mode 1 in section 2.3.1) are shown in Table 2.1.

Figure 2-8 shows that through most of the stratosphere, water vapor concentrations are ∼4-8% lower in the *Aura* MLS period than in 1990-1999. Adopting a cutoff altitude at the tropopause, the global RF associated with these changes is -0.045 Wm^{-2}, as shown in Table 2.1. This forcing is smaller than the forcing associated

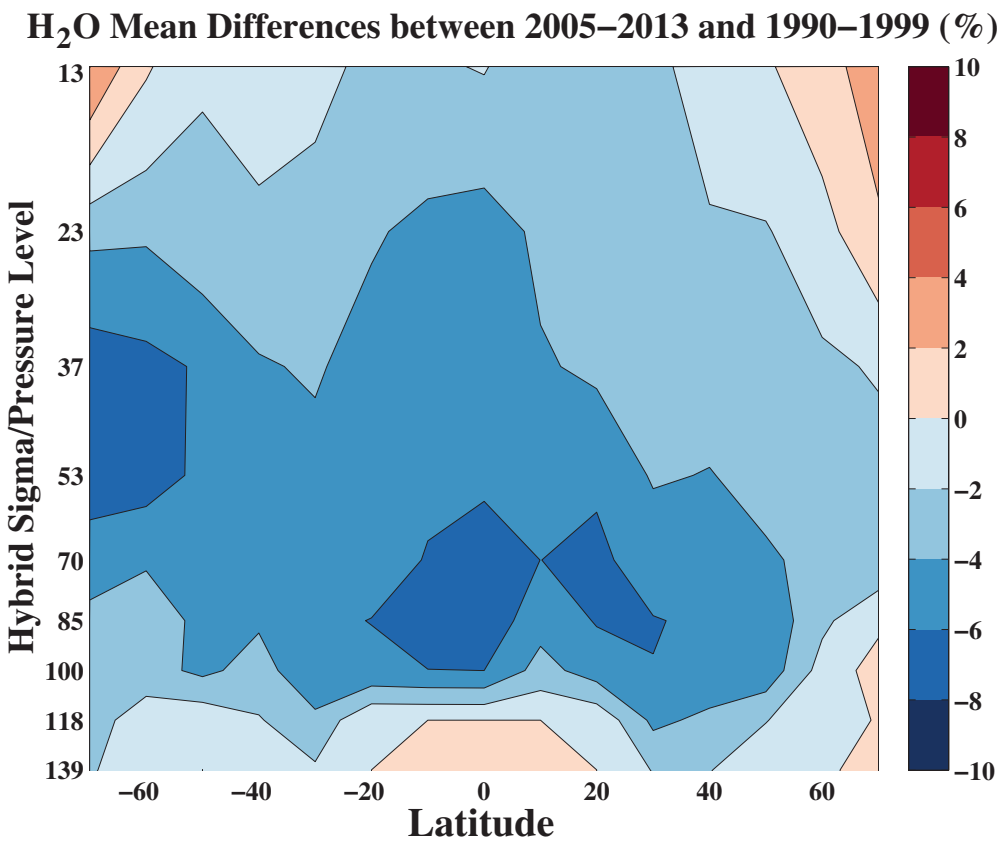

Figure 2-8: Zonal-mean distribution of percentage mean water vapor differences between the Aura MLS period (Aug. 2004-Dec. 2013) and 1990-1999 (excluding the two-year period following the Pinatubo eruption, June 1991-May 1993) using SWOOSH combined data. These changes are used to perturb the radiative transfer model (PORT), and thus are shown on the PORT grid for comparison with radiation results. Contour intervals are 2%.

with the 2000 abrupt drop as reported in Solomon et al. (2010), in part because the water vapor averaged over the *Aura* MLS period from 2004-2013 is higher than the period from June 2001-May 2005 used in Solomon et al. (2010). For comparison the average carbon dioxide radiative forcing between 2004-2014 and 1990-1999 as calculated by the NOAA Annual Greenhouse Gas Index (Hofmann et al., 2006; Butler and Montzka, 2015) is $+0.37\ Wm^{-2}$.

To illustrate the 2011 abrupt drop in the context of the long-term concentrations of water vapor, a time series of SWOOSH water vapor anomalies at 82 hPa and averaged over 30°S-30°N is shown in Figure 2-9 (solid black curve). Anomalies are deseasonalized and are relative to the SWOOSH water vapor time mean over 1990-

2013 (horizontal solid black line). The anomalies during the *Aura* MLS period are highlighted (solid blue curve) in Figure 2-9, along with the 5-year running mean at 82 hPa over 30°S-30°N for reference (solid gray curve). The time means of anomalies over 1990-1999 and the *Aura* MLS period are shown as black dashed and blue dashed horizontal lines, respectively, whereas the time means of anomalies during the 2010-2011 and 2012-2013 periods of the 2011 abrupt drop are shown as red dashed horizontal lines. The global radiative forcing values (with the tropopause as the cutoff altitude) associated with the long-term changes in water vapor (RF1) and the 2011 abrupt drop (RF2) are shown on the right hand side of the figure.

Figure 2-9 shows the evolution of TTL water vapor concentrations since 1990. Following the 2000 abrupt drop, water vapor concentrations slowly rose toward their 1990-1999 mean values, reaching a local maximum in September 2011. However, water vapor concentrations did not remain high; instead the occurrence of the 2011 abrupt drop over the next ∼21 months reduced the mean water vapor propagating through the TTL, keeping stratospheric water vapor concentrations low relative to the 1990-1999 levels (note the 5-year mean values remain close to the *Aura* MLS period mean following the 2011 abrupt drop). In the context of long-term changes in stratospheric water vapor therefore, the role of the 2011 abrupt drop was to extend the period of relatively low concentrations after the 2000 abrupt drop and to prolong their radiative impacts. Whether water vapor concentrations following the 2011 abrupt drop will remain low has yet be determined; observations following 2013 will be needed to make this assessment.

2.4 Summary

Aura Microwave Limb Sounder (MLS) observations show that beginning in 2011 an abrupt drop in temperatures, water vapor, and ozone occurred in the tropical tropopause layer (TTL). Temperature, water vapor, and ozone are all significantly positively correlated over the 100-82 hPa levels and during the two years (2011-2012) of the abrupt drop event. The abrupt drop is likely related to increased stratospheric

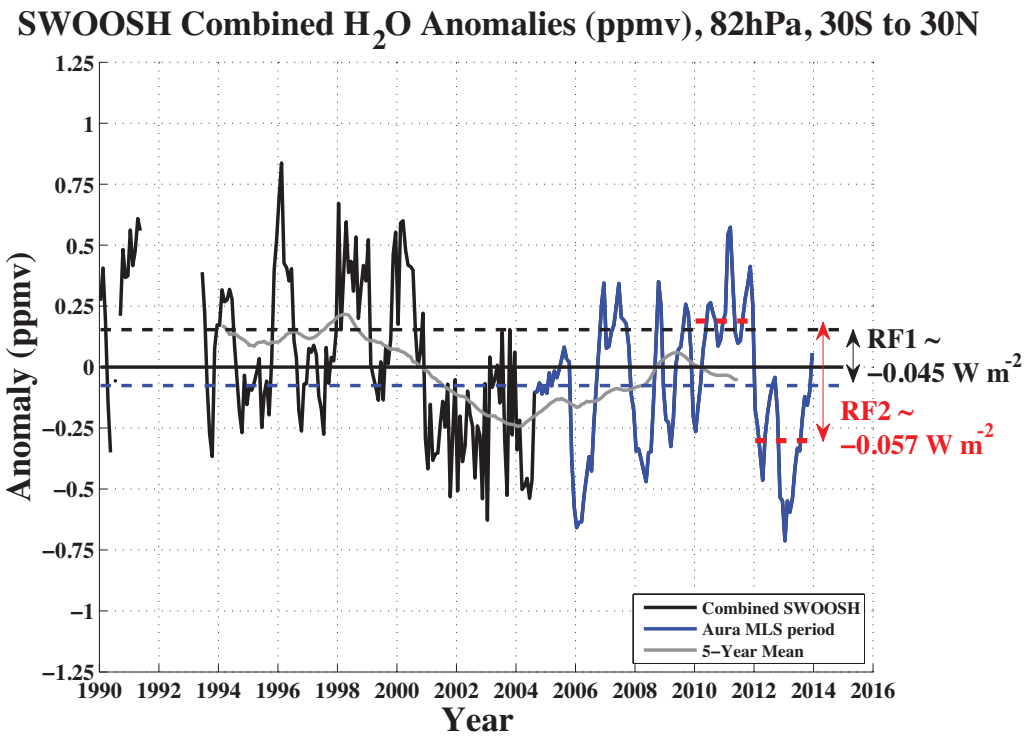

Figure 2-9: Monthly time series of deseasonalized water vapor anomalies from the combined SWOOSH dataset averaged over 30°S-30°N at 82 hPa. The combined SWOOSH data product is a weighted mean of HALOE, UARS MLS, SAGE, and *Aura* MLS satellite measurements. The two-year period following the Pinatubo eruption (June 1991-May 1993) is excluded from these analyses. The 5-year running mean anomaly is calculated from the SWOOSH combined product over 30°S-30°N at 82 hPa (grey curve). SWOOSH combined data during the *Aura* MLS period (Aug. 2004-Dec. 2013) is shown in the blue curve, while SWOOSH combined data prior to the *Aura* MLS period (Jan. 1990-July 2004) is shown in the black curve. The solid black horizontal line denotes the mean of the SWOOSH combined data from 1990-2013, averaged over 30°S-30°N at 82 hPa. The dashed black curve indicates the average level of water vapor from 1990-1999 relative to the SWOOSH combined data mean. The dashed blue horizontal line indicates the average level of water vapor during the Aura MLS period relative to the SWOOSH combined data mean. The dashed red horizontal lines indicate the average water vapor levels during 2010-2011 and 2012-2013, respectively, relative to SWOOSH combined data mean. The globally averaged radiative forcings associated with the total water vapor differences above the tropopause are shown on the right-hand side of the figure: RF1) between the *Aura* MLS period (blue dashed line) and 1990-1999 (black dashed line), and RF2) between the 2010-2011 and 2012-2013 periods of the 2011 abrupt drop (red dashed lines).

circulation and anomalous upwelling in the TTL (e.g. Dessler et al., 2013) enhanced by local ozone radiative feedback (e.g. Polvani and Solomon, 2012), and is accompa-

nied by positive ozone anomalies at higher latitudes that likely result from increased downwelling. In this study we have focused on the radiative effects of water vapor and ozone changes associated with the 2011 abrupt drop. The global radiative forcing associated with the 2011 abrupt drops in water vapor and ozone as calculated by the Parallel Offline Radiative Transfer (PORT) model (Conley et al., 2013) are -0.057 Wm^{-2} and -0.005 Wm^{-2}, respectively (Figure 2-7), and similar values are obtained with an independent line-by-line code (-0.049 Wm^{-2} and +0.003 Wm^{-2}, Figure 2-10). The radiative forcing varies by latitude in agreement with the latitudinal dependence of the ozone and water vapor abrupt drop patterns.

In this study we have shown several new results that have increased understanding of TTL abrupt drops and their radiative effects:

1) The quasi-isentropic poleward propagation of water vapor reductions during the 2011 abrupt drop led to considerable reductions in the extratropics, displaying a "wing" reduction behavior (Figure 2-3). Reductions in extratropical water vapor concentrations contribute considerably to the global radiative impacts associated with the 2011 abrupt drop period, with ∼57% of the global cosine-weighted radiative forcing attributable to reductions poleward of 35°.

2) Ozone reductions in the TTL during the 2011 abrupt drop are offset by high-latitude increases in ozone, congruent with temperature anomalies and consistent with increases in stratospheric circulation and anomalous ozone advection during the period. The radiative result of these anti-correlations during the 2011 abrupt drop is a near-zero global cosine-weighted radiative forcing, due to offsetting radiative impacts between the low and high latitudes. This offset appreciably reduces the overall global radiative impact of the ozone abrupt drop. Such behavior should be expected whenever large ozone variability is congruent with large temperature variability, related to increased/decreased stratospheric circulation (see Figure 2-5 for useful diagnostics of such signatures).

3) The 2011 abrupt drops in TTL water vapor and ozone lead to same-signed cooling radiative temperature adjustments in the atmospheric layers just below the tropopause (Figure 2-6). Purely radiative adjustments are between about -0.25 K

and -0.5 K across the 192-118 hPa levels, in the radiatively dominated region referred to as the substratosphere (e.g. Thuburn and Craig, 2002).

The magnitude of the radiative forcing associated with water vapor reductions is sensitive to the level chosen as the cutoff altitude (the level at and above which perturbations are considered), indicating that radiative calculations are very sensitive to constituent changes close to the tropopause (Forster et al., 1997). Selecting the tropopause as the cutoff altitude is conservative in calculating radiative forcing, as a large portion of observed water vapor reductions during the 2011 abrupt drop are found just below the cold-point tropopause (Figure 2-3 and Table 2.1).

A consequence of the 2011 abrupt drop is prolonged low concentrations of stratospheric water vapor relative to the mean concentrations from 1990-1999. Although stratospheric water vapor appeared to be rising to near the mean levels prior to the 2000 abrupt drop, the 2011 abrupt drop prevented concentrations from reaching those levels for several more years (Figure 2-9). Stratospheric water vapor concentrations from 1990-1999 were 4-8% higher than concentrations during the *Aura* MLS period (August 2004-December 2013) as shown in Figure 2-8, resulting in a global radiative forcing of -0.045 Wm^{-2} between these two periods (Table 2.1). Such forcing is about 12% of, and opposite in sign to, the carbon dioxide forcing over the period. This result suggests a significant climate role for stratospheric water vapor changes on decadal time scales between 1990 and 2014. Future forcing associated with stratospheric water vapor, and the long-term impacts of the 2011 abrupt drop, will depend on the future evolution of water vapor concentrations.

The use of fixed-dynamical heating to assess temperature changes permits understanding of pure radiative impacts, but this study has only assessed the first-order radiative feedback associated with dynamical driving of water vapor and ozone during the 2011 abrupt drop period. Dynamical changes themselves during the abrupt drop period (which are large) have not been accounted for in this study, and a dynamical feedback following the assessed radiative impacts has not been determined. In addition, this study has not accounted for other radiative active components of the climate system that may have been perturbed during the abrupt drop period, such as

aerosols and clouds. More work is needed to understand the role of these constituents in affecting the TTL and surface climate during abrupt drops.

2.5 Appendix A: Linear Decomposition of Ozone and Temperature Time Series

Following on (Thompson and Solomon, 2009), we decompose anomalous time series of temperature and ozone in the lower stratosphere. Specifically, the portion of zonal-mean temperature anomalies linearly congruent with ozone anomalies (T_{O_3}) is found with:

$$T_{O_3}(y,t) = \frac{\overline{T(y,t)O_3(y,t)}}{[O_3(y,t)]^2} \times O_3(y,t) \tag{2.1}$$

where O_3 are zonal-mean anomalies of ozone averaged over 68-100 hPa, T are zonal-mean anomalies of temperature averaged over 68-100 hPa, y is latitude dependence, t is time dependence, and the overbar denotes the time average. The fraction term in Equation 2.1 is the temporal regression of temperature anomalies onto ozone anomalies: a constant value at each latitude. Temperature anomalies can thus be divided into a linearly congruent portion (T_{O_3}) and a residual (such that $T = T_{O_3} + T_{residual}$). Residuals represent the portion of the temperature anomaly time series not correlated with ozone anomalies at particular latitudes. We perform this analysis with the *Aura* MLS data (from 2005-2013) described in section 2.2.1. Anomalies, congruent temperatures, and residuals are plotted in Figure 2-5.

2.6 Appendix B: PORT Model Description and Implementation

The Parallel Offline Radiative Transfer (PORT) model, described in Conley et al. (2013), employs radiative parameterizations developed by Briegleb (1992), Collins (1998),Ramanathan and Downey (1986), and Collins (2002). There is no scattering

in the longwave, and absorption/emission are calculated with a broadband model using 8 longwave bands. In the shortwave, PORT uses parallel-plane compositions and a two-stream method to compute multiple scattering and absorption over 18 shortwave bands. More detailed descriptions of the model radiative calculations are found in Neale et al. (2010).

For each calculation, PORT is run for 16 months total: a 4-month spin-up period and 12-month period for analysis. The 12-month analysis period is averaged to yield radiative forcing at the tropopause and temperature adjustments. Analysis time steps of just over 1.5 days are used to optimize model efficiency and accuracy (Conley et al., 2013), subsampled from 73 individual 30-minute PORT calculation time steps. As noted in the PORT documentation (Conley et al., 2013), this choice of subsampling evenly samples all seasons and samples numerous solar angles representative of its annual variability. There is a less than 0.1% relative error between fully sampled model time step (72-daily) net fluxes and subsampled net fluxes averaged over the 12-month analysis period, see Table 1 in Conley et al. (2013). In total there are 240 analysis time steps in the 12-month analysis period.

PORT has 26 vertical levels from 992.6 to 3.54 in hybrid sigma/pressure coordinates. There are 16 total levels from 313.5 hPa to 3.54 hPa. The model is run at a horizontal resolution of 10° latitude by 15° longitude. Constituent perturbations on the MLS horizontal grid (5°x5°, see section 2.2.1) are regridded to the PORT horizontal grid before they are applied to the model.

Background (boundary) model conditions, including temperature, water vapor, ozone, and clouds, are generated with a 16-month simulation of CESM1 (in accordance with the methodology outlined in Conley et al. (2013)) using a present-day climatology component-set (with monthly-fixed aerosols, fixed topography, and fixed present-day concentrations of methane, carbon dioxide, nitrous oxide and chlorofluorocarbons). PORT runs are all-sky and include background cloud fields determined during the CESM1 simulations (the cloud fields are unchanged between PORT runs). Results are not sensitive to the background cloud fractions or optical depths.

PORT uses a seasonally evolving fixed-dynamical heating (FDH) approximation

to calculate temperature adjustments to heating rate perturbations implied by perturbations in composition (Conley et al., 2013; Forster et al., 1997). Temperature adjustments (T_{adj}) assuming FDH are computed above a level specified by the user (taken in this study to be the model's climatological tropopause in run mode [1], or 400 hPa below the climatological tropopause in run mode [2], see section 2.3.1), and reach quasi-equilibrium (with changes due to changes in climatological background compositions or seasonal solar heating) after the model's 4-month spin-up period. The use of FDH also allows computation of adjusted radiative forcing (RF) as defined by the IPCC (2013). RF values are calculated from PORT by differencing the perturbed and unperturbed net radiative fluxes at the tropopause after FDH adjustments, where the unperturbed fluxes are calculated from a control-run with model background compositions. The model tropopause altitude varies by latitude, longitude, and month.

2.7 Appendix C: PORT Model Evaluation and Performance

PORT is compared to the line-by-line (LBL) code in Solomon et al. (2010). It is found that the magnitude of the adjusted RF kernel function is larger for PORT than the LBL, particularly at the tropopause levels, suggesting that in general PORT is more sensitive to changes in water vapor at and above the tropopause. For further validation, we compare the adjusted RF results reported herein (see section 2.3.2) computed with PORT to those computed with the LBL model (Figure 2-10). Consistent with the kernel function comparison, globally averaged RF associated with the abrupt drop in water vapor is smaller in magnitude for LBL results than for PORT results, but the latitudinal patterns in both model results are consistent. Similarly, for ozone, RF is smaller in magnitude in the LBL results but similar in spatial pattern. Weaker magnitudes could arise due to differences in model background concentrations, radiation parameterizations, or gridding differences.

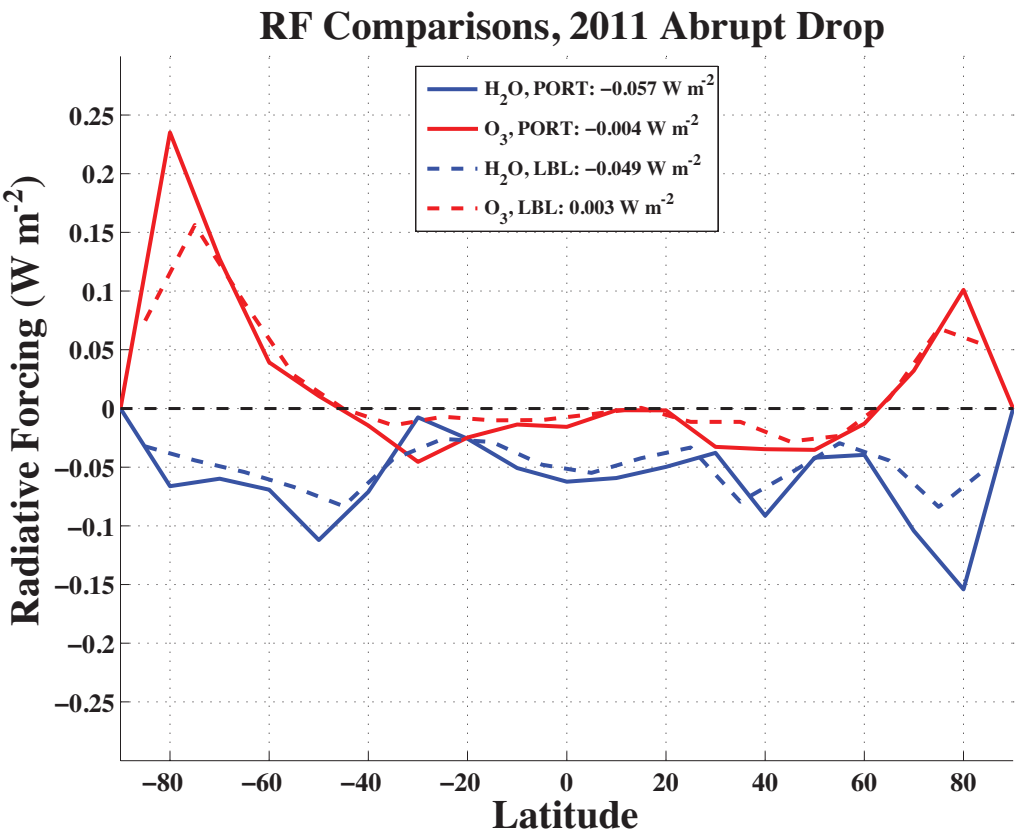

Figure 2-10: Radiative forcing by latitude comparing results from the PORT (solid curves) and LBL (dashed curves) radiative codes. Results are associated with applications of three-dimensional perturbations (mean absolute differences between 2012-2013 and 2010-2011 concentrations) to water vapor (blue curves) and ozone (red curves) fields, respectively. All perturbations were applied at and above the CPT native to the models. The global average radiative forcing from each run is shown in the legend.

Previously, Maycock and Shine (2012) examined the instantaneous radiative forcing calculation uncertainties associated with stratospheric water vapor changes by comparing a LBL radiative model and three broadband radiative models. Setting the background levels of stratospheric (from the CPT to 3.54 hPa) water vapor uniformly to 3 ppmv, they perturbed their atmosphere by adding 0.7 ppmv uniformly in the stratosphere and calculated the resulting instantaneous radiative forcing (RF_{inst}) at the tropopause. For their LBL model (averaged for a standard tropical profile) they found $RF_{inst} = 0.260\ Wm^{-2}$, while the broadband codes RF_{inst} differed non-systematically by up to $\pm 40\%$. Major differences/uncertainties likely arise from water

vapor transmittance parameterizations. For comparison, we repeat the Maycock and Shine (2012) methodology by setting the stratospheric water vapor background in PORT to 3 ppmv and then perturb it by uniformly adding 0.7 ppmv. Averaging over the tropics (20°S-20°N), we find that PORT $RF_{inst} = 0.189\ Wm^{-2}$ which is ∼27% smaller RF_{inst} than the Maycock and Shine (2012) reported LBL model forcing from the same water vapor perturbation. This forcing is within the range of broadband code uncertainties described in Maycock and Shine (2012) and is similar (within 0.02 Wm^{-2}) to the results of the radiative transfer code of Zhong and Haigh (1995) based on a common radiation scheme (Morcrette, 1991). This gives confidence that PORT is performing similarly to typical broadband codes, and simultaneously cautions that there are some uncertainties with PORT radiative forcing calculations compared with LBL calculations.

Chapter 3

Radiative Effects of Stratospheric Seasonal Cycles in the Tropical Upper Troposphere and Lower Stratosphere

Abstract

Water vapor and ozone are powerful radiative constituents in the tropical lower stratosphere, impacting the local heating budget and nonlocally forcing the troposphere below. Their near-tropopause seasonal cycle structures imply associated "radiative seasonal cycles" in heating rates that could affect the amplitude and phase of the local temperature seasonal cycle. Overlying stratospheric seasonal cycles of water vapor and ozone could also play a role in the lower stratosphere and upper troposphere heat budgets through nonlocal propagation of radiation. Previous studies suggest that the tropical lower stratospheric ozone seasonal cycle radiatively amplifies the local temperature seasonal cycle by up to 35%, while water vapor is thought to have a damping effect an order of magnitude smaller. This study uses *Aura* Microwave Limb Sounder observations and an offline radiative transfer model to examine ozone, water vapor, and temperature seasonal cycles and their radiative linkages in the lower

This chapter was published in the *Journal of Climate* (Gilford and Solomon, 2017) and is reproduced with permission. The publication and its supplement are available at `https://doi.org/10.1175/JCLI-D-16-0633.1`.

stratosphere and upper troposphere. Radiative sensitivities to ozone and water vapor vertical structures are explicitly calculated, which has not been previously done in a seasonal cycle context. Results show that the water vapor radiative seasonal cycle in the lower stratosphere is not sensitive to the overlying water vapor structure. In contrast, about one-third of ozone's radiative seasonal cycle amplitude at 85 hPa is associated with longwave emission above 85 hPa. Ozone's radiative effects are not spatially homogenous: for example, the Northern Hemisphere tropics have a seasonal cycle of radiative temperature adjustments with an amplitude 0.8 K larger than the Southern Hemisphere tropics.

3.1 Introduction

Hemispheric asymmetries in stratospheric wave driving suggest a seasonal cycle in tropical lower stratospheric upwelling (Yulaeva et al., 1994; Rosenlof, 1995; Randel et al., 2002a,b; Ueyama and Wallace, 2010; Fueglistaler et al., 2011). Whereas dynamical-forcing in each hemisphere commonly maximizes in its respective winter season, Northern Hemisphere wave driving is large compared with Southern Hemisphere wave driving. Consequently, there is stronger tropical lower stratospheric upwelling in boreal winter than in boreal summer. Corresponding to this seasonal cycle of upwelling are seasonal cycles in temperature, water vapor, and ozone above the tropical tropopause (among other tracer-like chemical constituents such as carbon monoxide, Schoeberl et al., 2006, 2008; Folkins et al., 2006; Abalos et al., 2012, 2013), each with distinct spatial patterns of variability (e.g. Fueglistaler et al., 2009a; Ploeger et al., 2011). A portion of the tropical lower stratospheric temperature seasonal cycle is likely related to the dynamically-driven ozone seasonal cycle through radiative amplification (Chae and Sherwood, 2007; Fueglistaler et al., 2011). Water vapor and ozone are strong radiatively-active constituents in the tropical lower stratosphere, having both local radiative impacts on temperature and long-term implications for radiative forcing of climate change (Forster et al., 1997; Forster and Shine, 1999; Stuber et al., 2001; Gettelman et al., 2004; Randel et al., 2006; Solomon

et al., 2010; Maycock et al., 2011, 2014; Dessler et al., 2013; Wang et al., 2016, as we showed in chapter 2, see also). In this chapter we investigate the radiative effects of water vapor and ozone seasonal cycles in the lower stratosphere in detail. In particular we explore radiative sensitivities to the overlying vertical structures of these seasonal cycles along with their latitudinal variability.

Tropical lower stratospheric water vapor displays a consistent seasonal cycle known as the "tropical tape recorder" (Mote et al., 1996). Water vapor anomalies are created when air parcels are freeze dried as they pass upward through the cold tropopause region (e.g. Hartmann et al., 2001; Liu et al., 2007; Schoeberl and Dessler, 2011). As the parcels propagate into the warmer stratosphere, water vapor anomalies are preserved, creating a "tape recorder" effect (see Fig. 3-1b). At any given point in a year, the consistent tape recorder spatial structure results in seasonal anomalies at higher stratospheric levels (above about 20 km) that overlie opposite-signed seasonal anomalies maximizing at lower levels near the tropopause. Mixing with older stratospheric air, increases in stratospheric water vapor from methane oxidation, and vertical diffusion jointly lead to reductions in tape recorder anomalies at middle stratospheric altitudes (Mote et al., 1996, 1998). However, memory of tropopause temperatures in the overlying water vapor structure may still be observed up to at least 30 hPa in the tropics (see Fig. 3-1b).

The seasonal cycle of tropical lower stratospheric ozone is driven primarily by local vertical advection near the tropopause (Randel et al., 2007; Schoeberl et al., 2008; Abalos et al., 2012). Unlike water vapor, ozone seasonal anomalies decay rapidly as they propagate away from their near-tropopause source because ozone's chemical lifetime becomes shorter than the transport time scale at increasing heights (e.g. Brasseur and Solomon, 1986). This results in a seasonal signal in tropical lower stratospheric ozone that is shallower than the water vapor tape recorder (see Fig. 3-1c). Horizontal in-mixing from the extra-tropics during each hemisphere's respective summer also contributes to ozone's tropical seasonal cycle, amplifying it and contributing to hemispheric asymmetries (Konopka et al., 2010; Ploeger et al., 2011, 2012; Stolarski et al., 2014, discussed further in sections 3.2 and 3.3). The tropical ozone seasonal cycle

transitions from an annual to a semi-annual cycle between about 55 and 30 hPa. The tropical semi-annual oscillation in temperature (SAO, e.g. Reid, 1994; Reed, 1962) observed at higher stratospheric levels (∼30 hPa and above) is related to the semi-annual signal in ozone (Hirota, 1980; Maeda, 1987; Perliski et al., 1989; Gebhardt et al., 2013) through chemical and radiative coupling, with a much smaller effect on water vapor (Mote et al., 1998).

Previous studies have shown that the local water vapor seasonal cycle is not very radiatively important for local lower stratospheric temperatures, whereas local ozone changes strongly influence the seasonal cycle in tropical lower stratospheric radiative heating (Folkins et al., 2006) and may radiatively amplify the lower stratospheric temperature seasonal cycle by 20-35% (Chae and Sherwood, 2007; Fueglistaler et al., 2011). While some studies have examined long-term vertical radiative coupling between ozone and temperature using decadal trends (Forster et al., 2007; Grise et al., 2009), nonlocal radiative impacts associated with the overlying constituent seasonal cycles have not been previously studied. If the vertical structures do have notable nonlocal radiative effects, then accurate representation of constituent seasonal cycles with altitude would be important for evaluation of diabatic heat budgets (Fueglistaler et al., 2009b; Wright and Fueglistaler, 2013). It is important to understand the radiative dependencies of near-tropopause temperatures because several processes, such as the amount of water vapor entering the stratosphere (Mote et al., 1996; Randel, 2010; Randel et al., 2006; Fueglistaler and Haynes, 2005; Fueglistaler et al., 2005; Schoeberl and Dessler, 2011; Dessler et al., 2016) and the intensity of tropical cyclones (e.g. Bister and Emanuel, 1998; Emanuel et al., 2013), are sensitive to near-tropopause temperatures.

The primary goals of this study are: (1) quantify and compare the radiative impacts of observed stratospheric water vapor and ozone seasonal cycles in the tropical lower stratosphere and upper troposphere; (2) investigate the sensitivity of radiative responses to the overlying vertical structures of water vapor and ozone seasonal cycles, in order to identify local and nonlocal radiative influences; (3) separate longwave and shortwave radiative effects to determine their individual contributions to the

results, and (4) elucidate the latitudinal variability of the results. The chapter is organized as follows. Section 3.2 describes the satellite observations of water vapor and ozone seasonal cycles along with the broadband radiative transfer model used to calculate their radiative impacts. Radiative calculations, sensitivity test results, and the latitudinal variability of results are discussed in section 3.3, and conclusions are summarized in section 3.4.

3.2 Data and Methods

3.2.1 Observations

To study the radiative impacts of constituent seasonal cycles, we use the *Aura* Microwave Limb Sounder (MLS) observations of water vapor, ozone, and temperature described in chapter 2 (section 2.2.1). The ∼300 km native horizontal resolution in the tropical tropopause region is fine enough to explore the latitudinal structure of the ozone seasonal cycle and its radiative effects (see section 3.3.2). The *Aura* MLS cold-point tropopause is estimated as the coldest level in a given temperature profile; this estimate compares well with estimates from higher vertical resolution GPS occultation measurements (e.g. Kim and Son, 2012; Randel and Wu, 2014).

We extract monthly mean seasonal cycles of temperature, water vapor, and ozone from *Aura* MLS data at each horizontal and vertical location. We define the amplitude of each seasonal cycle as the absolute range between the seasonal cycle minimum and maximum (i.e. the "peak-to-peak" amplitude at monthly temporal resolution). Note that the Quasi-Biennial Oscillation (QBO) is also an important driver of stratospheric variability (e.g. Schoeberl et al., 2008). To ensure that the QBO was not aliased in our seasonal cycle, we examined the seasonal cycles of individual years with high and low QBO-index values (from Berlin, 2016) during our period of record (2005-2013). Depending on the phasing between the lower stratospheric seasonal cycles and the QBO, differences between the easterly and westerly phases of QBO in any given month are up to ∼3 K in temperature, 25% in water vapor, and 10% in ozone (not

shown). However, we find that the annual cycle remains the prominent feature in lower stratospheric temperature, water vapor, and ozone variability. Therefore while the details (amplitude and phase) of stratospheric ozone and water vapor seasonal cycles vary with the QBO, our results are representative of typical seasonal cycle variability within this time period.

We define the tropics in this study as an average between the 20°S and 20°N latitude band. A recent study by Stolarski et al. (2014) found that asymmetrical upwelling and mixing between the northern and southern hemispheres (NH and SH, respectively) leads to a larger amplitude ozone seasonal cycle in the NH (0°-20°N) than the SH (20°S-0°). In particular, lower stratospheric upwelling and horizontal mixing impacts on ozone are in phase and additive in the NH tropics, whereas they are out of phase in the SH tropics. We explore the radiative impacts of such hemispheric variability in ozone's seasonal cycle in section 3.3.2.

Fig. 3-1 shows the tropical mean MLS temperature, water vapor, and ozone seasonal cycles relative to the long-term mean (2005-2013). Seasonal cycles are shown on the radiative transfer model's grid for direct comparison with radiative results (see model description in section 3.2.2). The climatological tropical monthly-mean model tropopause is shown as the white-dashed curve for reference.

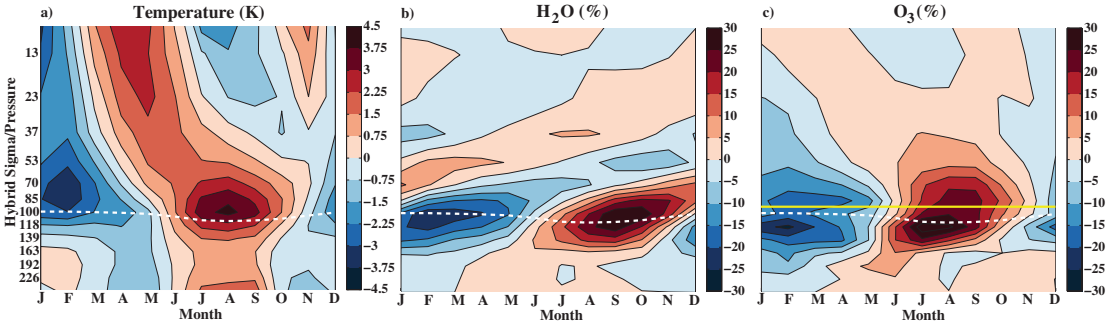

Figure 3-1: Observed Aura MLS seasonal cycles of (a) temperature (b) water vapor, and (c) ozone, averaged between 20°S-20°N on PORT's grid. Contour intervals are 0.75 K in (a) and 5% in (b) and (c). The white dashed curve denotes the PORT climatological tropopause averaged between 20°S-20°N. The solid yellow line in (c) illustrates the 85 hPa pressure level used in a radiative sensitivity experiment (see text).

In the tropical lower stratosphere the observed seasonal cycles of temperature,

ozone, and water vapor are approximately in phase because of their common origins in anomalous seasonal upwelling. The tropical-mean amplitude of observed seasonal temperature oscillations maximizes with a ∼7 K amplitude at the 85 hPa level (Fig. 3-1a). Ozone has a very shallow tape-recorder like signal stretching from the upper troposphere up to about 50 hPa (Fig. 3-1b), as noted by Randel et al. (2007). Above the tropical tropopause, ozone's tropical-mean seasonal amplitude ranges from about 40% of the mean at 100 hPa to 17% of the mean at 53 hPa. Between 53 hPa and the upper stratosphere, ozone and temperature show a similar SAO pattern that propagates downward in time (e.g. Hirota, 1980; Reid, 1994). Throughout the stratosphere, the water vapor structure matches the typical tropical tape-recorder signal, maximizing near the annual-mean tropopause level (∼100 hPa) with a tropical-mean amplitude of about half of the mean. Next, we use the water vapor and ozone seasonal cycle structures to perturb a radiative transfer model and determine radiative impacts.

3.2.2 Radiative Transfer Calculations

Radiative calculation are performed with the Parallel Offline Radiative Transfer model (PORT Conley et al., 2013) employed and described in chapter 2. PORT's background heating rates are similar to those of previous studies (e.g. Gettelman et al., 2004; Fueglistaler and Fu, 2006; Abalos et al., 2012), though there are some differences likely associated with radiative code and constituent backgrounds (Supplemental Fig. S1). In this chapter, PORT is run on a 1.9° x 2.5° horizontal grid, and above the tropopause we replace the climatological backgrounds of water vapor and ozone with *Aura* MLS annual concentrations averaged over 2005-2013. As in chapter 2, PORT simulations are run for 16-months, with a 4-month spin-up period followed by a 12-month analysis period. We retain our perturbation methodology preserving the distribution of water vapor and ozone seasonal cycles relative to the tropopause (white dashed curves in Fig. 3-1 and 3-2). Further descriptions of PORT radiative calculations can be found in Conley et al. (2013), Neale et al. (2010), and in chapter 2 of this thesis (sections 2.3 and 2.6).

As noted in chapter 2, PORT assumes seasonally evolving fixed-dynamical heating (SEFDH Forster et al., 1997) to calculate the radiative responses of heating rates and temperatures to the seasonal cycles of water vapor and ozone. These temperature changes are referred to as "temperature adjustments." The fixed-dynamical heating approach has been commonly used in studies of lower stratospheric radiative temperature adjustments and radiative forcing (e.g. Forster et al., 2007; Maycock et al., 2014; Grise et al., 2009; Solomon et al., 2010, and chapter 2). Dynamical forcing is the leading cause of composition and temperature seasonal cycles in the tropical lower stratosphere (see section 3.1), and SEFDH assumes that the temperature seasonal cycle is primarily driven by dynamics with a fixed seasonal cycle (Forster et al., 1997). In reality a percentage of seasonal radiative heating perturbations from constituent seasonal cycles may be balanced by amplification or damping of upwelling rather than changes in temperature (e.g. Ming et al., 2016). A limitation of the SEFDH method, therefore, is that computed temperature adjustments are an upper bound on how radiative heating impacts temperatures.

Fueglistaler et al. (2011) previously applied SEFDH to explore the radiative impacts of water vapor and ozone seasonal cycles on lower stratospheric temperatures. Chae and Sherwood (2007) instead used a radiative-convective model including an imposed seasonal cycle of residual vertical velocity to study radiative seasonal cycle effects. Both studies consistently showed that ozone significantly amplified the temperature seasonal cycle in the tropical lower stratosphere by 2-3 K. Taken together, these studies suggest that seasonal variations in ozone heating will be realized in the lower stratosphere's temperature seasonal cycle, and that to first-order SEFDH is a good approximation for these effects. SEFDH is therefore a useful formulation for our purpose of bracketing and describing the radiative impacts of constituent seasonal cycles. Irrespective of potential limitations of the SEFDH formulation (excepting longwave Planck feedbacks associated with ozone heating, see discussion in section 3.2.2 and Supplemental Fig. S2), changes in radiative heating rates associated with the ozone and water vapor seasonal cycles will be important for the lower stratospheric heating budget.

We perform radiative experiments by applying three-dimensional seasonal cycles of water vapor and ozone as perturbations to the background climatology, and then run PORT assuming SEFDH. The pure radiative temperature adjustments associated with these perturbations are hereafter referred to as "radiative seasonal cycles." Following our method in chapter 2, temperatures are allowed to adjust up to 400 hPa below the tropopause level. Water vapor and ozone seasonal cycle perturbations (illustrated in Fig. 3-1) are applied between the tropopause and top of the model ($\sim$3 hPa); we refer to the output of these runs as the "full structure" radiative seasonal cycles. Consistent with chapter 2 (section 2.3.1), water vapor and ozone radiative effects remain approximately linearly additive.

To test the dependence of radiative impacts of the vertical structures of water vapor and ozone seasonal cycles, we also perform sensitivity experiments with seasonal cycle perturbations applied only between the tropopause and three vertical levels: 53 hPa, 70 hPa, and 85 hPa (i.e. a thin layer right above the tropopause). For example, in the 85 hPa sensitivity experiment, three-dimensional concentration perturbations from the seasonal cycles of water vapor and ozone are applied between the tropopause and PORT's 85 hPa level (yellow line in Fig. 3-1c). Above the 85 hPa level in this sensitivity experiment, ozone and water vapor concentrations remain at their climatological average values (i.e. they have no seasonal cycles). Sensitivity experiments with larger vertical ranges were performed and found to be qualitatively consistent with those presented here (not shown for brevity).

We apply seasonal cycle perturbations at and above the tropopause, as in previous studies (Grise et al., 2009; Solomon et al., 2010; Maycock et al., 2011, 2014, and chapter 2). However, radiative effects are vertically coupled (as we show in section 3.3.2) and seasonal cycles at levels below the tropopause may also impact temperatures above the tropopause. Accordingly, we also performed runs where constituent seasonal cycles down to 5 vertical model levels below the tropopause ($\sim$6 km) were included as radiative perturbations (cf. "cutoff" experiments in 2.3.3). The key results from these runs are: (1) temperature adjustments are qualitatively similar to those when only perturbations above the tropopause are considered; increasing the

depth of seasonal cycle perturbations expands the regions of local and nonlocal temperature adjustments in the upper troposphere, (2) ozone seasonal cycles below the tropopause have small absolute amplitudes (<70 ppbv) and smaller impacts on lower stratospheric temperatures than ozone seasonal cycles above the tropopause (consistent with the findings of Forster et al. (2007)), (3) the radiative response of upper tropospheric water vapor is largest in the tropopause region, and is therefore very sensitive to the location of the tropopause (e.g. Forster et al., 1997; Solomon et al., 2010, and chapter 2). However, these effects are local to the immediate tropopause levels (between 85 and 118 hPa); consistent local temperature adjustments associated with the water vapor seasonal cycle fall off sharply below 118 hPa. We therefore choose to restrict our analyses in the following section to results with perturbations considered only above the tropopause.

3.3 Results

3.3.1 Full Structure Temperature Adjustments and Heating Rates

The tropical-mean seasonal cycles of temperature adjustments associated with the full structures of water vapor and ozone seasonal cycles (i.e. the "radiative seasonal cycles") are shown in Fig. 3-2. The tropical-mean peak-to-peak amplitudes (in K) of the MLS observed temperature seasonal cycle, the water vapor radiative seasonal cycle, and the ozone radiative seasonal cycle are shown in Fig. 3-3 relative to the annual-mean tropopause height (along with sensitivity experiments discussed in section 3.3.2). Positive amplitudes in Fig. 3-3 show where the radiative seasonal cycles have a similar phase to the temperature seasonal cycle at that altitude (e.g. lower stratospheric ozone and temperature minimizing in boreal winter/spring and maximizing in boreal summer/fall); negative amplitudes show where radiative seasonal cycles have a phase opposite to the temperature seasonal cycle at that altitude. Seasonal cycle radiative adjustments represent the upper bound on ozone and water

vapor radiative contributions to amplifying (in the case of ozone) or damping (in the case of water vapor) stratospheric temperature seasonal cycles.

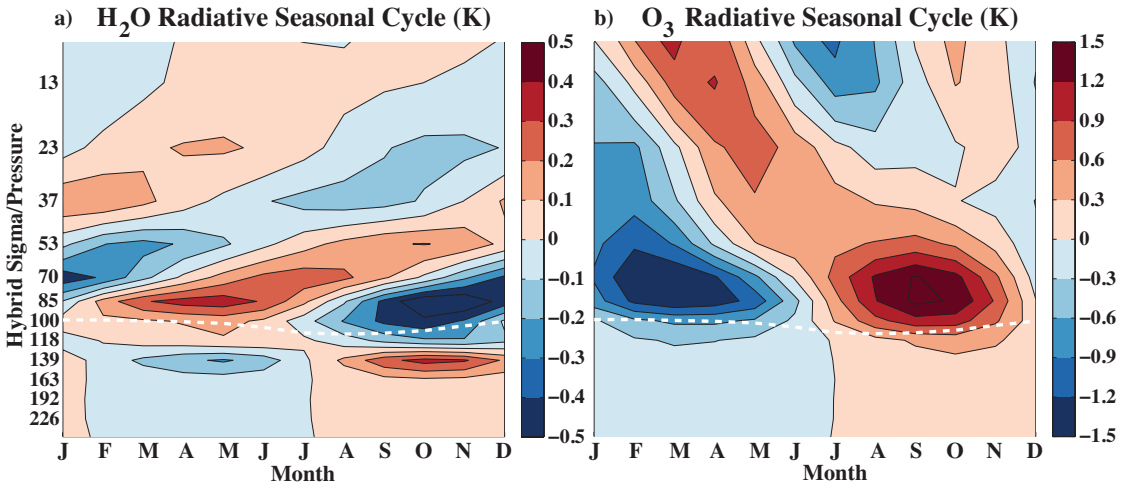

Figure 3-2: Vertical structure of radiative temperature adjustments (K) associated with observed (a) water vapor and (b) ozone seasonal cycles (see Fig. 3-1), averaged between 20°S-20°N. Contour intervals are 0.1 K in (a) and 0.3 K in (b). The white dashed curve denotes the PORT tropopause averaged between 20°S-20°N.

Radiative adjustments (Fig. 3-2) lag seasonal cycle perturbations (Fig. 3-1) by 1-2 months in the tropical lower stratosphere. This lag is associated with the seasonal heating rate anomalies (i.e. temperature adjustments maximize when heating rate anomalies transition from positive to negative or vice versa, see Fig. 3-4) and is on the order of the thermal radiative damping timescales near the tropical tropopause (Newman and Rosenfield, 1997; Randel et al., 2002a; Gettelman et al., 2004; Randel and Wu, 2014). In the tropical lower stratosphere there are significant correlations between temperature, water vapor, and ozone primarily through upwelling and thermodynamics (see section 2.2.1). The lower stratospheric radiative time-lag therefore implies that radiative contributions to the temperature seasonal cycle should act to shift its phase (consistent with Chae and Sherwood (2007)). The phase-shift implies that amplifying or damping effects will have a smaller effect on the total amplitude of lower stratospheric temperatures than they would if there was no time-lag, particularly for water vapor contributions (discussed below). However, radiative contributions from ozone and water vapor still remain important terms in the *overall*

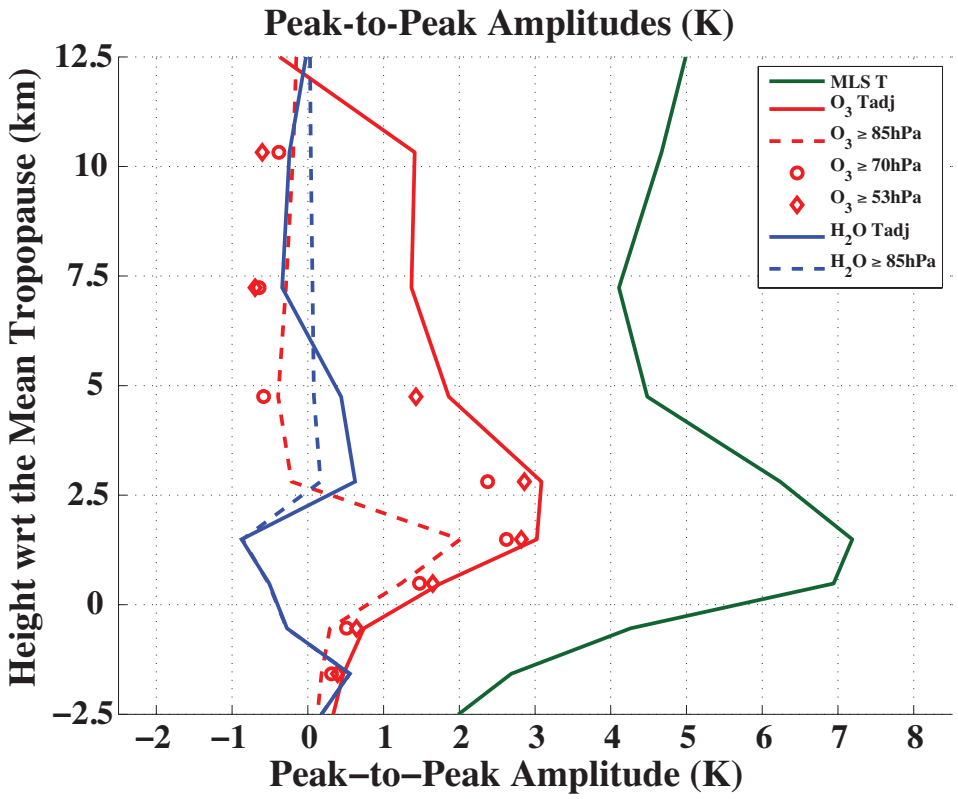

Figure 3-3: The peak-to-peak seasonal cycle amplitudes (K) relative to the tropopause height (log-pressure km) of observed MLS temperature (green curve), ozone and water vapor radiative temperature adjustments (T_{adj}) associated with seasonal cycles between the tropopause and the top of the stratosphere (red and blue solid curves, respectively), ozone and water vapor radiative temperature adjustments associated with seasonal cycles considered between the tropopause and 85 hPa (red and blue dashed curves, respectively), and ozone radiative temperature adjustments associated with seasonal cycles considered between the tropopause and 70 hPa (red circles) and 53 hPa (red diamonds). All amplitudes are averaged between 20°S-20°N. Positive amplitudes represent potential amplification of the temperature seasonal cycle (i.e. the maxima occurs in summer/fall), while negative amplitudes represent potential damping of the temperature seasonal cycle (i.e. the maxima occurs in winter/spring).

budgets of lower stratospheric seasonal cycles of temperatures and heating rates.

The tropical-mean full structure of the water vapor radiative seasonal cycle (Fig. 3-2a) shows radiative adjustments that maximize just above the tropopause (∼85 hPa) with a range of 0.9 K, and then propagate upward into the stratosphere: a radiative tape-recorder effect. Above the tropopause, water vapor's radiative seasonal cycle is consistent with its role of net cooling to space (Gettelman et al., 2004):

reductions in water vapor lead to net warming in the boreal winter/spring, whereas increases in water vapor lead to net cooling in the boreal summer/fall. If these purely radiative adjustments were linearly removed from the temperature seasonal cycle, the seasonal temperature amplitude at 85 hPa would be increased by ∼0.2 K (about 3%). Because of the phase offset between temperature and water vapor's radiative seasonal cycle, water vapor's radiative effect acts to shift the temperature seasonal cycle towards earlier annual extrema. Water vapor's radiative seasonal cycle maximizes in the lower stratosphere both because a) it is the location of water vapor's maximum seasonal cycle amplitude (Fig. 3-1b) and because b) it is the location of maximum radiative sensitivity to tropical water vapor perturbations (e.g. Forster and Shine, 1999; Solomon et al., 2010).

Below the tropical tropopause, the radiative response to the tropical water vapor tape recorder switches sign: there is net cooling in the boreal winter/spring, net warming in the boreal summer/fall, and near-zero temperature adjustments across the tropopause level itself, consistent with our previous study of the radiative effects of lower stratospheric water vapor anomalies (section 2.3.2). Physically, an opposite-signed radiative effect in the upper troposphere arises because of a) changes in the amount of longwave radiation propagating down through the tropopause (which scale with water vapor concentration), and b) changes in the lower stratosphere opacity (allowing the layers below to transmit longwave radiation and cool more or less efficiently to space).

The tropical-mean radiative seasonal cycle associated with ozone's full structure shows radiative adjustments that maximize at 70-85 hPa (Fig. 3-3). Ozone perturbations drive changes in shortwave absorption that strongly affect local temperature, and in turn lead to changes in longwave emission through a Planck feedback (Ramanathan and Dickinson, 1979; Gettelman et al., 2004; Grise et al., 2009, and chapter 2). The SEFDH methodology enables exploration of the Planck feedback; its impacts on ozone's tropical lower stratospheric radiative heating are explicitly shown in Supplemental Fig. S2. The net radiative effect of ozone's seasonal cycle is to cool the tropical lower stratosphere in the boreal winter/spring and warm the tropical lower

stratosphere in the boreal summer/fall. The amplitude of ozone's radiative seasonal cycle at 85 hPa is about 3 K (∼31% of the *Aura* MLS temperature amplitude at that altitude).

Changes in tropical lower stratospheric ozone's longwave propagation also result in a radiative seasonal cycle below the tropopause that cools upper tropospheric temperatures in the boreal winter/spring and warms in the boreal summer/fall (Ramanathan and Dickinson, 1979; Grise et al., 2009). Shortwave heating from changes in the penetration of solar radiation slightly damps the longwave effect (not shown). Ozone's radiative seasonal cycle in the upper troposphere falls off sharply with depth: the 1.75 K seasonal cycle range near the tropopause is reduced to about 0.5 K at 139 hPa. In the upper troposphere, water vapor radiative effects are same-signed and approximately in-phase with ozone effects, leading to the sum of their radiative seasonal cycle amplitudes at 139 hPa being about 1 K. Water vapor effects between 139 hPa and the tropopause are smaller because it is the crossover (near-zero adjustment) region between local stratospheric effects and nonlocal upper tropospheric effects, while nonlocal ozone effects continue to fall off below this level. Therefore, there is a specific vertical region in the upper troposphere where both the overlying stratospheric water vapor and ozone are significant contributors to a radiative seasonal cycle.

Fueglistaler et al. (2011) found that the seasonal ozone radiative response in the lower stratosphere (67 hPa level) was an order of magnitude larger than the water vapor response. In this chapter we find that the amplitude of the tropical-mean ozone radiative seasonal cycle at 70 hPa is ∼5 times larger than the water vapor seasonal cycle (∼3.1 K compared with ∼ -0.6 K). However, it is clear from Fig. 3-2 and Fig. 3-3 that the water vapor radiative seasonal cycle maximizes at altitudes below the 70 hPa level, whereas the ozone radiative seasonal cycle maximizes more broadly over 70-85 hPa. This is likely because of a) water vapor's strong radiative sensitivity to the tropopause altitude (e.g. Solomon et al., 2010), and b) the amplitude of ozone's concentration seasonal cycle is larger at higher altitudes. At the two levels just above the annual mean tropopause (85 and 100 hPa), the tropical-mean ozone radiative seasonal cycle is ∼3.4 times larger than the water vapor radiative seasonal cycle (∼3

K compared with ∼ -0.9 K, and ∼1.75 K compared with ∼ -0.5 K, respectively, Fig. 3-3). Therefore at near-tropopause levels we find that water vapor seasonal radiative effects are small compared with ozone, but not negligible.

Fig. 3-4 shows the seasonal cycles of computed lower stratospheric heating rate anomalies (from the climatological background heating rates) associated with ozone and water vapor seasonal cycles. For comparison, the absolute value of the annual-mean net heating rate at 85 hPa is 0.33 K/day (see Supplemental Fig. S1). PORT-computed radiative heating rates in the tropical lower stratosphere have similar seasonal cycles and absolute magnitudes to those of Abalos et al. (2012), though there are some differences likely related mainly to seasonal cycle depictions and background climatology.

We find that ozone's lower stratospheric radiative temperature amplification is a mixture of longwave and shortwave effects (consistent with Forster et al., 2007) that have different phases but result in net warming rates from April to August and net cooling rates from September to March (Fig. 3-4). Shortwave effects follow ozone seasonal cycle concentrations, while longwave effects are modulated by a nearly linear combination of the radiation a) following ozone concentrations, and b) tracking increases or decreases in local temperature adjustments (Planck feedback, see Supplemental Fig. S2). The net ozone radiative heating rate anomaly amplitude at 85 hPa is ∼0.06 K/day, of similar magnitude to the ozone heating rate seasonal cycle amplitude found at 17 km (∼90 hPa) by Folkins et al. (2006, their Figure 4), although our calculations are adjusted rather than instantaneous heating rates.

Observational estimates of lower stratospheric dynamical cooling through tropical upwelling by Abalos et al. (2012) are of comparable magnitude to radiative heating and vary inversely, driving seasonal temperature tendencies in the tropical lower stratosphere towards zero K/day (see also Rosenlof, 1995). The amplitude of the seasonal cycle of the dynamical cooling at 80 hPa is about 0.2 K/day (Abalos et al., 2012, their Figure 5). The ozone seasonal cycle radiative heating anomalies (Fig. 3-4) share a similar phase with adiabatic cooling anomalies (minimum heating in boreal winter and maximum in boreal summer), and ozone's radiative heating amplitude is

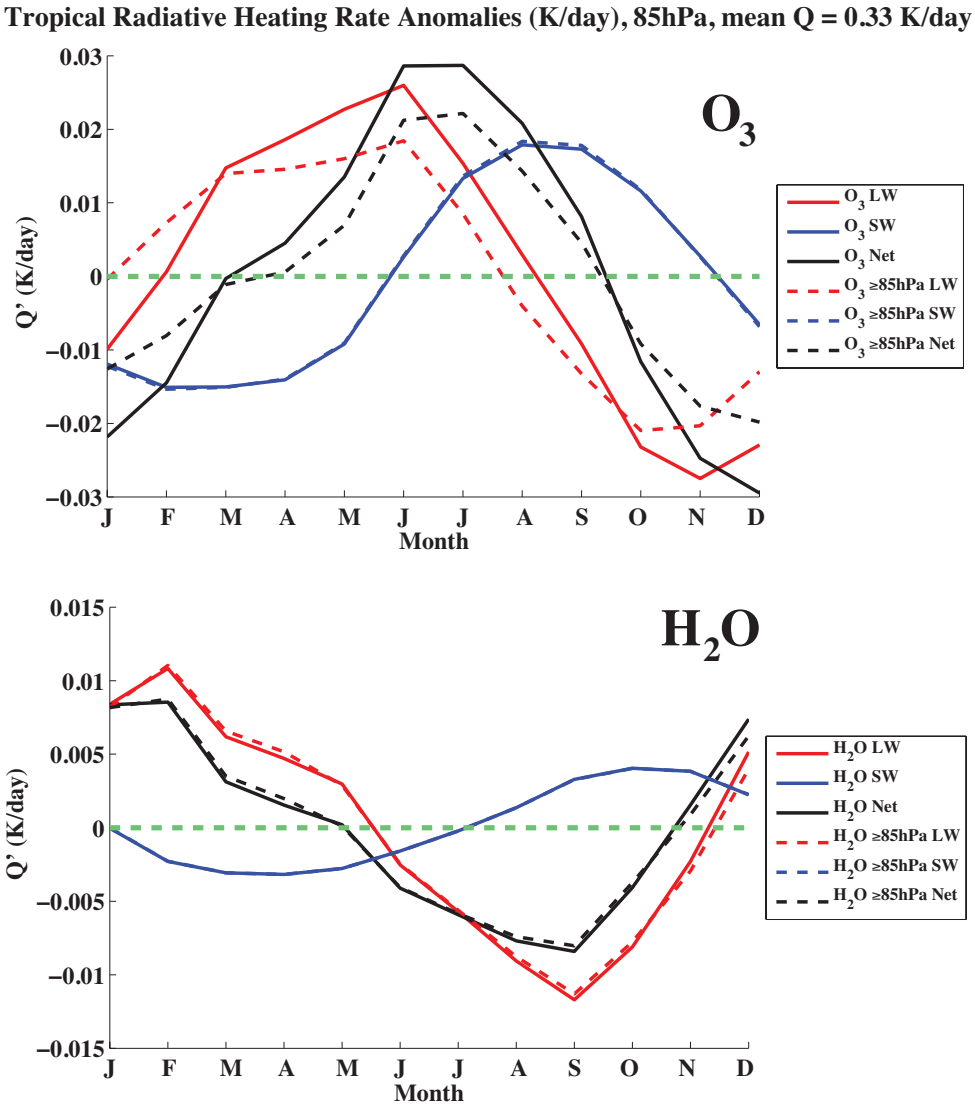

Figure 3-4: Seasonal cycles of calculated radiative heating rate anomalies (K/day) from the climatological average heating rates, averaged between 20°S-20°N on the 85hPa level. Heating rate anomalies are associated with the seasonal cycles of ozone (top panel) and water vapor (bottom panel). Heating rates are separated into longwave (red curves), shortwave (blue curves), and net (black curves) components. Solid curves show the heating rates obtained when the constituent seasonal cycles are considered throughout the stratosphere (from the tropopause to model top, ∼3 hPa). The heating rates obtained when constituent seasonal cycles are considered only between the tropopause and 85 hPa are shown with the dashed curves. The green dashed curve in each panel denotes zero K/day, where heating rates pass from positive (converging towards warmer temperatures) to negative (converging towards cooler temperatures), or vice versa. For reference, the annual-mean heating rate at 85 hPa is shown in the figure title.

about a third of the dynamical seasonal amplitude. Because of its relative magnitude, we conclude that ozone radiative heating is an important term in the seasonal heating budget and acts to amplify the seasonal cycle of lower stratospheric temperatures. This agrees well with our comparison between temperature adjustments and observed temperatures (with temperature adjustments at 85 hPa having an amplitude that is ∼31% of the MLS observed temperature amplitude), and the previous findings of Chae and Sherwood (2007) and Fueglistaler et al. (2011).

Water vapor seasonal cycles of shortwave and longwave heating rates in the lower stratosphere have opposing signs (e.g. Gettelman et al., 2004) with longwave radiation being the larger term. The competing effects result in net cooling in the boreal summer and warming in the boreal winter (an amplitude of a little less than ∼0.02 K/day at 85 hPa). We conclude that while water vapor's seasonal radiative effects near the tropical tropopause are not negligible (in contrast to Folkins et al. (2006) who found no seasonal water vapor radiative signal at ∼90 hPa), they are about a third of those associated with ozone.

3.3.2 Sensitivity Experiments and Latitudinal Variability

We now explore the importance of overlying seasonal cycle structures for lower stratospheric radiative seasonal cycles. Fig. 3-5 shows the radiative seasonal cycles of water vapor and ozone on the 85 hPa level associated with full structure experiments and the 85 hPa, 70 hPa, and 53 hPa sensitivity experiments. The MLS observed seasonal cycle of temperature anomalies (divided by two for scale) is also shown in Fig. 3-5 for comparison with the radiative seasonal cycles. MLS temperature seasonal cycle anomalies minimize in February (∼ -3 K) and maximize in August (∼4.5 K) with a total amplitude of ∼7.5 K. For reference, Fig. 3-3 also shows the tropical-mean peak-to-peak amplitudes of full structure experiments vs. select sensitivity experiments.

At 85 hPa the water vapor radiative seasonal cycle associated with the full vertical structure of perturbations (solid blue curve) is very similar to the radiative seasonal cycles when changes above 85 hPa (dashed blue curve), 70 hPa (blue diamonds), or 53 hPa (blue circles) are not considered (there is <10% difference, <0.1 K, between

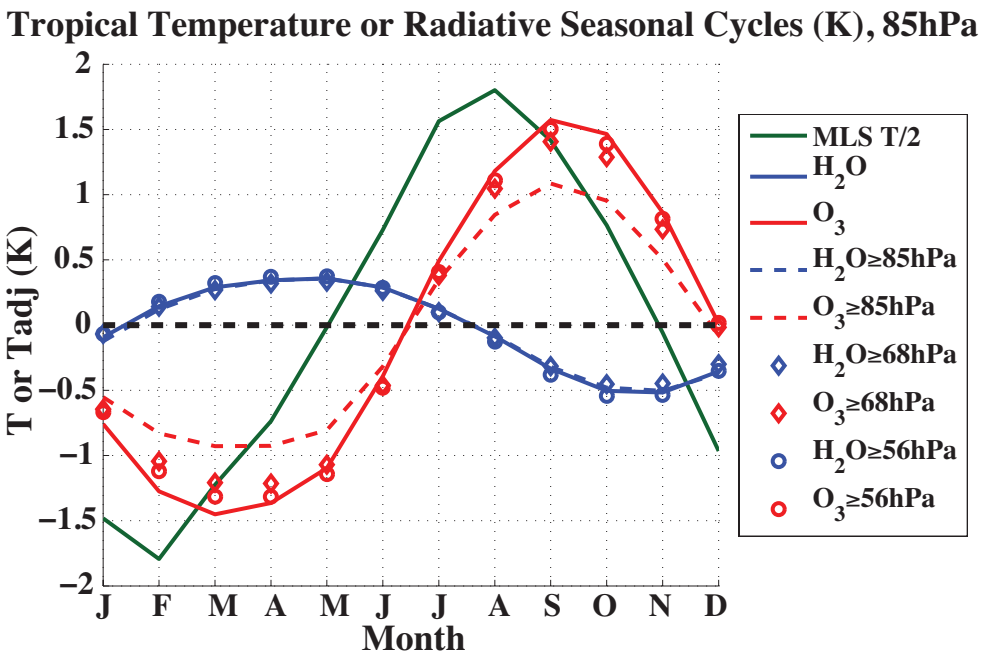

Figure 3-5: Seasonal cycles of MLS observed temperatures divided by two (green curve), and the temperature adjustments associated with the observed seasonal cycles in water vapor (blue curves/symbols) and ozone (red curves/symbols) on the 85 hPa pressure level and averaged between 20°S-20°N. The solid curves show the radiative seasonal cycles obtained when the constituent seasonal cycles are considered throughout the stratosphere (from the tropopause to model top, ∼3 hPa). Radiative seasonal cycles obtained when constituent seasonal cycles are considered only between the tropopause and 85 hPa are shown with the dashed curves. Likewise for constituent seasonal cycles considered between the tropopause and 70 hPa (diamonds), and 53 hPa (circles).

the amplitudes of any of their radiative cycles). This result indicates that the radiative effect of water vapor's seasonal cycle on the temperature seasonal cycle at 85 hPa is almost entirely local, and is insensitive to the vertical structure of overlying water vapor anomalies. While this result is consistent in the context of the water vapor radiative kernel function maximum at near-tropopause levels (e.g. Solomon et al., 2010), the radiative seasonal cycle was not constrained to be strictly local. The lack of overlying effects demonstrates that understanding what sets the seasonality of water vapor concentrations right at the tropical tropopause level is the most important factor in determining water vapor's lower stratospheric seasonal radiative effects. Comparison with the amplitudes in Fig. 3-3 shows that the radiative effect

of water vapor between the tropopause and 85 hPa falls off to near zero in the layers above 85 hPa, missing the canonical tape-recorder structure evident in full structure calculations. Given the smaller magnitude of water vapor radiative seasonal cycle in the lower stratosphere and its lack of vertical structure sensitivity, we focus the remainder of our analysis on the ozone radiative seasonal cycle.

An important finding of this study is that, in contrast to water vapor, ozone's seasonal radiative effects in the lower stratosphere are sensitive to nonlocal overlying changes in ozone. The deviations between radiative seasonal cycles associated with ozone's full vertical structure and the sensitivity experiments (Fig. 3-3 and Fig. 3-5) indicate that the amplitude of ozone's radiative seasonal cycle at 85 hPa depends on both local and nonlocal ozone changes. By considering perturbations between the tropopause and the 85 hPa or 70 hPa levels, for instance, only $\sim$66% or $\sim$87% (respectively) of the full radiative seasonal cycle amplitude is recovered (amplitude differences of $\sim$1 K and 0.4 K, respectively). To capture $>$90% of the full radiative seasonal cycle amplitude, the ozone seasonal cycles up to $\sim$50 hPa or above must be considered. Overlying stratospheric ozone anomalies are therefore important for seasonal lower stratospheric radiative impacts. Therefore, simulating ozone's seasonal radiative influences on lower stratospheric temperatures and dynamics requires ozone anomalies both near and away from the tropopause to be well depicted. Further, future long-term trends in the seasonal cycles of tropical lower and middle stratospheric ozone should be significant for the future evolution of the near-tropopause diabatic heat budget and temperatures (e.g. Forster et al., 2007; Polvani and Solomon, 2012).

Heating rate anomalies show that ozone sensitivities to the overlying vertical structure are related to changes in longwave heating (Fig. 3-4). When seasonal cycles above 85 hPa are not considered in the sensitivity experiment (red dashed curve, top panel of Fig. 3-4), the radiative seasonal amplification of temperatures in the layers above 85 hPa disappears (in fact these seasonal cycles damp slightly, see the dashed red curve in Fig. 3-3), reducing these layers' transmission of nonlocal Planck feedbacks to the 85 hPa level. The damped overlying temperature seasonality combined with the lack of overlying ozone concentration seasonality damps the longwave heating at

85 hPa, driving ozone's vertical structure sensitivity shown in Fig. 3-3 and Fig. 3-5. Shortwave contributions to the 85 hPa ozone radiative seasonal cycle (blue curves, top panel of Fig. 3-4) are local to the layer between the tropopause and 85 hPa to within <1%.

The latitudinal structure of the area-weighted (multiplied by the cosine of latitude) ozone radiative seasonal cycle at 85 hPa is shown in Fig. 3-6b. Temperature adjustments from the full vertical structure of the ozone seasonal cycle are shown, along with temperature adjustments when considering only the ozone seasonal cycle between the tropopause and 85 hPa (i.e. the 85 hPa sensitivity experiment) minus the temperature adjustments from the full vertical structure experiment. Contours overlying shading of opposite sign indicate where excluding the ozone seasonal cycle above 85 hPa damps the amplitude of the ozone radiative seasonal cycle at 85 hPa (cf. Fig. 3-5). For reference, Fig. 3-6a shows the latitudinal structure of *Aura* MLS area-weighted ozone seasonal cycles on the 85 hPa surface. The full range of results from 75°S-75°N is shown for comparison with Fueglistaler et al. (2011, their Figure 5); the yellow lines in Fig. 3-6b denote the tropical region specifically considered in this study. The full structure of the radiative seasonal cycle in Fig. 3-6 is qualitatively consistent with that in Fueglistaler et al. (2011, their Figure 5b) at 67 hPa, but further elucidates the spatial structure of the lowermost stratosphere's sensitivity to overlying ozone seasonal cycles. To clarify the differences between the two hemispheres, Fig. 3-7 shows the observed ozone seasonal cycles and their associated full structure radiative seasonal cycles averaged between the SH tropics (20°S-0°, Fig. 3-7a and 3-7c) and the NH tropics (0°-20°N, Fig. 3-7b and 3-7d).

Just above the tropopause in the NH tropics (0°-20°N), the full vertical structure ozone radiative seasonal cycle has a maximum amplitude at ∼12°N, with maximum radiative cooling (adjustments of ∼ -.2 K) between February and March, and maximum radiative warming (adjustments of up to ∼ 2.2 K) in September (Fig. 3-6). The amplitude averaged between 0°-20°N is about 3.8 K. When ozone perturbations above 85 hPa are not considered, the amplitude of the NH tropical ozone radiative seasonal cycle is reduced by ∼35%. There is only a 1-month phase shift in the NH

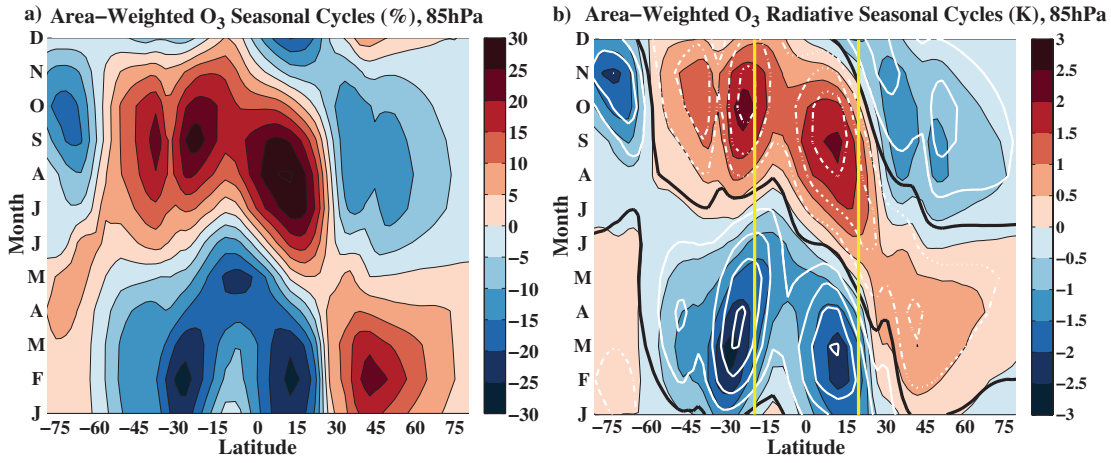

Figure 3-6: (a) The area-weighted ozone seasonal cycle on the 85 hPa pressure level (%); the contour interval is 5%. (b) Colored shading shows the area-weighted latitudinal structure of temperature adjustments, on the 85 hPa pressure level, obtained when the full structure of the ozone seasonal cycle is considered throughout the stratosphere (from the tropopause to model top, ∼3 hPa). The shading contour interval is 0.5 K. White contours show the area-weighted temperature adjustments obtained when the ozone seasonal cycles is considered only between the tropopause and 85 hPa minus the temperature adjustments obtained when considering the full structure (i.e. the shading). Positive/negative differences are denoted with solid/dash-dot white lines. The bold black line is the 0 K contour line for the differences. The white contour interval is 0.2 K. The yellow lines denote the tropical range from 20°S to 20°N.

ozone radiative seasonal cycle when seasonal cycles above the 85 hPa level are not considered (Fig. 3-6), because the ozone seasonal cycle in the NH tropics is nearly in-phase between 100 and 50 hPa (Fig. 3-7b).

The SH radiative seasonal cycle (ranging between 20°S-0°) associated with the full vertical structure of the ozone seasonal cycle has a smaller amplitude than the NH tropics (3 K compared with 3.8 K) and is less homogenous across the SH tropical band (Fig. 3-6). The maximum radiative cooling is found in April, ranging from -1.8 K at 20°S to -1 K at 10°S. The maximum radiative warming is found in October, ranging from 2.3 K at 20°S to 1.2 K at 10°S. This result is consistent with Stolarski et al. (2014), who emphasized that the tropical lower stratosphere ozone seasonal cycle is smaller in the SH than the NH, and SH seasonal cycle lags the NH cycle by 1-2 months (cf. Fig. 3-6a, Fig. 3-7a-b). At latitudes between the equator and 15°S, there is less sensitivity to overlying changes than in the NH tropics; the radiative seasonal cycle

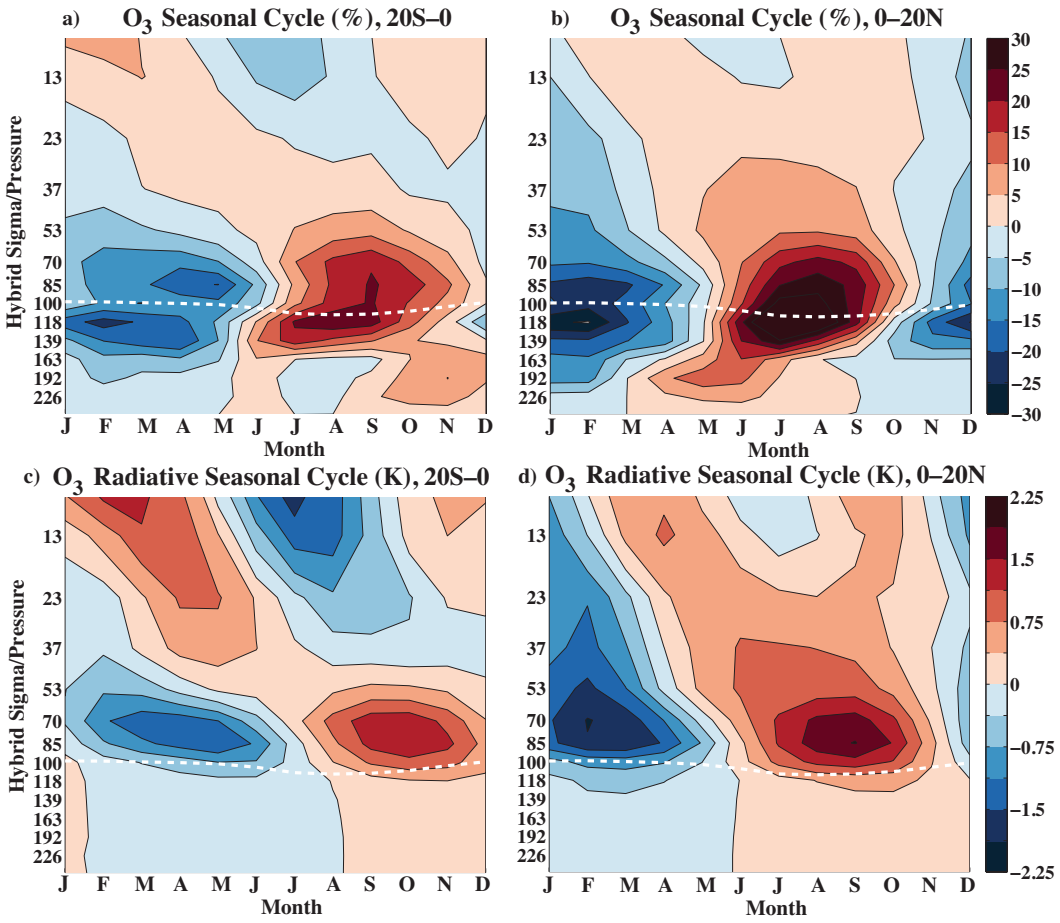

Figure 3-7: (a) and (b) following Fig. 3-1c, except for ozone observations averaged between 20°S-0° (a) and 0°-20°N (b). The contour interval is 5%. (c) and (d) following Fig. 3-2b, except for radiative temperature adjustments associated with ozone averaged between 20°S-0° (c) and 0°-20°N (d). The contour interval is 0.375 K. The white dashed curve in each figure denotes each region's PORT climatological tropopause.

averaged over this range is damped by only ∼27% when contributions from the ozone seasonal cycle above 85 hPa are not considered (compared with a ∼35% damping in the NH tropics), and phase-changes are also small. The SH tropical (20°S-0°) ozone seasonal cycle (Fig. 3-7a) and the associated full structure radiative seasonal cycle (Fig. 3-7c) are shallower than those of the NH (Fig. 3-7b and 3-7d), contributing to the reduced radiative sensitivity to seasonality above 85 hPa.

At higher southern latitudes largely outside the traditional tropical band, there is a strong ozone concentration and radiative seasonal cycle on the 85 hPa level stretching from 35°S-15°S (Fig. 3-6). This feature arises because of the migration of the tropical

region on the 85 hPa pressure surface, moving northward in the boreal summer and southward in the austral summer (Stolarski et al., 2014). Strong upwelling and weak horizontal in-mixing across the subtropical jet promotes reductions in ozone at these latitudes from January to March (Chen, 1995; Stolarski et al., 2014). As the tropical lower stratosphere retreats northward in the boreal summer, it is replaced in this region by extra-tropical air with higher concentrations of ozone. The result is a consistent strong seasonal cycle of ozone that is in-phase between the tropopause and ∼50 hPa, with large seasonal cycle amplitudes between 50% and 23%, respectively (Supplemental Fig. S3). Because the overlying seasonal cycles are in-phase with the cycles below (Fig. S3), the local and nonlocal radiative effects compound and lead to a radiative seasonal cycle that maximizes at ∼24°S with an amplitude of 4.9 K. When the seasonal cycle above 85 hPa is not considered, the average amplitude of the radiative seasonal cycle between 35°S-15°S at 85 hPa is reduced to about 3.1 K (a 26% reduction from the full structure ozone radiative seasonal cycle). While these changes are physical, they are only relevant for the tropical lower stratosphere during the austral summer months when the SH tropics extend to these latitudes.

The distinct horizontal patterns in NH and SH ozone, related to the increased mixing in the NH surf-zone region, the migration of the tropical lower stratosphere, and the phasing of upwelling and horizontal mixing in the two hemispheres (Stolarski et al., 2014), result in meridionally asymmetric radiative effects in the tropics. When considering the impacts of radiative effects on lower stratospheric or near-tropopause phenomena in detail (such as the outflow of tropical cyclones or the amount of water vapor entering the stratosphere), the latitudinal variability examined here should be accounted for. Notably, seasonal cycle amplitudes of tropical lower stratospheric temperatures maximize in the NH tropics (Reed and Vlcek, 1969; Randel, 2003; Fueglistaler et al., 2009a; Grise and Thompson, 2013). Our results indicate that the ozone radiative effects amplify this hemispheric asymmetry.

3.4 Summary

This study has used *Aura* Microwave Limb Sounder (MLS) observations of tropical stratospheric water vapor and ozone and a radiative transfer model to determine their purely radiative impacts on the upper troposphere and lower stratosphere. The radiative sensitivities to the specific vertical structures of water vapor and ozone seasonal cycles have been investigated to ascertain how overlying seasonal cycles nonlocally impact radiative temperature adjustments in the lower stratosphere. Hemispheric asymmetries in ozone's seasonal radiative effects and sensitivities have also been elucidated.

The key findings of this chapter are:

1) Ozone's seasonal radiative effect is broad across the tropical lower stratosphere, whereas water vapor's seasonal radiative effect maximizes just above the tropopause. Ozone is the larger contributor to the seasonal radiative impacts in the tropical lower stratosphere—at levels just above the tropical tropopause, ozone's seasonal cycle of radiative temperature adjustments has a peak-to-peak amplitude that is ∼3.4 times that of water vapor—but water vapor's seasonal radiative effects are more influential than was previously thought, suggesting that neglecting water vapor seasonality when considering the radiative budget of the tropical stratosphere could miss important variability (Folkins et al., 2006; Chae and Sherwood, 2007; Fueglistaler et al., 2011). Water vapor's signal is about a third that of ozone primarily because of offsetting longwave and shortwave effects. Ozone's larger heating rates are the sum of shortwave effects following ozone concentrations and longwave effects following both concentrations and associated temperature adjustments (Planck feedback).

2) The radiative impacts of water vapor's seasonal cycle in the lower stratosphere are not sensitive to the overlying water vapor structure. That is, local radiative responses largely drive water vapor's "radiative tropical tape-recorder". In contrast, 33% of the radiative effects of ozone's seasonal cycle at 85 hPa are associated with longwave emission from ozone seasonal cycles overlying the 85 hPa level. To recover 90% or more of ozone's seasonal radiative response near the tropical tropopause,

ozone seasonal cycles up to at least ∼50 hPa must be included in radiative calculations. It is therefore important that ozone's nonlocal radiative effects above the lower stratosphere be accounted for when characterizing the seasonal radiative budget in the tropical lower stratosphere.

3) Ozone's lower stratospheric seasonal radiative effects are asymmetric about the equator: the radiative seasonal cycle amplitude in the northern hemisphere tropics (0°-20°N) is 27% larger (0.8 K) than that in the southern hemisphere tropics (20°S-0°). Additionally, ozone radiative impacts in the northern hemisphere tropical lower stratosphere have 8% greater absolute sensitivity to the overlying seasonal ozone structure than the southern hemisphere tropics. These results are linked to the observed asymmetrical ozone concentration seasonal cycle detailed by Stolarski et al. (2014). More work is needed to understand how ozone's radiative asymmetry about the equator contributes to the observed meridional asymmetry in tropical lower stratospheric temperature seasonal cycles (e.g. Randel, 2003).

In this study we have not assessed the seasonal radiative effects of other lower stratospheric constituents such as nitrous oxide or methane (although these effects would likely be minor, Gettelman et al. (2004)), aerosols, or clouds, each of which could play a role in the seasonal radiative budget in the tropical lower stratosphere (e.g. Fueglistaler et al., 2009a). A further limitation of this study is the reliance on seasonally evolving fixed dynamical heating (SEFDH, Forster et al., 1997) to estimate the radiative seasonal cycles of water vapor and ozone. Whereas SEFDH is useful for determining the pure radiative temperature response to observed constituent changes in the stratosphere, it is only an upper bound estimate of radiative effects on temperature, because dynamics could to some extent respond, thus balancing seasonal anomalies in radiative heating (e.g. Ming et al., 2016). Radiative contributions to temperatures in the lower stratosphere may consequently be lower than the upper bound determined herein.

We have also calculated the heating rates associated with observed water vapor and ozone seasonal cycles, which are observationally constrained and only depend on SEFDH to the extent that it is used to estimate longwave adjusted heating rates

(Planck feedback). The amplitude of ozone heating rates is about a third of estimated dynamical heating rate amplitudes in the tropical lower stratosphere (Abalos et al., 2012), suggesting that ozone does substantially contribute to the seasonal heating budget and by extension the seasonal temperature budget in the tropical lower stratosphere.

As the stratospheric circulation is expected to change over this century in response to climate change (e.g. McLandress and Shepherd, 2009; Fu et al., 2015), understanding the factors which impact radiative heating in the tropical lower stratosphere will be important for model and reanalysis representations of the stratosphere and tropopause. The work presented herein suggests that misrepresenting the ozone seasonal cycle in the lower stratosphere and the layers above will have consequences for seasonal radiative heating near the tropical tropopause. Along with seasonal trends in stratospheric temperatures and/or stratospheric circulation (such as those suggested by Fu et al. (2010)), seasonal radiation could also change and indirectly affect physical phenomena that depend on future near-tropopause temperatures, such as the amount of water vapor entering the overworld or the intensity of tropical cyclones.

---

to the AMS Permissions Officer at permissions@ametsoc.org. Additional details are provided in the AMS Copyright Policy statement, available on the AMS website (http://www.ametsoc.org/CopyrightInformation).

Chapter 4

On the Seasonal Cycles of Tropical Cyclone Potential Intensity

Abstract

Recent studies have investigated trends and interannual variability in the potential intensity (PI) of tropical cyclones (TCs), but relatively few have examined TC PI seasonality or its controlling factors. Potential intensity is a function of environmental conditions that influence thermodynamic atmosphere-ocean disequilibrium and the TC thermodynamic efficiency—primarily sea surface temperatures and the TC outflow temperatures—and therefore varies spatially across ocean basins with different ambient conditions. This chapter analyzes the seasonal cycles of TC PI in each main development region using reanalysis data from 1980 to 2013. TC outflow in the western North Pacific (WNP) region is found above the tropopause throughout the seasonal cycle. Consequently, WNP TC PI is strongly influenced by the seasonal cycle of lower-stratospheric temperatures, which act to damp its seasonal variability and thereby permit powerful TCs any time during the year. In contrast, the other main development regions (such as the North Atlantic) exhibit outflow levels in the troposphere through much of the year, except during their peak seasons. Mathematical decomposition of the TC PI metric shows that outflow temperatures damp WNP

This chapter was published in the *Journal of Climate* (Gilford et al., 2017) and is reproduced with permission. The publication and its supplement are available at `https://doi.org/10.1175/JCLI-D-16-0827.1`.

TC PI seasonality through thermodynamic efficiency by a quarter to a third, whereas disequilibrium between SSTs and the troposphere drives 72-85% of the seasonal amplitude in the other ocean basins. Strong linkages between disequilibrium and TC PI seasonality in these basins result in thermodynamic support for powerful TCs only during their peak seasons. Decomposition also shows that the stratospheric influence on outflow temperatures in the WNP delays the peak month of TC PI by a month.

4.1 Introduction

It is important to understand the intensity of tropical cyclones (TCs) because coastal societies are vulnerable to their dangerous and costly impacts (e.g. Pielke and Pielke, 1997). Studies over the last few decades have established a theoretical framework for investigating the "potential intensity" (PI) that a TC may reach given local environmental conditions (e.g. Emanuel, 1986; Holland, 1997; Bister and Emanuel, 1998, 2002). Evidence suggests that variations in actual tropical cyclone intensities scale with variability in potential intensity on multiple timescales (Emanuel, 2000; Wing et al., 2007, explored further in chapter 5). While it is recognized that warming sea surface temperatures (SSTs) have been and will continue to be a key driver for TC PI trends under anthropogenic climate forcing (e.g. Henderson-Sellers et al., 1998; Emanuel, 2005; Knutson et al., 2010; Holland and Bruyère, 2014; Strazzo et al., 2014; Walsh et al., 2016, *and references therein*), recent work has also focused on how lower stratospheric temperatures influence TC PI (e.g. Emanuel et al., 2013; Ramsay, 2013; Wang et al., 2014). Some studies have explored stratospheric linkages with TC PI trends over the past three decades (Emanuel et al., 2013; Wing et al., 2015), in the future under anthropogenic climate forcing (Vecchi et al., 2014; Sobel et al., 2016; Walsh et al., 2016), and in a Montreal Protocol world-avoided scenario (Polvani et al., 2016). Less attention has been given to interannual variability in TC PI and its connections with the upper atmosphere (Wing et al., 2015), and only a few studies have considered the seasonality of potential intensity (Free et al., 2004; Tonkin et al., 2000). In this chapter we calculate the seasonal cycles of tropical cyclone potential in-

tensity in the main TC development regions with 34-years of reanalysis data, and use a decomposition method to determine the main factors that drive TC PI seasonality in these regions.

Tonkin et al. (2000) investigated the seasonal cycles of TC potential intensity with a set of radiosonde stations in the Northwest Pacific, Australian Southwest Pacific, and North Atlantic regions. Potential intensity calculations using the early Emanuel (1986, 1991) method and the Holland (1997) method were compared to one another and to observed TC intensities. Tonkin et al. (2000) found that both methods generally performed well at predicting observed seasonal intensities in the tropics (though each was overly sensitive to certain environmental conditions). However, their study did not directly attribute the seasonal cycles to local thermodynamic contributions beyond SSTs, and their data were spatially limited. Free et al. (2004) also explored potential intensity seasonal cycles. Using data from fourteen radiosonde stations, they showed that there were seasonal differences in TC PI across the tropics. In the Caribbean these differences were attributed to each station's distance from the equator (with calculations showing larger seasonal cycle amplitudes at stations farther from the equator), whereas no explanation was offered for the Pacific basin differences. Further, no analysis was performed to determine the thermodynamic conditions contributing to the seasonal cycles in each ocean basin. In this chapter, we will show that spatial differences in the seasonal cycles of TC PI are linked to the seasonality of each ocean basin's sea surface temperatures, TC outflow levels, and outflow temperatures. Note that we do not explore the seasonality of other factors known to be important for the genesis or intensity of tropical cyclones, such as vertical wind shear (e.g. Frank and Ritchie, 2001; Emanuel, 2006).

The goals of this chapter are to characterize the seasonal cycles of TC PI pertaining to the main TC development regions in each ocean basin, and to identify the key factors contributing to these cycles. In section 4.2, we describe the TC PI calculation and decomposition, along with the reanalysis data used to compute TC PI. Section 4.3 shows the resulting TC PI seasonal cycles and quantifies the thermodynamic contributions to these cycles. The study is summarized in section 4.4.

4.2 Data and Methods

Tropical cyclone potential intensity (V_p) is defined following Bister and Emanuel (1998) as:

$$(V_p)^2 = \frac{C_k}{C_D}\frac{(T_S - T_0)}{T_0}(h_o^* - h^*) \tag{4.1}$$

where C_k and C_D are the enthalpy and momentum surface exchange coefficients, respectively, T_S is the sea surface temperature, T_0 is the mean outflow temperature, h_o^* is the saturation moist static energy at the sea surface, and h^* is the moist static energy of the free troposphere. The ratio $\frac{C_k}{C_D}$ is an uncertain quantity and determining its value is an area of active research (e.g. Emanuel, 2003, *and references therein*), but it is typically taken to be a constant. Here we set $\frac{C_k}{C_D} = 0.9$ following the precedent of previous studies (Wang et al., 2014; Wing et al., 2015), but we have tested a range of reasonable ratios ($0.4 - 1.0$) and found our results to be qualitatively insensitive to the choice. The term $\frac{(T_S - T_0)}{T_0}$ is the thermodynamic efficiency of the potential tropical cyclone. It is readily determined that kelvin-for-kelvin the efficiency term is more sensitive to T_0 than T_S. However, T_S seasonal amplitude is generally larger than that of T_0, and T_S and T_0 may be related to one another through the outflow level, with key implications for the seasonal cycles of TC PI (see section 4.3). The final term, $(h_o^* - h^*)$, is the thermodynamic disequilibrium between the sea surface and the free troposphere, which is principally controlled by sea surface temperatures (e.g. Emanuel, 2007).

We compute the potential intensity using the algorithm of (Bister and Emanuel, 2002, hereafter BE02). The BE02 scheme is more accurate for TC PI calculations in the tropics than directly calculating and summing each individual term on the right-hand-side of Equation 4.1 because of its incorporation of water loading and virtual temperature (Garner, 2015; Wing et al., 2015). Besides its increased accuracy over direct computation of Equation 4.1, the BE02 algorithm is advantageous because it has been frequently employed in previous studies of PI (e.g. Emanuel, 2007; Sobel and Camargo, 2011; Emanuel et al., 2013; Wang et al., 2014; Wing et al., 2015;

Polvani et al., 2016), allowing straightforward comparisons between those studies and this work. We computed TC PI directly with Equation 4.1 and found that the thermodynamic disequilibrium term is larger than that inferred from the BE02 algorithm by 10-25%, but results are qualitatively similar to those in section 4.3.

The BE02 algorithm requires profiles of temperature and humidity, along with sea surface temperatures and mean sea-level pressures. The algorithm is configured to output V_p, the outflow temperature, and the outflow temperature level (OTL). The OTL is the level of neutral buoyancy for an air parcel saturated at sea-level pressure, corresponding to the outflow temperature. Outflow temperatures allow direct calculation of the efficiency term (second term on the right-hand-side of Equation 4.1) at each temporal and spatial location. Given the output potential intensity and efficiency, the thermodynamic disequilibrium $(h_o^* - h^*)$ can be derived from Equation 4.1. In the BE02 algorithm, parcels are lifted assuming reversible adiabatic ascent. Assuming pseudo-adiabatic ascent instead leads to qualitatively similar results, except that OTLs are typically found at higher altitudes, allowing more stratospheric influence on TC PI in all regions (see section 4.3). We decompose Equation 4.1 by taking the natural logarithm of both sides:

$$2 \times log(V_p) = log(\frac{C_k}{C_D}) + log(\frac{T_S - T_0}{T_0}) + log(h_o^* - h^*) \tag{4.2}$$

This log-additive model is advantageous because it is quantifies thermodynamic disequilibrium and thermodynamic efficiency contributions to TC PI at every spatial and temporal location.

Temperature, water vapor, sea surface temperature, and mean sea-level pressure data from 1980-2013 are taken from the second Modern-Era Retrospective analysis for Research and Applications (MERRA2, Bosilovich et al., 2016) and the Interim European Centre for Medium-Range Weather Forecasts Re-Analysis (ERA-I, Dee et al., 2011). 6-hourly data from both reanalyses are regridded onto a monthly 2.5° x 2.5° grid. As we average over tropical cyclone main development regions (see below), the horizontal resolution is not expected to play a significant role in the results. Previ-

Table 4.1: Tropical cyclone main development regions and their geographical ranges. Regions (except NA; see text) defined following Emanuel (2005) and Wing et al. (2015).

Basin	Range
North Atlantic (NA)	8.75°–31.25°N, 266.25°–308.75°E
Eastern North Pacific (ENP)	3.75°–16.25°N, 191.25°–268.75°E
Western North Pacific (WNP)	3.75°–16.25°N, 131.25°–178.75°E
North Indian (NI)	3.75°–21.25°N, 51.25°–108.75°E
Southern Hemisphere (SH)	18.75°–3.75°S, 61.25°–178.75°E

ous work by Kossin (2015) validated observed TC cloud-top brightness temperatures against MERRA/ERA-I outflow temperatures and found that they vary consistently with one another on multiple timescales, suggesting that seasonal evaluation of TC outflow temperatures and potential intensity with these reanalyses is appropriate. For clarity and brevity we show only the MERRA2 results herein; ERA-I results are largely consistent with MERRA2 and are shown in the publication Supplement (Fig. S1-S4).

Our methodology is designed to evaluate the seasonal cycles of potential intensity dictated by seasonal atmospheric and ocean states. We determine the monthly means of each state variable from reanalyses, and compute TC PI with the BE02 algorithm at every ocean grid point. Monthly means of state variables and algorithm outputs are then time-averaged over the 34-year period and area-averaged over the tropical cyclone main development regions in each ocean basin (Table 4.1) following Emanuel (2005) and Wing et al. (2015), except that we retain the full seasonal cycle in each case (rather than averaging over the peak months) and use a somewhat different NA main development region definition than Wing et al. (2015). Our NA region focuses specifically on TC PI in the far western Atlantic and Gulf of Mexico, where tropical cyclones frequently develop (e.g. Gray, 1984); results for the NA are qualitatively insensitive to whether we use this definition or that of Wing et al. (2015). Furthermore, results for each main development region in Table 4.1 are qualitatively robust to modest ($\sim$5°) poleward shifts (see Fig. 4-2).

We do not account for interannual variability in our results (e.g. ENSO, QBO, volcanoes), but the 34-year period averages are expected to smooth such variability

and demonstrate typical TC PI seasonal cycles in each ocean basin. To test the sampling uncertainty in the mean seasonal cycles we employ an empirical bootstrap method (Efron and Gong, 1983) in Appendix A (section 4.5). Results from this exercise show that each of these seasonal cycles averaged over the main development regions are statistically robust (see Fig. 4-6 and Table 4.3).

4.3 Results

4.3.1 Seasonal Cycle Overview

We first provide an overview of the seasonal cycles of TC PI and associated atmospheric conditions in each main development region. Figure 4-1 shows the seasonal cycles of sea surface temperature, outflow temperature, the outflow temperature pressure level, and TC PI for each main development region from MERRA2 data. The seasonal cycles calculated with ERA-I data are similar to those of MERRA2 (see Supplemental Figures S1-S2). Figure 4-2 shows the horizontal structures of the monthly peak-to-peak seasonal cycle amplitudes (hereafter "amplitudes") of SSTs, outflow temperature, and TC PI from MERRA2. Positive amplitudes in Figure 4-2 indicate that the seasonal cycle maximizes in the boreal summer and negative amplitudes indicate that the seasonal cycle maximizes in the boreal winter; boxes outlining each main development region are also included (except NI, see below).

SST variability is driven by complex interactions in the coupled ocean-atmosphere system (e.g. Deser et al., 2010). SST seasonal cycles in the NA, ENP, WNP, and SH regions (Fig. 4-1a) each have a single annual maxima and a single annual minima which coincide with their hemispheric summer or winter, respectively. The phase of the SST seasonal cycle is delayed by several months relative to the annual solar cycle due to atmosphere-ocean thermal inertia (e.g. Cronin and Emanuel, 2013). In the NI the monsoonal circulation drives a semi-annual seasonal cycle in SSTs (Schott and McCreary, 2001; Schott et al., 2009, *and references therein*). Because our amplitude definition does not account for a semi-annual component, we do not consider the NI

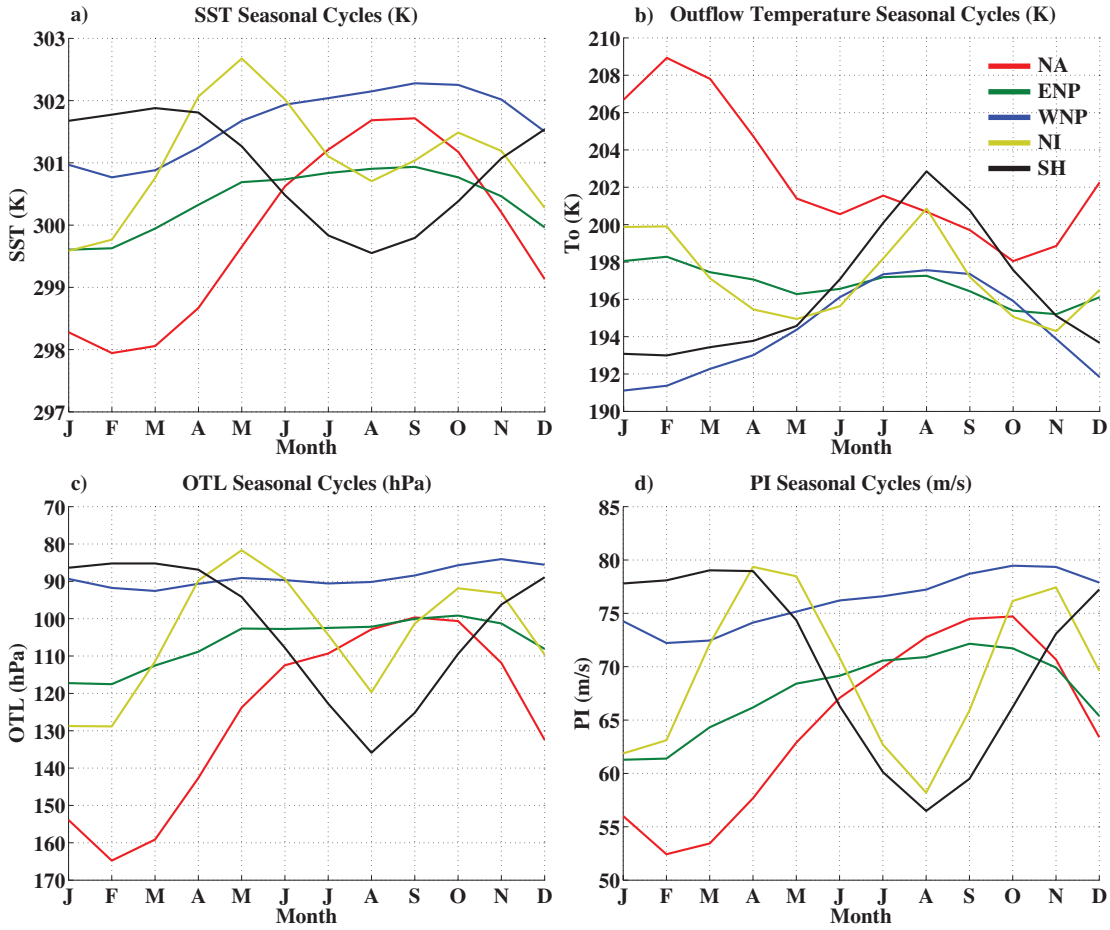

Figure 4-1: Seasonal cycles of (a) sea surface temperature, (b) TC outflow temperature, (c) outflow temperature level, and (d) TC potential intensity using MERRA2 data averaged over 1980-2013 and the TC development regions. The main development regions are North Atlantic (red), Eastern North Pacific (green), Western North Pacific (blue), North Indian (yellow), and Southern Hemisphere (black), as defined in Table 4.1.

region in our seasonal amplitude analyses (i.e. Fig. 4-2, Table 4.2).

In the WNP SSTs have limited seasonality (Fig. 4-1a) and are above the canonical 26.5°C threshold for TC development year-round (e.g. Palmen, 1948). This requisite has been recently reexamined, and its specific value is expected to increase with climate change (Vecchi and Soden, 2007a; Johnson and Xie, 2010; McTaggart-Cowan et al., 2015). The deep mixed-layer in the Pacific Warm Pool region results in a weak SST seasonal cycle (mean amplitude of 1.5 K) at the lower tropical latitudes (Fig. 4-2a Wyrtki, 1961; Schneider and Zhu, 1998). The ENP region also has weak

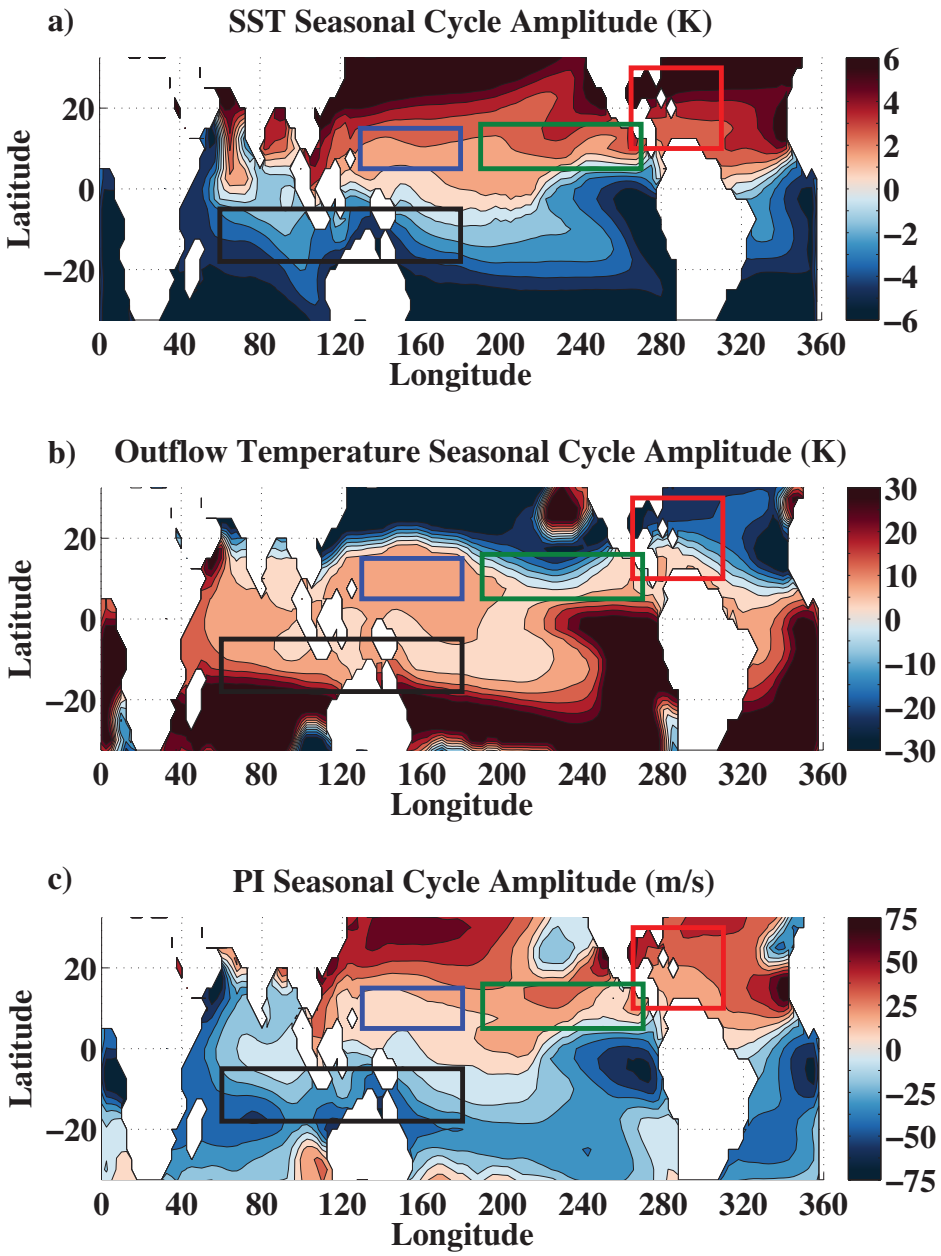

Figure 4-2: The seasonal cycle monthly peak-to-peak amplitudes of (a) sea surface temperatures, (b) tropical cyclone outflow temperatures, and (c) tropical cyclone potential intensity. Data are from MERRA2 averaged over 1980-2013. Contour intervals are every 1 K, 5 K, and 12.5 ms^{-1}, respectively. Contours saturate at each respective colorbar extent, and are smoothed with a 3x3 grid-point uniform boxcar filter. The main development regions indicated by boxes are Western North Pacific (blue), Eastern North Pacific (green), North Atlantic (red), and Southern Hemisphere (black), as in Table 4.1.

seasonality (amplitude of 1.3 K), but SSTs are cooler by 1-1.5 K (Fig. 4-1a) and have a less homogenous seasonal cycle across the region (Fig. 4-2a). The NA and SH regions both have larger seasonal amplitudes in SST (3.8 K and 2.3 K, respectively) that are spatially inhomogeneous and associated with seasonally varying mixed layer depths (de Boyer Montegut et al., 2004).

Figure 4-3 shows the annual mean OTLs in the tropics (Fig. 4-3a), along with the seasonal cycles of the OTL pressure minus the lapse rate tropopause pressure averaged over each main development region (Fig. 4-3b). Here the lapse rate tropopause is defined as the lowest height where the lapse rate falls below 2 K/km (WMO, 1957) and was determined with MERRA2 data following the methodology of Reichler et al. (2003). A positive difference in Fig. 4-3b indicates that the monthly mean OTL is at a higher pressure (lower altitude) than the monthly mean tropopause. Note that the height of the tropical tropopause also has a consistent seasonal cycle: it is found at minimum pressures in the boreal winter and maximum pressures in the boreal summer (e.g. Kim and Son, 2012). For reference, Figure 4-4 shows the seasonal anomalies of air temperature (with the annual mean at each pressure level removed) in tropical troposphere and lower stratosphere, the lapse rate tropopause pressure, the outflow temperature levels, and the seasonal cycles of SSTs in each main development region.

The seasonal cycles in outflow temperature (Fig. 4-1b) are tightly linked to outflow temperature levels (Fig. 4-1c, Fig. 4-3). While the OTL remains in the troposphere, lower pressures are associated with cooler outflow temperatures (as temperatures decrease with height up to the cold-point). Although there are temperature seasonal cycles in the tropical troposphere, their amplitudes on any tropospheric pressure level are small ($<$4 K, Fig. 4-4, cf. Donohoe and Battisti (2013)), and instead the lapse rate and OTL pressure dominates outflow temperature seasonality. Recall that the OTL is the level of neutral buoyancy for a saturated air-parcel lifted from sea level, and is hence thermodynamically coupled to local SSTs (section 4.2, Fig. 4-4): warmer SSTs will be associated with higher (and therefore cooler) outflow levels, whereas cooler SSTs with be associated with lower (and warmer) outflow levels. Outflow temperatures and SSTs are therefore generally opposite-phased when outflow is found in the

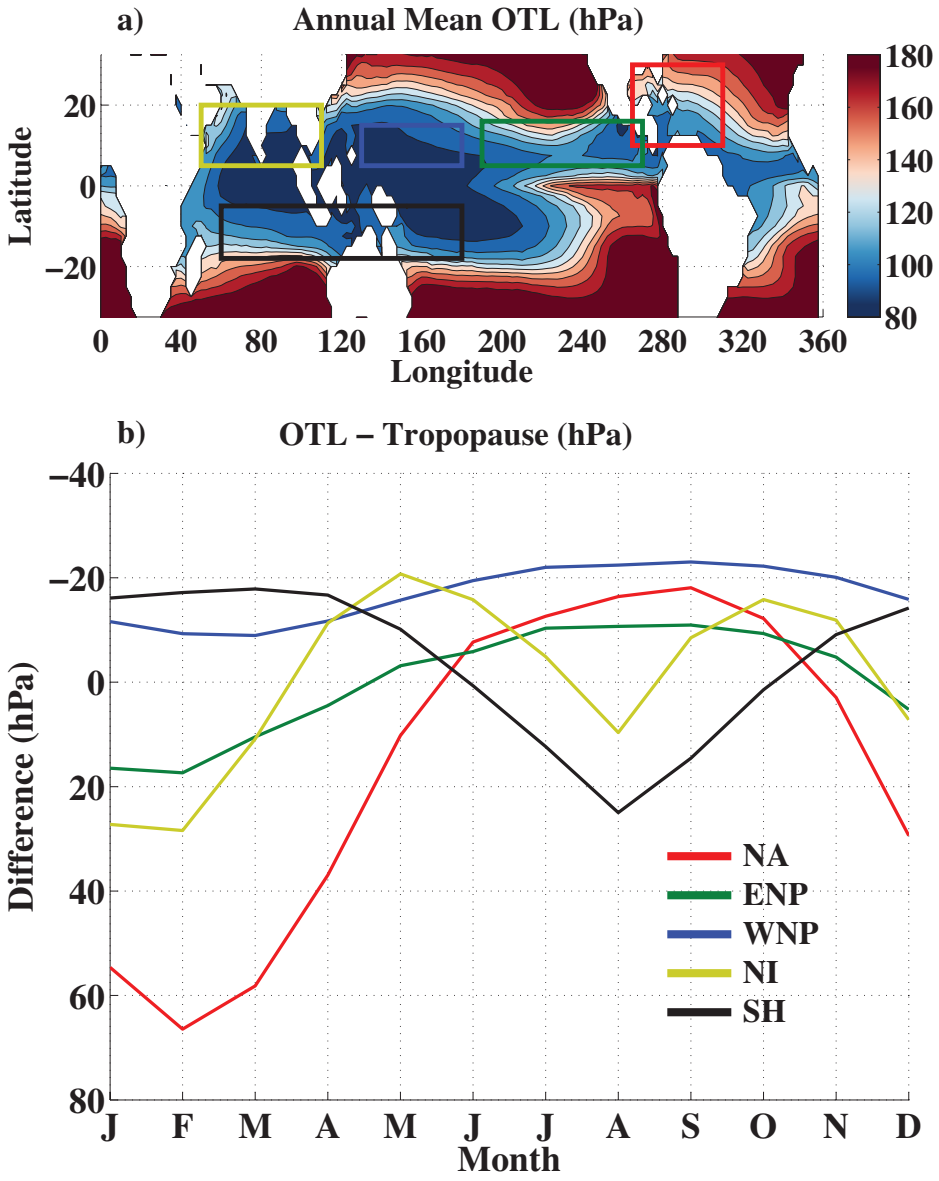

Figure 4-3: (a) The annual mean outflow temperature level, computed with MERRA2 data over 1980-2013. Contour interval is every 10 hPa. Contours saturate at the colorbar extent. (b) The seasonal cycle of the outflow temperature level minus the WMO tropopause height (in hPa), using MERRA2 data averaged over 1980-2013 and the TC main development regions defined in Table 4.1. Boxes and line colors follow the region convention in Figures 4-1 and 4-2.

troposphere (e.g. in the NA region from November to May, Fig. 4-3b). This inverse relationship has important implications for TC PI seasonality, because the difference between SSTs and outflow temperatures determines the thermodynamic efficiency of the TC PI (Equation 4.1). When the OTL migrates across the tropopause into the

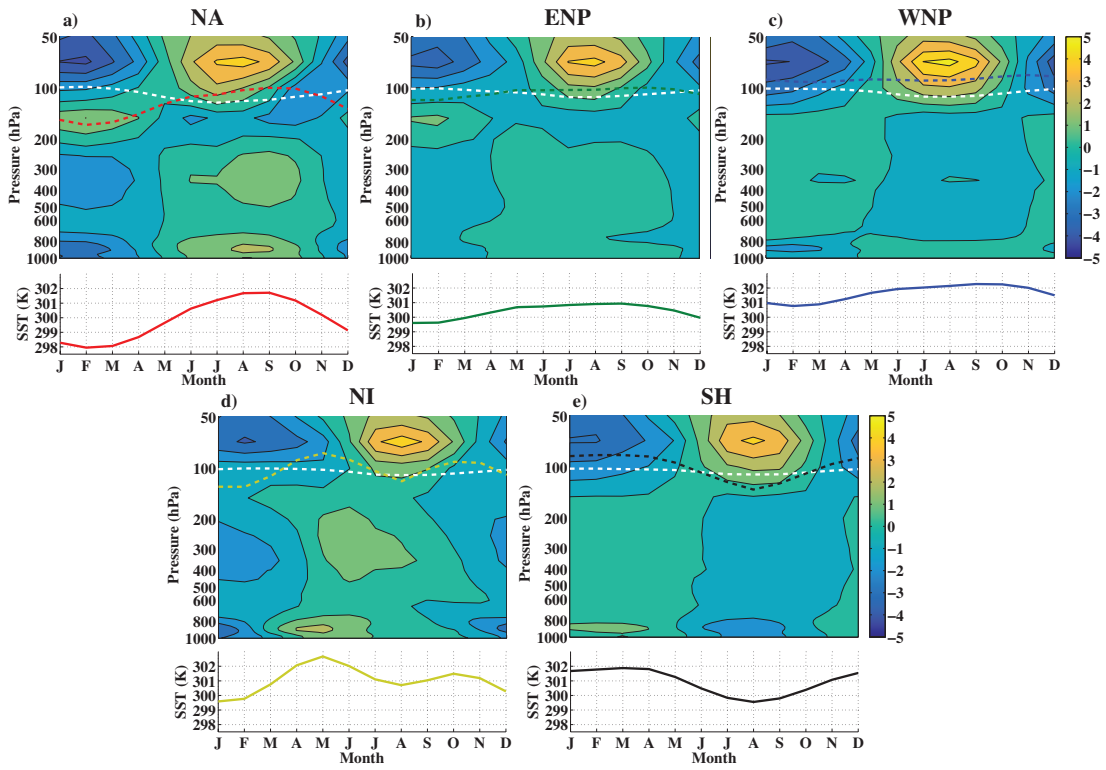

Figure 4-4: Seasonal anomalies of air temperature (K) at each pressure level (top panels, contours) and seasonal cycles of sea surface temperatures (K, bottom panels, solid lines) for the (a) North Atlantic, (b) Eastern North Pacific, (c) Western North Pacific, (d) North Indian, and (e) Southern Hemisphere main development regions defined in Table 4.1. Overlaid on the contours are seasonal cycles of the WMO lapse rate tropopause pressure (white dashed curves) and outflow temperature level (colored dashed curves). Data are from MERRA2 averaged over 1980-2013.

stratosphere, however, outflow temperatures are regulated by the lower stratospheric temperature seasonal cycle. In each region OTLs penetrate the stratosphere at some point in the seasonal cycle, typically during their periods of largest PI (Fig. 4-3b-d, Fig. 4-4).

Annual mean OTLs in the WNP (Fig. 4-3a) are largely homogeneous over the region and are always found in the stratosphere (<95 hPa, Fig. 4-3b, Fig. 4-4c). This is consistent with the annual presence of the Western Pacific Warm Pool which "anchors" the ITCZ perennial deep convection in the west Pacific (Wyrtki, 1961, 1989; Mitchell and Wallace, 1992). In contrast, annual mean OTLs over the NA vary considerably from ∼90 hPa in the southwest part of the region to ∼150 hPa in the northeast. Consistent with the observed seasonal shifts of the ITCZ (Mitchell

and Wallace, 1992), the NA OTL only penetrates the stratosphere climatologically during the boreal summer and fall months (Fig. 4-3b, Fig. 4-4a), i.e. during the peak NA hurricane season. The other main development regions (ENP, NI, and SH) exhibit similar annual OTL inhomogeneity and seasonal variance, with their OTLs penetrating the stratosphere primarily during their peak-TC seasons (Fig. 4-3b). Notably, observed tropical cyclones are important and disproportionately large contributors to annual overshooting convection in the tropics, especially in the Western North Pacific (Romps and Kuang, 2009). Our results suggest that TCs attaining their potential intensity would exhibit similar overshooting behavior with regionally dependent seasonal variance (Fig. 4-3b).

The seasonality of NA OTLs results in a large outflow temperature seasonal cycle amplitude (10.9 K) that maximizes in the boreal winter and minimizes in the boreal fall (Fig. 4-1b), with a considerable gradient across the basin (Fig. 4-2b). The ENP and SH both have seasonal cycles of outflow temperature that are inversely related to their seasonal SSTs when their outflow is found in the troposphere, and like the NA these effects are not spatially homogenous. The semi-annual cycles of NI SSTs also tracks inversely with regional average outflow temperatures when its outflow is found in the troposphere. In each region, the outflow temperature seasonal amplitude is dominated by the vertical migrations of their OTLs in the troposphere.

The perennial penetration of the WNP OTL into the stratosphere contrasts with the other regions, and has important implications for WNP TC PI seasonality. By "seeing" the lower stratosphere year-round, WNP seasonal outflow temperatures are set by the factors controlling tropical lower stratospheric temperatures. The seasonal cycle of tropical lower stratospheric temperatures is annual rather than semi-annual (Reed and Vlcek, 1969), maximizing in the boreal summer and minimizing in the boreal winter, and is driven primarily by planetary wave-forcing from the troposphere (e.g. Reid, 1994; Yulaeva et al., 1994; Fueglistaler et al., 2009a, 2011). Enhanced wave driving in the northern hemisphere compared with the southern hemisphere results in an annual cycle of upwelling, adiabatically cooling lower stratospheric temperatures in the boreal winter, and warming them in the boreal summer. Recent studies have

shown that this seasonal cycle is modified radiatively by the correlated upwelling of ozone, which amplifies the annual cycle by ∼30% (Folkins et al., 2006; Chae and Sherwood, 2007; Fueglistaler et al., 2011, and chapter 3). The net result is an annual cycle across the tropical lower stratosphere with an amplitude peaking at ∼8 K (e.g. Reid, 1994; Randel and Wu, 2014). Although this seasonal cycle does not vary much in the zonal average between the two hemispheres (Fig. S5), the largest seasonal amplitudes of lower stratospheric temperatures are found over the Western Pacific and Caribbean regions, with important implications for tropical cyclones (Fig. S6, Fig. 4-4, see section 4.3.2). Because the outflow of WNP TCs is always within the stratosphere (Fig. 4-3b), the outflow temperature seasonal cycle follows that of the lower stratosphere, maximizing in the boreal summer and minimizing in the boreal winter (Fig. 4-1b, Fig. 4-4c).

Like the WNP, the other basins show signs of lower stratospheric influences on their monthly mean outflow temperatures in those months when their OTLs penetrate into the stratosphere (Fig. 4-4). Outflow temperatures in the northern hemisphere main development regions show similar curvature to the WNP outflow temperatures from August through November, when outflow temperatures are falling from ∼198K to ∼194K following the stratospheric seasonal cycle (Fig. 4-1b, Fig. 4-4). The NA region being more poleward than the other main development regions (Table 4.1) results in warmer average outflow temperatures during the boreal summer and fall, delaying the NA outflow temperature minima until October (Fig. 4-1b). NI outflow reaches the stratosphere in both the boreal spring and fall, incidentally missing the seasonal maximum in lower stratospheric temperatures (Fig. 4-4d) and resulting in an inverse relationship between SSTs and outflow temperatures in these seasons (Fig. 4-1b). In the months that SH OTLs are found in the stratosphere, November through May (Fig. 4-3b, Fig. 4-4e), the magnitude and shape of the SH outflow temperatures resemble those in the WNP (Fig. 4-1b) and follows the lower stratospheric seasonal cycle (Fig. 4-4e).

TC PI seasonality reflects regional differences in sea surface temperatures and outflow temperatures (Fig. 4-1d). The NA TC PI seasonal cycle has large amplitude

($\sim$22 ms^{-1}) and maximizes in September/October, coinciding with a large amplitude seasonal cycle in SSTs. The seasonal cycles in the ENP are spatially inconsistent within the region (Fig. 4-2c), but on average show similar structure to their SSTs (compare Fig. 4-1a and 4-1d). The SH seasonal cycle amplitude is similar to the NA ($\sim$23 ms^{-1}), maximizing in the austral fall. The NI seasonality highlights the important influence of the monsoonal circulation in setting TC potential intensity in this region. In the WNP, TC PI is strong year-round (always $>$ 72 ms^{-1}), and has a small seasonal amplitude ($\sim$6 ms^{-1}) relative to the other regions. This small amplitude indicates that either the disequilibrium term has similar weak seasonality, the thermodynamic efficiency term is damping TC PI because of stratospheric influences, or both. The relative contributions from these terms are explicitly investigated in section 3b.

In contrast to the proposal of Free et al. (2004), Figure 4-2c shows that TC PI seasonal cycles are not simply zonal in nature. For instance, although the ENP and WNP have similar latitudinal ranges (Table 4.1) they have distinct seasonal cycle structures in part because of zonal asymmetries in SSTs and outflow temperatures (Fig. 4-2a-b).

The TC PI seasonal cycles in Fig. 4-1d compare generally well with those found by Tonkin et al. (2000). In the NA, both studies find large amplitude TC PI seasonality, with values maximizing during the peak-season months (Fig. 4-1d). Their TC PI seasonal cycles in the low latitude Pacific stations (equatorward of 15°N), also agree with our finding of a weak WNP TC PI seasonal cycle. Tonkin et al. (2000) also show good agreement between observed TC intensities and TC PI, and taken together our results are illustrative of why powerful TCs have been observed at all times of year in the lower latitudes of the Western Pacific basin (particularly shown by Guam station data; 14°N, 145°E, their Figure 5).

4.3.2 Potential Intensity Decomposition

We have shown that the seasonal cycle of WNP outflow temperatures is perennially linked to lower stratospheric temperatures, whereas outflow temperatures in the

Table 4.2: The monthly peak-to-peak seasonal cycle amplitudes of TC Potential Intensity in each main development region (excluding NI), and the percent change in the TC PI term amplitude when either the Disequilibrium or Efficiency term is linearly removed (following Equation 4.2). A negative amplitude indicates the seasonal cycle maximizes in the austral summer. A positive percentage change indicates that the term climatologically damps the TC PI seasonal cycle, whereas a negative percentage indicates that the term amplifies the TC PI seasonal cycle on average. Values are calculated using MERRA2 data from 1980-2013.

Main Development Region	TC PI Seasonal Amplitude [and Annual Mean] (ms^{-1})	Change when Disequilibrium term is removed (%)	Change when Efficiency term is removed (%)
NA	22.3 [64.6]	-72.0	-26.0
ENP	10.8 [67.6]	-84.5	-11.1
WNP	7.25 [76.1]	-58.7	26.7
SH	-22.5 [70.6]	-77.3	-21.8

other regions are found in the troposphere except during their peak-seasons. These differences are broadly consistent with the derived TC PI in each main development region (Fig. 4-1d). We now employ the decomposition in Equation 4.2 to specifically quantify to what extent these differences affect TC PI seasonality. Figure 4-5 shows the seasonal anomalies (annual means removed) of the decomposed terms averaged over the main development regions. The monthly variations in disequilibrium and efficiency terms show their specific monthly contributions to the TC PI magnitude, and these seasonal cycles are statistically robust to sampling uncertainty (Table 4.4). Note that is a constant that does not contribute to seasonal variability. Table 4.2 shows the TC PI seasonal cycle amplitudes (from Fig. 4-1d) in each region excluding the NI, along with the percent changes in the TC PI term amplitude if the efficiency or disequilibrium term seasonal cycles are subtracted from the TC PI term seasonal cycle. A negative percent change indicates that the term climatologically amplifies the TC PI seasonal cycle, whereas a positive percent change indicates that the term climatologically damps the TC PI seasonal cycle. Percent changes do not add to 100% because of seasonal phase differences between the terms (discussed below). We see from Table 4.2 that in every region the disequilibrium term is the largest overall driver of TC PI seasonality, and hence always amplifies TC PI seasonal cycles.

The disequilibrium and efficiency terms in the NA (Fig. 4-5a) both maximize in

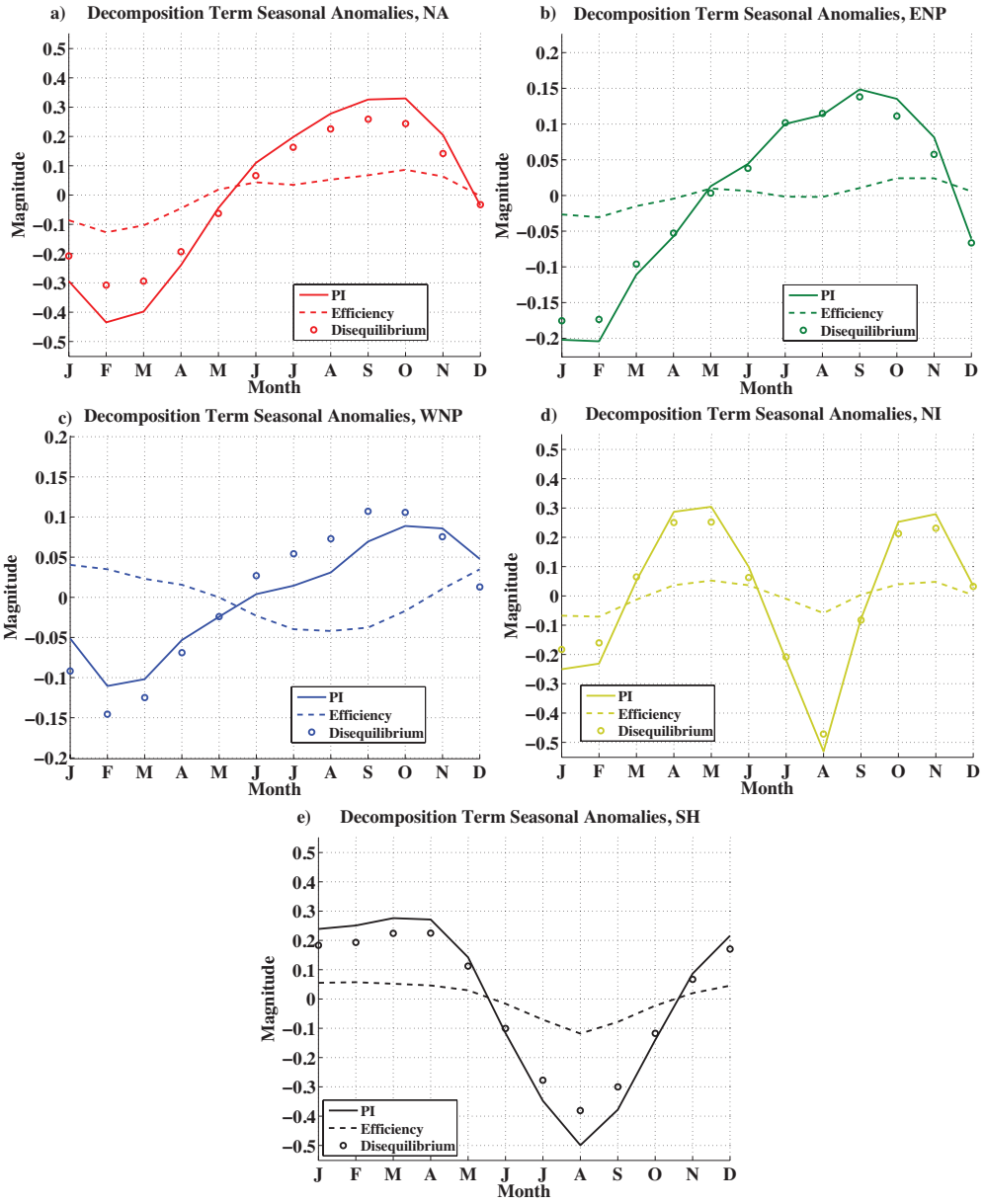

Figure 4-5: Seasonal anomalies of the logarithm of tropical cyclone potential intensity times two (solid curves, LHS of Equation 4.2), the logarithm of thermodynamic efficiency (dashed curves, second term on RHS of Equation 4.2), and the logarithm of thermodynamic disequilibrium (circles, third term on RHS of Equation 4.2), using MERRA2 data averaged over 1980-2013 and the (a) North Atlantic, (b) Eastern North Pacific, (c) Western North Pacific, (d) North Indian, and (e) Southern Hemisphere TC main development regions defined in Table 4.1.

the boreal summer/fall and minimize in the boreal winter/spring. SSTs and outflow temperatures both overall amplify the efficiency seasonality in the NA (Fig. 4-1a-b, Table 4.2), but the disequilibrium term—driven principally by SSTs—is a much larger

contributor to TC PI (Table 4.2). Consequently, NA TC PI has strong seasonality (with an amplitude that is 35% of its annual average value) linked to the SST seasonal cycle, whereas stratospheric temperatures play a secondary role. The main influences of the NA stratospheric temperatures (when OTLs reach the stratosphere from June to October, Fig. 4-3b) are to slightly reduce the magnitude of the efficiency term (Fig. 4-5a) and slightly delay the peak-month of the TC PI seasonal cycle (compare the peak-month between the NA disequilibrium term and the TC PI term). Overall the NA environment is thermodynamically most conducive for intense TCs in the boreal summer/fall, consistent with the observed NA hurricane season.

Results for the SH and ENP regions generally agree with the NA: SSTs dominate the seasonal cycle through the disequilibrium term (Fig. 4-5b and 4-5e), and the efficiency term is a minor amplifier (Table 4.2). Note that because the seasonal cycle of lower stratospheric temperatures is similar across the tropics in both hemispheres (Fig. 4-4, Fig. S5), the seasonal cycle of stratospheric outflow temperatures in the SH (over November-May, Fig. 4-3b) amplifies the efficiency seasonal cycle (and hence TC PI) in that region rather than damping it (Table 4.2, Fig. 4-5e). TC PI in the NI region is strongly coupled to the disequilibrium term, and the efficiency term only slightly amplifies its seasonal variability (Fig. 4-5d).

WNP disequilibrium and efficiency terms have opposing signs and more comparable magnitudes (Fig. 4-5c, Table 4.2). The phase of the efficiency term seasonal cycle, maximizing in January-February and minimizing in August-September, is indicative that this term is principally controlled by lower stratospheric outflow temperatures. Contributions from the disequilibrium term maximize in September-October and minimize in February, following regional SSTs (Fig. 4-1a). The weak seasonality of WNP SSTs (amplitude of 1.5 K) coupled with the relatively strong seasonality in lower stratospheric outflow temperatures (amplitude of 6.4 K) allows efficiency impact to TC PI seasonality on the order of thermodynamic disequilibrium's impact (Table 4.2). The efficiency term damps the amplitude of the WNP TC PI seasonal cycle by about 26%. Because efficiency and TC PI are seasonally out of phase, the efficiency term's influence on PI is in fact larger than the amplitude metric shows. If, for example,

the efficiency term were phase-shifted by two months so that the minima in efficiency aligned with the maxima in TC PI, the WNP efficiency term would damp the TC PI seasonal cycle by 39%.

The phase-offsets between the efficiency and disequilibrium terms in the WNP depress TC PI in the boreal summer. Because SSTs lagging the seasonal insolation (e.g. Braconnot et al., 2000) are offset from the asymmetric wave-forcing on lower stratospheric temperatures (e.g. Yulaeva et al., 1994), the WNP peak-season occurs later than would expected if SSTs were the only driver of WNP TC PI seasonality (shifting its TC PI maxima from September into October, Fig. 4-5c). The positive contribution of the NA efficiency term also delays the TC PI peak in that region, resulting in nearly equal monthly averages of NA TC PI in September and October.

To gauge the relative importance of each term in Equation 4.2 between the main development regions, we examine the ratios of their amplitudes (see Table S2). If TC PI seasonality is influenced by the same factors in two regions, contributions from each term should scale consistently between those regions. Here we take the ratio of the NA and WNP term amplitudes, as they show the most dramatic contrasts in how the stratosphere impacts TC PI through the efficiency term (the NA region is characteristic of the behavior in the ENP, NI, and SH regions). We find that the amplitude ratio of NA/WNP TC PI terms is 3.8, whereas the amplitude ratios of the disequilibrium and efficiency terms are 2.2 and -2.6, respectively. Although the absolute magnitudes of their influences are different (e.g. vertical axes of Fig. 4-5), the differences between their proportionalities make clear that the NA seasonality (and by extension the ENP, NI, and SH regional seasonality) is strongly driven by SST seasonality through both thermodynamic disequilibrium and efficiency, whereas the WNP seasonal cycle is effectively damped by stratospheric influences on thermodynamic efficiency.

4.4 Summary

The seasonal cycles of tropical cyclone (TC) potential intensity (PI) have been calculated with 34-years of reanalysis data across five TC main development regions. Potential intensity depends not only on sea surface temperatures driving thermodynamic disequilibrium with the atmosphere, but also on the difference between the sea surface temperatures and TC outflow temperatures (e.g. Emanuel, 1986, 2003). Whereas previous studies have focused primarily on the long-term trends and interannual variability in TC PI, in this chapter we have elucidated the seasonality of PI and determined the relative seasonal contributions of thermodynamic disequilibrium and thermodynamic efficiency with a decomposition method.

Environmental conditions in the Western North Pacific imply that the region has perennial outflow levels that penetrate into the stratosphere, and outflow temperatures that are stratospherically controlled. In contrast, outflow temperatures in the North Atlantic main development region are generally found at lower and warmer tropospheric altitudes except during the boreal summer and fall seasons (June through October). The net result is a large amplitude ($\sim$22 ms^{-1} peak-to-peak) TC PI seasonal cycle in the North Atlantic that maximizes in the Atlantic hurricane season, compared with the weaker amplitude but perpetually powerful ($>$ 70 ms^{-1}) TC PI seasonal cycle in the Western North Pacific. Although SSTs can be thought of as dictating the seasonal cycles in all basins, in the Western North Pacific they do so in part by allowing TC outflow to be influenced by the stratosphere year-round, whereas in the other main developments regions SSTs are linked more directly to tropospheric outflow temperatures through seasonal variations in the outflow level.

Decomposing the TC PI metric reveals that thermodynamic disequilibrium is the main driver of TC PI seasonal cycles, contributing 72-85% of the seasonal variability in each region except the Western North Pacific. Thermodynamic efficiency contributions in these regions are smaller and amplify the seasonal cycle of TC PI because they are tropospherically controlled (through SSTs) during most of the year. In the Western North Pacific, however, efficiency damps TC PI by between a quarter and a

third because TC outflow temperatures there are linked to the seasonal cycles of lower stratospheric temperatures, which enhance TC PI in the boreal winter and decrease it in the boreal summer. Furthermore, the stratospheric influence on Western North Pacific outflow temperatures delays the peak-month of TC PI by about a month relative to the peak implied by SST seasonality alone.

Our results imply that thermodynamic conditions in the Western North Pacific are ripe for intense TCs throughout the year, whereas ambient conditions in the North Atlantic region typically support powerful TC intensities only during the peak hurricane season (late boreal summer and fall). In this chapter we have only assessed the thermodynamic conditions for intense tropical cyclones. Although powerful typhoons have been observed year-round in the Western Pacific, there remains clear seasonality in their frequency (Sopko and Falvey, 2014). This distinction is likely owing to other factors such as wind shear and mid-tropospheric humidity, which are not accounted for in our methodology.

4.5 Appendix A: Monte Carlo Simulations

To assess the robustness of our results, we examined the uncertainty with an empirical bootstrapping method (Efron and Gong, 1983). We constructed 1000 simulations of 34-years, drawing from 1980-2013 MERRA2 data with replacement. For each of the 1000 simulations we recalculated the mean seasonal cycle for each state variable and BE02 algorithm output. The result reproducing Fig. 4-1, is shown in Figure 4-6.

The error bars for each basin, month, and variable show the 95% confidence intervals from the bootstrapping. We find that in each basin and for each variable, the amplitudes of the seasonal cycle are robust, being larger than any given month's uncertainty at 95% confidence. We also specifically calculate the largest uncertainty in any month for each variable and compare it to the seasonal amplitudes; the results are reported in Table 4.3. These results are consistent with the relatively small SST variance in these regions (cf. (Deser et al., 2010), their Figure 4).

Further, we calculate the logarithmic decomposition (following Eqn. 4.2) for each

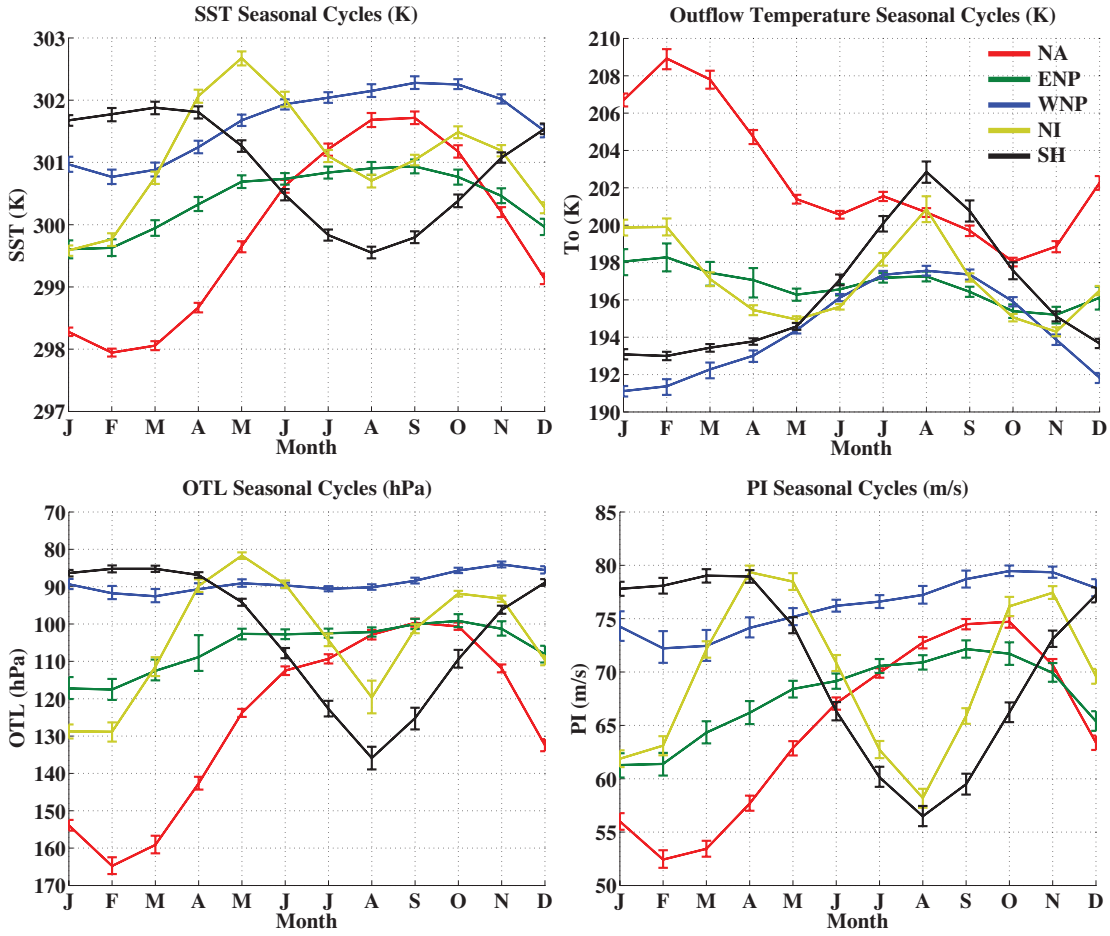

Figure 4-6: As in Figure 4-1 except that error bars show the 95% confidence intervals on monthly means calculated from a 1000-member resample, with replacement, of 34-years of MERRA2 data from 1980-2013.

of the 1000 simulations (Table 4.4). We find that the efficiency term has very little uncertainty, and the uncertainty in the TC PI term is on the order of that of the disequilibrium term. Because of the limited uncertainty in efficiency, a more amplified year in disequilibrium is also associated with a larger amplitude year in TC PI. This is consistent with the conclusion that the disequilibrium term sets the base magnitude of the TC PI seasonal cycle, and efficiency consistently modulates TC PI by damping (in the WNP) or amplifying (in the NA) its seasonal variability (cf. Table 4.2). Between the two basins the uncertainty in the disequilibrium term is about the same magnitude (Table 4.4), although this is more important in the WNP because the overall magnitudes of each decomposition term are smaller. For each decomposition

Table 4.3: The peak-to-peak seasonal cycle amplitudes of monthly SSTs, outflow temperatures, outflow temperature levels, and TC Potential Intensity, in each main development region. Negative amplitudes indicate the seasonal cycle maximizes (for OTL, minimizes) in the austral summer. Values are calculated with MERRA2 data from 1980-2013. Brackets show the maximum ranges of the 95% confidence intervals in any month of the seasonal cycle for that variable and region (i.e. the height of the largest error bar for each variable and region in Fig. 4-6). Note that NI "amplitudes" are just the absolute ranges of its semi-annual seasonal cycles.

Region	SST (K)	T_0 (K)	OTL (hPa)	TC PI (ms^{-1})
NA	3.77 [0.23]	-10.9 [1.1]	65.1 [4.7]	22.3 [1.7]
ENP	1.33 [0.29]	-3.1 [1.6]	18.4 [9.6]	10.9 [2.3]
WNP	1.51 [0.24]	6.4 [0.8]	8.5 [3.5]	7.25 [3.0]
NI	3.09 [0.24]	-6.6 [1.4]	47.2 [8.8]	21.2 [1.8]
SH	-2.33 [0.21]	9.9 [1.1]	-50.7 [6.1]	-22.5 [2.0]

Table 4.4: As in Table 4.3, except for each decomposition term in Equation 4.2.

Region	$log(V_p)$ (K)	$log(\frac{T_S - T_0}{T_0})$ (K)	$log(h_o^* - h^*)$
NA	0.765 [0.070]	0.566 [0.056]	0.214 [0.018]
ENP	0.353 [0.081]	0.314 [0.066]	0.055 [0.025]
WNP	0.199 [0.087]	0.253 [0.078]	-0.082 [0.013]
NI	0.835 [0.168]	0.724 [0.148]	0.123 [0.029]
SH	-0.775 [0.073]	-0.606 [0.059]	-0.176 [0.021]

term in each region, the seasonal amplitude is significantly larger than the uncertainty in any given month, supporting consistently robust results.

4.6 Appendix B: Testing TC PI Robustness with Hadley Centre SSTs

Vecchi and Soden (2007b) showed that when comparing reconstructed and interpolated sea surface temperature (SST) products, product differences are able to impact potential intensity estimates. In their context of studying long-term trends in 20th century, the spatial patterns of a robust warming signal differed significantly, suggesting a lower bound for uncertainty in their potential intensity calculations.

Such spatial pattern differences could be especially important when considering specific main development regions, as we have in this chapter. Reanalysis SSTs are

aggregated mixtures of interpolated sea surface temperature products, chosen with a goal of preserving continuous boundary conditions for the atmospheric forecast model. Descriptions of these aggregated products are found in Bosilovich et al. (2016) and Dee et al. (2011) for MERRA2 and ERA-I, respectively. While the supplemental material of Gilford et al. (2017) shows that results are largely consistent between the ERA-I and MERRA2 reanalyses, it is useful to recalculate potential intensity with an additional SST product to further test the robustness of TC PI seasonal cycles.

To do so we draw monthly SST data from the Hadley Centre Global Sea Ice and Sea Surface Temperature 1° x 1° fields (HadISSTs Rayner et al., 2003) over the 1980-2013 period. For consistency with the reanalyses products introduced in section 4.2, bilinear interpolation is used to regrid the HadISST data onto the 2.5° x 2.5° grid shared by MERRA2 and ERA-I. We find the long-term mean and seasonal cycle of HadISSTs, and then substitute HadISSTs for the SSTs in MERRA2 and recompute the climatological seasonal cycles of TC PI with the BE02 algorithm (this computation is referred to hereafter as MERRA2-HadISST).

The spatial structure of the differences in the long-term means of HadISSTs and MERRA2 SSTs is shown in Figure 4-7a. In the main development regions, HadISSTs are generally warmer than MERRA2 SSTs by about 0.1-0.3 K. However, in the monthly seasonal amplitudes (Figure 4-7b), the differences are more consistently distributed about zero, without any obvious systematic biases. Figure 4-8a shows the seasonal cycles of HadISSTs averaged over the five main development regions, along with those of MERRA2 and ERA-I (reproduced from Fig. 4-1). The monthly structure of SST seasonality is consistent across each dataset; HadISSTs magnitudes fall between MERRA2 and ERA-I SSTs in the ENP and SH regions, and are typically slightly warmer than MERRA2 and ERA-I in the WNP, NA, and NI regions.

The impact of these biases on TC PI seasonality is shown in 4-8b. While the PI values in MERRA2-HadISST are higher in the regions with warmer HadISSTs (consistent with Equation 4.1), the monthly seasonal structure is very similar to those in Fig. 4-1. Therefore, while the absolute magnitudes of TC PI climatologies are sensitive to the choice of SST product, the seasonal structures are not. This

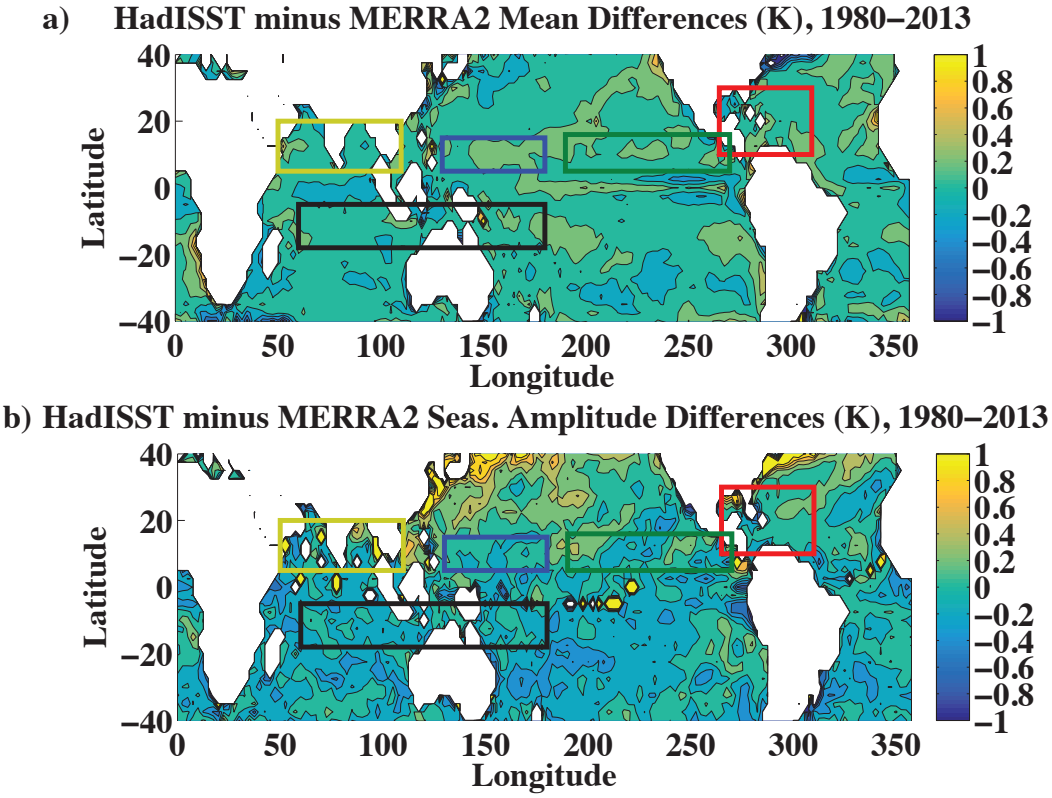

Figure 4-7: (a) Differences in the long-term mean SSTs. (b) Differences in the seasonal cycle monthly peak-to-peak amplitudes of SSTs. Differences in (a) and (b) are HadISSTs minus MERRA2 SSTs, and are averaged over 1980-2013. Contour intervals are every 0.2 K and contours saturate at the colorbar extents. The main development regions indicated by boxes are NA (red), ENP (green), WNP (blue), NI (yellow), and SH (black), as defined in Table 4.1.

is coherent with the sensitivities of TC PI calculations to the $\frac{C_k}{C_D}$ ratio, the choice of parcel ascent assumption (reversible vs. pseudo-adiabatic lift), and the choice of computational method (Bister and Emanuel (1998) direct calculation vs. the BE02 algorithm). Each of these uncertainties scales the magnitude but not the seasonality of TC PI.

Looking at thermodynamic efficiency, outflow temperatures, and outflow temperature levels (not shown), there is strong agreement between MERRA2 and MERRA2-HadISST, suggesting that the difference in their SSTs is not a factor in the contributions of near-tropopause temperatures to TC PI seasonality. This is especially true in months where outflow penetrates the tropopause. The strong vertical thermal strat-

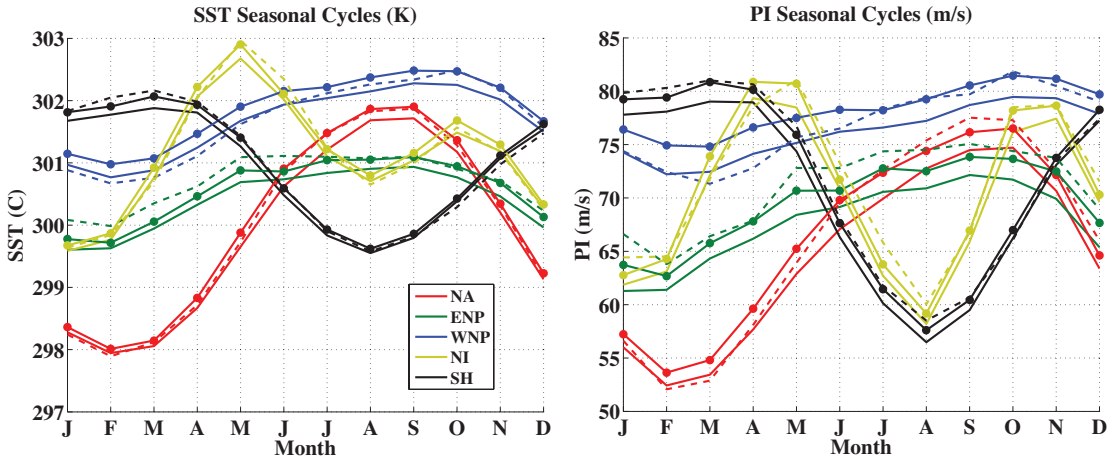

Figure 4-8: (a) Seasonal cycles of sea surface temperatures from MERRA2 (solid curve), ERA-I (dashed curve), and MERRA2-HadISST (solid/dot curve). (b) Seasonal cycles of tropical cyclone potential intensity calculated with SSTs in (a). Note that MERRA2-HadISST potential intensity is calculated with SSTs from the Hadley Centre and air temperatures, humidity, and pressure from MERRA2. The main development regions are NA (red), ENP (green), WNP (blue), NI (yellow), and SH (black), as defined in Table 4.1. All data averaged over 1980-2013.

ification of the lower stratosphere means that small positive biases in SSTs do not noticeably affect the outflow temperature in these periods (for instance, the difference between MERRA2 and MERRA2-HadISST outflow temperatures in any month of each basin's TC season is $<$0.5K).

Coupled with the Monte Carlo results shown in Appendix A (section 4.5), we conclude that the climatological seasonal cycles of TC PI, and their contributing factors, are robust to the choice of sea surface temperature product. SSTs remain the primary driver of TC PI seasonality in every ocean basin (see Table 4.2), while the seasonality of outflow temperatures found in the lower stratosphere is pronounced and important for TC PI in primarily the WNP main development region, playing only a minor role during each other region's TC season.

4.7 Appendix C: An Upper Bound on Ozone's Role in TC PI Seasonality

In chapter 4 we showed that ozone seasonal cycles, through radiative amplification, are a critical component of lower stratospheric temperature seasonality (in contrast to water vapor, which has a limited/phase-shifted damping effect). Here we briefly explore how ozone radiative amplification could affect the climatological seasonal cycles of tropical cyclone potential intensity.

Recall that the estimates of ozone radiative seasonal cycles in chapter 4 requires the use of SEFDH, which implies that the ozone radiative temperature adjustments are an upper bound (because dynamics could damp its effects, see discussions in sections 3.2.2 and 6.2.2). Ozone's estimated radiative impacts on TC outflow temperatures will therefore also be an upper bound. We also neglect the in-situ influences of tropical cyclones on ozone concentrations (e.g. Das et al., 2015; Ratnam et al., 2016), as our goal is to determine the climatological influences of ozone on outflow temperature seasonality (consistent with the methodology outlined in this chapter).

Matching across the tropopause altitude as was done with constituent perturbations in chapters 2 and 3, we acquire the temperature adjustments on the MERRA2 grid associated with ozone's full structure radiative seasonal cycle (Fig. 3-2b), and the 85 hPa sensitivity experiment. We form climatological baseline profiles of MERRA2 state variables (1980-2013) for the WNP and NA main development regions, and from these we linearly remove ozone's seasonal temperature adjustments. These profiles, with ozone radiative temperature adjustments removed, are idealized representations of what the NA and WNP basins temperatures would be without ozone's radiative seasonal impacts.

Potential intensity and its associated variables are computed with the BE02 algorithm for each of these profiles. TC PI and outflow temperature differences between the baseline and ozone-removed thermal profiles are shown in Figure 4-9. Positive PI differences, for example, indicate that baseline profiles (which implicitly include ozone radiative effects) have greater potential intensities than those with ozone's ef-

fects linearly removed.

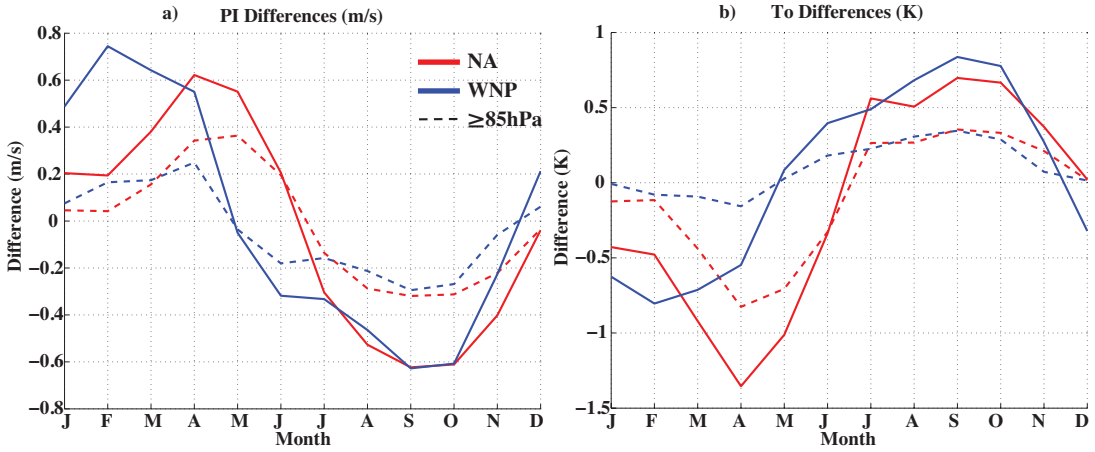

Figure 4-9: The (a) potential intensity and (b) outflow temperature differences (ms^{-1} and K) when the or ozone radiative seasonal cycles temperature adjustments (Fig 3-2b) are linearly removed from the temperature profiles in the NA (red curves) and WNP (blue curves) main development regions (defined in Table 4.1). Differences with the removal of temperature adjustments associated with seasonal cycles throughout the stratosphere (solid curves) and when ozone seasonality is ozone considered only between the tropopause and 85 hPa (dashed curves) are both shown for comparison (cf. Fig. 3-5).

Ozone's radiative seasonal cycles cool the lower stratosphere in the boreal winter and warm it in the lower stratosphere, apparent in the outflow temperatures which reach the upper troposphere/lower stratosphere (Fig. 4-9b). This results in increased PI in the boreal winter and decreased PI in the boreal summer in both the NA and WNP regions. In both basins, therefore, ozone amplifies the outflow temperature seasonal cycles and damps the PI seasonality. The maximum cooling is phase-shifted to the boreal spring in the NA likely because that is when NA OTLs approach the tropopause (Fig. 4-3) and ozone cooling remains strong in those months (Fig. 3-5). The NA PI damping is mostly irrelevant, however, because the efficiency term plays a very minor role in NA PI seasonality (Table 4.2); we estimate ozone's role in the amplitude of the PI seasonal cycle is overall about 3%. In contrast, ozone's radiative amplification of average WNP lower stratospheric temperatures accounts for about 1.5 K of the 6.4 K outflow seasonal cycle amplitude, and damps the average WNP PI seasonal cycle by ∼38% relative to what it would be without ozone influence. While

this is only an upper bound estimate, ozone is clearly an important player in the limited WNP PI seasonality, encouraging more powerful storms to form in the boreal winter months when its radiative cooling is strongest.

We note that the majority of this ozone radiative effect is associated with ozone seasonality above the 85 hPa level (dashed curves in Fig. 4-9, cf. Fig. 3-3 and 3-5). Ozone's impacts on WNP PI seasonality are much weaker when only the ozone seasonal cycles between 85 hPa and the tropopause are radiatively considered. This implies that in order to accurately model the seasonal cycles of WNP TC PI, one must appropriately portray ozone seasonality and its radiative effects above the lowermost stratosphere.

Chapter 5

Seasonal Cycles of Along-Track Tropical Cyclone Maximum Intensity

Abstract

A tropical cyclone (TC) potential intensity (PI) seasonal cycle climatology has been established in the main development regions (MDR), but the real-world application and emergence of this seasonality remains critical to evaluate. This study investigates whether observed TC maximum intensities exhibit a seasonal cycle similar to that of potential intensity. To directly compare observed and potential intensities, one must account for month-to-month variability in TC tracks and storm frequencies. Historical TC best track data and MERRA2 PI calculations are combined to develop an along-track record of observed maximum and potential intensities for each storm in the satellite-era (1980-2015). Overall, observed maximum intensity seasonal cycles agree well with those of along-track potential intensity. Consistent with previous studies, when observed lifetime maximum wind speeds are normalized by PI, their distributions appear uniform. This property is used to show that at least 25 storms must be observed in a given month to have 99% confidence that the most intense observed wind speeds follow along-track PI seasonality. In the North Atlantic and Southern Hemisphere regions, there are few observed storms outside their respective TC seasons, limiting the applicability of PI theory across their seasonal cycles. There is very limited month-to-month variation in mean along-track PI in

these regions, and monthly variations are strongly tied to TC thermodynamic disequilibrium (and hence sea surface temperatures). Thermodynamic disequilibrium also drives Eastern North Pacific along-track PI and observed maximum intensity to have opposite-signed seasonal cycles from that of MDR-average PI: they minimize in August, and maximize in June and October. Western North Pacific along-track PI and observed maximum intensity seasonal cycles are relatively flat, and have a local minimum in August because of reduced thermodynamic efficiency, through anomalously warm near-tropopause outflow temperatures. Powerful ($>65\ ms^{-1}$) TCs historically occur in every month of the year (except January) in the Western Pacific, in part because of tropopause region influences.

5.1 Introduction

The development of potential intensity (PI) theory (e.g. Emanuel, 1986) has provided the tropical cyclone (TC) research community with a useful way to understand how environmental conditions affect local upper limits on TC intensity. However, the relevance of these theoretical limits for the intensities of real-world tropical cyclones is an ongoing area of investigation. Relationships between observed and potential intensities have been studied in a number of different contexts, including climatology, trends, interannual variability, and "superintensity". (e.g. Emanuel, 2000; Persing and Montgomery, 2003; Wing et al., 2007; Zeng et al., 2007; Holland and Bruyère, 2014; Kossin, 2015; Sobel et al., 2016).

Chapter 4 showed that the seasonal cycle of Western North Pacific (WNP) TC PI is damped relative to the seasonalities of the North Atlantic (NA) and other main development regions (Fig. 4-1). Because WNP outflow reaches the tropopause in every month (recall that outflow level is a strong function of SSTs, cf. section 4.3.1), WNP outflow temperatures follow tropopause seasonality: they are cold in the boreal winter and warm in the boreal summer. These near-tropopause outflow temperatures damp PI seasonality by 30-40% through thermodynamic efficiency (Table 4.2 and Fig. 4-5). In contrast, SST seasonality completely dominates the NA TC PI seasonal

cycle, and also strongly controls the TC PI seasonal cycles in the Eastern North Pacific (ENP), North Indian (NI), and Southern Hemisphere (SH) regions.

By definition, operational (in-situ) potential intensity should limit the intensity of a given tropical cyclone, so that lifetime maximum intensities (LMI) of the most intense observed TCs should approach the thermodynamic limit of PI. Emanuel (2000) was the first to show empirically that every TC of at least hurricane strength has an equal probability of attaining any LMI up to its potential intensity. This result implies that PI variability (or a PI increase in the case of climate change, Sobel et al. (2016)) should be accompanied by like-changes in observed intensity, and the highest percentiles of observed LMI distributions should scale with PI.

The relationships between observed and potential intensity on interannual timescales were assessed by Wing et al. (2007). Their study shows that there are significant correlations between interannual observed LMIs and potential intensities in the NA and WNP regions. This result indicates that potential intensity theory is an important factor in the actual tropical cyclone intensities not only climatologically, but also year-to-year. The goal of this chapter is to extend the findings of Emanuel (2000) and Wing et al. (2007) to a seasonal cycle context and to determine whether there are real-world manifestations of the intensity seasonal cycles presented in chapter 4.

PI seasonal cycles in chapter 4 were calculated as averages over each ocean basin's main development region (MDR, Table 4.1), which have been traditionally used in TC studies (e.g. Emanuel, 2005; Wing et al., 2007, 2015). MDR-averaging in this context implicitly assumes that seasonal excursions in TC tracks are small relative to the intraseasonal variability of environmental variables. It further assumes that TCs develop and strengthen within the confines of the defined MDR regions. However, in each basin the historical record shows that there are substantial month-to-month differences in tropical cyclone tracks (e.g. Fig. 5-2). As tracks migrate, storms will sample different regions of PI (Wing et al., 2007; Kossin and Vimont, 2007), which could have profound effects on the PI estimates and bias comparisons with actual intensity. Wing et al. (2007), for instance, found that accounting for track variability generally improved the correlations between observed maximum intensities and PI.

Kossin et al. (2010) showed that the magnitudes and interpretation of PI trends and variability depends on whether or not track differences are accounted for. To account for monthly track migrations, in this chapter we develop an along-track dataset of tropical cyclone PI for each storm in the satellite era (1980-2015). The resultant along-track seasonal cycles of PI (and associated along-track environmental conditions, e.g. SSTs, outflow levels/temperatures, etc.) are then directly comparable with observed TC maximum wind speeds. We also compare results from the along-track method to the MDR-averages of chapter 4 to assess the usefulness of MDR-averages.

Another challenge for assessing the applicability of potential intensity seasonality is the clear seasonal cycle in TC frequencies in each ocean basin (e.g. Landsea, 1993; NHC, 2017, cf. Fig. 5-1). In this study we use the properties of the TC along-track observed and potential intensity distributions—namely the uniformity of normalized wind (observed intensity divided by potential intensity) distributions described in Emanuel (2000)—to determine which months in each basin have enough historical storms to assess the intraseasonal veracity of PI theory. Although several studies have corroborated the Emanuel (2000) result that maximum observed intensities should scale to some extent with PI (Zeng et al., 2007; Swanson, 2008), none have examined this question in the seasonal cycle context.

The chapter is organized as follows. Section 5.2 describes our development of an along-track dataset of tropical cyclone observed and potential intensities, and discusses relationships between empirical and theoretical normalized wind distributions. The seasonal cycles of along-track observed and potential intensities are explored in section 5.3. We summarize the results in section 5.4 and discuss their implications.

5.2 Data and Methods

5.2.1 Best Track Observations

To determine the seasonal cycles of observed TC intensity and develop an along-track TC maximum intensity dataset (section 5.2.2), we use a best track archive (e.g. Knapp

et al., 2010, available at `ftp://texmex.mit.edu/pub/emanuel/HURR/tracks/`). Best tracks from the NA and ENP TC regions are from the National Oceanographic and Atmospheric Administration's National Hurricane Center/Tropical Prediction Center, and best tracks from the WNP, NI, and SH regions are provided by the US Navy's Joint Typhoon Warning Center. For consistency with the time period considered in chapter 4 we draw data over 1980-2015; the final observed Atlantic hurricane in the dataset is Hurricane Kate (November 2015). An advantage of limiting our study to the satellite-era is that best track quality is improved compared with earlier periods (though there are still sources of uncertainty up to 5 ms^{-1}, (Torn and Snyder, 2012; Landsea and Franklin, 2013)).

Best track data are reported every 6-hours and include TC latitude/longitude storm center positions and the maximum 1-minute averaged sustained winds at 10 meters (i.e. the along-track observed intensity). Storm track observations are occasionally provided at intra-6-hourly periods, but we restrict our analyses to the 6-hourly observations to ensure consistent analysis/interpretation across all storms in the dataset (e.g. Wing et al., 2007). Observed wind speeds are reported with a precision of 5 knots ($\sim$2.57 ms^{-1}). We refer to lifetime maximum intensity (LMI) of each storm as the *first time* a storm achieves its maximum intensity (as some storms may have multiple maxima because of data precision, e.g. Emanuel, 2000). We neglect tropical depressions (LMI < 18 ms^{-1}) in the best track archive, focusing instead on storms that reach at least tropical storm strength or greater.

In order to be consistent about how the maximum observed intensities of best track tropical cyclones are defined, we first separate the observed TCs into three different classifications (analogous to those in Emanuel (2000)):

1. Storms that make landfall within 24 hours after their LMI,

2. Storms that intensify to at least 40 ms^{-1} and have an observed intensity that exceeds PI ($V > PI$) within 24 hours after their LMI (but do not make landfall),

3. Storms with intensities that do not exceed potential intensity or make landfall within 24 hours after their LMI.

Table 5.1: Number of historical storms (1980-2015) in each classification (see text) and TC development region. All classifications (whether a storm's intensity does/does not exceed potential intensity, or a storm makes landfall) apply within 24 hours of each storm's LMI. Each classification's percentage of the total storm count (far right column) is shown in brackets.

Basin	Landfall	$V > PI$	$V < PI$	Total
NA	119 [33%]	14 [4%]	227 [63%]	**360**
ENP	78 [14%]	98 [17%]	392 [69%]	**568**
WNP	209 [24%]	76 [9%]	582 [67%]	**867**
NI	94 [62%]	1 [1%]	56 [37%]	**151**
SH	149 [17%]	31 [4%]	663 [79%]	**843**

Our results are not qualitatively different if a 48 hour window is used instead. Potential intensity values (V_p) are found along the track of each storm using the methodology in section 5.2.2, and are defined to be zero over land. Storms that re-emerge after landfall but experience their LMI within 24 hours of landfall are still placed into classification 1. The number of storms for each classification, as well as each classification's percentage of total storms in each TC region, are shown in Table 5.1.

We next define a quantity, V_{max}, which is hereafter referred to as the "observed maximum intensity". For storms with intensities which do not exceed PI (classification 3) V_{max} is exactly the LMI. In the case of the first and second classifications, if a storm's observed wind speed exceeds PI or a storm is over land ($V_p = 0$) at the time of the LMI, then its V_{max} is defined instead at the observation 6 hours prior to exceeding PI/making landfall. There is a corner-case in the classification scheme, where TCs making landfall within 24 hours of their LMI still sustained $V_{max} > V_p$ at the LMI location (<1% of all storms in the dataset). In these cases we retain the V_{max} value and location, because it is the most relevant intensity for its possible coastal impact (for instance, the 2015 ENP Hurricane Patricia). In all other cases V_{max} is either equal to or less than V_p.

About 4.9% of all non-landfalling storms fall into classification 2 and have $V > PI$ at the time of their LMI (3.8% of total storms). Therefore, while the majority of non-landfalling cases do not transiently violate PI theory at the LMI, there is a small subset

of storms that transiently achieve superintensity (Persing and Montgomery, 2003) and are beyond the valid range of PI theory. This superintensity may occur because a) actual TC intensities are never truly in equilibrium (a condition for which PI is strictly valid), or b) the temporal/spatial resolutions of PI and observed intensity vectors are inadequate to account for rapid changes in TC intensity, or c) the PI definition used in this study is climatological rather than operational (see discussion in section 5.2.2), or through some combination of these uncertainties. Including superintense storms in our along-track dataset (section 5.2.2) would significantly distort along-track PI seasonal cycles, because often these storms reach their LMI over cold waters (with anomalously low PI, not shown). While our V_{max} definition (stepping back in time before superintensity occurs) is an imperfect solution, it does permit meaningful comparisons between observed and potential intensity.

Normalized wind speed results (section 5.2.3) are not sensitive to whether storms that exceed PI within 24 hours after their LMI—classifications 1 or 2—are included. However, the seasonal cycles of observed maximum wind speeds (results in section 5.3.1) will vary as a function of which storms are included, in part because of frequency changes (section 5.2.3), and in part because each individual storm has a unique evolution and maximum. If we examine the seasonal cycles of only those storms that do not exceed potential intensity (classification 3) we find that they are qualitatively similar to results with a simple classification which excludes storms that have observed maximum winds exceeding the potential intensity at their LMI (not shown, see Wing et al., 2007). We argue, however, that it is important to include landfalling storms in our seasonal cycle analyses because they are most relevant for societal impacts. Accordingly, in the remainder of this work we choose to use the set of storms that fall into any of the three classifications, to gain a broad view of maximum intensity seasonal cycles.

We use the observed maximum intensity to categorize storms into tropical storms ($18\ ms^{-1} \leq V_{max} < 32\ ms^{-1}$) and tropical cyclones that attain at least hurricane strength intensity ($V_{max} \geq 32\ ms^{-1}$). These categories have distinct wind speed distributions (Emanuel, 2000) which are discussed in section 5.2.3.

As motivated in section 5.1, investigating the seasonal cycles of TC maximum intensity requires one to account for seasonal cycles in TC frequency and track. Figure 5-1 illustrates the seasonal frequency of (a) all TCs in each region, and (b) separated into tropical storms or hurricane strength storms. The intraseasonal variation of TC frequency is well-established, generally showing a peak in TC activity in a basin's late summer/early fall and a minimum in TC activity in the winter and spring (e.g. Landsea, 1993; Nuemann, 1993). The North Indian region is an exception to this behavior because of Monsoonal effects (e.g. Mohapatra, 2014)—the NI region is discussed further in section 5.2.4. There are similar counts of tropical storms and hurricane strength storms in ENP, NA, and SH regions, but in the WNP hurricane strength storms far exceed tropical storms. Additionally, hurricane strength storms tend to be slightly more frequent in the late peak seasons in each basin. The seasonal frequencies are in part due to the seasonal cycles of vertical wind shear, which can limit both the development and strengthening of TCs in the winter months (e.g. Merrill, 1988; DeMaria et al., 1994; Aiyyer and Thorncroft, 2006; Hendricks et al., 2010; Tippett et al., 2011; Wang et al., 2015). We implement a statistical framework in section 5.2.3 to assess how the seasonality of storm frequencies constrains our ability to observe storms with maximum intensities near the potential intensity.

Tropical cyclone tracks also show month-to-month variability (Figure 5-2). WNP TC tracks are more equatorward in the boreal winter months and more poleward in the boreal summer months (e.g. Wang et al., 2015). Monthly averages of the locations of first observed intensities (a proxy for genesis, Fig. 5-2 crosses) and maximum intensity (Fig. 5-2 filled circles) explicitly display this systematic seasonal migration in the WNP (not shown). A seasonal signal in the NA and other basins is less obvious, in part because there are far fewer storms in the winter months (cf. Fig. 5-1), but there are still some seasonal migrations. For instance, storms appear to form/maximize further west in the basin or in the Gulf of Mexico during the very early or very late months of the NA hurricane season (e.g. McAdie et al., 2009), and ENP tracks follow a similar North/South month-to-month shifts as the WNP. Seasonal track migrations imply that storms will sample regions of stronger or weaker PI at different times in

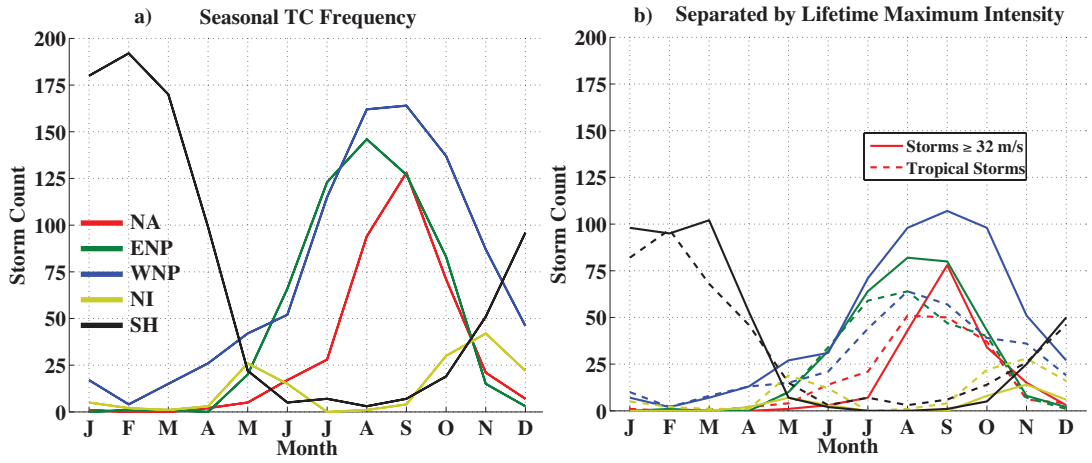

Figure 5-1: (a) Seasonal cycles of tropical cyclone frequencies in each TC development region, for storms in the best track data archive that reach a lifetime maximum intensity of at least 18 ms^{-1}. The month of occurrence for each storm is assigned by the date of its lifetime maximum intensity (see text). The regions are NA (red), ENP (green), WNP (blue), NI (yellow), and SH (black). (b) As in (a), but separated into storms which have a lifetime maximum intensity of hurricane strength (solid curves) or tropical storm strength (dashed curves).

the seasonal cycle (Kossin and Vimont, 2007; Kossin and Camargo, 2009). MDR definitions (Table 4.1, overlaid boxes in Fig. 5-2) are clearly inadequate to describe the environmental conditions experienced by many storms along their tracks. In the next section, we create an along-track dataset of tropical cyclone potential intensity designed to address seasonal track differences.

5.2.2 Along-Track Intensity Dataset

We construct an along-track dataset of tropical cyclone potential intensities, using the climatology calculated with the Bister and Emanuel (2002, BE02) algorithm and MERRA2 environmental conditions described in chapter 4 (section 4.2). MERRA2 data is updated through 2016, but the addition of three years from 2014-2016 makes very little difference in the TC PI climatology, because the interannual variability of environmental conditions is typically much smaller than the seasonal variability (Deser et al., 2010, cf. Fig. 4-6 and Monte Carlo simulations in section 4.6). The raw potential intensities calculated with the BE02 algorithm are reduced by 20% as

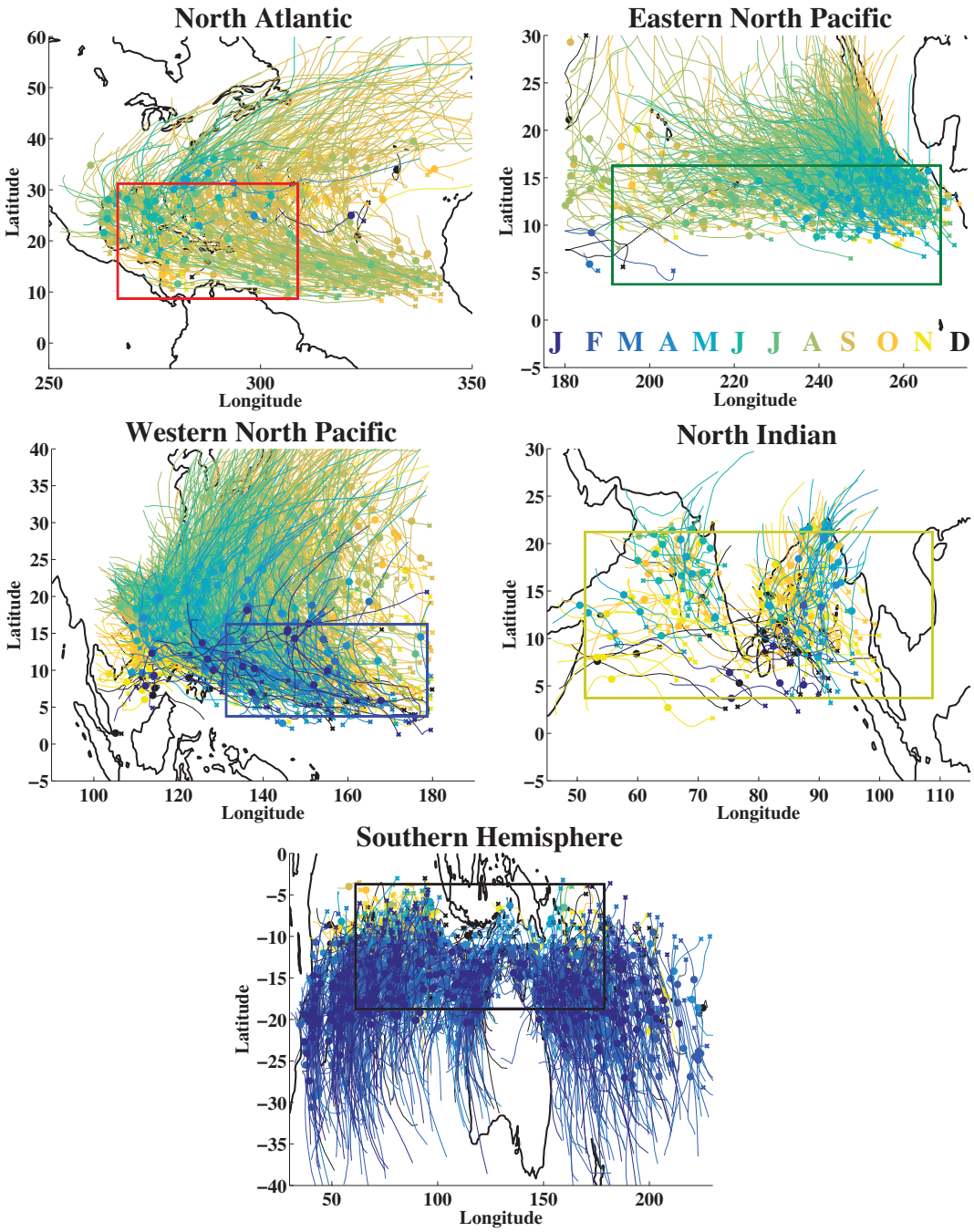

Figure 5-2: Tracks of tropical cyclones from the best track data archive over 1980-2015 for each TC region. Locations of each storm's first observed intensity and lifetime maximum intensity are shown in crosses and filled circles, respectively. Each storm's track is color-coded by the month of its lifetime maximum intensity, with darker/cooler colors representing boreal winter and spring months and brighter/warmer colors representing boreal summer and fall months (see legend). Colored boxes indicate the main development regions, as defined in Table 4.1.

a crude approximation for the scaling between gradient and 10 meter winds (Powell, 1980), allowing comparisons between observed and BE02 potential intensities.

The MERRA2 PI climatology—37-year means at each month/latitude/longitude on a 2.5° x 2.5° grid—is bilinearly interpolated to every TC position in the best track dataset. A cubic spline-fit is used to temporally interpolate the monthly PI climatology to the best track 6-hourly grid, where the monthly means are assumed to represent the central day of each month. Potential intensities along the track of Hurricane Jeanne (2004) are shown as an example of the interpolation method in Figure 5-3a. The along-track PI values (filled circles) are nearly indistinguishable from the background September-mean PI (contours), indicating that the temporal spline-fitting is much less important than the PI spatial variations sampled over the lifetime of Hurricane Jeanne.

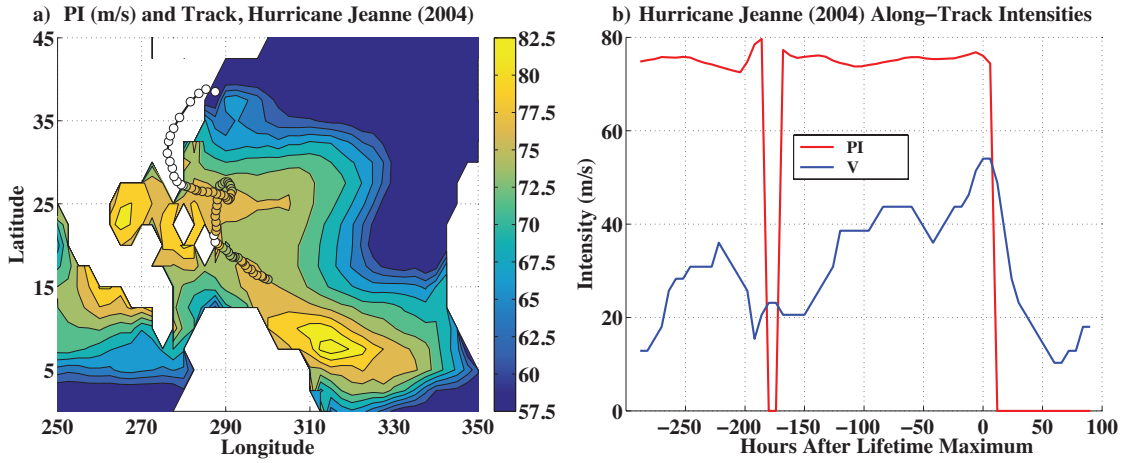

Figure 5-3: (a) The North Atlantic climatological potential intensity in September (contoured) and the interpolated along-track potential intensity of Hurricane Jeanne (13-29 Sept. 2004, filled circles). Contours are every 2.5 ms^{-1} and saturate at the colorbar's extent. White filled circles indicate where the track made landfall ($V_p = 0$). Mismatched intensities between the track and contours illustrate the minor effects of the temporal spline fitting (see text). (b) The along-track observed wind speeds from the best track archive (blue curve) and potential intensity (red curve) of Hurricane Jeanne before and after its lifetime maximum intensity. Hurricane Jeanne is classified as a landfalling storm (classification 2, see text).

The time-evolution of Hurricane Jeanne's along-track observed intensity and potential intensity is shown in Fig. 5-3b. As it made landfall in the Caribbean ∼175

hours before its LMI, Hurricane Jeanne's PI briefly dropped to zero (cf. Fig. 5-3a). Jeanne next traveled back over open water and looped once, then reached its LMI just before a final landfall in Florida in late September. At the LMI Jeanne had an observed maximum intensity at 71% of its potential intensity. Jeanne's observed intensity then quickly fell until the storm dissipated on September 29th, 2004.

Climatological potential intensities used in this study obviously differ from the operational potential intensity that a storm would experience in-situ (such as the daily potential intensities calculated/visualized by the Center for Ocean-Land-Atmosphere studies at `http://wxmaps.org/pix/hurpot.html`). We chose to use monthly climatologies of PI for three reasons. First, PI calculations are roughly linear, so that the average PI calculated with a series of environmental conditions is very similar to the PI calculated with an average of those environmental conditions (not shown, see also Swanson, 2008). While individual storms may sample variable PI values in-situ, long-term averages of along-track PI (like those discussed in section 5.3.1) should be robust if TC track distributions are representative. Second, our goal is to develop an along-track dataset useful for exploring the seasonal cycles of potential intensities that a "typical" TC would experience. For this purpose the operational environments of individual historical storms (which will be sparse in space/time when considered along-track, and will be drawn from a range of internal climate variability) should be less relevant than seasonal climatologies of PI, which are robust to interannual variability (section 4.5). Finally, along-track values using climatological PI may be directly compared to the MDR averages in chapter 4 (e.g. Fig. 4-1).

It is important to note inherent uncertainties in potential intensity that could affect our results. Some relevant physical processes may not be appropriately represented in the PI metric (e.g. Bryan and Rotunno, 2009; Frisius and Schonemann, 2012), e.g., the $\frac{C_k}{C_D}$ ratio directly scales the PI magnitude and has a broad possible range (e.g. Emanuel, 2003, *and references therein*, see Eqn. 4.1), and operational PI for any given storm could be appreciably higher than the climatological values used to create our dataset. These uncertainties could contribute to the 3.8% of storms which we observe to be superintense at their LMI.

Relating along-track observed and potential intensity invites another ambiguity, namely, the contributions of TC translation velocity to best track ground-relative wind speeds. Previous studies (DeMaria et al., 1994; Zeng et al., 2007) have shown that accounting for storm translation velocity may improve comparisons between best track and potential intensities. But the relationship between PI and translation velocity is unclear, in part because ground-relative winds may be more relevant for the air-sea exchanges (which PI theory relies upon) than rotational winds (Emanuel, 2000). Herein we neglect the effects of translation velocity; this assumption is relaxed in Appendix B (section 5.6) and a short assessment of its implications is presented.

5.2.3 Normalized Wind Distributions

The normalized wind speed along the track of a tropical cyclone (e.g. Emanuel, 2000) is:

$$\nu = \frac{V_{max}}{V_p} \tag{5.1}$$

where V_p is the potential intensity at the same location and time as V_{max}. For example, the normalized wind for Hurricane Jeanne is $\frac{54ms^{-1}}{76ms^{-1}} = 0.71$ (Fig. 5-3b).

In each TC development region and over all storms we find the empirical cumulative distribution function (CDF), $F_e(\nu)$, by binning ν values into intervals of 0.01. Consistent with Emanuel (2000), the historical probability distributions of ν appear approximately uniform (e.g. Fig. 5-4). Although the physical reasons for this uniformity are not known (section 6.2.3), it is found consistently in studies of TC intensity, even when subjected to different physical assumptions for maximum potential intensity (e.g. Swanson, 2008; Zeng et al., 2007). In Appendix A (section 5.5), a Monte Carlo approach is applied to explore the uniform property in greater depth.

We assume ν values in the empirical distribution are drawn from a theoretical uniform distribution defined as:

$$F(\nu) = \begin{cases} 0, & \text{for } \nu < \alpha \\ \frac{\nu-\alpha}{\beta-\alpha}, & \text{for } \alpha \leq \nu \leq \beta \\ 1, & \text{for } \nu > \beta \end{cases} \tag{5.2}$$

where $F(\nu)$ is linear between the bounds α and β with a slope of $\frac{1}{\beta-\alpha}$ and a y-intercept $-\frac{\alpha}{\beta-\alpha}$. The empirical and theoretical distributions of North Atlantic normalized wind speeds separated by hurricane or tropical storm strength are shown in Figure 5-4.

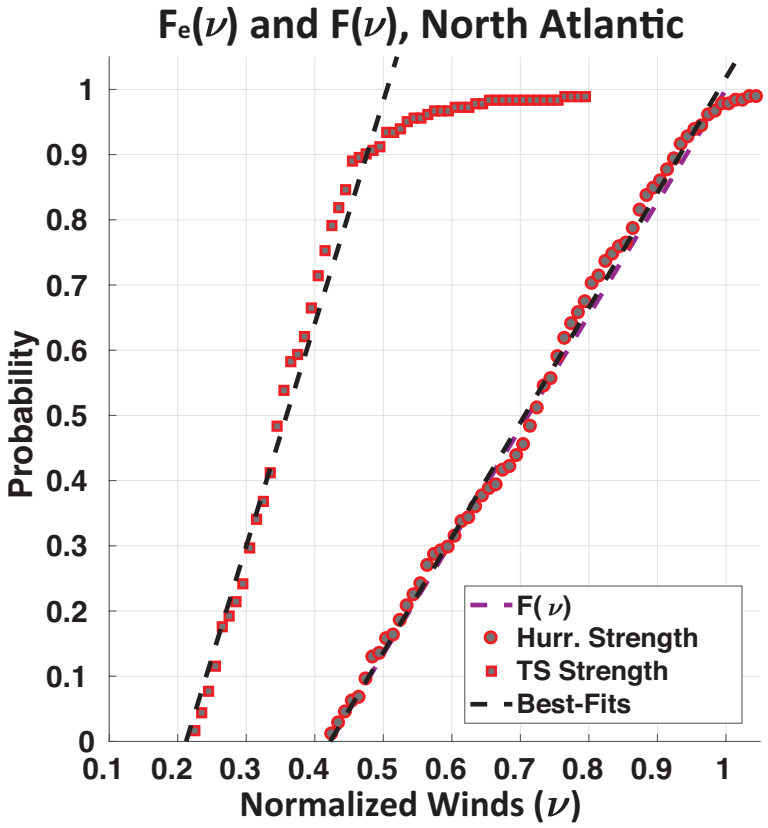

Figure 5-4: The empirical (symbols) and theoretical (purple dashed curve) cumulative probability distributions functions of normalized wind speeds (defined by equation 5.1) at the locations of lifetime maxima for all classified TCs in the North Atlantic (see text). TC distributions are separated by category: tropical storms (squares) or hurricane-strength (circles). Included are the best-fit lines to the empirical distributions (black dashed curves); goodness-of-fit metrics are reported in Table 5.3.

To fit the theoretical distribution to $F_e(\nu)$, one must determine parameters for the lower and upper bounds, α and β. In Emanuel (2000) linear functions were fit

to the empirical ν distributions and a significant correlation ($R^2 \geq 0.98$) was found for both NA and WNP. The black dashed line in Fig. 5-4 shows an example of this method applied to NA distributions in this study; the NA linear best-fit remain strongly correlated with the empirical CDF ($R^2 = 0.99$) for storms that reach at least hurricane intensity (Table 5.3). Approximations of the distribution bounds may be found at the ν values where this best-fit line intercepts with Probability=0.0 (to find α) and 1.0 (to find β). However, these bounds have important implications for the interpretation of PI (discussed below and in section 6.2.3), so a closer investigation is warranted.

Theoretically, the upper bound β should be predictable and constrained. By the potential intensity definition and classification constraints, $V_{max} \leq V_p \rightarrow \nu \leq 1.0$, so that $\beta = 1.0$. A best-fit estimate of β that is greater or less than this value implies that there is uncertainty in either the PI calculation (e.g. scaling differences through the uncertain $\frac{C_k}{C_D}$ ratio), observed winds, or both. In each basin we find that the upper bound probability intercepts falls within 0.1 of $\nu = 1.0$ (Fig. 5-4 and 5-5). In the remainder of this study we use a fixed $\beta = 1.0$ for each theoretical distribution, assuming that observed storms should have intensities consistent with our V_{max} and PI definitions. Assigning β apart from empirical estimates also permits more concise analysis of each empirical distribution's genuine uniformity (Appendix A, section 5.5).

Unlike β, the lower bound α is not theoretically constrained and must be empirically derived. But the properties of α, and how it could shift in a changing climate or from season-to-season, are critical for PI's interpretation. Wing et al. (2007) showed that if the lower bound α is a fixed value (i.e. the lower bound on observed maximum intensity is a fixed fraction of PI), then a percentage change in average PI should be accompanied by the same percentage change in average observed maximum intensity. If instead there is a fixed absolute lower bound on tropical cyclone maximum intensity (δ in Wing et al. 2007), then α should decrease in a climate in which PI increases (as $\alpha = \frac{\delta}{V_p}$), and the accompanying increases in average observed maximum intensity will be smaller.

There are several methods to estimate α. An absolute empirical minimum for α

Table 5.2: Estimated lower bounds on TC normalized wind (ν) distributions for storms that reach at least hurricane intensity and do not exceed potential intensity within 24 hours of their LMI (classification 3). Estimates are from Emanuel (2000) best-fit intercepts (E00), and from this study based on the maximum PI in each region ($max(V_p)$), the best-fit intercept where Probability=0.0 (Fit), and the minimum observed ν in each region ($min(\nu)$).

Lower Bound	NA	ENP	WNP	NI	SH
α_{E00}	0.45	–	0.47	–	–
$\alpha_{max(V_p)}$	0.39	0.37	0.36	0.37	0.35
α_{Fit}	0.47	0.45	0.48	–	0.40
$\alpha_{min(\nu)}$	0.44	0.40	0.43	0.42	0.38

is given by the maximum observed along-track PI value and the TC category filters assumed in 5.2.1. For example, the largest observed along-track PI in the Atlantic basin is $\sim$82 ms^{-1}. For the tropical storm distribution, $18ms^{-1} \leq V_{max}$ by definition, so that if a storm reaches the marginal tropical storm speed in the maximum PI location, then $\alpha \approx \frac{18ms^{-1}}{82ms^{-1}} \approx 0.22$. Similarly, for the Atlantic hurricane distribution, this method estimates $\alpha \approx \frac{32ms^{-1}}{82ms^{-1}} \approx 0.39$.

Any given storm is not likely to concurrently sample from these maximum observed historical PI values and have a V_{max} at the margins of hurricane or tropical storm intensity. Instead, intercept estimates from the best-fit curves (described above) may be more appropriate (e.g. the ν value where the black dashed line in Fig. 5-4 intercepts with Probability=0.0). Another simple empirical estimate for α is the minimum observed ν value for any storm in the basin over the historical period. Note that α estimates from these two methods should always be equal to or smaller than the absolute minimum α estimated from the maximum observed along-track PI.

Table 5.2 shows a summary of α estimates from each of these methods (and compared with those in (Emanuel, 2000)) across each region for storms that do not exceed PI or make landfall within 24 hours after their LMI (classification 3). Results from the set of all storms regardless of classification are similar, but α estimates are usually slightly smaller (Fig. 5-4 and 5-5). The majority of α estimates fall between 0.4-0.5, consistent with rigorously derived bootstrap estimates in Appendix A (section 5.5). Although each empirical estimate could be appropriate, we use the

best-fit method to estimate α for the remainder of this study because it is the most flexible, and it inherently preserves the shape of empirical distributions.

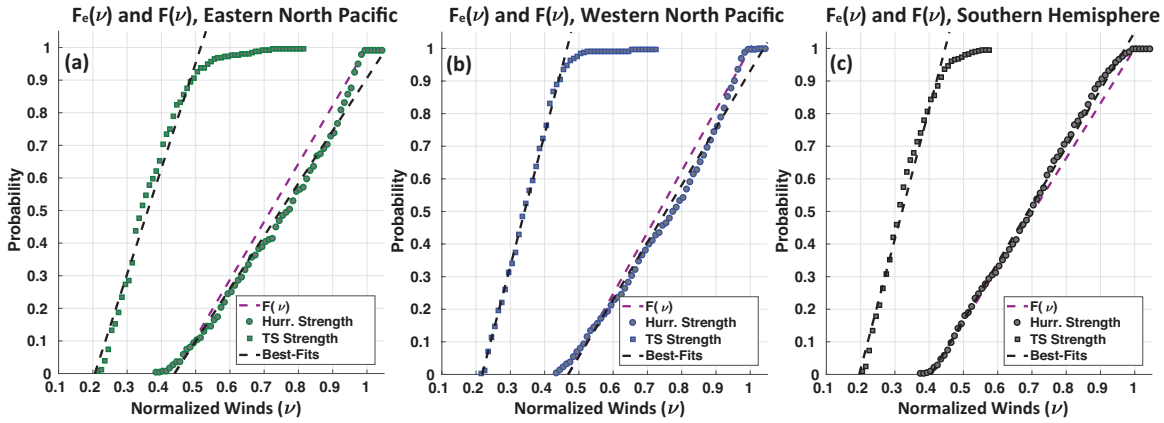

Figure 5-5: As in Fig. 5-4, but for the (a) Eastern North Pacific, (b) Western North Pacific, and (c) Southern Hemisphere regions.

Equipped with α and β estimates, we form theoretical distributions for each basin (Eqn. 5.2), which are shown (purple dashed curves) compared to their best-fits and empirical distributions in Figures 5-4 and 5-5. Best-fits and theoretical distributions are both linear by design, and differ only by their $\nu = 1.0$ intercept. We also show tropical storm distributions and associated best-fits for completeness. Tropical storm distributions remain approximately uniform but they do not reach large ν values and they have a steeper slope (cf. Emanuel, 2000); considering tropical storm and hurricane strength storms together forms a single piecewise-uniform distribution (not shown). The NA CDF is very linear across its range (Fig. 5-4). WNP and ENP empirical distributions have probabilities below $F(\nu)$ in the central portions of the distribution (Fig. 5-5, see discussion in Appendix A, section 5.5). In contrast, empirical ν values in the SH are more frequent than $F(\nu)$ in the central and upper portions of the distribution.

$F_e(\nu)$ and $F(\nu)$ are strongly correlated in each region (Table 5.3, $R^2 \geq 0.94$). However, this quantity does not constitute a strict test for uniformity. The traditional statistical test for this property is the Kolmogorov-Smirnov test (KS test, e.g. Wilks, 1995), but a key KS test assumption, namely that the parameters of the theoretical uniform distribution be independent of the empirical distribution, does not necessarily

Table 5.3: Total number of storms that reach at least hurricane intensity (Hurr.) or tropical storm intensity (TS) in each TC region over 1980-2015 and all classifications. Included are the Pearson correlation coefficients (squared) between the empirical normalized wind cumulative distributions ($F_e(\nu)$) and either the best-fit lines (dashed black curves in Fig. 5-4 and 5-5) or the theoretical normalized wind cumulative distributions ($F(\nu)$, dashed purple curves in Fig. 5-4 and 5-5).

Region	# Hurr.	$F(\nu)$ R^2	Fit R^2 (Hurr.)	# TS	Fit R^2 (TS)
NA	178	0.99	0.99	182	0.97
ENP	312	0.96	0.99	256	0.97
WNP	539	0.97	0.99	328	0.99
NI	40	0.94	0.98	111	0.97
SH	434	0.99	0.99	409	0.98

hold in our study. We apply a Monte Carlo approach to expand on the KS Test and explore ν distribution uniformity in Appendix A (section 5.5). The assumption of uniformity we have used here is a powerful constraint on $F_e(\nu)$, so firmly establishing (or disproving) it is an important goal for future work (see section 6.2.3).

Using $F(\nu)$, we can determine the number of TCs that must be observed to encounter a storm with a ν value above a specific threshold. From univariate extreme value theory,

$$P(\nu > Z) = 1 - (F(Z))^n \tag{5.3}$$

where Z is some threshold ν value, P is the success probability of *at least* one occurrence of $\nu > Z$, and n is the number of Bernoulli trials performed with probability of occurrence $F(Z)$ (Wilks, 1995). With some minor manipulation, equation 5.3 becomes,

$$n = \frac{ln(1-P)}{ln(F(Z))} \tag{5.4}$$

so that the number of Bernoulli trials that must be performed to encounter *at least* one ν value larger than Z follows a geometric distribution. In the context of historical TCs, this property shows how many storms drawn from $F(\nu)$ must be observed to find at least one TC with $\nu > Z$, with a given confidence level (P). Hereafter we refer to n as the "storm count threshold".

If we seek to observe at least one storm (of at least hurricane strength) with an observed maximum wind speed within 10% of PI ($\nu > 0.9$) at a 99% confidence level ($P = 0.99$), then we may apply Eqn. 5.4 across each region. $F(\nu = 0.9)$ ranges (as a function of α) across the basins between 0.81 (WNP/NA) and 0.83 (SH/ENP), so that ∼22-25 storms must be observed (Fig. 5-4 and 5-5). Assuming that $F(\nu)$ holds over every month, any given month with at least 25 observed storms of hurricane strength is therefore extremely likely have at least one observed storm with V_{max} within 10% of V_p. Referring back to Fig. 5-1, we now have a constraint on how storm frequency affects the applicability of potential intensity theory which we can apply over every month and region. Note that in principle any given month with fewer than 25 storms may still exhibit one or more V_{max} values close to V_p; the probability of this is given by Eqn. 5.3, with n being the total number of observed storms in that month. Our choice to seek storms with V_{max} within 10% of PI is arbitrary, but results show (section 5.3.1) it is useful because in months with at least 25 storms, the highest V_{max} percentiles (≥90%) consistently fall near PI.

Note that the assumption of drawing each ν from $F(\nu)$ is not strictly necessary for the application of Eqn. 5.3. In practice, historical normalized winds are drawn exactly from each $F_e(\nu)$, suggesting that $F_e(\nu = 0.9)$ would be an ideal historical predictor for the number of storms needed to observe a maximum intensity within 10% of the potential intensity. Therefore, even in cases where the historical distributions may not be strictly uniform (Appendix A, section 5.5), one should be able to determine the storm count threshold. But because $F_e(\nu)$ monthly dependency may not resemble $F_e(\nu)$ from the full set of storms in each basin (unknown a priori), we have chosen to proceed with a storm count threshold from regional $F(\nu)$ distributions that are grounded, in part, in theory rather than pure empiricism. In all regions except the SH, a theoretical storm count threshold of 25 is actually conservative, because empirical distributions fall below or align with the theoretical distributions at $\nu = 0.9$. In the SH, $F_e(\nu = 0.9)$ is larger than $F(\nu = 0.9)$, resulting in an empirical estimate of $n \approx 45$. But the seasonal frequency distribution in the SH is sharp enough that only a single month (November) is between the theoretical and empirical estimates for the

storm count threshold. The mismatch, by chance, has no bearing on the historical efficacy of potential intensity theory in that month (section 5.3.1, Fig. 5-9).

5.2.4 Neglecting the North Indian Region

The best track data archive for the North Indian TC region is very sparse. Only two months (October and November) exceed 25 total storms, and the majority of these reach only tropical storm strength (Fig. 5-1). In total only 40 TCs of hurricane strength are found in the basin (Table 5.3). If the 1980-2015 rate of about 1.11 observed hurricane-strength storms per year were maintained, it would take ∼125 more years of observations (until 2140) for the NI region to have a total storm count similar to the NA. With so little data (and given exceptionally large uncertainty in NI tracks, e.g. Kossin et al. (2013)), there are no robust conclusions that can be made about the seasonality of NI TC intensity and even a best-fit α estimate is highly uncertain (and was accordingly neglected in Table 5.2). A reliable reanalyses of NI historical storms and continued storm monitoring should permit future examination of intensity seasonality, but these are long-term goals (Mohapatra, 2014). We therefore exclude the NI region for the remainder of the study.

5.3 Results

5.3.1 Maximum Intensity Seasonal Cycles

The along-track average potential intensities and the MDR-averaged potential intensities for each TC region are shown in Figures 5-6 through 5-9. The figures also show the monthly distributions of observed V_{max} with box-and-whisker plots: boxes show the inter-quartile range (IQR) of V_{max}, whiskers show the full V_{max} range, red ticks show the distribution medians, and outliers (values $> 1.5 \times IQR$) are shown as red '+' symbols. If potential intensity theory holds over the seasonal cycle, then the seasonality of the most intense monthly observed intensities (the upper percentiles of the V_{max} distributions) should fall very close to PI seasonal cycles. For reference, we

have included the V_{max} 95th percentiles in each month (P_{95}) as a solid black dot. Because no individual V_{max} is tied directly to the mean along-track PI, we also show the monthly PI IQR, which demonstrates PI's intra-monthly variability and allows reasonable comparisons with V_{max}. Integers above the horizontal axis indicate monthly storm frequencies (reproduced from hurricane-strength counts in Fig. 5-1b). Months whose frequencies meet the storm count threshold ($n = 25$) have color-shaded PI IQRs, whereas those with less than 25 historical storms have gray-shaded PI IQRs.

All quantities in Fig. 5-6 through 5-9 are for storms that fall into one of the three classifications and reach at least hurricane intensity. When monthly frequencies increase with the inclusion of tropical storms (Fig. 5-1), the interpretation of which months should exhibit behavior consistent with potential intensity theory (via the storm count threshold) is distorted, because storms that reach only tropical storm strength by definition have smaller V_{max} values and associated ν values (Fig. 5-4 and 5-5). The upper percentiles of V_{max}, which are of most relevance in this study, should always be tied to hurricane-strength storms.

Maximum intensity seasonal cycles in the NA region (Fig. 5-6) are marked by a strong dependence on storm frequency (cf. Figure 5-1). Only three months (August-October) exceed the storm count threshold, and only six months have more than a single historical storm that reaches hurricane intensity over 1980-2015. The sharp seasonal gradient in frequency, as noted in section 5.2.2, is likely related to NA seasonal cycles in vertical wind shear (Aiyyer and Thorncroft, 2006; Tippett et al., 2011). One consequence is that there are very few months where comparisons between PI and observed maximum intensity are possible.

From June to November the NA average along-track PI is very similar, but smaller, than NA MDR-averages. In the months where the storm count threshold is met (August-October), the along-track IQR encompasses MDR average PI, so that MDR-averages are a reasonable proxy for some storms in the region. November storms have the largest variability in along-track PI (IQR), suggesting that their tracks sample a wider range of environmental conditions. Overall, the seasonal cycle of along-track PI has a weak amplitude in the months with the most frequent storms. Consistent with

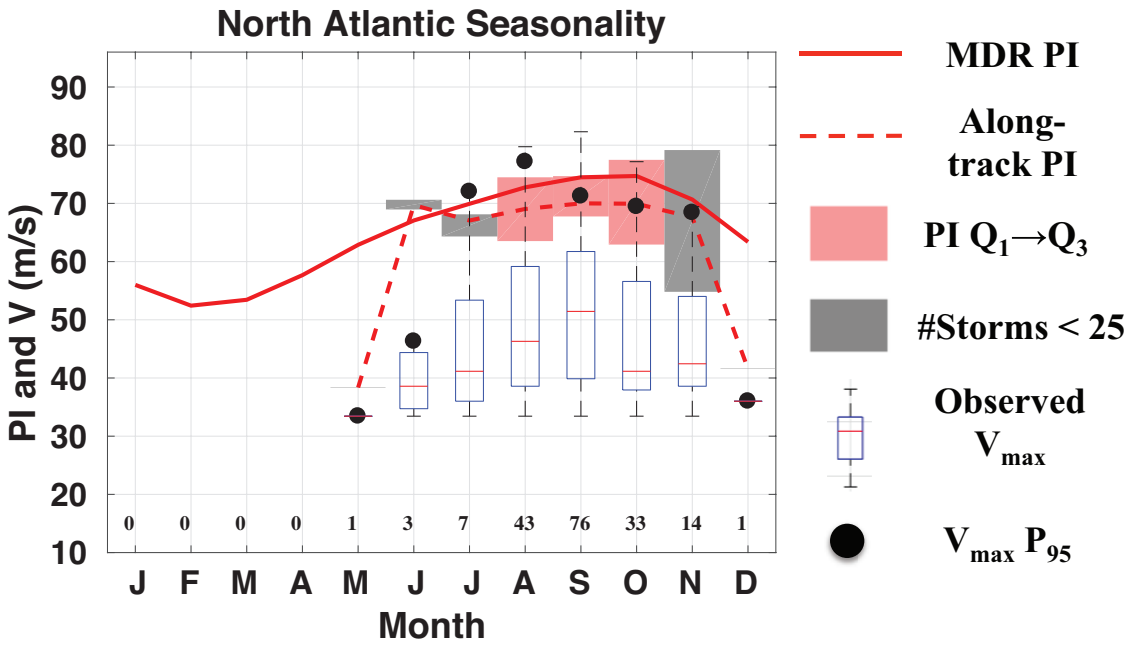

Figure 5-6: Seasonal cycles of North Atlantic potential intensity averaged over the main development region (solid curve, Table 4.1, reproduced from Fig. 4-1), and averaged along-track over all observed TCs (dashed curve) in the satellite-era (1980-2015). Box and whiskers show the monthly distributions of North Atlantic observed maximum intensities (V_{max}). Black dots show the observed distributions' 95th percentiles. Along-track potential and observed intensities are for storms that achieve at least hurricane strength. Numbers below each distribution indicate storm frequency in each month. Shaded boxes show the interquartile range of each month's along-track PI distribution; boxes are colored if the month's storm frequency is at least 25 storms, and are gray otherwise.

chapter 4, the limited variability that does exist between these months is a result of NA SST seasonality (discussed further in section 5.3.2).

Comparing NA observed maximum intensities (V_{max}) to along-track potential intensity, it is clear that several storms (four between July and September) meet the corner case of $V_{max} > V_p$ for landfalling storms; these disappear when translation velocity is accounted for (Appendix B, section 5.6). Beyond these outliers, along-track PI performs well as a predictor of the high percentiles of V_{max}, acting as a consistent limit on climatological tropical cyclone wind speeds during the NA hurricane season.

V_{max} medians shift month-to-month, do not have the same constraint as the upper percentile range of V_{max} (Eqn. 5.3 does not apply to specific median values), and

their seasonality is not robust to translation velocity (Appendix B, section 5.6). In principle, median V_{max} values could be estimated with the theoretical median of ν in each region and the average PI, and then compared with observed median. Errors in the observed median should be expected to decrease with increasing storm counts (e.g. Konczak, 2014). But as our goal is to examine the seasonal cycles of maximum intensity in the context of potential intensity, this is reserved for future work.

In both July and November, when the NA storm counts remain small (<15), upper percentiles of historical observed maximum intensity still exhibit values near the along-track PI, highlighting that meeting the storm count threshold is not a necessary condition for potential intensity to bound climatological maximum intensities in a given month (although it is less probable, with P given by the month's frequency n and Eqn. 5.3).

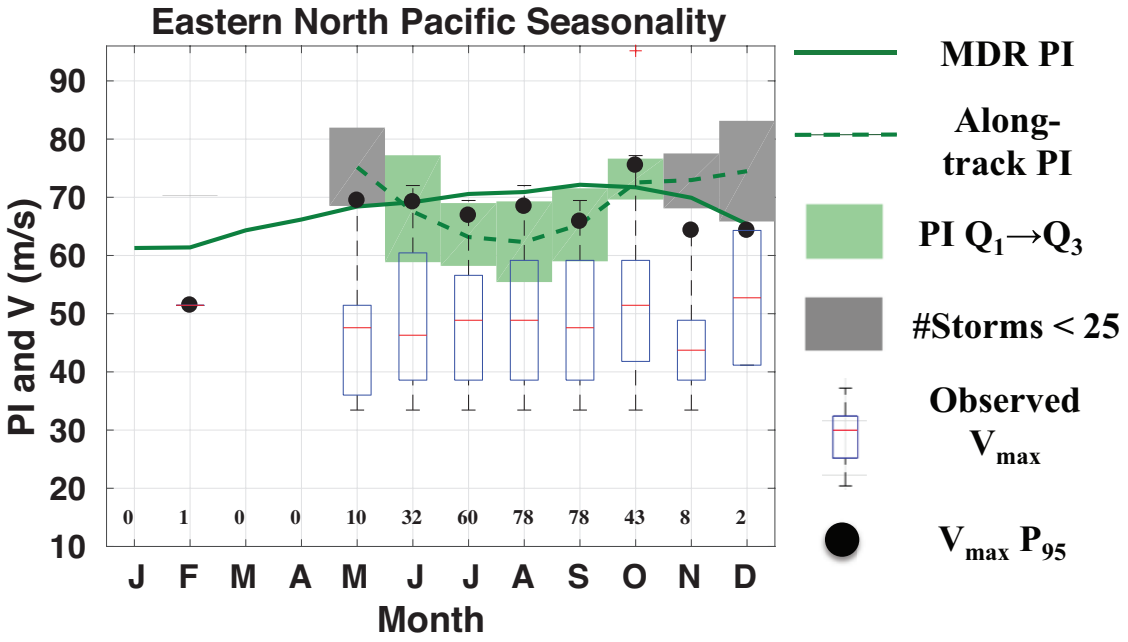

Figure 5-7: As in Fig. 5-6, but for the Eastern North Pacific region.

In the ENP region (Fig. 5-7) one finds that there are very few storms that occur outside the hurricane season (May through November), similar to the NA. In contrast to the NA region, however, the average along-track PI seasonal cycle exhibits a different shape than that of the MDR-average PI (which increases steadily from a minima

in January to a peak in September). The along-track PI seasonal cycle minimizes in the central months of the hurricane season and maximizes near the edge months of June and October. The contrasting seasonal cycle shapes between along-track and MDR-average PI result from two key differences. First, the average latitude of boreal summer maximum locations is higher (and has colder SSTs) than the extent of the MDR (whereas the edge month maximum locations are closer to the MDR region). Second, the discrete monthly tracks sample a wider variety of environmental conditions than the MDR. Indeed, there is a significant mismatch between actual ENP tracks and the MDR itself (Fig. 5-2). This result emphasizes the value of developing an along-track database rather than only relying on MDR-averages. Decomposition (section 5.3.2) shows that the minimum in August is related to a local minimum in thermodynamic disequilibrium and to a lesser extent decreases in efficiency (through cooler monthly SSTs and warmer monthly outflow temperatures).

ENP V_{max} distributions once again show that high percentile observed maximum intensities are within the ranges of along-track PI. August is anomalous in that its range spans above the along-track PI IQR, because a single storm has $V_{max} > V_p$ (when translation speed is accounted for, August is more consistent with along-track PI, see Appendix B, section 5.6). ENP results also show that intra-monthly variance in along-track PI (which occurs through track variance because our PI is climatological) allows the highest percentiles to often reach above the along-track PI average. Therefore track variability from one year to the next plays an important role in whether a hurricane season's observed maximum intensities will follow the seasonal average PI pattern.

A final note on the ENP region is the extreme outlier of the record-breaking Hurricane Patricia (October 2015, $V_{max} = 94\ ms^{-1}$, $\nu = 1.18$). Patricia was the most intense storm (by central pressure, or tied by maximum wind speeds) ever observed in the Western Hemisphere (WMO Weather and Climate Extremes Archive, online at `https://wmo.asu.edu`). The "extraordinary" storm (Rogers et al., 2017) rapidly intensified under very anomalous local environmental conditions (Huang et al., 2017), and it is therefore unsurprising that our climatological PI values are not a viable speed

limit on Patricia's strength. Incredibly cold outflow temperatures were observed in Hurricane Patricia (Doyle et al., 2017), which might have significantly raised the in-situ PI (and interannual variability in TC outflow temperatures is known to be important for ENP potential intensities, Wing et al. (2015)). An along-track PI operational dataset would be needed to investigate further. In this work, Patricia demonstrates that although climatological PI is useful for aggregated historical analyses, it is not always sufficient to predict the intensity limits of an individual storm. Furthermore, Patricia highlights that the seasonal along-track PI values herein are not applicable bounds on the lifetime maximum intensities of the superintense storms (∼5%) in the best track archive.

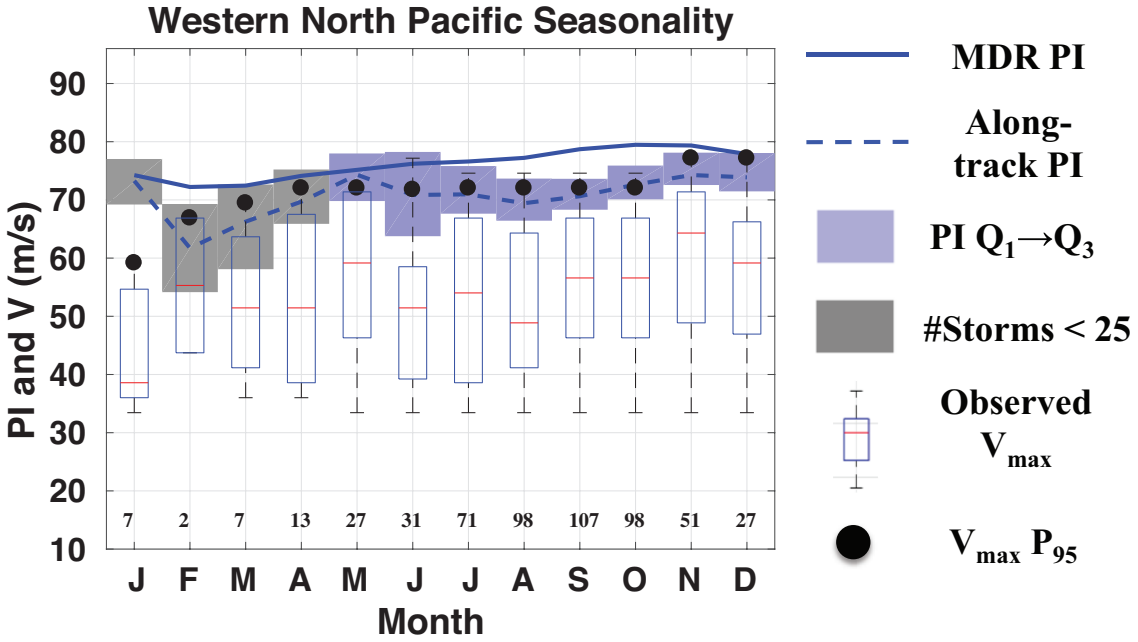

Figure 5-8: As in Fig. 5-6, but for the Western North Pacific region.

WNP seasonal cycles of along-track PI and MDR-average PI are somewhat similar in shape, but along-track PI has depressions in both the boreal winter and summer months (Fig. 5-8). The overall seasonality of along-track PI remains relatively flat (consistent with the results in chapter 4), with averages remaining between 63 and 73 ms^{-1} throughout the year. One of the distinctions of the WNP region is that monthly frequencies exceed the storm count threshold in 8 months (May-December),

and 3 of the remaining months (January, March, April) have along-track PI IQRs that encompass the MDR averages. Matches between along-track and MDR-average PIs in boreal winter/spring months are not surprising, as their tracks are equatorward of the peak month tracks and are often within the MDR (Fig. 5-2, cf. Table 4.1). Instead, the surprising feature in WNP along-track PI is the secondary local minima in August. Decomposition indicates that this minimum is related to a negative monthly anomaly in thermodynamic efficiency (section 5.3.2), arising from seasonally warm along-track outflow temperatures in the lower stratosphere (not shown, similar to Fig. 4-1c-d). It is notable that the largest observed V_{max} and along-track values are found when outflow temperatures are cooler and efficiency is strongly positive compared with the rest of the year (November and December, see decomposition in section 5.3.2).

Distributions of WNP V_{max} are this study's clearest example of the value of potential intensity theory in the seasonal cycle context. The highest V_{max} percentiles scale consistently with the along-track PI (compare P_{95} values with PI IQRs) in every month except January. V_{max} distributions in February, March, and April remain consistent with along-track PI, even though their frequencies fall below the storm count threshold. The probability of this occurrence in February (with only historical two storms, and having a maximum ν of 0.97) was only $\sim$12%, so it is fortunate that the applicability of PI in February is demonstrable. The consistent match between WNP PI and V_{max} is good evidence that the environmental conditions that set the seasonal cycles of WNP potential intensity are also relevant for the seasonality of typical real-world Typhoon intensities. Furthermore, historical maximum intensities illustrate that powerful WNP Typhoons ($>$65 ms^{-1}) can occur (and have occurred) throughout the year, confirming a key conclusion made based on PI theory in chapter 4.

The comparison between SH along-track PI seasonal cycles and MDR-averages is qualitatively similar to that in the NA region. Average along-track PI falls below the MDR-averages in the months where the storm count threshold is exceeded, and storm frequencies strongly limit the applicability of potential intensity in the seasonal cycle context. In the months where there are sufficient SH storms (November through

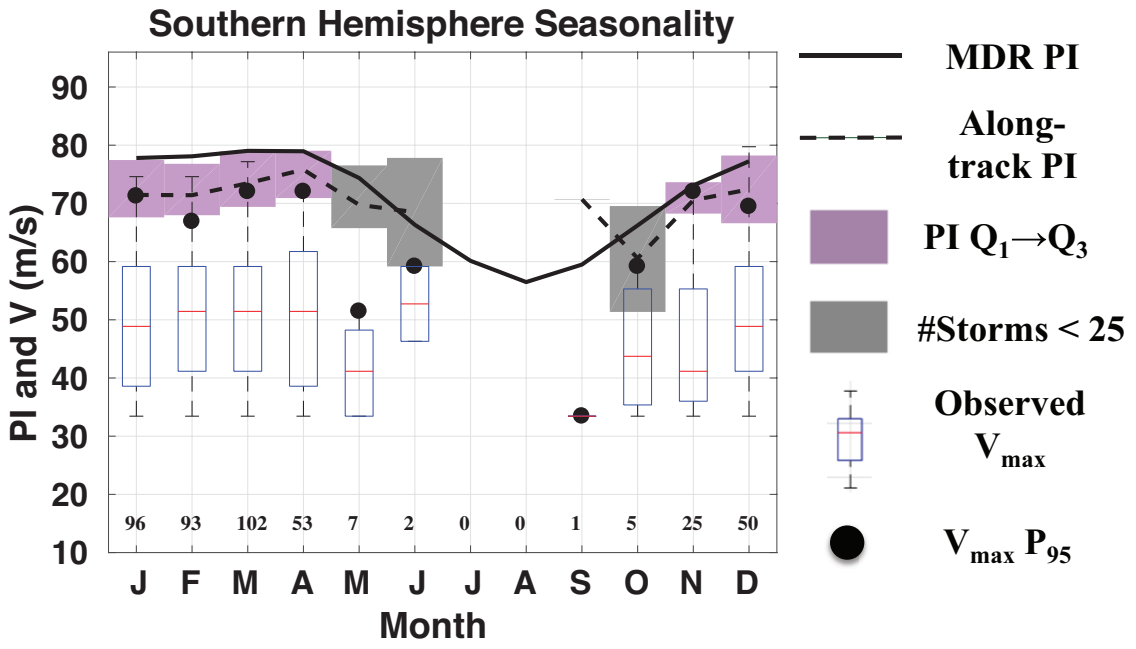

Figure 5-9: As in Fig. 5-6, but for the Southern Hemisphere region.

April) there is very little change in the along-track PI or its ranges (around 73 ms^{-1} in these months).

The SH V_{max} distribution in May shows a clear example of a month with insufficient observed storms for potential intensity to hold. Between November and April the upper percentiles of the observed maximum intensities are consistent with PI. It is apparent that SH MDR-averages are a reasonable approximation of the seasonal cycle of SH PI and observed maximum intensities, but there are very few monthly differences within the TC season itself. The region's seasonality instead is storm frequency dependent.

Summarizing these results, good overall agreements between MDR-averaged PI, along-track PI, and upper percentiles of observed maximum intensity (in months with at least 25 storms) underscore that there is still some value in MDR-averages, especially if TC tracks are not known a priori. MDR is a better proxy in the NA and SH regions, and less applicable in Pacific regions. The differences between along-track PI and MDR-averages suggest that most storms reach their LMI at higher latitudes that the MDR bounds (associated with lower average-PI values) as seen in TC tracks

(Fig. 5-2). Additionally, there are subtleties with physical origins in along-track PI seasonality that are not captured with MDR-averages (e.g. the highest average-PI values are found in the edge months of the ENP hurricane season).

Historical seasonal TC frequencies constrain the links between observed maximum and potential intensities, but an extreme value theory application helps identify the extent of this constraint. In the months with at least 25 storms, the SH and NA regions display very little month-to-month differences in their observed maximum intensities and along-track PI, suggesting that the seasonal cycles of TC PI (chapter 4) are less relevant in those regions. In contrast, Pacific (ENP and WNP) tropical cyclones have interesting month-to-month structures in along-track PI and V_{max}, implying that the seasonality of environmental and associated thermodynamic conditions are important for their typical real-world TCs. We explore the relevance of the along-track thermodynamic contributions in the following section.

5.3.2 Decomposition of Along-Track TC PI

Because high-percentile observed maximum intensities are consistent with climatological along-track PI seasonality, it is particularly critical to investigate how climatological environmental conditions might contribute to the most intense real-world storms. In this section we apply the log-additive model introduced in chapter 4 (Eqn. 4.2) to along-track PI seasonal cycles.

In each region we include any months that have >10 storms of at least hurricane intensity. We compute the average of each term in Eqn. 4.2 over the set of all included months and remove this from each month's individual average value to recover seasonal anomalies. Results from this analysis are presented in Figure 5-10. Note that these are not directly comparable with results from chapter 4 (Fig. 4-5), because the set of months included in each mean will be different. Recall that the thermodynamic disequilibrium term is found as a residual in our methodology, and is strongly associated with SSTs (e.g. Emanuel, 2007; Wing et al., 2015). The efficiency term is computed directly with SSTs and outflow temperatures from the BE02 algorithm. In the Northern Hemisphere regions, when efficiency is in phase with disequilibrium

then the variability in the efficiency term is largely dominated by SST variability, whereas when it is out of phase with the disequilibrium term (or the disequilibrium is close to zero across the seasonal cycle) then outflow temperatures are playing the primary role in efficiency variability.

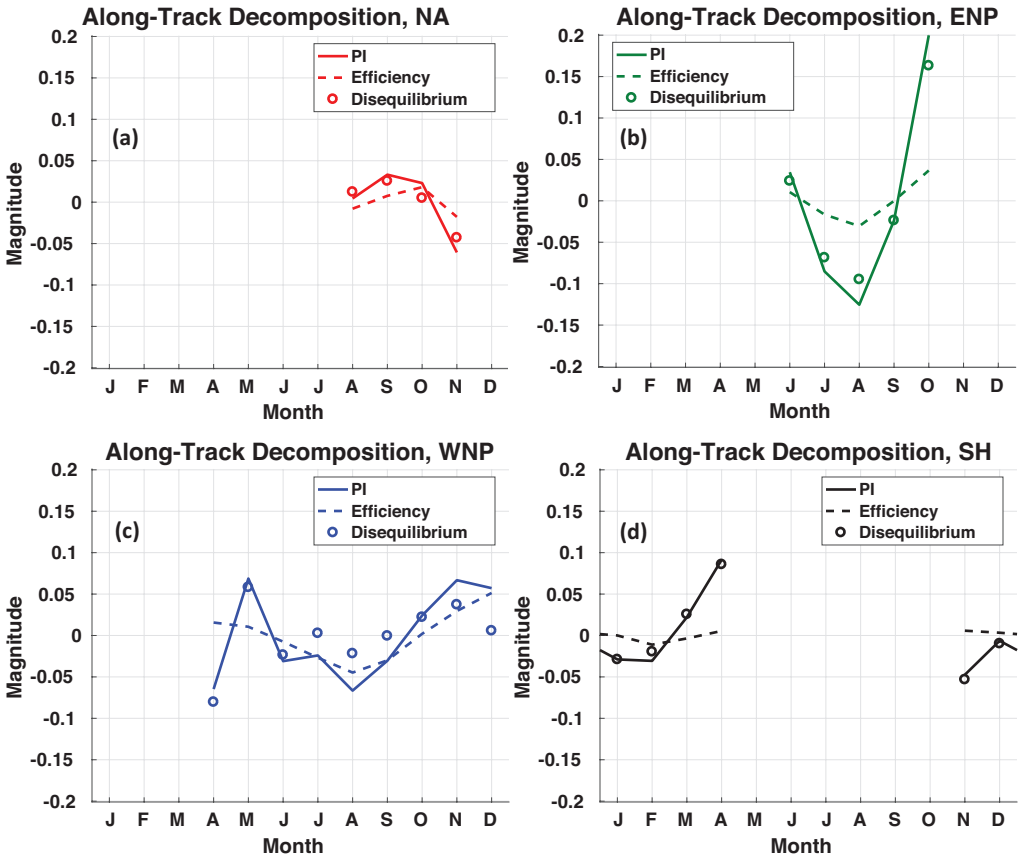

Figure 5-10: Along-track seasonal anomalies of 2 times the logarithm of TC PI (solid curves; left-hand-side of Eqn. 4.2), the logarithm of thermodynamic efficiency (dashed curves; second term on right-hand-side of Eqn. 4.2), and the logarithm of thermodynamic disequilibrium (circles; third term on right-hand-side of Eqn. 4.2), for the (a) North Atlantic, (b) Eastern North Pacific, (c) Western North Pacific, and (d) Southern Hemisphere regions.

The SH and NA regions (Fig. 5-10a,d) have very limited along-track PI seasonal cycles over the months considered (ranges of 2.4 and 5.2 ms^{-1}, respectively). SH along-track PI is increased towards the end of the austral summer (consistent with MDR-averages in these months, Fig. 4-5), but outside of April the seasonality is small. The NA along-track PI has a very weak seasonal peak in September, with a hint of efficiency damping (via warmer outflow temperatures) in August. In both regions,

the small monthly variance that does exist is strongly coupled to the disequilibrium term (and thus largely SST variability), and the efficiency term is perennially close to zero (cf. Table 4.2 in chapter 4).

The largest average along-track PI seasonal range (10.2 ms^{-1}) is found in the ENP region (Fig. 5-10b), with maximum values in the edge months of June and October, and a minimum in the central hurricane season month of August. Consistent with results from chapter 4 (Fig. 4-5) the seasonality of ENP outflow temperatures compared with ENP seasonal SST variability is much smaller, but the depression in efficiency in the boreal summer months indicates a minor role for seasonally warm outflow. Still, it is the disequilibrium term that controls the overall shape of the average along-PI seasonal cycle. This negative disequilibrium anomaly is related to tracks maximizing over colder (higher latitude/farther west) SSTs in the central months of the hurricane season. In the edge months (June and October) tracks maximize much closer to the MDR and are typically found in eastern waters with shallower mixed layers (Bathen, 1972). These tracks therefore sample from warmer average SSTs and increase the seasonal disequilibrium anomalies in June and October.

Average WNP along-track PI (Fig. 5-10c) remains relatively flat (range of 4.9 ms^{-1}) over the 9 months considered (April through December), but there are physical nuances in the month-to-month differences that separate this behavior from that in the SH/NA regions. April and May have the largest disequilibrium term values on either side of zero, consistent with a sharp monthly gradient from cooler to warmer SSTs across those months. In the boreal summer months, however, the disequilibrium term remains closer to zero (and is noisy as a residual) and the PI term is driven more strongly by the efficiency term. The negative efficiency (June through September) is driven by warm along-track outflow temperatures (cf. 4-1b) associated with OTLs in the tropopause region (not shown). Thus along-track PI seasonality shares a similar mid-summer efficiency depression as the MDR-averaged PI shown in chapter 4, but is more impactful overall. The along-track PI has an associated local *minimum* in August because of warm outflow temperatures found in the lower-stratosphere, and the associated efficiency term plays a large role in the overall seasonality of along-

track PI than it does in the MDR-average PI. Consistency between V_{max} and average along-track PI seasonal cycles implies that warm near-tropopause temperatures have acted to climatologically limit the intensities of the most powerful historical WNP storms in the boreal summer months.

5.4 Summary

Historical tropical cyclone (TC) best track data were combined with MERRA2 climatologies of TC potential intensity to develop an along-track dataset of TC observed maximum intensities, potential intensities, and normalized intensities over 1980-2015. The along-track dataset was used to examine the observed and potential intensity seasonal cycles in the North Atlantic, Eastern North Pacific, Western North Pacific, and Southern Hemisphere TC development regions. Considering TC potential intensity (PI) along the track of TCs rather than averaging over main development regions (MDRs) accounted for seasonal track differences, which are especially relevant in the Pacific regions. Use of historical TC frequencies, and a simple application of extreme value theory, permitted the identification of months where observed maximum intensities should be consistent with potential intensity theory. Applying a linear decomposition method revealed the roles of thermodynamic efficiency and disequilibrium in the along-track estimates of potential intensity, which should also relate to typical observed tropical cyclone intensities in the months where potential intensity holds.

The observed maximum intensity of each storm was normalized by its along-track potential intensity at its maximum location. When best-fit linear curves are applied to the empirical cumulative distribution functions (CDF) of normalized wind speeds, the resultant CDFs appear uniform, in agreement with previous literature (Emanuel, 2000; Zeng et al., 2007; Swanson, 2008). The empirical values in each region and month are assumed to be drawn from a regional theoretical uniform CDF that is lower-bound with the best-fit line properties and capped by potential intensity (i.e. assuming normalized winds cannot exceed 1.0). A novel contribution of this work

is the use of these uniform distributions to constrain the applicability of potential intensity theory. Through extreme value theory, each region's uniform distributions imply that *at least* 25 storms must be observed in a given month to have 99% confidence that at least one of those storms will exhibit a maximum intensity within 10% of its potential intensity. This frequency threshold increases if a maximum observed intensity closer to potential intensity is sought. But we find in each region that months with at least 25 historical storms always have upper percentiles (>90%) of observed maximum intensity that agree with along-track potential intensities. This highlights the value of our statistical methodology, and confirms that the seasonal cycle of the most intense observed maximum intensities routinely follows that predicted by along-track potential intensities.

Of particular concern are the mixed results when the uniformity of normalized wind speeds is considered with a strict statistical test (Appendix A, section 5.5): North Atlantic distributions are often found to be uniform, whereas the other development regions rarely exhibit strictly uniform distributions. Because the links between potential and observed intensity variance depend critically on this assumption (e.g. Wing et al., 2007, and results herein), identifying and addressing the root causes of the contributing uncertainties, as well as the physical mechanisms driving the normalized wind distribution shape, will be critical next steps for research (section 6.2.3).

Seasonal cycles of along-track observed and potential intensities in the North Atlantic and Southern Hemisphere regions are primarily influenced by TC seasonal frequencies. There is very little month-to-month variability in average along-track potential intensity in these regions (except a small increase in the late boreal winter/early boreal spring months of the SH), and what variability exists is dominated by SSTs through thermodynamic disequilibrium between the ocean and atmosphere.

Average along-track potential intensities in the Eastern North Pacific exhibit a unique seasonality, maximizing in the months at the edge of hurricane season (June and October) and minimizing in the heart of the hurricane season (August). This is in contrast with the main development region averages which predict a steady

increase in potential intensity from June to September. The result highlights the value of accounting for intraseasonal tropical cyclone tracks as opposed to relying on simple main development region averages. Decomposition shows that the monthly variability is tied to thermodynamic disequilibrium, with SSTs being on average colder (and found at higher latitudes/further west longitudes) in the central months of the hurricane season, and vice versa in the edge months of the season. Eastern Pacific outflow temperatures (which are warm in the boreal summer) play a minor role in this seasonality through thermodynamic efficiency.

Western North Pacific tropical cyclones have an along-track potential intensity seasonal cycle that is muted throughout the year. In the months with at least 25 historical storms (May-December) the potential intensity range is 4.9 ms^{-1}, and there is a local minimum in August. Decomposition shows that this local minimum is related to warm outflow temperatures found in the tropical tropopause region, which reduces the tropical cyclone efficiency and depresses the potential intensity in the boreal summer months (similar to results from chapter 4). The limited number of storms in the boreal winter months (January through April) reduce confidence in the precise average along-track potential intensity in those months, but each month across the seasonal cycle (except January) shows a good agreement between along-track PI and the highest percentiles of observed maximum intensities. The tight agreement between observed maximum intensities and along-track potential intensities is strong evidence that the most intense real-world Western Pacific tropical cyclones have reduced wind speeds in the boreal summer because of anomalously warm lower stratospheric temperatures and increased wind speeds in the boreal winter because of anomalously cool lower stratospheric temperatures (section 4.3.1).

The development of an along-track dataset of potential intensity allowed direct comparison with observed maximum intensities in the seasonal cycle context, but results were generally similar to main development region-averaged PI seasonal cycles in the North Atlantic and Southern Hemisphere regions—there are subtle distinctions in the Pacific regions, as discussed above. In the absence of predicted or observed tracks, there is still some value in using averages across main development regions

as a first approximation of potential intensity limits on real-world tropical cyclone intensity in each ocean basin (chapter 4).

This study has not considered the seasonal cycles of vertical wind shear in its analyses. A cursory implementation of the ventilation index (Tang and Emanuel, 2012) in the seasonal cycle context suggests that tropical cyclogenesis and TC intensification should be heavily influenced by vertical wind shear (not shown). With an empirical index that includes wind shear, Tippett et al. (2011) examined the seasonality of TC genesis, and found that vertical wind shear may often be a limiting factor in the seasonality of TC genesis. To the extent that vertical wind shear effects are implicit in the historical intraseasonal TC frequencies, they may constrain the applicability of TC PI theory through the statistical methods used herein. Furthermore, although wind shear is an important component in limiting tropical cyclone genesis in the first place, in periods of quiescent shear (when a tropical cyclone is more likely to develop) the potential intensity metric in this study should be relevant for actual TC intensity.

The climatological averages presented here are not directly applicable to any given specific storm, but instead show the properties of the aggregated historical seasonal cycles of maximum intensity. In the absence of superintense storms (about 5% of storms in this study), typical TC seasons should be expected to evolve in accordance with these seasonal cycles. Future work should expand on the methodology presented here to account for superintensity in the seasonal cycle context. Storms such as the record-breaking Hurricane Patricia (2015), in particular, will be subject to in-situ environmental conditions that may significantly alter their operational potential intensities and their actual intensities (Rogers et al., 2017). Only very recently are high resolution measurements of very intense storms permitting a complete observational perspective of how outflow can impact TC intensity and intensification (Doyle et al., 2017). With additional and improved TC observations in the future, a more complete picture of the operational seasonal cycles of TC intensity and outflow temperature influences may emerge.

Only a handful of studies comparing observed and potential intensities have been performed (Emanuel, 2000; Wing et al., 2007). This chapter has elucidated the value

of this exercise in a new context, increasing understanding of the seasonal cycles of tropical cyclone maximum intensities. Given the inherent uncertainties in both observed and potential intensities, it is reassuring to see the consistent usefulness of the potential intensity metric for the majority of observed storms.

5.5 Appendix A: Uniformity of Normalized TC Wind Speeds

Although linear fits to the empirical distributions in section 5.2.3 have been argued to constitute evidence for uniformity (e.g. black dashed lines in Fig. 5-4 and 5-5, and Emanuel (2000))—and indeed suggest that the distributions are close to uniform—it is both unclear what the physical reasoning behind these uniform distributions is, and to what extent in a rigorous statistical sense these distributions are uniform. While the former question is beyond the scope of this work, comparisons between the theoretical CDF, $F(\nu)$, defined by this work in Eqn. 5.2 and the empirical distribution $F_e(\nu)$, are well suited for more thorough statistical analysis.

The Kolmogorov-Smirnov test (KS test) is designed to test the goodness-of-fit between two distributions (e.g. Wilks, 1995):

$$D_{KS} = \max |F(\nu) - F_e(\nu)| \tag{5.5}$$

Where D_{KS} is the test statistic measuring the largest difference between two distributions, evaluated over all N samples in $F_e(\nu)$. The null hypothesis of the test is that the observed data in the empirical distribution were drawn from the theoretical distribution; if D_{KS} exceeds some critical value (i.e. $D_{KS} > D_{crit}$) the null hypothesis is rejected. The KS test requires that the theoretical distribution being tested remain independent of the empirical distribution, but in practice theoretical distributions are often "tuned" by parameter-fitting with the empirical sample (as was done with αin this study, Eqn. 5.2). This can result in an overfit, where the null hypothesis is rejected less frequently than it should be (Crutcher, 1975).

In our analyses, the choice of α as a lower bound of the theoretical uniform distribution implies that a blind application of the KS test would be errant. The KS test must be adjusted to account for the parameterization of the theoretical distribution. Lilliefors (1967) and Crutcher (1975) showed that tables of D_{crit} must accordingly increase relative to a standard KS test. For instance, at 95% confidence for $N > 30$, $D_{crit} = 0.886/\sqrt{N}$ (Wilks, 1995, their Table 5.2). In Figure 5-11 we compare the computed KS test statistics (D_{KS}) for each region against curves given by the adjusted KS test critical values (D_{crit}). Results show that the null hypothesis is rejected at high confidence in the ENP, WNP, and SH regions, but it is not rejected in the NA region.

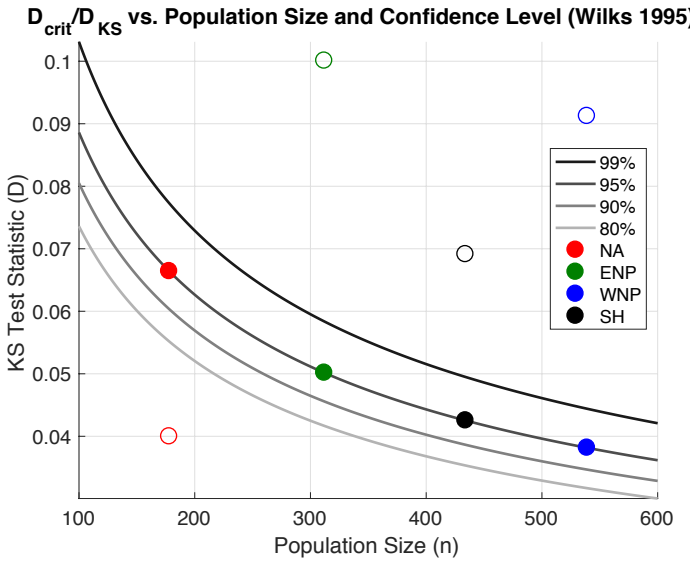

Figure 5-11: KS test statistics (open circles), applying Eqn. 5.5 to the empirical and theoretical distributions in each region (Fig. 5-4 and 5-5), as a function of population size. Critical values (e.g. Wilks, 1995) are shown at various confidence levels (gray curves) and specifically for each region at the 95% confidence level (filled circles). Open circles that lie above a given confidence level curve indicate that the KS test null hypothesis may be rejected in that region at that confidence level or higher.

It is unclear to what extent biased or limited sampling could affect the goodness-of-fit between our distributions, or how uncertainties in the estimate parameter α could obscure whether TC normalized wind speed distributions are indeed uniform (e.g. Table 5.2). We therefore next apply a Monte Carlo approach to apply the KS test and investigate these properties. The method is as follows.

Repeat the following K times:

1. Randomly split the empirical data with sample length n into two separate populations, a training population of size p, and test population of size n-p. Implicitly, our test will be a function of the test population size (n-p).

2. Estimate the lower bound of a theoretical distribution $F_p(\nu)$, α_p, from the training population. $F_p(\nu)$ is upper bounded by 1.0.

3. Perform the KS test (Eqn. 5.5) with an empirical distribution composed of the test population, $F_{(n-p)}(\nu)$, and the theoretical distribution $F_p(\nu)$.

4. Compare the resulting KS test statistics, D_k, with the critical KS test statistic (e.g. Fig. 5-11).

The method may be repeated for any reasonable values of p; here we choose p=50 because it represents a balance between the number of storms needed to estimate appropriately find α with training data, and a reasonably high count of storms to populate our test data (see storm counts for each region in Table 5.3). We set K=1000, a typical number of bootstrap simulations. We estimate α from the training population with the best-fit method described in section 5.2.3. The test is performed for each individual TC region (except NI), over storms that reach at least hurricane intensity. The result is a distribution of 1000 D_k values that fall either above or below the critical KS test statistic D_{crit} (Figure 5-12).

Results starkly differ between the NA and other regions. More than half (56%) of the NA KS test statistics fall below the critical value, implying that for many realizations of NA along-track intensity (Fig. 5-12a) the normalized wind distributions could be uniform. In the WNP, every computed D_k is found above the critical value, so that for every respective $F_e(\nu)$ we reject the null hypothesis that it is drawn from $F(\nu)$ at 95% confidence. ENP and SH show similar results to the WNP (not shown), with zero percent of their simulations having $D_k < D_{crit}$. These results (for both NA and the other regions) are strongly robust to the method for estimating α, varying by only a few percent in each region (not shown). Considering only storms

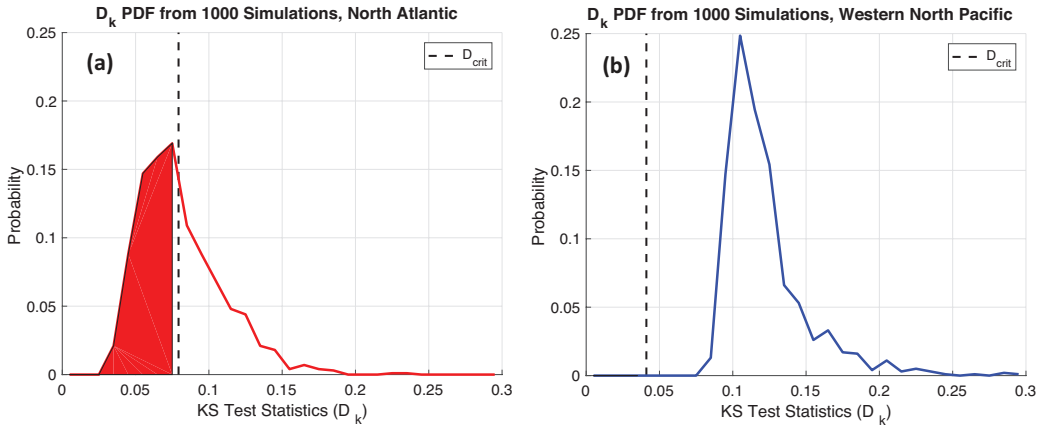

Figure 5-12: North Atlantic (a) and Western North Pacific (b) probability distribution functions of the KS test statistics from 1000 estimates with our Monte Carlo approach (see text), and the critical KS test statistic (see Fig. 5-11) at 95% confidence for each TC region (dashed line).

in classification 3 (storms that do not exceed potential intensity within 24 hours of their LMI) does not qualitatively change these results. Implicitly, our process allows us to gauge the robustness of our best-fit α estimates: their simulation distributions appear normal (in the NA, $\mu = 0.42$, $\sigma = 0.027$) falling within the ranges outlined in Table 5.2.

The mismatched result between the regions is concerning. We have found with strong statistical confidence that the empirical distributions for the WNP, ENP, and SH regions (and nearly half of randomly NA distributions) do not have the same shape as their best-fit uniform theoretical distributions. However, *why* this result arises is difficult to know. One might presume that the choice of the theoretical upper bound $\beta = 1.0$ is too strong an assumption, given the uncertainties in the PI exchange coefficients $\frac{C_k}{C_D}$, the choice of using climatological rather than operational PI, and the scaling between gradient and surface winds. But when theoretical distributions, $F_p(\nu)$, are created to match actual best-fit curves (black dashed curves in Fig. 5-4 and 5-5) with an updated β, the results remain qualitatively similar to those in Fig. 5-12 in the WNP and ENP; there are marginal improvements in the SH fit which allow about 2% of resampled distributions to not reject the null hypothesis at 95% confidence (not shown).

In short, the results above imply that the shapes of the ENP, WNP, SH, and to some extent NA, regional normalized wind distributions differ from uniform statistically (even through their best-fits have high correlations, Table 5.3). Figure 5-5 shows that these differences are found in the distribution centers, hinting the that a "Dvorak Gap" could be a culprit. The Dvorak technique (Dvorak, 1975) which is heavily used to populate TC intensity estimates in best track archives, significantly detects fewer category 3 storms than any other category (Torn and Snyder, 2012), tending to either under- or overestimate peak wind speeds (Velden et al., 2006). In our methodology, this bias likely exhibits by shifting probability from the central parts of distributions into the edges. The consistent rejection of the KS test null hypothesis in the ENP and WNP regions could result from this.

Data quality in the best track archive can also vary from basin to basin because of temporal heterogeneities, even in the satellite era (Knapp et al., 2010; Kossin et al., 2013). It may be that an improvement in historical and future intensity estimates would show that WNP, ENP, and SH TCs have uniform distributions, or that NA biases themselves allow more distribution subsets of to appear uniform than nature would permit. The smaller storm count in the NA basin could also be suspect (cf. Table 5.2, Fig. 5-12). Without a unifying theory for why the distributions of normalized TC intensity should be uniform, it is difficult to speculate further.

The property of uniformity is a useful constraint for evaluating potential intensity theory (section 5.2.3). While this work makes strides towards understanding the uniformity (or lack thereof) of TC intensity distributions, the physical reasons for this behavior remain elusive. Future work should endeavor to resolve this problem and improve upon intensity estimates, especially because there are significant implications for PI interpretation and the predicted future changes in TC intensity due to anthropogenic climate forcing (section 6.2.3).

5.6 Appendix B: TC Translation Speed

Following DeMaria et al. (1994), one may account for the translation speed of TCs when comparing observed and potential wind speeds. We estimate the translation speed along the track of each storm in the along-track dataset by calculating the distance between the 6-hourly best track positions and dividing by time. An example lifetime evolution of translation speed for Hurricane Jeanne is found in Figure 5-13a, where the time-axis is relative to the original lifetime maximum before translation velocity was removed. The probability distribution function of NA translation velocities is presented in Fig. 5-13b, for all observations in the NA (blue curve) and centered on the time of each storm's updated LMI after translation velocity has been removed (black curve). The translation velocities in Fig. 5-13 are consistent with contemporary estimates (e.g. Rios-Berrios and Torn, 2017).

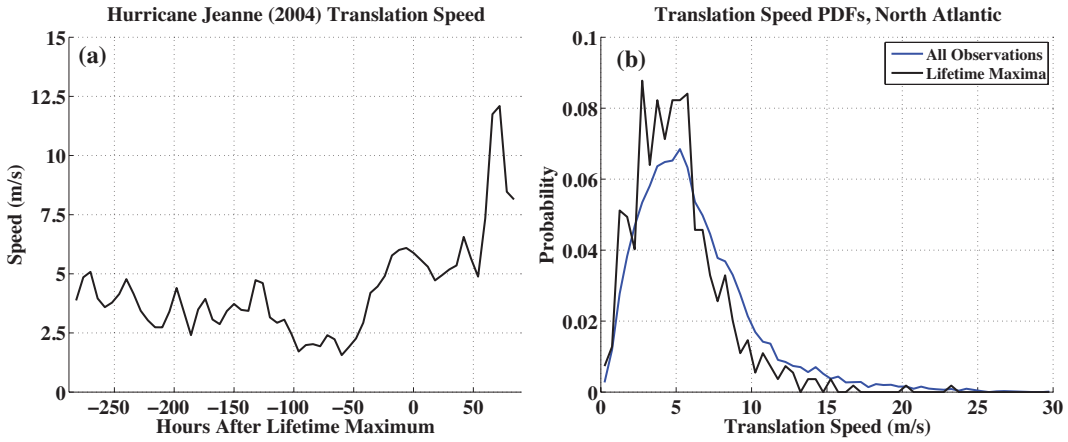

Figure 5-13: (a) The along-track translation velocity of Hurricane Jeanne (2004) before and after its original lifetime maximum intensity. (b) The probability distribution functions of North Atlantic along-track translation velocities of all storm observations in the best-track archive (blue curve) and of observations at the time of each storm's updated (with translation velocities removed) lifetime maximum intensity (black curve).

We subtract the translation velocity from best track (ground-relative) wind speeds, to acquire an estimate of each storm's rotational velocity along its track. Note that the time and location of the lifetime maximum intensity (and hence V_{max}, V_p, and ν) may change when translation velocity is removed. Direct subtraction as we have done

here is the upper bound on the contribution of translation wind speed to the observed ground-relative wind, because it assumes the same orientation between the vectors of rotational and translation velocity at the location of ground-relative measurement. Scaling factors of translation velocity between 0.0 and 1.0 have been applied in previous literature (e.g. Jelesnianski et al., 1992; Emanuel, 2000; Emanuel et al., 2006; Lin et al., 2012). Lin et al. (2012) performed an in-depth analysis and found that a reasonable scale factor is about 0.55, and that the ground-relative wind is typically rotated about 20° clockwise from the translation velocity. Here we use the highest scaling of 1.0 to get a sense of the range of impacts that translation velocity could have on our seasonal cycles of maximum intensity.

Storms are re-classified and re-categorized based on the new rotational wind estimates of V_{max}, Normalized winds (Eqn. 5.1) are recomputed for each storm, and empirical distributions are formed again for each TC region (not shown). Results are very similar to those in Emanuel (2000, their Fig. 1c-d); the distributions still appear uniform (consistent with Zeng et al. (2007)), but the probability of the higher ν values is depressed. NA and SH distributions become partially distorted, leading to reduced R^2 values between the empirical and theoretical distributions of 0.94 and 0.96, respectively (cf. Table 5.3). In contrast, the original WNP and ENP empirical distributions slightly overestimated $F(\nu)$ at higher normalized winds and underestimated at lower values (Fig. 5-5), so removal of translation velocities actually slightly improves correlations with the theoretical distributions (R^2 values increase from 0.96 and 0.97, to 0.98 and 0.99, respectively). These mixed results highlight the challenge with considering translation velocity in the context of PI (Emanuel, 2000), and suggests that data quality (e.g. uncertainties in track locations between basins, (Torn and Snyder, 2012)) probably contribute to the interpretation of ν distribution shapes. The Dvorak technique relied upon for most track/intensity observations outside the NA region includes a climatological translation velocity (Knaff et al., 2010; Velden et al., 2006), which further complicates the interpretation of these results.

The critical question for our study is how translation velocity affects TC intensity seasonality. Figure 5-14 recreates the seasonal cycle Figure 5-6 for each TC region, but

with the translation velocities (red curve in Fig. 5-13b) removed from each storm's V_{max}.

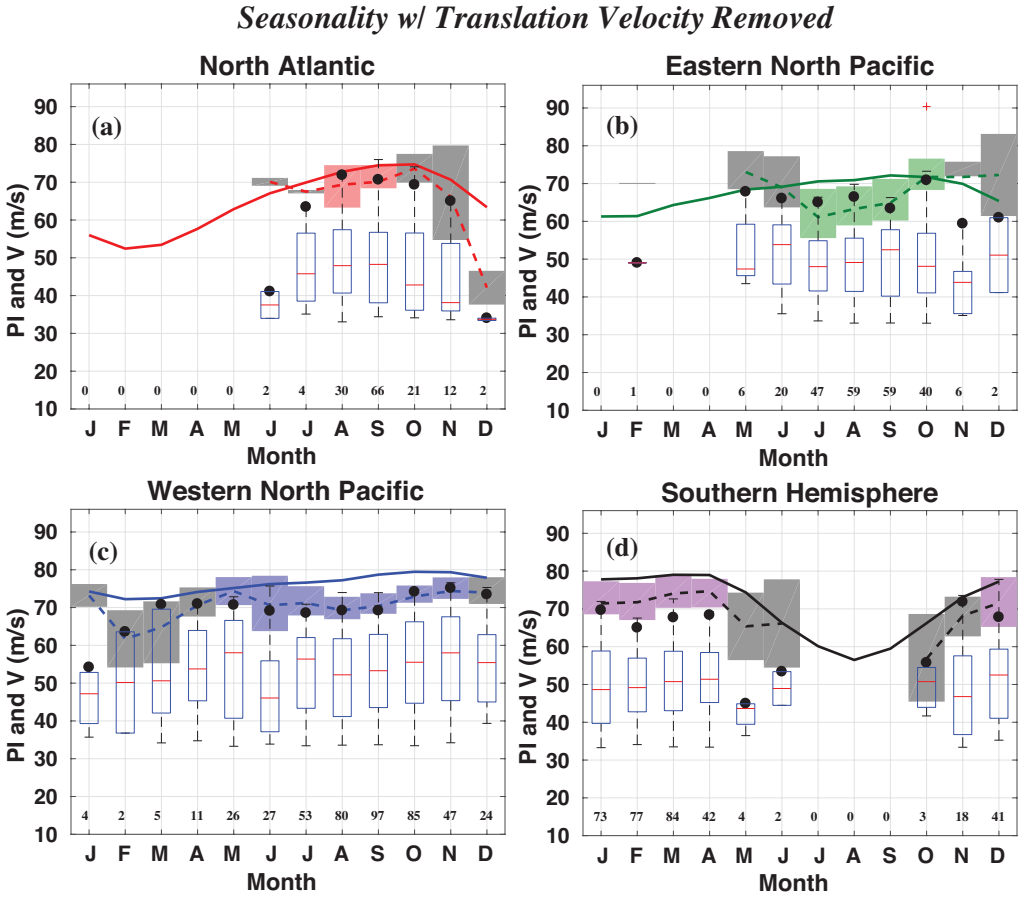

Figure 5-14: As in Fig. 5-6, but with translational velocities removed from V_{max}, for the (a) North Atlantic, (b) Eastern North Pacific, (c) Western North Pacific, and (d) Southern Hemisphere regions.

The extent to which accounting for the translation velocity affects TC intensity seasonal cycles varies by basin. Because V_{max} values are reduced by translation velocities, some storms are re-categorized to tropical storm strength, leading to reductions in storm frequencies that may consequently fall below the storm count threshold (e.g. October in the NA). The most notable decrease in the high percentiles of V_{max} are found in the SH region, where the maximum observed V_{max} values does not approach PI in April (suggesting a breakdown of potential intensity theory in those months). Even fewer landfalling storms than originally had $V_{max} > PI$ now have V_{max} values that exceed PI; this is most clearly seen in the NA highest V_{max} percentiles in August

and September. The NA seasonality now has even less seasonality in observed maximum intensity distributions in the early boreal autumn months, consistent with PI. ENP seasonality maintains its local minimum in the central boreal summer months, but it has shifted to July and has become more noisy. The WNP seasonality remains relatively flat in both observed winds and along-track PI. We conclude that the seasonal cycles of TC maximum intensity appear qualitatively robust to the neglect or inclusion of translation velocities.

Chapter 6

Conclusions

6.1 Summary and Key Results

I have explored the radiative processes and importance of the region trapped between the atmospheric layer filled with water and the atmospheric layer dominated by ozone. It is useful to summarize the novel contributions of this thesis and to reflect on the broad lessons learned at the tropopause interface.

I began with an investigation of water vapor and ozone radiative effects in the tropopause region. In stark contrast with the abundant water observed on the Blue Marble (Fig. 1-1a), water vapor concentrations are extremely limited at and above the tropopause. The dry overlying stratosphere, and very cold temperatures, make the tropopause region radiatively sensitive to even minor absolute concentration fluctuations (<0.5 ppmv) in water vapor. Although the shortwave absorption of ozone peaks at altitudes much higher in the stratosphere (where it completely dominates the thermal structure), the tropopause region is also radiatively sensitive to ozone variations. Observed tropopause region "abrupt drops" are large percentage swings in water vapor and ozone, making them ideal case studies of the signals of these radiative effects. Examining both the 2011 and 2000 abrupt drops in chapter 2 led us to the first key lesson in the thesis: **the structures of constituent anomalies are important for their radiative effects**. The isentropic poleward propagation of low water vapor concentrations following the 2011 abrupt drop accounts for nearly

half of the abrupt drop radiative forcing. In contrast, offsetting ozone radiative forcings between the tropics and high latitudes arises because of the ozone abrupt drop structure, which is driven by the advective relationship between ozone anomalies and stratospheric circulation. Another example of structural importance for radiative effects is found in the seasonal cycle, where ozone seasonality is much larger in the northern hemisphere tropics than the southern hemisphere, driving larger radiative responses there.

Furthermore, **it is important to think about the radiative effects of chemical constituents contextually**. While water vapor and ozone changes during the 2011 abrupt drop share a common origin in anomalous upwelling, their *combined* effects on temperatures are opposite-signed in the lower stratospheric and same-signed in the substratosphere. Ozone and water vapor effects have different timescales, however. Stratospheric water vapor reductions following the 2000 and 2011 abrupt drops were persistent (with long memory of very cold abrupt drop tropopause temperatures), driving radiative forcing which offset about 12% of anthropogenic carbon dioxide forcing over 1990-2013. In contrast, ozone concentrations in the abrupt drop period were driven by transient near-tropopause advection anomalies, resulting in less persistent radiative effects. A complete picture of abrupt drop period radiation requires full consideration the concurrent structures in water vapor and ozone.

Linked with anomaly structures was the finding that **tropopause region radiation often exhibits nonlocal effects**. These effects should particularly be considered when water vapor or ozone variance is not homogeneous. While this is not an entirely new result, my studies show several prime examples where nonlocal radiative effects cannot be ignored. For instance, the 2011 abrupt drops in water vapor and ozone combine to cool the substratosphere by up to half a degree kelvin. Additionally, the depth of the constituent changes considered is critical for their nonlocal impacts, allowing them to range from almost zero effect (considering only changes several layers above the tropopause) to very effective (considering changes all the way down to the layers below the tropopause). Discovering and elucidating these effects led us to wonder whether more consistent water vapor and ozone vertical structures, in par-

ticular their seasonal cycles, could have nonlocal implications. "Radiative seasonal cycles" (chapter 3) revealed that water vapor seasonal effects are largely confined to the immediate tropopause region, while the nonlocal effects from ozone seasonality above the tropopause are much more important. The majority of ozone's nonlocal impacts are derived from Planck feedback, where changes in shortwave radiation alter the layer temperature—and by extension the layer emission—which then radiatively impacts the surrounding layers. Overall, ozone amplifies tropopause temperature seasonal cycles by about 30%, and about a third of *that* radiative amplification is driven nonlocally by ozone seasonality above the tropopause region.

The first half of this thesis advances our understanding of the processes driving near-tropopause temperatures; in the second half of the thesis (chapters 4 and 5), these tropopause region temperatures are shown to be important for tropical cyclone potential intensities. I found that **the level of tropical cyclone outflow is critical for the interpretation of potential intensity**, especially in an annual cycle context and across different ocean basins. Often large monthly-mean variations in outflow level, as computed with the Bister and Emanuel (2002) algorithm, show that a fixed pressure-level proxy for the outflow level will not always be appropriate. This is especially true in basins like the North Atlantic, which has large seasonal cycles in sea surface temperatures and ocean mixed layer depth. In the Western North Pacific the climatological outflow level is found perennially near the tropopause, so in that region a fixed near-tropopause proxy level would be more fitting. An outflow level near the tropopause allows the tropopause region thermal structure to impact tropical cyclone potential intensities. Kelvin-for-kelvin tropical cyclone thermodynamic efficiency is more sensitive to outflow temperatures than sea surface temperatures, so the relative variance in these temperatures (and the monthly variability in climatological thermodynamic disequilibrium) determines how impactful the tropopause region thermal structure can be for tropical cyclones.

By computing the first comprehensive seasonal cycle climatology of tropical cyclone potential intensity, I determined that **the drivers of tropical cyclone intensity seasonal cycles vary from basin to basin**. In nearly all previous literature,

tropical cyclone potential intensity was evaluated by taking the mean over the typical "hurricane seasons" in each basin. But intense Western Pacific tropical cyclones may occur in any month, because the tropopause region thermal structure sets monthly climatological outflow temperatures that act to flatten the potential intensity seasonality. Moreover, although along-track intensity seasonal cycles in the North Atlantic and Southern Hemisphere regions do not vary much from month-to-month, the along-track intensity seasonal cycles in the Eastern and Western North Pacific basins have important differences from one month to the next. The delineation that I identified over the Pacific seasonal cycles wouldn't emerge from seasonal means, and month-to-month differences imply associated tropical cyclone impacts that otherwise wouldn't be quantified. Characterizing potential intensities of individual months also enabled comparisons between real-world tropical cyclone intensity and potential intensity in a brand-new context.

6.2 Open Questions

In this section, I highlight four big questions which are raised by my work and found at the tropopause interface. Each of these have appreciable ramifications for understanding and interpreting aspects of the Blue Marble's climate system.

6.2.1 Causes and Importance of Abrupt Drops

The 2000 and 2011 abrupt drops studied in chapter 2 had important implications for both the transient local thermal structure and climate forcing. The main drivers of these abrupt drops, however, were not investigated. Various physical explanations for their existence have been put forth. Randel et al. (2006), highlighted the 2000 temperature and water vapor reductions for the first time (and coined the term "abrupt drop" used in this thesis). They asserted that an increase in the speed of the Brewer-Dobson circulation (BDC) was responsible. Several studies have argued that a consequence of anthropogenic climate change is such an increase in stratospheric circulation (e.g. Butchart et al., 2006; McLandress and Shepherd, 2009; Butchart,

2014, and many others), and the proposed increase could manifest in temperature and water vapor reductions as a byproduct. Although models consistently predict increased stratospheric circulation, historical observational evidence has been mixed (e.g Engel et al., 2008; Garcia et al., 2011; Stiller et al., 2012), and novel approaches are being developed to continue probing this question with observations and reanalyses (Fu et al., 2015; Linz, 2017).

In contrast to this "top-down" perspective is the consideration of "bottom-up" impacts, where changes in (primarily) western and central Pacific convection could drive trends in tropopause region water vapor and temperature. Rosenlof and Reid (2008) framed this idea by showing a strong cooling trend in western Pacific sea surface temperatures correlated with temperature and water vapor reductions in the 2000 abrupt drop. A more recent thorough analysis by Ding and Fu (2017) details the physical mechanism for this, a Gill-like tropopause region response (Gill, 1980) to warm SSTs in the central Pacific. They find that this response explains about 30% of the 2000 abrupt drop water vapor changes. In the context of the seasonal cycle, this bottom-up approach may also be appealed to (with implications for analyses of potential intensity seasonality, for instance), and the zonally-asymmetries in the near-tropopause temperature seasonal cycles are indeed strongly linked to the bottom-up effects of equatorial waves (Grise et al. (2009), see Fig. 4-4 and Supplemental Fig. S6 of Gilford et al. (2017))

Other investigations have considered how the El Niño Southern Oscillation (ENSO) could affect large variability events in stratospheric water vapor (Calvo et al., 2004; Garfinkel et al., 2017, *and references therein*), though whether these effects are actually top-down (through ENSO's known impacts on stratospheric circulation), or bottom-up (through a tropical-wave response to anomalous SSTs), or both, is not entirely clear. ENSO definitions can also be disparate and have different associated effects (including, for instance, Modoki ENSO, e.g. Xie et al. (2014)) and ENSO effects may also be non-linear, making them more challenging to analyze in the water vapor record (Garfinkel et al., 2017).

Central to the investigation of what causes abrupt drops are their definitions

and time scales. While both 2000 and 2011 abrupt drops likely had transient local radiative effects on the tropopause region thermal structure (as I showed in chapter 2), the long-term impacts on the climate system through radiative forcing will be effective only if the observed water vapor reductions are persistent. The basis of our estimate that the 2000 abrupt drop offset about 12% of carbon dioxide forcing between 1990 and 2013 was that low water vapor concentrations were observed in the tropopause region over that multidecadal period. Short-term drops like that in 2011-2012 and more recently in 2016-2017 (Avery et al., 2017), are effective for significant climate forcing only in that they maintain the status quo of reduced water vapor prior to the 2000 drop (see section 2.3.4). Both the consequences and identification of the abrupt drop causes depend critically on their definitions. Dessler et al. (2014) suggested that the 2000 and 2011 drops were both short-term and resulted from a linear combination of Quasi-Biennial Oscillation (QBO) and BDC effects, but because these phenomena are not fully orthogonal to one another it is difficult to contextualize their result. Ding and Fu (2017) noted that the QBO is unable to explain early century long-term changes in water vapor because of its short time-scale of variability (about 22-34 months), but it should be relevant if the drop is very transient (such as that in 2011 and possibly 2016). Until there is more clarity on what drives these abrupt drops, studies should endeavor to be consistent in their definitions, and both top-down and bottom-up approaches should be explored.

The conflicting perspectives on abrupt drop timescales and drivers confound our ability to fully understand lower stratospheric water vapor in the context of climate change. Whether the 2000 abrupt drop, and the persistent low concentrations since then, are driven by internal variability or climate change (through BDC or SST changes) is important for future analyses and predictions. A review of pre-industrial control runs of high-top models with realistic stratospheres and interactive ozone (such as the Whole Atmosphere Community Climate Model, Marsh et al. (2013)) could help answer this question. Although the extent of "global warming hiatus" in the early 21st century is still being discussed (Karl et al., 2015; Medhaug et al., 2017), we do know that lower stratospheric water vapor played some role in reducing

radiative forcing over this period (chapter 2 and Wang et al., 2017), in addition to the prominent negative forcing of sulfuric volcanic aerosols (Solomon et al., 2011; Santer et al., 2014), and changes in ocean circulation and heat storage (McGregor et al., 2014).

This thesis does not address why the 2000 and 2011 abrupt drops occurred, but I have shown that they have important local and nonlocal impacts on the climate system. It is therefore critical that we maintain observing systems that can monitor upper tropospheric and lower stratospheric water vapor (Urban et al., 2014). Longer records may improve our understanding of what causes these abrupt drops, permit comparisons with models, and allow continued estimates of the radiative forcing attributable to lower stratospheric water vapor.

6.2.2 Relative Contributions of Near-tropopause Dynamics and Radiation

The primary assumption I used to estimate radiative responses to anomalies in water vapor and ozone in chapters 2 and 3 is seasonally-evolving fixed dynamical heating (SEFDH, e.g. Fels et al., 1980). In our context, SEFDH is used to estimate the radiative feedback to constituent anomalies; anomalies which principally arise from dynamical forcing in the first place (section 2.2.2). The assumption of fixed-dynamics, therefore, is not truly accurate, and in principle dynamical heating should also respond to radiative feedbacks (e.g. Ming et al., 2016). As noted in chapter 3, this implies that computed temperature adjustments (such as the ozone radiative seasonal cycles) are radiative upper bounds rather than comprehensive estimates.

Such a discrepancy makes interpretation of SEFDH results difficult. Seasonal cycle studies consistently indicate that the response to the tropopause region ozone seasonal cycle is always about a 30-35% amplification of local temperature seasonality, even when dynamics are allowed to adjust to the forcing (Chae and Sherwood, 2007; Fueglistaler et al., 2011; Birner and Charlesworth, 2017, and chapter 3). Meanwhile, a few studies have shown with budgetary considerations that radiation should

simply balance dynamical heating (e.g. Rosenlof, 1995; Abalos et al., 2013), but specific comparisons with anomalous periods in water vapor and ozone (e.g. chapter 2) cannot be made with this approach. The models used to estimate the dynamical response to radiative heating (e.g. Ming et al., 2016) are also sometimes suspect because their circulations may not match real-world circulations (the diagnostics of which are themselves uncertain, e.g. Wright and Fueglistaler, 2013).

The agreement between seasonal cycle studies is promising, and simple models have made some progress (Birner and Charlesworth, 2017), but the relative contributions of dynamical and radiative heating remains an unanswered question. How relevant the horizontal and vertical structures of constituent anomalies are for actual temperature structures—such as the northern hemisphere ozone radiative seasonal cycle (section 3.3.2) and its possible manifestation in observed temperatures, (Randel, 2003; Grise and Thompson, 2013)—depends strongly on the answer to this question, so it is critical to continue fundamental research in this area.

6.2.3 Uniformity and Maximum Intensities

Statistical analyses in Appendix A of chapter 5 revealed that the assumption that tropical cyclone normalized winds (i.e. observed maximum intensities divided by potential intensities) are drawn from a strictly uniform distribution is not always justified (section 5.5). In the North Atlantic region, a little more than half of randomly resampled distributions *could* be uniform, but in the other regions (Eastern North Pacific, Western North Pacific, and Southern Hemisphere) the null hypothesis that these distributions are uniform is almost always rejected at 95% confidence (regardless of resampling).

As pointed out by Wing et al. (2007), the shape of tropical cyclone distributions has implications for how the mean observed maximum intensity scales with changes in potential intensity. If the normalized wind distribution is a fixed shape, this implies that a percentage change in potential intensity (due to e.g. warming SSTs, cooling near-tropopause outflow temperatures, etc.) will shift the mean observed maximum intensities by the same percentage. If, however, the true distribution of normalized

winds has a different shape than that empirically derived, the implications for potential intensity changes will be different. For instance, if the shape of the Southern Hemisphere empirical distribution (where the upper tail normalized wind probabilities exceed the theoretical distribution) were for some reason to become more uniform under climate change (Fig. 5-4), then one might expect to observe fewer very intense storms as the shape changes. Additionally, if the distribution's lower bound (α) were to shift with climate change, then the shape of the distributions would also shift, along with the impacts of potential intensity changes on maximum intensity.

An interesting result by Webster et al. (2005) (and corroborated by Elsner et al., 2008) showed that historically the largest positive intensity trends were in the most intense (category 4 and 5) storms. When this result was revisited a decade later, however, it was not found to be robust to updates in the observational dataset (Klotzbach and Landsea, 2015). This highlights how critical observational capacity is in furthering our understanding of observed and future changes in tropical cyclone maximum intensity, and provides a clue as to how and why normalized wind distributions might change over time.

Complicating an understanding of normalized wind distributions are uncertainties in the potential and observed intensities upon which they rely. While the mismatch between the upper bound on normalized winds (β) and 1.0 may be a good bulk indicator of the ratio of enthalpy and drag coefficients $\frac{C_k}{C_D}$ (see section 4.2), it is not guaranteed that this ratio is a single value, it instead could have a distribution. Using operational rather than climatological potential intensities would also likely result in different distributions. Furthermore, the Dvorak (1975) technique relied upon for many observational estimates of tropical cyclone intensity (and most of the estimates in basins outside the North Atlantic) could affect the distributions by specifically limiting category 3 storms (Torn and Snyder, 2012). Finally, the (lack of) inclusion of translation velocities in observed estimates of tropical cyclone intensity—including within the Dvorak technique, which automatically incorporates climatological translation (Knaff et al., 2010; Velden et al., 2006)—could also play a role.

Central to this discussion is the fact that there are no unifying theories for why normalized wind distributions might be uniform. Emanuel (2000) noted that a negative feedback between tropical cyclone and its environment, such as the sea surface cooling feedback when a cyclone stirs the mixed layer (e.g. Schade and Emanuel, 1999; Lloyd and Vecchi, 2011), could be responsible. Whether using a modified potential intensity accounting for this interaction (e.g. that of Lin et al., 2013) would still show uniformity could be interesting to explore, but it is beyond the scope of this thesis. A closer look at the lower bound (α) could also provide more clarity (determining its properties would likely either result in, or arise from, a theory for normalized winds).

In this thesis I showed the value of assuming a theoretical uniform distribution from which tropical cyclone normalized intensities are drawn. Development of a unified theory for the distributions of normalized winds would improve our understanding of underlying uncertainties in empirical intensity estimates and increase our understanding of how climate change could affect tropical cyclone intensities.

6.2.4 Outflow Temperatures and Climate Change

The links between climate change and tropical cyclones are broad and often uncertain (e.g. Knutson et al., 2010; Walsh et al., 2016, *and references therein*). These include changes in destructive potential (e.g. Emanuel, 2005), track changes (e.g. Wang and Wu, 2015; Kossin, 2017), changes in seasonal frequency and genesis (e.g. Zhang et al., 2017), and many others. It is well established that future warming SSTs should increase tropical cyclone potential intensities (e.g. Henderson-Sellers et al., 1998; Holland and Bruyère, 2014; Strazzo et al., 2014; Walsh et al., 2016). In chapters 4 and 5 I found that outflow temperatures are critical to the seasonal cycles of potential intensity, which raises the question, "how will outflow temperatures respond to climate change?"

As noted above (section 6.2.1), stratospheric circulation is expected to increase with climate change (e.g. Butchart et al., 2006); such increases in circulation are expected to cool tropical lower stratospheric temperatures in the long-term (see the review in Seidel et al., 2011) in collaboration with ozone's radiative cooling (Polvani

and Solomon, 2012). Emanuel et al. (2013) showed that historically there appears to be a negative trend in tropical cyclone outflow temperatures which results in an overall strengthening in potential intensities, but this trend is not robust to the choice of dataset or reanalysis. One would hope that in-situ radiosonde observations (such as the RATPAC-lite, e.g. Randel et al., 2009) would improve these estimates, but we have discovered many discontinuities in these data because of changes in recording practices/instruments (Gilford and Randel, 2017; Randel and Wu, 2006; Sun et al., 2013, e.g. San Juan observations in Figure 6-1), and moreover these data are spatially sparse.

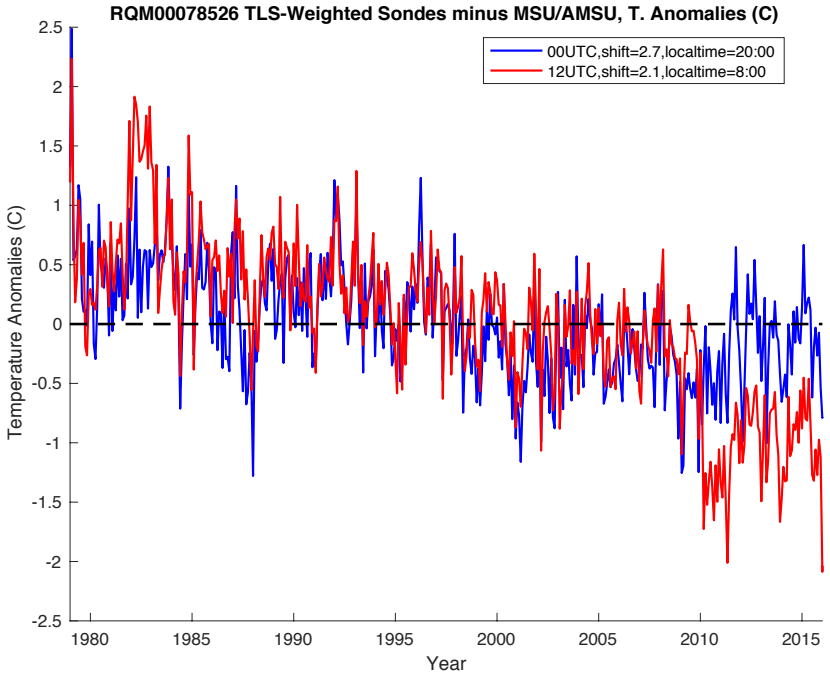

Figure 6-1: Differences between RSS MSU lower stratospheric temperatures (channel 4) and 00UTC (blue curve)/12UTC (red curve) San Juan radiosonde observations ('RQM00078526' from IGRA2, see Durre and Yin (2008)) integrated with the lower stratospheric MSU weighting. The ∼2010 jump in the 12UTC measurements indicates a strong radiosonde discontinuity, a result that is common in nearly every radiosonde record at some point (even those from RATPAC-lite). Figure reproduced from Gilford and Randel (2017).

Fu et al. (2010) found that a challenge in diagnosing changes in the strength of the BDC and lower stratospheric temperatures is that temperature trends are not equal across all months. While such a response to climate change makes deciphering annual

mean trends difficult, it is actually well suited for consideration in the seasonal cycle context of our chapter 4 results. Fu et al. (2010) show with Microwave Sounding Unit observation that the largest tropical lower stratospheric cooling trends in the satellite-era are found in the boreal summer, but this trend disappears in the boreal winter. The implication for potential intensity is a decreasing mid-summer depression effect, which would increase potential intensity in those months (and this particular effect may be contributing to the Hurricane-season average trends in Emanuel et al. (2013)). A cursory look at satellite-era trends of tropopause region temperatures in reanalyses data (which admittedly could be unreliable because of data assimilation discontinuities) suggests that outflow levels have largely increased in each basin between the 1980s and 2000s (following warming SSTs). But there are there are inconsistent seasonal responses in outflow/lower stratospheric temperatures between MERRA2 and ERA-I (not shown). How lower stratospheric trends (including intraseasonal trends) will manifest in the future in response to stratospheric circulation changes remains an active area of research.

Over the 21st century, warming SSTs, accompanying changes in the outflow levels, and cooling outflow temperatures will each be important for how potential intensity (and its seasonal cycles) respond to climate change. Establishing a clear understanding of what the basic historical climatology is, as I have herein, was a critical and necessary first step in answering this question. Better understanding of the physical mechanisms of stratospheric circulation, and verification of circulation changes with more certain observations, should light the way for how future potential intensity—and its implications for human societies—will change during this century.

6.3 Closing Remarks

At the risk of falling into reductionism, I imagine that the inquiries posed and explored in this thesis are unified by a simpler question, "How do distant physical phenomena affect me?" When a November supertyphoon devastates a Pacific island, do communities ponder how cold tropopause temperature pre-conditioned the inten-

sity of the storm? When the scientist wonders why temperatures are cooler at the turn of a century, is she awed by the powerful radiative influence of only a half a part per million drop in lower stratospheric water? When the psalmist considers "Who causes the vapors to ascend from the ends of the earth", is he aware of how far reaching and complicated and beautiful that contemplation is? Distant effects with local implications make the climate system simultaneously confusing and fascinating.

Reflecting a final time on the Blue Marble (Fig. 1-1), the sphere we call home appears isolated and vulnerable against the backdrop of the dark reaches of space. The vulnerability felt when viewing this image, however, is not a new sensation but a nostalgic one. As a species we have often experienced dangers posed by our environment which we could not see, but that had very real impacts on our lives. The interactions between the human and climate systems are not one-way. Rather, humans have significantly altered the color, ecosystems, energy, atmospheric chemistry, and hydrological cycle of our home planet. Often these effects are distant and their negative effects are not experienced by those who drive them (what economists call "externalities"). Much like a consideration of distant climate phenomena helps one understand their local realities, the more difficult—but more valuable—consideration of how one may distantly impact the lives and environments of others will enrich and progress our societies.

It is my hope that this thesis sparks in you, as it has in me, a newfound respect for the influences of the distant tropopause region on the climate system in which we live. While I have outlined several gaps in our understanding that need further exploration, there are many more challenges, especially with regards to human influences on the climate system, than I can expound upon here. Scientifically uncovering and societally meeting these climate obstacles is likely to be the defining challenge of our day; I pray future generations will look upon the distant "us" with grace-filled indulgence and, if we continue to make meaningful progress, gratitude.

Bibliography

Abalos, M., W. J. Randel, D. E. Kinnison, and E. Serrano, 2013: Quantifying tracer transport in the tropical lower stratosphere using WACCM. *Atmospheric Chemistry and Physics*, **13**, 10591–10607, doi:10.5194/acp-13-10591-2013.

Abalos, M., W. J. Randel, and E. Serrano, 2012: Variability in upwelling across the tropical tropopause and correlations with tracers in the lower stratosphere. *Atmospheric Chemistry and Physics*, **12**, 11505–11517, doi:10.5194/acp-12-11505-2012.

Aiyyer, A. and C. D. Thorncroft, 2006: Climatology of vertical wind shear over the tropical Atlantic. *Journal of Climate*, **19**, 2969–2983, doi:10.1175/JCLI3685.1.

Avery, M. A., S. M. Davis, K. H. Rosenlof, H. Ye, and A. E. Dessler, 2017: Large anomalies in lower stratospheric water vapour and ice during the 2015–2016 El Niño. *Nature Geoscience*, **10**, 405–410.

Bandoro, J., S. Solomon, A. Donohoe, D. W. J. Thompson, and B. D. Santer, 2014: Influences of the Antarctic Ozone Hole on Southern Hemispheric Summer Climate Change. *Journal of Climate*, **27**, 6245–6264, doi:10.1175/JCLI-D-13-00698.1.

Bathen, K. H., 1972: On the seasonal changes in the depth of the mixed layer in the north pacific ocean. *Journal of Geophysical Research*, **77**, 7138–7150, doi:10.1029/JC077i036p07138.

Berlin, F. U., 2016: The Quasi-Biennial Oscillation (QBO) data series. URL `http://www.geo.fu-berlin.de/en/met/ag/strat/produkte/qbo/`

Birner, T. and E. J. Charlesworth, 2017: On the relative importance of radiative and dynamical heating for tropical tropopause temperatures. *Journal of Geophysical Research: Atmospheres*, **122**, 6782–6797, doi:10.1002/2016JD026445, 2016JD026445.

Bister, M. and K. A. Emanuel, 1998: Dissipative heating and hurricane intensity. *Meteorology and Atmospheric Physics*, **65**, 233–240, doi:10.1007/BF01030791.

Bister, M. and K. a. Emanuel, 2002: Low frequency variability of tropical cyclone potential intensity 1. Interannual to interdecadal variability. *Journal of Geophysical Research: Atmospheres*, **107**, doi:10.1029/2001JD000776.

Bosilovich, M. G., R. Lucchesi, and M. Suarez, 2016: MERRA-2: File Specification. Technical report, GMAO Office Note 9 (version 1.1) - NASA.

Braconnot, P., O. Marti, S. Joussaume, and Y. Leclainche, 2000: Ocean feedback in response to 6 kyr BP insolation. *Journal of Climate*, **13**, 1537–1553, doi:10.1175/1520-0442(2000)013<1537:OFIRTK>2.0.CO;2.

Brasseur, G. P. and S. Solomon, 1986: *Aeronomy of the Middle Atmosphere*. Springer Netherlands, 452 pp.

Bretherton, C. S., M. Widmann, V. P. Dymnikov, J. M. Wallace, and I. Bladé, 1999: The effective number of spatial degrees of freedom of a time-varying field. *Journal of Climate*, **12**, 1990–2009, doi:10.1175/1520-0442(1999)012<1990:TENOSD>2.0.CO;2.

Brewer, A. W., 1949: Evidence for a world circulation provided by the measurements of helium and water vapour distribution in the stratosphere. *Quarterly Journal of the Royal Meteorological Society*, **75**, 351–363, doi:10.1002/qj.49707532603.

Briegleb, B. P., 1992: Delta-Eddington Approximation for Solar Radiation in the NCAR Community Climate Model. **97**, 7603–7612.

Bryan, G. H. and R. Rotunno, 2009: Evaluation of an analytical model for the maximum intensity of tropical cyclones. *Journal of the Atmospheric Sciences*, **66**, 3042–3060, doi:10.1175/2009JAS3038.1.

Butchart, N., 2014: The brewer-dobson circulation. *Reviews of Geophysics*, **52**, 157–184, doi:10.1002/2013RG000448.

Butchart, N., A. A. Scaife, M. Bourqui, J. Grandpré, S. H. E. Hare, J. Kettleborough, U. Langematz, E. Manzini, F. Sassi, K. Shibata, D. Shindell, and M. Sigmond, 2006: Simulations of anthropogenic change in the strength of the Brewer-Dobson circulation. *Climate Dynamics*, **27**, 727–741, doi:10.1007/s00382-006-0162-4.

Butler, J. H. and S. A. Montzka, 2015: The NOAA Annual Greenhouse Gas Index (AGGI).
URL `http://www.esrl.noaa.gov/gmd/aggi/aggi.html`

Calvo, N., Fernandez, E. H. Martin, R. R. Garcia, L. G. Presa, and P. R. Rodriguez, 2004: Analysis of the enso signal in tropospheric and stratospheric temperatures observed by msu, 1979-2000. *Journal of Climate*, **17**, 3934–3946, doi:10.1175/1520-0442(2004)017<3934:AOTESI>2.0.CO;2.

Chae, J. H. and S. C. Sherwood, 2007: Annual temperature cycle of the tropical tropopause: A simple model study. *Journal of Geophysical Research*, **112**, D19111, doi:10.1029/2006JD007956.

Chen, P., 1995: Isentropic cross-tropopause mass exchange in the extratropics. *Journal of Geophysical Research*, **100**, 16661–16673, doi:10.1029/95JD01264.

Collins, W. D., 1998: A global signature of enhanced shortwave absorption by clouds. *Journal of Geophysical Research*, **103**, 31669–31679, doi:10.1029/1998JD200022.

— 2002: An updated parameterization for infrared emission and absorption by water vapor in the National Center for Atmospheric Research Community Atmosphere Model. *Journal of Geophysical Research*, **107**, 4664, doi:10.1029/2001JD001365.

Conley, a. J., J.-F. Lamarque, F. Vitt, W. D. Collins, and J. Kiehl, 2013: PORT, a CESM tool for the diagnosis of radiative forcing. *Geoscientific Model Development*, **6**, 469–476, doi:10.5194/gmd-6-469-2013.

Cronin, T. W. and K. A. Emanuel, 2013: The climate time scale in the approach to radiative-convective equilibrium. *Journal of Advances in Modeling Earth Systems*, **5**, 843–849, doi:10.1002/jame.20049.

Crutcher, H. L., 1975: A Note on the Possible Misuse of the Kolmogorov-Smirnov Test. *Journal of Applied Meteorology and Climatology*, **14**, 1600–1603.

Das, S. S., M. V. Ratnam, K. N. Uma, K. V. Subrahmanyam, and I. A. Girach, 2015: Influence of tropical cyclones on tropospheric ozone: possible implications. *Atmospheric Chemistry and Physics (Discussions)*, **15**, 19305–19323, doi:10.5194/acpd-15-19305-2015.

Davis, S. M. and K. H. Rosenlof, 2013: User's guide to the Stratospheric Water and OzOne Satellite Homogenized (SWOOSH) data set.
URL `https://www.esrl.noaa.gov/csd/groups/csd8/swoosh/`

de Boyer Montegut, C., G. Madec, A. S. Fischer, A. Lazar, and D. Iudicone, 2004: Mixed layer depth over the global ocean: An examination of profile data and a profile-based climatology. *Journal of Geophysical Research: Oceans*, **109**, C12003, doi:10.1029/2004JC002378.

Dee, D. P., S. M. Uppala, a. J. Simmons, P. Berrisford, P. Poli, S. Kobayashi, U. Andrae, M. a. Balmaseda, G. Balsamo, P. Bauer, P. Bechtold, a. C. M. Beljaars, L. van de Berg, J. Bidlot, N. Bormann, C. Delsol, R. Dragani, M. Fuentes, a. J. Geer, L. Haimberger, S. B. Healy, H. Hersbach, E. V. Hólm, L. Isaksen, P. Kållberg, M. Köhler, M. Matricardi, a. P. McNally, B. M. Monge-Sanz, J.-J. Morcrette, B.-K. Park, C. Peubey, P. de Rosnay, C. Tavolato, J.-N. Thépaut, and F. Vitart, 2011: The ERA-Interim reanalysis: configuration and performance of the data assimilation system. *Quarterly Journal of the Royal Meteorological Society*, **137**, 553–597, doi:10.1002/qj.828.

DeMaria, M., M. DeMaria, J. Kaplan, and J. Kaplan, 1994: A Statistical Hurricane Intensity Prediction Scheme (SHIPS) for the Atlantic Basin. *Weather and Forecasting*, **9**, 209–220, doi:10.1175/1520-0434(1994)009<0209.

Deser, C., M. A. Alexander, S.-P. Xie, and A. S. Phillips, 2010: Sea Surface Temperature Variability: Patterns and Mechanisms. *Annu. Rev. Mar. Sci*, **2**, 115–143, doi:10.1146/annurev-marine-120408-151453.

Dessler, A., H. Ye, T. Wang, M. Schoeberl, L. Oman, A. Douglass, A. Butler, K. Rosenlof, S. Davis, and R. Portmann, 2016: Transport of ice into the stratosphere and the humidification of the stratosphere over the 21st century. *Geophysical Research Letters*, 1–7, doi:10.1002/2016GL067991.

Dessler, A. E., M. R. Schoeberl, T. Wang, S. M. Davis, and K. H. Rosenlof, 2013: Stratospheric water vapor feedback. *Proceedings of the National Academy of Sciences*, 1–5, doi:10.1073/pnas.1310344110.

Dessler, A. E., M. R. Schoeberl, T. Wang, S. M. Davis, K. H. Rosenlof, and J. Vernier, 2014: Variations of stratospheric water vapor over the past three decades. *Journal of Geophysical Research: Atmospheres*, **119**, 1–11, doi:10.1002/2014JD021712.

Dhomse, S., M. Weber, and J. Burrows, 2008: The relationship between tropospheric wave forcing and tropical lower stratospheric water vapor. *Atmos. Chem. Phys.*, **8**, 471–480.

Ding, Q. and Q. Fu, 2017: A warming tropical central Pacific dries the lower stratosphere. *Climate Dynamics*, 1–15, doi:10.1007/s00382-017-3774-y.

Dobson, G. M. B., 1956: A discussion on radiative balance in the atmosphere - origin and distribution of the polyatomic molecules in the atmosphere. *Proceedings of the Royal Society of London A: Mathematical, Physical and Engineering Sciences*, **236**, 187–193, doi:10.1098/rspa.1956.0127.

Donohoe, A. and D. S. Battisti, 2013: The seasonal cycle of atmospheric heating and temperature. *Journal of Climate*, **26**, 4962–4980, doi:10.1175/JCLI-D-12-00713.1.

Doyle, J. D., J. R. Moskaitis, J. W. Feldmeier, R. J. Ferek, M. Beaubien, M. M. Bell, D. L. Cecil, R. L. Creasey, P. Duran, R. L. Elsberry, W. A. Komaromi, J. Molinari, D. R. Ryglicki, D. P. Stern, C. S. Velden, X. Wang, T. Allen, B. S. Barrett, P. G. Black, J. P. Dunion, K. A. Emanuel, P. A. Harr, L. Harrison, E. A. Hendricks, D. Herndon, W. Q. Jeffries, S. J. Majumdar, J. A. Moore, Z. Pu, R. F. Rogers, E. R. Sanabia, G. J. Tripoli, and D.-L. Zhang, 2017: A view of tropical cyclones from above: The tropical cyclone intensity experiment. *Bulletin of the American Meteorological Society*, **98**, 2113–2134, doi:10.1175/BAMS-D-16-0055.1.

Durre, I. and X. Yin, 2008: Enhanced radiosonde data for studies of vertical structure. *Bulletin of the American Meteorological Society*, **89**, 1257–1262, doi:10.1175/2008BAMS2603.1.

Dvorak, V. F., 1975: Tropical Cyclone Intensity Analysis and Forecasting from Satellite Imagery. *Monthly Weather Review*, **103**, 420–430, doi:10.1175/1520-0493(1975)103<0420:TCIAAF>2.0.CO;2.

Efron, B. and G. Gong, 1983: A leisurely look at the bootstrap, the jackknife, and cross-validation. *The American Statistician*, **37**, 36–48, doi:10.1080/00031305.1983.10483087.

Elsner, J. B., J. P. Kossin, and T. H. Jagger, 2008: The increasing intensity of the strongest tropical cyclones. *Nature*, **455**, 92–95, doi:10.1038/nature07234.

Emanuel, K., S. Solomon, D. Folini, S. Davis, and C. Cagnazzo, 2013: Influence of Tropical Tropopause Layer Cooling on Atlantic Hurricane Activity. *Journal of Climate*, **26**, 2288–2301, doi:10.1175/JCLI-D-12-00242.1.

Emanuel, K. A., 1986: An Air-Sea Interaction Theory for Tropical Cyclones. Part I: Steady-State Maintenance. *Journal of the Atmospheric Sciences*, **43**, 585–605, doi:10.1175/1520-0469(1986)043<0585:AASITF>2.0.CO;2.

— 1991: The Theory Of Hurricanes. *Annual Review of Fluid Mechanics*, **23**, 179–196, doi:10.1146/annurev.fluid.23.1.179.

— 2000: A Statistical Analysis of Tropical Cyclone Intensity. *Monthly Weather Review*, **128**, 1139–1152, doi:10.1175/1520-0493(2000)128<1139:ASAOTC>2.0.CO;2.

— 2003: Tropical Cyclones. *Annual Review of Earth and Planetary Sciences*, **31**, 75–104, doi:10.1146/annurev.earth.31.100901.141259.

— 2005: Increasing destructiveness of tropical cyclones over the past 30 years. *Nature*, **436**, 686–688, doi:10.1038/nature03906.

— 2006: Climate and Tropical Cyclone Activity : A New Model Downscaling Approach. *Journal of Climate*, **19**, 4797–4802, doi:10.1175/JCLI3908.1.

— 2007: Environmental factors affecting tropical cyclone power dissipation. *Journal of Climate*, **20**, 5497–5509, doi:10.1175/2007JCLI1571.1.

Emanuel, K. A., S. Ravela, E. Vivant, and C. Risi, 2006: A statistical deterministic approach to hurricane risk assessment. *Bulletin of the American Meteorological Society*, **87**, 299–314, doi:10.1175/BAMS-87-3-299.

Engel, a., T. Möbius, H. Bönisch, U. Schmidt, R. Heinz, I. Levin, E. Atlas, S. Aoki, T. Nakazawa, S. Sugawara, F. Moore, D. Hurst, J. Elkins, S. Schauffler, A. Andrews, and K. Boering, 2008: Age of stratospheric air unchanged within uncertainties over the past 30 years. *Nature Geoscience*, **2**, 28–31, doi:10.1038/ngeo388.

Fels, S. B., J. D. Mahlman, M. D. Schwarzkopf, and R. W. Sinclair, 1980: Stratospheric Sensitivity to Perturbations in Ozone and Carbon Dioxide: Radiative and Dynamical Response. *Journal of the Atmospheric Sciences*, **37**, 2265–2297, doi:10.1175/1520-0469(1980)037<2265:SSTPIO>2.0.CO;2.

Folkins, I., P. Bernath, C. Boone, G. Lesins, N. Livesey, a. M. Thompson, K. Walker, and J. C. Witte, 2006: Seasonal cycles of O3 , CO, and convective outflow at the tropical tropopause. *Geophysical Research Letters*, **33**, L16802, doi:10.1029/2006GL026602.

Folkins, I., M. Loewenstein, J. Podolske, and J. Oltmans, 1999: A barrier to vertical mixing at 14 km in the tropics: Evidence from ozonesondes and aircraft measurements. *Journal of Geophysical Research*, **104**, 22095–22102.

Folkins, I., S. J. Oltmans, and A. M. Thompson, 2000: Tropical convective outflow and near surface equivalent potential temperatures. *Geophysical Research Letters*, **27**, 2549–2552.

Forster, P. M., G. Bodeker, R. Schofield, S. Solomon, and D. Thompson, 2007: Effects of ozone cooling in the tropical lower stratosphere and upper troposphere. *Geophysical Research Letters*, **34**, L23813, doi:10.1029/2007GL031994.

Forster, P. M., R. S. Freckleton, and K. P. Shine, 1997: On aspects of the concept of radiative forcing. *Climate Dynamics*, **13**, 547–560.

Forster, P. M. and K. P. Shine, 1997: Radiative forcing and temperature trends from stratospheric ozone changes. *Journal of Geophysical Research*, **102**, 10841–10855.

— 1999: Stratospheric water vapour changes as a possible contributor to observed stratospheric cooling. *Geophysical Research Letters*, **26**, 3309–3312, doi:10.1029/1999GL010487.

— 2002: Assessing the climate impact of trends in stratospheric water vapor. *Geophysical Research Letters*, **29**, 10–1–10–4, doi:10.1029/2001GL013909.

Frank, W. M. and E. A. Ritchie, 2001: Effects of Vertical Wind Shear on the Intensity and Structure of Numerically Simulated Hurricanes. *Monthly Weather Review*, **129**, 2249–2269, doi:10.1175/1520-0493(2001)129<2249:EOVWSO>2.0.CO;2.

Free, M., M. Bister, and K. Emanuel, 2004: Potential intensity of tropical cyclones: Comparison of results from radiosonde and reanalysis data. *Journal of Climate*, **17**, 1722–1727, doi:10.1175/1520-0442(2004)017<1722:PIOTCC>2.0.CO;2.

Frisius, T. and D. Schonemann, 2012: An extended model for the potential intensity of tropical cyclones. *Journal of the Atmospheric Sciences*, **69**, 641–661, doi:10.1175/JAS-D-11-064.1.

Fu, Q., P. Lin, S. Solomon, and D. L. Hartmann, 2015: Observational evidence of strengthening of the Brewer-Dobson circulation since 1980. *Journal of Geophysical Research: Atmospheres*, **120**, 10214–10228, doi:10.1002/2015JD023657.

Fu, Q., S. Solomon, and P. Lin, 2010: On the seasonal dependence of tropical lower-stratospheric temperature trends. *Atmospheric Chemistry and Physics*, **10**, 2643–2653, doi:10.5194/acp-10-2643-2010.

Fueglistaler, S., M. Bonazzola, P. H. Haynes, and T. Peter, 2005: Stratospheric water vapor predicted from the Lagrangian temperature history of air entering the stratosphere in the tropics. *Journal of Geophysical Research D: Atmospheres*, **110**, 1–10, doi:10.1029/2004JD005516.

Fueglistaler, S., A. E. Dessler, T. J. Dunkerton, I. Folkins, Q. Fu, and P. W. Mote, 2009a: Tropical Tropopause Layer (A review), 1–31. doi:10.1029/2008RG000267.1.

Fueglistaler, S. and Q. Fu, 2006: Impact of clouds on radiative heating rates in the tropical lower stratosphere. *Journal of Geophysical Research*, **111**, D23202, doi:10.1029/2006JD007273.

Fueglistaler, S. and P. H. Haynes, 2005: Control of interannual and longer-term variability of stratospheric water vapor. *Journal of Geophysical Research*, **110**, D24108, doi:10.1029/2005JD006019.

Fueglistaler, S., P. H. Haynes, and P. M. Forster, 2011: The annual cycle in lower stratospheric temperatures revisited. *Atmospheric Chemistry and Physics*, **11**, 3701–3711, doi:10.5194/acp-11-3701-2011.

Fueglistaler, S., B. Legras, A. C. M. Beljaars, J.-J. Morcrette, A. J. Simmons, A. M. Tompkins, and S. M. Uppala, 2009b: The diabatic heat budget of the upper troposphere and lower/mid stratosphere in ECMWF reanalyses. *Quarterly Journal of the Royal Meteorological Society*, **135**, 21–37.

Garcia, R. R., W. J. Randel, and D. E. Kinnison, 2011: On the Determination of Age of Air Trends from Atmospheric Trace Species. *Journal of the Atmospheric Sciences*, **68**, 139–154, doi:10.1175/2010JAS3527.1.

Garfinkel, C. I., A. Gordon, L. D. Oman, F. Li, S. Davis, and S. Pawson, 2017: Nonlinear response of tropical lower stratospheric temperature and water vapor to enso. *Atmospheric Chemistry and Physics Discussions*, **2017**, 1–35, doi:10.5194/acp-2017-520.

Garner, S., 2015: The Relationship between Hurricane Potential Intensity and CAPE. *Journal of the Atmospheric Sciences*, **72**, 141–163, doi:10.1175/JAS-D-14-0008.1.

Gebhardt, C., a. Rozanov, R. Hommel, M. Weber, H. Bovensmann, J. P. Burrows, D. Degenstein, L. Froidevaux, and a. M. Thompson, 2013: Stratospheric ozone trends and variability as seen by SCIAMACHY during the last decade. *Atmospheric Chemistry and Physics Discussions*, **13**, 11269–11313, doi:10.5194/acpd-13-11269-2013.

Gettelman, A., P. M. Forster, M. Fujiwara, Q. Fu, H. Vomel, L. K. Gohar, C. Johanson, and M. Ammerman, 2004: Radiation balance of the tropical tropopause layer. *Journal of Geophysical Research*, **109**, D07103, doi:10.1029/2003JD004190.

Gilford, D. M. and W. J. Randel, 2017: Analyzing nearly four decades of historical radiosonde observations of tropical tropopause layer and cold-point temperatures. Observations and Modeling of the Upper Troposphere and Lower Stratosphere III, AGU 2017 Fall Meeting.

Gilford, D. M. and S. Solomon, 2017: Radiative Effects of Stratospheric Seasonal Cycles in the Tropical Upper Troposphere and Lower Stratosphere. *J. Climate*, **30**, 2769–2783, doi:10.1175/JCLI-D-16-0633.1.

Gilford, D. M., S. Solomon, and K. A. Emanuel, 2017: On the Seasonal Cycles of Tropical Cyclone Potential Intensity. *J. Climate*, **30**, 6085–6096, doi:10.1175/JCLI-D-16-0827.1.

Gilford, D. M., S. Solomon, and R. W. Portmann, 2015: Radiative Impacts of the 2011 Abrupt Drops in Water Vapor and Ozone in the Tropical Tropopause Layer. *J. Climate*, **29**, 595–612, doi:10.1175/JCLI-D-15-0167.1.

Gill, A. E., 1980: Some simple solutions for heat-induced tropical circulation. *Quarterly Journal of the Royal Meteorological Society*, **106**, 447–462, doi:10.1002/qj.49710644905.

Gray, W. M., 1984: Atlantic Seasonal Hurricane Frequency. Part I: El Niño and 30 mb Quasi-Biennial Oscillation Influences. *Monthly Weather Review*, **112**, 1649–1668, doi:10.1175/1520-0493(1984)112<1649:ASHFPI>2.0.CO;2.

Grise, K. M. and D. W. Thompson, 2013: On the Signatures of Equatorial and Extratropical Wave Forcing in Tropical Tropopause Layer Temperatures. *Journal of the Atmospheric Sciences*, **70**, 1084–1102, doi:10.1175/JAS-D-12-0163.1.

Grise, K. M., D. W. J. Thompson, and P. M. Forster, 2009: On the Role of Radiative Processes in StratosphereâĂŞTroposphere Coupling. *Journal of Climate*, **22**, 4154–4161, doi:10.1175/2009JCLI2756.1.

Harries, J. E., J. M. R. Iii, A. F. Tuck, L. L. Gordley, P. Purcell, K. Stone, R. M. Bevilacqua, and W. A. Traub, 1996: Validation of measurements of water vapor from the Halogen Occultation Experiment (HALOE). *Journal of Geophysical Research*, **101**, 10205–10216.

Hartmann, D. L., J. R. Holton, and Q. Fu, 2001: The heat balance of the tropical tropopause, cirrus, and stratospheric dehydration. *Geophysical Research Letters*, **28**, 1969–1972.

Hegglin, M. I., S. Tegtmeier, J. Anderson, L. Froidevaux, R. Fuller, B. Funke, a. Jones, G. Lingenfelser, J. Lumpe, D. Pendlebury, E. Remsberg, a. Rozanov, M. Toohey, J. Urban, T. von Clarmann, K. a. Walker, R. Wang, and K. Weigel, 2013: SPARC Data Initiative: Comparison of water vapor climatologies from international satellite limb sounders. *Journal of Geophysical Research: Atmospheres*, **118**, 1–23, doi:10.1002/jgrd.50752.

Henderson-Sellers, A., H. Zhang, G. Berz, K. Emanuel, W. Gray, C. Landsea, G. Holland, J. Lighthill, S. L. Shieh, P. Webster, and K. McGuffie, 1998: Tropical Cyclones and Global Climate Change: A Post-IPCC Assessment. *Bulletin of the American Meteorological Society*, **79**, 19–38, doi:10.1175/1520-0477(1998)079<0019:TCAGCC>2.0.CO;2.

Hendricks, E. A., M. S. Peng, B. Fu, and T. Li, 2010: Quantifying Environmental Control on Tropical Cyclone Intensity Change. *Monthly Weather Review*, **138**, 3243–3271, doi:10.1175/2010MWR3185.1.

Hirota, I., 1980: Observational evidence of the semiannual oscillation in the tropical middle atmosphere-A review. *Pure and Applied Geophysics*, **118**, 217–238, doi:10.1007/BF01586452.

Hofmann, D. J., J. H. Butler, E. J. Dlugokencky, J. W. Elkins, K. Masarie, S. a. Montzka, and P. Tans, 2006: The role of carbon dioxide in climate forcing from 1979 to 2004: Introduction of the Annual Greenhouse Gas Index. *Tellus, Series B: Chemical and Physical Meteorology*, **58**, 614–619, doi:10.1111/j.1600-0889.2006.00201.x.

Holland, G. and C. L. Bruyère, 2014: Recent intense hurricane response to global climate change. *Climate Dynamics*, **42**, 617–627, doi:10.1007/s00382-013-1713-0.

Holland, G. J., 1997: The maximum potential intensity of tropical cyclones. *Journal of the Atmospheric Sciences*, **54**, 2519–2541, doi:10.1175/1520-0469(1997)054<2519:TMPIOT>2.0.CO;2.

Holton, J. R., P. H. Haynes, M. E. McIntyre, A. R. Douglass, R. B. Rood, and L. Pfister, 1995: Stratosphere-Troposphere Exchange. *Review of Gephysics*, **33, 4**, 403–439.

Huang, H.-C., J. Boucharel, I.-I. Lin, F.-F. Jin, C.-C. Lien, and I.-F. Pun, 2017: Air-sea fluxes for hurricane patricia (2015): Comparison with supertyphoon haiyan (2013) and under different enso conditions. *Journal of Geophysical Research: Oceans*, **122**, 6076–6089, doi:10.1002/2017JC012741.

IPCC, 2013: *Climate Change 2013: The Physical Science Basis. Contribution of Working Group I to the Fifth Assessment Report of the Intergovernmental Panel on Climate Change*. Cambridge University Press, Cambridge, United Kingdom and New York, NY, USA, 1535 pp.
URL `www.climatechange2013.org`

Jelesnianski, C. P., J. Chen, and W. A. Shaffer, 1992: SLOSH: Sea, lake, and overland surges from hurricanes. Technical report, NOAA Tech. Rep. NWS 48, NOAA AOML Library, Miami, Fla.

Johnson, N. C. and S.-P. Xie, 2010: Changes in the sea surface temperature threshold for tropical convection. *Nature Geosci*, **3**, 842–845.

Joshi, M. M. and G. S. Jones, 2009: The climatic effects of the direct injection of water vapour into the stratosphere by large volcanic eruptions. *Atmos. Chem. Phys.*, **9**, 6109–6118.

Joshi, M. M., M. J. Webb, a. C. Maycock, and M. Collins, 2010: Stratospheric water vapour and high climate sensitivity in a version of the HadSM3 climate

model. *Atmospheric Chemistry and Physics*, **10**, 7161–7167, doi:10.5194/acp-10-7161-2010.

Karl, T. R., A. Arguez, B. Huang, J. H. Lawrimore, J. R. McMahon, M. J. Menne, T. C. Peterson, R. S. Vose, and H.-M. Zhang, 2015: Possible artifacts of data biases in the recent global surface warming hiatus. *Science*, **348**, 1469–1472, doi:10.1126/science.aaa5632.

Kim, J. and S. W. Son, 2012: Tropical cold-point tropopause: Climatology, seasonal cycle, and intraseasonal variability derived from COSMIC GPS radio occultation measurements. *Journal of Climate*, **25**, 5343–5360, doi:10.1175/JCLI-D-11-00554.1.

Klotzbach, P. J. and C. W. Landsea, 2015: Extremely intense hurricanes: Revisiting Webster et al. (2005) after 10 years. *Journal of Climate*, **28**, 7621–7629, doi:10.1175/JCLI-D-15-0188.1.

Knaff, J. A., D. P. Brown, J. Courtney, G. M. Gallina, and J. L. Beven II, 2010: An Evaluation of Dvorak Technique - Based Tropical Cyclone Intensity Estimates. *Weather and Forecasting*, **25**, 1362–1379, doi:10.1175/2010WAF2222375.1.

Knapp, K. R., M. C. Kruk, D. H. Levinson, H. J. Diamond, and C. J. Nuemann, 2010: The International Best Track Archive for Climate Stewardship (IBTrACS). *Bulletin of the American Meteorological Society*, 215–221, doi:10.1007/978-90-481-3109-9-26.

Knutson, T. R., J. L. McBride, J. Chan, K. Emanuel, G. Holland, C. Landsea, I. Held, J. P. Kossin, A. K. Srivastava, and M. Sugi, 2010: Tropical cyclones and climate change. *Nature Geoscience*, **3**, 157–163.

Konczak, G., 2014: On the resampling method in sample median estimation. *Folia Oeconomica*, **3(302)**, 51–61.

Konopka, P., J.-U. Grooß, G. Günther, F. Ploeger, R. Pommrich, R. Müller, and N. Livesey, 2010: Annual cycle of ozone at and above the tropical tropopause: observations versus simulations with the Chemical Lagrangian Model of the Stratosphere (CLaMS). *Atmospheric Chemistry and Physics*, **10**, 121–132, doi:10.5194/acp-10-121-2010.

Konopka, P., J.-U. Grooß, F. Plöger, and R. Müller, 2009: Annual cycle of horizontal in-mixing into the lower tropical stratosphere. *Journal of Geophysical Research*, **114**, D19111, doi:10.1029/2009JD011955.

Kossin, J. P., 2015: Validating atmospheric reanalysis data using tropical cyclones as thermometers. *Bulletin of the American Meteorological Society*, **96**, 1089–1096, doi:10.1175/BAMS-D-14-00180.1.

— 2017: Hurricane intensification along United States coast suppressed during active hurricane periods. *Nature*, **541**, 390–394, doi:10.1038/nature20783.

Kossin, J. P. and S. J. Camargo, 2009: Hurricane track variability and secular potential intensity trends. *Climatic Change*, **97**, 329–337, doi:10.1007/s10584-009-9748-2.

Kossin, J. P., S. J. Camargo, and M. Sitkowski, 2010: Climate modulation of north atlantic hurricane tracks. *Journal of Climate*, **23**, 3057–3076, doi:10.1175/2010JCLI3497.1.

Kossin, J. P., T. L. Olander, and K. R. Knapp, 2013: Trend analysis with a new global record of tropical cyclone intensity. *Journal of Climate*, **26**, 9960–9976, doi:10.1175/JCLI-D-13-00262.1.

Kossin, J. P. and D. J. Vimont, 2007: A more general framework for understanding atlantic hurricane variability and trends. *Bulletin of the American Meteorological Society*, **88**, 1767–1781, doi:10.1175/BAMS-88-11-1767.

Lamarque, J. F. and S. Solomon, 2010: Impact of changes in climate and halocarbons on recent lower stratosphere ozone and temperature trends. *Journal of Climate*, **23**, 2599–2611, doi:10.1175/2010JCLI3179.1.

Landsea, C. W., 1993: A Climatology of Intense (or Major) Atlantic Hurricanes. *Monthly Weather Review*, **121**, 1703–1713, doi:10.1175/1520-0493(1993)121<1703:ACOIMA>2.0.CO;2.

Landsea, C. W. and J. L. Franklin, 2013: Atlantic hurricane database uncertainty and presentation of a new database format. *Monthly Weather Review*, **141**, 3576–3592, doi:10.1175/MWR-D-12-00254.1.

Lilliefors, H. W., 1967: On the Kolmogorov-Smirnov Test for Normality with Mean and Variance Unknown. *Journal of the American Statistical Association*, **62**, 399–402.

Lin, I.-I., P. Black, J. F. Price, C.-Y. Yang, S. S. Chen, C.-C. Lien, P. Harr, N.-H. Chi, C.-C. Wu, and E. A. D'Asaro, 2013: An ocean coupling potential intensity index for tropical cyclones. *Geophysical Research Letters*, **40**, 1878–1882, doi:10.1002/grl.50091.

Lin, N., K. Emanuel, M. Oppenheimer, and E. Vanmarcke, 2012: Physically based assessment of hurricane surge threat under climate change. *Nature Clim. Change*, **2**, 462–467.

Linz, M., 2017: *Age of Air and the Circulation of the Stratosphere*. Ph.D. thesis, MIT.

Liu, C., E. Zipser, T. Garrett, J. H. Jiang, and H. Su, 2007: How do the water vapor and carbon monoxide "tape recorders" start near the tropical tropopause? *Geophysical Research Letters*, **34**, 1–6, doi:10.1029/2006GL029234.

Livesey, N., W. G. Read, P. A.Wagner, L. Froidevaux, A. Lambert, G. L.Manney, L. F. Valle, H. C. Pumphrey, M. L. Santee, M. J. Schwartz, S. Wang, R. A. Fuller, R. F. Jarnot, B. W. Knosp, and E. Martinez, 2014: Aura Microwave Limb Sounder (MLS) Version 4.2x Level 2 data quality and description document. Technical report.

Lloyd, I. D. and G. A. Vecchi, 2011: Observational evidence for oceanic controls on hurricane intensity. *Journal of Climate*, **24**, 1138–1153, doi:10.1175/2010JCLI3763.1.

Maeda, K., 1987: Annual and semiannual oscillations of stratospheric ozone. *Pure and Applied Geophysics*, **125**, 147–165, doi:10.1007/BF00878619.

Marsh, D. R., M. J. Mills, D. E. Kinnison, J.-F. Lamarque, N. Calvo, and L. M. Polvani, 2013: Climate Change from 1850 to 2005 Simulated in CESM1(WACCM). *Journal of Climate*, **26**, 7372–7391, doi:10.1175/JCLI-D-12-00558.1.

Maycock, a. C., M. M. Joshi, K. P. Shine, S. M. Davis, and K. H. Rosenlof, 2014: The potential impact of changes in lower stratospheric water vapour on stratospheric temperatures over the past 30 years. *Quarterly Journal of the Royal Meteorological Society*, **140**, 2176–2185, doi:10.1002/qj.2287.

Maycock, a. C. and K. P. Shine, 2012: Stratospheric water vapor and climate: Sensitivity to the representation in radiation codes. *Journal of Geophysical Research*, **117**, D13102, doi:10.1029/2012JD017484.

Maycock, a. C., K. P. Shine, and M. M. Joshi, 2011: The temperature response to stratospheric water vapour changes. *Quarterly Journal of the Royal Meteorological Society*, **137**, 1070–1082, doi:10.1002/qj.822.

McAdie, C. J., C. W. Landsea, C. J. Neumann, J. E. David, E. S. Blake, and G. R. Hammer, 2009: Tropical Cyclones of the North Atlantic Ocean 1851-2006. *Historical Climatology Series*, **6**, 1–239.

McGregor, S., A. Timmermann, M. F. Stuecker, M. H. England, M. Merrifield, F.-F. Jin, and Y. Chikamoto, 2014: Recent Walker circulation strengthening and Pacific cooling amplified by Atlantic warming. *Nature Clim. Change*, **4**, 888–892.

McLandress, C. and T. G. Shepherd, 2009: Simulated Anthropogenic Changes in the Brewer-Dobson Circulation, Including Its Extension to High Latitudes. *Journal of Climate*, **22**, 1516–1540, doi:10.1175/2008JCLI2679.1.

McTaggart-Cowan, R., E. L. Davies, J. G. Fairman, T. J. Galarneau, and D. M. Schultz, 2015: Revisiting the 26.5 C sea surface temperature threshold for tropical cyclone development. *Bulletin of the American Meteorological Society*, **96**, 1929–1943, doi:10.1175/BAMS-D-13-00254.1.

Medhaug, I., M. B. Stolpe, E. M. Fischer, and R. Knutti, 2017: Reconciling controversies about the global warming hiatus. *Nature*, **545**, 41–47, doi:10.1038/nature22315.

Mendelsohn, R., K. Emanuel, S. Chonabayashi, and L. Bakkensen, 2012: The impact of climate change on global tropical cyclone damage. *Nature Climate Change*, **2**, 205–209, doi:10.1038/nclimate1357.

Merrill, R. T., 1988: Environmental Influences on Hurricane Intensification. *Journal of the Atmospheric Sciences*, **45**, 1678–1687, doi:10.1175/1520-0469(1988)045<1678:EIOHI>2.0.CO;2.

Ming, A., P. Hitchcock, and P. Haynes, 2016: The response of the lower stratosphere to zonally symmetric thermal and mechanical forcing. *Journal of the Atmospheric Sciences*, **73**, 1902–1922, doi:10.1175/JAS-D-15-0294.1.

Mitchell, T. P. and J. M. Wallace, 1992: The Annual Cycle in Equatorial Convection and Sea Surface Temperature. *Journal of Climate*, **5**, 1140–1156.

Mohapatra, M., 2014: Construction and quality of best tracks parameters for study of climate change impact on tropical cyclones over the North Indian Ocean during satellite era. Technical report, Monitoring and Prediction of Tropical Cyclones in the Indian Ocean and Climate Change.

Morcrette, J.-J., 1991: Radiation and cloud radiative properties in the European Centre for Medium Range Weather Forecasts forecasting system. *Journal of Geophysical Research*, **96**, 9121, doi:10.1029/89JD01597.

Morrisette, P. M., 2009: The evolution of policy responses to stratospheric ozone depletion. *Natural Resources Journal*, **29**, 793–820.

Mote, P. W., T. J. Dunkerton, M. E. McIntyre, E. a. Ray, P. H. Haynes, and J. M. Russell, 1998: Vertical velocity, vertical diffusion, and dilution by midlatitude air in the tropical lower stratosphere. *Journal of Geophysical Research*, **103**, 8651–8666, doi:10.1029/98JD00203.

Mote, P. W., K. H. Rosenlof, E. Mcintyre, E. S. Carr, J. C. Gille, R. Holton, S. Kinnersley, H. C. Pumphrey, M. Russell, and J. W. Wal, 1996: An atmospheric tape recorder: The imprint of tropical tropopause temperatures on stratospheric water vapor. *Journal Geophysical Research*, **101**, 3989–4006.

Neale, R. B., A. J. Conley, P. H. Lauritzen, D. L. Williamson, P. J. Rasch, S. J. Vavrus, M. A. Taylor, U. C. Berkeley, L. Berkeley, and S.-j. Lin, 2010: Description of the NCAR Community Atmosphere Model (CAM 4.0).

Newman, P. A. and J. E. Rosenfield, 1997: Stratospheric thermal damping times. *Geophysical Research Letters*, **24**, 433–436, doi:10.1029/96GL03720.

NHC, 2017: Tropical Cyclone Climatology. Accessed: 2017-10.
URL `http://www.nhc.noaa.gov/climo/`

Nuemann, C., 1993: "Global Overview" - Chapter 1" Global Guide to Tropical Cyclone Forecasting. Technical report.

Palmen, E., 1948: On the formation and structure of tropical hurricanes. *Geophysica 3.1*, 26–38, doi:10.3103/S1068373908060034.

Perliski, L. M., S. Solomon, and J. London, 1989: On the interpretation of seasonal variations of stratospheric ozone. *Planetary and Space Science*, **37**, 1527–1538, doi:10.1016/0032-0633(89)90143-8.

Persing, J. and M. T. Montgomery, 2003: Hurricane Superintensity. *Journal of the Atmospheric Sciences*, **60**, 2349–2371, doi:10.1175/1520-0469(2003)060<2349:HS>2.0.CO;2.

Pielke, R. A. J. and R. A. S. Pielke, 1997: *Hurricanes: Their Nature and Impacts on Society*. John Wiley and Sons, 279 pp.

Ploeger, F., S. Fueglistaler, J.-U. Grooß, G. Günther, P. Konopka, Y. Liu, R. Müller, F. Ravegnani, C. Schiller, a. Ulanovski, and M. Riese, 2011: Insight from ozone and water vapour on transport in the tropical tropopause layer (TTL). *Atmospheric Chemistry and Physics*, **11**, 407–419, doi:10.5194/acp-11-407-2011.

Ploeger, F., P. Konopka, R. Müller, S. Fueglistaler, T. Schmidt, J. C. Manners, J.-U. Grooß, G. Günther, P. M. Forster, and M. Riese, 2012: Horizontal transport affecting trace gas seasonality in the Tropical Tropopause Layer (TTL). *Journal of Geophysical Research*, **117**, D09303, doi:10.1029/2011JD017267.

Polvani, L. M., S. J. Camargo, and R. R. Garcia, 2016: The Importance of the Montreal Protocol in Mitigating the Potential Intensity of Tropical Cyclones. *Journal of Climate*, **29**, 2275–2289, doi:10.1175/JCLI-D-15-0232.1.

Polvani, L. M. and S. Solomon, 2012: The signature of ozone depletion on tropical temperature trends, as revealed by their seasonal cycle in model integrations with single forcings. *Journal of Geophysical Research*, **117**, 1–8, doi:10.1029/2012JD017719.

Powell, M. D., 1980: Evaluations of Diagnostic Marine Boundary-Layer Models Applied to Hurricanes. *Monthly Weather Review*, **108**, 757–766, doi:10.1175/1520-0493(1980)108<0757:EODMBL>2.0.CO;2.

Ramanathan, V. and R. E. Dickinson, 1979: The role of stratospheric ozone in the zonal and seasonal radiative energy balance of the earth-troposphere system. *Journal of Atmospheric Sciences*, **36**, 1084–1104.

Ramanathan, V. and P. Downey, 1986: A nonisothermal emissivity and absorptivity formulation for water vapor. *Journal of Geophysical Research*, **91**, 8649–8666.

Ramsay, H. a., 2013: The Effects of Imposed Stratospheric Cooling on the Maximum Intensity of Tropical Cyclones in Axisymmetric RadiativeâĂŞConvective Equilibrium. *Journal of Climate*, **26**, 9977–9985, doi:10.1175/JCLI-D-13-00195.1.

Randel, W. J., 2003: Thermal variability of the tropical tropopause region derived from GPS/MET observations. *Journal of Geophysical Research*, **108**, doi:10.1029/2002JD002595.

— 2010: Variability and Trends in Stratospheric Temperature and Water Vapor, 123–135.

Randel, W. J., R. R. Garcia, and F. Wu, 2002a: Time-Dependent Upwelling in the Tropical Lower Stratosphere Estimated from the Zonal-Mean Momentum Budget. *Journal of the Atmospheric Sciences*, **59**, 2141–2152.

Randel, W. J. and E. J. Jensen, 2013: Physical processes in the tropical tropopause layer and their roles in a changing climate. *Nature Geoscience*, **6**, 169–176, doi:10.1038/NGEO1733.

Randel, W. J., M. Park, F. Wu, and N. Livesey, 2007: A Large Annual Cycle in Ozone above the Tropical Tropopause Linked to the Brewer-Dobson Circulation. *Journal of the Atmospheric Sciences*, **64**, 4479–4488, doi:10.1175/2007JAS2409.1.

Randel, W. J., K. P. Shine, J. Austin, J. Barnett, C. Claud, N. P. Gillett, P. Keckhut, U. Langematz, R. Lin, C. Long, C. Mears, A. Miller, J. Nash, D. J. Seidel, D. W. J. Thompson, F. Wu, and S. Yoden, 2009: An update of observed stratospheric temperature trends. *Journal of Geophysical Research*, **114**, D02107, doi:10.1029/2008JD010421.

Randel, W. J. and F. Wu, 2006: Biases in Stratospheric and Tropospheric Temperature Trends Derived from Historical Radiosonde Data. *Journal of Climate*, **19**, 2094–2104.

— 2014: Variability of zonal mean tropical temperatures derived from a decade of GPS radio occultation data. *Journal of the Atmospheric Sciences*, **72**, 1261–1275, doi:10.1175/JAS-D-14-0216.1.

Randel, W. J., F. Wu, and R. Stolarski, 2002b: Changes in Column Ozone Correlated with the Stratospheric EP Flux. *Journal of the Meteorological Society of Japan*, **80**, 849–862, doi:10.2151/jmsj.80.849.

Randel, W. J., F. Wu, H. Vömel, G. E. Nedoluha, and P. Forster, 2006: Decreases in stratospheric water vapor after 2001: Links to changes in the tropical tropopause and the Brewer-Dobson circulation. *Journal of Geophysical Research*, **111**, D12312, doi:10.1029/2005JD006744.

Rappaport, E. N., 2014: Fatalities in the united states from atlantic tropical cyclones: New data and interpretation. *Bulletin of the American Meteorological Society*, **95**, 341–346, doi:10.1175/BAMS-D-12-00074.1.

Ratnam, V. M., R. S. Babu, S. S. Das, G. Basha, B. V. Krishnamurthy, and B. Venkateswararao, 2016: Effect of tropical cyclones on the stratosphere-troposphere exchange observed using satellite observations over the north Indian

Ocean. *Atmospheric Chemistry and Physics*, **16**, 8581–8591, doi:10.5194/acp-16-8581-2016.

Rayner, N. A., D. E. Parker, E. B. Horton, C. K. Folland, L. V. Alexander, D. P. Rowell, E. C. Kent, and A. Kaplan, 2003: Global analyses of sea surface temperature, sea ice, and night marine air temperature since the late nineteenth century. *Journal of Geophysical Research: Atmospheres*, **108**, doi:10.1029/2002JD002670.

Reed, R. J., 1962: Some features of the annual temperature regime in the tropical stratosphere. *Monthly Weather Review*, **90**, 211–215.

Reed, R. J. and C. L. Vlcek, 1969: The annual temperature variation in the lower tropical stratosphere. *Journal of Atmospheric Sciences*, **26**, 163–167, doi:10.1175/1520-0469(1969)026<0163:TATVIT>2.0.CO;2.

Reichler, T., M. Dameris, and R. Sausen, 2003: Determining the tropopause height from gridded data. *Geophysical Research Letters*, **30**, doi:10.1029/2003GL018240.

Reid, G. C., 1994: Seasonal and interannual temperature variations in the tropical stratosphere. *Journal of Geophysical Research*, **99**, 18923–18932.

Rios-Berrios, R. and R. D. Torn, 2017: Climatological Analysis of Tropical Cyclone Intensity Changes under Moderate Vertical Wind Shear. *Monthly Weather Review*, **145**, 1717–1738, doi:10.1175/MWR-D-16-0350.1.

Rogers, R. F., S. Aberson, M. M. Bell, D. J. Cecil, J. D. Doyle, T. B. Kimberlain, J. Morgerman, L. K. Shay, and C. Velden, 2017: Rewriting the tropical record books: The extraordinary intensification of hurricane patricia (2015). *Bulletin of the American Meteorological Society*, **98**, 2091–2112, doi:10.1175/BAMS-D-16-0039.1.

Romps, D. M. and Z. Kuang, 2009: Overshooting convection in tropical cyclones. *Geophysical Research Letters*, **36**, 1–5, doi:10.1029/2009GL037396.

Rosenlof, K. H., 1995: Seasonal cycle of the residual mean meridional circulation in the stratosphere. *Journal of Geophysical Research*, **100**, doi:10.1029/94JD03122.

Rosenlof, K. H. and G. C. Reid, 2008: Trends in the temperature and water vapor content of the tropical lower stratosphere: Sea surface connection. *Journal of Geophysical Research*, **113**, D06107, doi:10.1029/2007JD009109.

Rosenlof, K. H., A. F. Tuck, K. K. Kelly, J. M. Russell, and M. P. McCormick, 1997: Hemispheric asymmetries in water vapor and inferences about transport in the lower stratosphere. *Journal of Geophysical Research*, **102**, doi:10.1029/97JD00873.

Santer, B., J. Boyle, and J. Hnilo, 2000: Statistical significance of trends and trend differences in layer-average atmospheric temperature time series. *Journal of Geophysical Research*, **105**, 7337–7356.

Santer, B. D., C. Bonfils, J. F. Painter, M. D. Zelinka, C. Mears, S. Solomon, G. A. Schmidt, J. C. Fyfe, J. N. S. Cole, L. Nazarenko, K. E. Taylor, and F. J. Wentz, 2014: Volcanic contribution to decadal changes in tropospheric temperature. *Nature Geoscience*, **7**, 185–189.

Schade, L. R. and K. A. Emanuel, 1999: The ocean's effect on the intensity of tropical cyclones: Results from a simple coupled atmosphere-ocean model. *Journal of the Atmospheric Sciences*, **56**, 642–651.

Schneider, E. K. and Z. Zhu, 1998: Sensitivity of the simulated annual cycle of sea surface temperature in the equatorial Pacific to sunlight penetration. *Journal of Climate*, **11**, 1932–1950, doi:10.1175/1520-0442(1998)011<1932:SOTSAC>2.0.CO;2.

Schoeberl, M. R. and a. E. Dessler, 2011: Dehydration of the stratosphere. *Atmospheric Chemistry and Physics*, **11**, 8433–8446, doi:10.5194/acp-11-8433-2011.

Schoeberl, M. R., A. R. Douglass, P. A. Newman, L. R. Lait, D. Lary, J. Waters, N. Livesey, L. Froidevaux, A. Lambert, W. Read, M. J. Filipiak, and H. C. Pumphrey, 2008: QBO and annual cycle variations in tropical lower stratosphere trace gases from HALOE and Aura MLS observations. *Journal of Geophysical Research*, **113**, D05301, doi:10.1029/2007JD008678.

Schoeberl, M. R., B. N. Duncan, a. R. Douglass, J. Waters, N. Livesey, W. Read, and M. Filipiak, 2006: The carbon monoxide tape recorder. *Geophysical Research Letters*, **33**, L12811, doi:10.1029/2006GL026178.

Schott, F. A. and J. P. McCreary, 2001: The monsoon circulation of the Indian Ocean. *Progress in Oceanography*, **51**, 1–123, doi:10.1016/S0079-6611(01)00083-0.

Schott, F. A., S.-P. Xie, and J. P. McCreary, 2009: Indian ocean circulation and climate variability. *Reviews of Geophysics*, **47**, RG1002, doi:10.1029/2007RG000245.

Seidel, D., N. P. Gillett, J. Lanzante, K. P. Shine, and P. Thorne, 2011: Stratospheric temperature trends: Our evolving understanding. *Wiley Interdisciplinary Reviews: Climate Change*, **2**, 592 – 616.

Shindell, D. T., 2001: Climate and ozone response to increased statospheric water vapor. *Geophys. Res. Lett.*, **28**, 1551–1554.

Sobel, A. H. and S. J. Camargo, 2011: Projected Future Seasonal Changes in Tropical Summer Climate. *Journal of Climate*, **24**, 473–487, doi:10.1175/2010JCLI3748.1.

Sobel, A. H., S. J. Camargo, T. M. Hall, C.-y. Lee, M. K. Tippett, and A. A. Wing, 2016: Human influence on tropical cyclone intensity. *Science*, **353**, 242–246.

Solomon, S., J. S. Daniel, R. R. Neely 3rd, J. P. Vernier, E. G. Dutton, and L. W. Thomason, 2011: The persistently variable "background" stratospheric aerosol layer and global climate change. *Science*, **333**, 866–870, doi:10.1126/science.1206027.

Solomon, S., K. H. Rosenlof, R. W. Portmann, J. S. Daniel, S. M. Davis, T. J. Sanford, and G.-K. Plattner, 2010: Contributions of stratospheric water vapor to decadal changes in the rate of global warming. *Science (New York, N.Y.)*, **327**, 1219–23, doi:10.1126/science.1182488.

Sopko, S. P. and R. J. Falvey, 2014: Annual tropical cyclone report. Technical report, Joint Typhoon Warning Center Rep.
URL `https://metoc.ndbc.noaa.gov/ProductFeeds-portlet/img/jtwc/atcr/2014atcr.pdf`

Stiller, G. P., T. von Clarmann, F. Haenel, B. Funke, N. Glatthor, U. Grabowski, S. Kellmann, M. Kiefer, a. Linden, S. Lossow, and M. López-Puertas, 2012: Observed temporal evolution of global mean age of stratospheric air for the 2002 to 2010 period. *Atmospheric Chemistry and Physics*, **12**, 3311–3331, doi:10.5194/acp-12-3311-2012.

Stolarski, R. S., D. W. Waugh, L. Wang, L. D. Oman, A. R. Douglass, Newman, and P. A., 2014: Seasonal variation of ozone in the tropical lower stratosphere: Southern tropics are different from northern tropics. *Journal of Geophysical Research: Atmospheres*, **119**, 6196–6206, doi:10.1002/2013JD021294.

Strazzo, S. E., J. B. Elsner, and T. E. LaRow, 2014: Quantifying the sensitivity of maximum, limiting, and potential tropical cyclone intensity to SST: Observations versus the FSU/ COAPS global climate model. *Journal of Advances in Modeling Earth Systems*, **6**, 513–526, doi:10.1002/2013MS000282.Received.

Stuber, N., R. Sausen, and M. Ponater, 2001: Stratosphere adjusted radiative forcing calculations in a comprehensive climate model. *Theor. Appl. Climatol.*, **135**, 125–135.

Sun, B., A. Reale, S. Schroeder, D. J. Seidel, and B. Ballish, 2013: Toward improved corrections for radiation-induced biases in radiosonde temperature observations. *Journal of Geophysical Research: Atmospheres*, **118**, 4231–4243, doi:10.1002/jgrd.50369.

Swanson, K. L., 2008: Nonlocality of Atlantic tropical cyclone intensities. *Geochemistry, Geophysics, Geosystems*, **9**, doi:10.1029/2007GC001844.

Tang, B. and K. Emanuel, 2012: A ventilation index for tropical cyclones. *Bulletin of the American Meteorological Society*, **93**, 1901–1912, doi:10.1175/BAMS-D-11-00165.1.

Tegtmeier, S., M. I. Hegglin, J. Anderson, a. Bourassa, S. Brohede, D. Degenstein, L. Froidevaux, R. Fuller, B. Funke, J. Gille, a. Jones, Y. Kasai, K. Krüger, E. Kyrölä, G. Lingenfelser, J. Lumpe, B. Nardi, J. Neu, D. Pendlebury, E. Remsberg, a. Rozanov, L. Smith, M. Toohey, J. Urban, T. von Clarmann, K. a. Walker,

and R. H. J. Wang, 2013: SPARC Data Initiative: A comparison of ozone climatologies from international satellite limb sounders. *Journal of Geophysical Research: Atmospheres*, **118**, 12229–12247, doi:10.1002/2013JD019877.

Thompson, D. W. J. and S. Solomon, 2009: Understanding Recent Stratospheric Climate Change. *Journal of Climate*, **22**, 1934–1943, doi:10.1175/2008JCLI2482.1.

Thuburn, J. and G. C. Craig, 2002: On the temperature structure of the tropical substratosphere. *Journal Geophysical Research*, **107**, 1–10.

Tippett, M. K., S. J. Camargo, and A. H. Sobel, 2011: A poisson regression index for tropical cyclone genesis and the role of large-scale vorticity in genesis. *Journal of Climate*, **24**, 2335–2357, doi:10.1175/2010JCLI3811.1.

Tonkin, H., G. J. Holland, N. Holbrook, and A. Henderson-Sellers, 2000: An Evaluation of Thermodynamic Estimates of Climatological Maximum Potential Tropical Cyclone Intensity. *Monthly Weather Review*, **128**, 746–762, doi:10.1175/1520-0493(2000)128<0746:AEOTEO>2.0.CO;2.

Torn, R. D. and C. Snyder, 2012: Uncertainty of Tropical Cyclone Best-Track Information. *Weather and Forecasting*, **27**, 715–729, doi:10.1175/WAF-D-11-00085.1.

Ueyama, R. and J. M. Wallace, 2010: To What Extent Does High-Latitude Wave Forcing Drive Tropical Upwelling in the Brewer-Dobson Circulation? *Journal of the Atmospheric Sciences*, **67**, 1232–1246, doi:10.1175/2009JAS3216.1.

Urban, J., S. Lossow, G. P. Stiller, and W. Read, 2014: Another Drop in Water Vapor. **95**, doi:10.1002/jgrd.50157.Fig.

Vecchi, G. A., T. Delworth, R. Gudgel, S. Kapnick, A. Rosati, A. T. Wittenberg, F. Zeng, W. Anderson, V. Balaji, K. Dixon, L. Jia, H. S. Kim, L. Krishnamurthy, R. Msadek, W. F. Stern, S. D. Underwood, G. Villarini, X. Yang, and S. Zhang, 2014: On the seasonal forecasting of regional tropical cyclone activity. *Journal of Climate*, **27**, 7994–8016, doi:10.1175/JCLI-D-14-00158.1.

Vecchi, G. A. and B. J. Soden, 2007a: Effect of remote sea surface temperature change on tropical cyclone potential intensity. **450**, 1066–1071, doi:10.1038/nature06423.

— 2007b: Effect of remote sea surface temperature change on tropical cyclone potential intensity. *Nature*, **450**, 1066–1070.

Velden, C., B. Harper, F. Wells, J. L. Beven, R. Zehr, T. Olander, M. Mayfield, C. C. Guard, M. Lander, R. Edson, L. Avila, A. Burton, M. Turk, A. Kikuchi, A. Christian, P. Caroff, and P. McCrone, 2006: The Dvorak tropical cyclone intensity estimation technique: A satellite-based method that has endured for over 30 years. *Bulletin of the American Meteorological Society*, **87**, 1195–1210, doi:10.1175/BAMS-87-9-1195.

Walsh, K. J. E., J. L. Mcbride, P. J. Klotzbach, S. Balachandran, S. J. Camargo, G. Holland, T. R. Knutson, J. P. Kossin, T. cheung Lee, A. Sobel, and M. Sugi, 2016: Tropical cyclones and climate change. *Wiley Interdisciplinary Reviews: Climate Change*, **7**, 65–89, doi:10.1002/wcc.371.

Wang, C. and L. Wu, 2015: Influence of future tropical cyclone track changes on their basin-wide intensity over the western north pacific: Downscaled cmip5 projections. *Advances in Atmospheric Sciences*, **32**, 613–623, doi:10.1007/s00376-014-4105-4.

Wang, S., S. J. Camargo, A. H. Sobel, and L. M. Polvani, 2014: Impact of the Tropopause Temperature on the Intensity of Tropical Cyclones: An Idealized Study Using a Mesoscale Model. *Journal of the Atmospheric Sciences*, **71**, 4333–4348, doi:10.1175/JAS-D-14-0029.1.

Wang, W., K. Matthes, N.-E. Omrani, and M. Latif, 2016: Decadal variability of tropical tropopause temperature and its relationship to the Pacific Decadal Oscillation. *Scientific Reports*, **6**, doi:10.1038/srep29537.

Wang, Y., Y. Rao, Z.-M. Tan, and D. Schönemann, 2015: A Statistical Analysis of the Effects of Vertical Wind Shear on Tropical Cyclone Intensity Change over the Western North Pacific. *Monthly Weather Review*, **143**, 3434–3453, doi:10.1175/MWR-D-15-0049.1.

Wang, Y., H. Su, J. H. Jiang, N. J. Livesey, M. L. Santee, L. Froidevaux, W. G. Read, and J. Anderson, 2017: The linkage between stratospheric water vapor and surface temperature in an observation-constrained coupled general circulation model. *Climate Dynamics*, **48**, 2671–2683, doi:10.1007/s00382-016-3231-3.

Webster, P. J., G. J. Holland, J. A. Curry, and H.-R. Chang, 2005: Changes in Tropical Cyclone Number, Duration, and Intensity in a Warming Environment. *Science*, **309**, 1844–1846, doi:10.1126/science.1116448.

Wenshou, T., 2009: Impact of Increasing Stratospheric Water Vapor. *Advances in Atmospheric Sciences*, **26**, 423–437, doi:10.1007/s00376-009-0423-3.1.

Wilks, D. S., 1995: *Statistical methods in the atmospheric sciences*. Academic Press San Diego.

Wing, A. A., K. Emanuel, and S. Solomon, 2015: On the factors affecting trends and variability in tropical cyclone potential intensity. *Geophysical Research Letters*, **42**, 8669–8677, doi:10.1002/2015GL066145.

Wing, A. A., A. H. Sobel, and S. J. Camargo, 2007: Relationship between the potential and actual intensities of tropical cyclones on interannual time scales. *Geophysical Research Letters*, **34**, 1–5, doi:10.1029/2006GL028581.

WMO, 1957: A three-dimensional science. *WMO Bull.*, **4**, 134–138.

Wright, J. S. and S. Fueglistaler, 2013: Large differences in the diabatic heat budget of the tropical UTLS in reanalyses. *Atmospheric Chemistry and Physics Discussions*, **13**, 8805–8830, doi:10.5194/acpd-13-8805-2013.

Wyrtki, K., 1961: Physical Oceanography of the Southeast Asian waters. Technical report, Scripps Institute of Oceanography NAGA Rep. 2.

— 1989: Some thoughts about the West Pacific warm pool. *Proc. of Western Pacific International Meeting and Workshop on TOGA COARE*, 99–109.

Xie, F., J. Li, W. Tian, Y. Li, and J. Feng, 2014: Indo-pacific warm pool area expansion, modoki activity, and tropical cold-point tropopause temperature variations. *Nature Scientific Reports*, **4**, 1–9.

Yulaeva, E., J. R. Holton, and J. M. Wallace, 1994: On the Cause of the Annual Cycle in Tropical Lower-Stratospheric Temperatures. *Journal of the Atmospheric Sciences*, **51**, 169–174, doi:10.1175/1520-0469(1994)051<0169:OTCOTA>2.0.CO;2.

Zeng, Z., Y. Wang, and C.-C. Wu, 2007: Environmental Dynamical Control of Tropical Cyclone Intensity - An Observational Study. *Monthly Weather Review*, **135**, 38–59, doi:10.1175/MWR3278.1.

Zhang, X., S. Zhong, Z. Wu, and Y. Li, 2017: Seasonal prediction of the typhoon genesis frequency over the western north pacific with a poisson regression model. *Climate Dynamics*, doi:10.1007/s00382-017-3654-5.

Zhong, W. and J. D. Haigh, 1995: Improved Broadband Emissivity Parameterization for Water Vapor Cooling Rate Calculations. *Journal of Atmospheric Sciences*, **52**, 124–138, doi:10.1175/1520-0469(1995)052<0124:IBEPFW>2.0.CO;2.

Zickfeld, K., S. Solomon, and D. M. Gilford, 2017: Centuries of thermal sea-level rise due to anthropogenic emissions of short-lived greenhouse gases. *Proc. Nat. Acad. Sci. USA*, **114**, 657–662, doi:10.1073/pnas.1612066114.